1-1-2015

Surface Chemistry Mediated Assembly of Polymer-Grafted Nanorods in Solution and Polymer Matrices

Robert Charles Ferrier
University of Pennsylvania, rferrier@seas.upenn.edu

Surface Chemistry Mediated Assembly of Polymer-Grafted Nanorods in Solution and Polymer Matrices

Abstract
In the dissertation, I investigate ways to assemble nanorods, typically made of gold, in solution and polymer matrices by controlling surface chemistry. Gold nanorods were anisotropically functionalized with polymer on the side and alkane dithiol on the end causing the gold nanorods to spontaneously assemble in solution. The assembly could be tuned by controlling the incubation time which affected the solution absorbance due to plasmon coupling. Linked gold nanorods were cast in polymer thin films and their optical properties were imparted to the film. This anisotropic functionalization method was utilized to placed DNA or peptides on the ends of the gold nanorods allowing for reversibly assembly. In the case of DNA, assembly was reversed upon heating and could be tuned by controlling the concentration of the complimentary DNA strand. In the case of the peptide, assembly was triggered by the presence of Zn2+ ions and could be reversed by adding in a chelater. Anisotropic modification of the nanorods could also be used to assemble organic semiconductors around the nanorods at specific facets. Here, organic semiconductors rhodamine-B, 5(6)-carboxyfluorescein, and cyanine-3 were assembled onto the surface of gold nanorods. By tuning the surface chemistry the organic semiconductors would assemble around the nanorods in different ways which resulted in unique optical properties. The dispersion of PMMA-grafted mesoscopic iron-oxide rods in polymer matrices was studied by varying the PMMA brush molecular weight (N) polymer matrix molecular weight (P), and polymer matrix type. Here, we found that the ratio of P/N and matrix type had little effect on dispersion of iron-oxide mesorods. N was found to be the main factor that determined dispersion, which is attributed to the large size of the mesorods. Long PS and short PMMA brushes were grafted to gold nanorod surfaces and the dispersion of this system in PS and PMMA was investigated by controlling matrix molecular weight. We found that the gold nanorods would disperse in PS matrices 24 times larger than the grafted brush, while in PMMA matrices the nanorods would aggregate. SCFT calculations revealed that the good dispersion is most likely due to the collapse of the short PMMA brush and the enthalpic penalty for the collapse of the PS brush onto the PMMA brush. Finally, PS-grafted gold nanorods were assembled in liquid crystals. Assembly was tuned by controlling temperature and liquid crystal defect structure in the presence of micropillar arrays. The assembly of the nanorods resulted in changes in characteristic absorbance peaks of over 100 nm. From these studies, we are able to predict and control the assembly of nanorods in both solution and polymer matrices allowing us to fine-tune optical properties.

Degree Type
Dissertation

Degree Name
Doctor of Philosophy (PhD)

Graduate Group
Chemical and Biomolecular Engineering

First Advisor
Russell J. Composto

Keywords
Colloids, Gold Nanorods, Polymer Physics, Surface Chemistry

Subject Categories
Chemical Engineering | Mechanics of Materials | Polymer Chemistry

SURFACE CHEMISTRY MEDIATED ASSEMBLY OF POLYMER-GRAFTED NANORODS IN SOLUTION AND POLYMER MATRICES

Robert Charles Ferrier, Jr.

A DISSERTATION

in

Chemical and Biomolecular Engineering

Presented to the Faculties of the University of Pennsylvania

in

Partial Fulfillment of the Requirements for the

Degree of Doctor of Philosophy

2015

Supervisor of Dissertation

_____

Russell J. Composto, Professor of Materials Science and Engineering

Graduate Group Chairperson

_____

John C. Crocker, Professor of Chemical and Biomolecular Engineering

Dissertation Committee

Daeyeon Lee, Associate Professor of Chemical and Biomolecular Engineering

Robert A. Riggleman, Assistant Professor of Chemical and Biomolecular Engineering

Karen I. Winey, Professor of Materials Science and Engineering

SURFACE CHEMISTRY MEDIATED ASSEMBLY OF POLYMER-GRAFTED NANORODS IN SOLUTION AND POLYMER MATRICES

Dedicated to:

Teresa A. Ferrier, in life.

Robert C. Ferrier, Sr., in death.

Xiaowen Tang, in marriage.

ACKNOWLEDGMENT

I read many theses to prepare for the writing of my own thesis. In doing so, I found myself being invariably drawn to the acknowledgments section. Hidden at the fore of these arcane tomes of scientific gobbledygook is a chapter rife with markedly human verbiage, full of emotion and complexity of character that was inexorably lost in the morass of technical writing present in the main document. Aside from this, the most striking feature of this section was it began the same way every single time: “science cannot be done by yourself.” I find this particularly true in my case; I have garnered a cavalcade of collaborators across three different continents during my tenure here at Penn. As a result, I have grown tremendously both as a scientist and as a person. I know that this section will not be able to fully communicate the immense gratitude I have for everyone mentioned here, but I hope that those reading know my sentiments in writing pales in comparison to my true feelings which I could never adequately express.

I also learned from my reading that I am supposed to thank my advisor first. So, Prof. Composto, Russ, you have truly left an indelible mark on me. You are the professor that I aspire to be. You let me make so many mistakes in the hopes that I would learn how to correct them, how to not make them again, how to grow from them. Truly, you taught me how to wrench success from the clutches of failure. From my first year in MSE, to my qualifier in CBE, to my proposal, to my lackadaisical attitude towards paper writing, you let me err constantly, always deep down trusting, hoping, that I would figure it out. Figure it out, I did, if this thesis is any evidence. Very few advisors would have given me, an OK student from Drexel, so many chances, so many passes. I remember at the end of my first

year, you told me, “I have never had a bad PhD student.” I am glad that I was not your first. As an advisor, you are top notch; you let me travel to research, you let me collaborate, do my own things, let me work on my own and helped me when I needed it. I have definitely come out better than I came in and for that I have you to thank.

I would also like to thank my committee members. I learned something important from each of you that I have incorporated into this thesis. Prof. Winey taught me to pay attention to the most minute of details even though you think no one will notice, someone will. This self-discipline is important to cultivate and I have been getting better about it as of late. I hope I haven’t made any errors here, in the dissertation. Prof. Riggleman taught me that 1) I could probably never do simulations and 2) simulations are an extremely useful tool to help explore the underlying physics of many phenomena we see. Prof. Lee showed me that even if something isn’t in your field you can still learn from it and adapt it to what you do. Prof. Lee and Prof. Riggleman also always got me excited about what I was doing, I always appreciated that. Sometimes it is hard to put your work into context, but they were always very forthcoming with context and advice.

Thank you to the staff especially Pat Overend, Vicky Lee, Irene Clements, Doug Yates, and Steve Szewczyk for all your help throughout the years. Doug would always answer my questions about the TEM even though they were dumb. Steve helped me and Elaine with the LC/AuNR project and he was also always around to talk about something if you could find him. Thanks to Pat, Vicky, and Irene who would always be there for a chat or to help send a package, get some mail, send an email or really just help with anything.

Variety is the spice of life and also science. I have had the distinct pleasure to work with so many talented people throughout my research career at Penn. I was lucky enough to

receive a fellowship from the NSF to research abroad in Japan at Kyoto University with Prof. Ohno. In Ohno-Sensei's lab I learned how to do research mostly by observing Huang Yun, Nakanishi-san, and Kyou-San, all three PhD students. Huang Yun, a Chinese, and I immediately hit it off due to our shared love of basketball and shared connection to China (although, perhaps, mine was tenuous at the time). Nakanishi-san and I bonded over our love of bourbon. Ohno-sensei welcomed me into his lab and taught me how to do living radical polymerization, a skill that I still treasure today. It is in this lab that I developed my love for Mahjong a game that I have learned to play with the Japanese, Chinese, and Taiwanese. I credit Mizuta Yuki and Araki Wakiuchi with this. I had so many great experiences in Japan: video game collecting, Mahjong playing, sight-seeing, alcohol drinking, food eating, and researching.

I was also lucky to receive, again from the NSF through the NBIC and also from the French Laboratoire d'excellence campaign through ARCANE, a fellowship to research in Grenoble, France. Here I met Patrice Rannou, my French advisor. Patrice is, bar none, the most scientifically excited person I have ever met. Eternally positive, energetic, and creative, it was truly a boon to work with Patrice. As a French, he is EXTREMELY careful. While I fought him on this initially such that I could gain autonomy in lab, I ultimately adopted some of his painstaking carefulness, which has been immensely useful in my scientific career. I was also co-advised by Brigitte Pépin-Donat and Didier Gasparutto. Brigitte was equally intelligent as she was adventurous. Whilst doing EPR experiments, experiments only a few people in the world can do and interpret, she would regale me with stories about flying to remote places in fog-clogged mountains such that she could climb a new challenge. She would talk about how she would frequently walk up to the bastille in

Grenoble and back down before or after work. I have done this particular trek exactly once and I can say that I would never want to do it again due to the shear tiredness. Like Patrice and Brigitte, Didier was also extremely positive and excited about research. Didier always had great ideas about what experiments we could do that would be interesting. It was in Didier's lab that I worked with Guillaume Gines and Dr. Christine St. Pierre. Christine was a tech in the lab and she would run the MALDI-TOF. She wanted to improve her already great English skills and as such would always talk to me about any topic asking me about English words for technical things. Guillaume taught me so much about DNA. Easily one of the most knowledgeable PhD students I have met, he would discuss at length with me about how to do particular procedures off the top of his head. We talked some about music, about his trip to the Czech Republic, about his thesis. His passion and intelligence truly informed the rest of my PhD work.

While abroad I worked with people that became my friends, at Penn I was friends with those that I worked with. Elaine Lee came to me one day, after I had been constantly pushing for months with my friends for potential collaborations, with an idea to use my gold nanorods in her liquid crystal / nanopillar assemblies. Obviously I immediately jumped at the chance and we were able to produce a functional, controllable, LC/NR/Nanopillar device. We worked well together despite my constant, random crooning and general ridiculousness. Jason Koski, whom I knew through Mike O'Reilly, turned friend to collaborator. I roomed with Jason, to his chagrin at my snoring I am sure, whilst we were in San Antonio for APS. I had recently done some work with mixed brush NRs and as it turned out he was presenting on theoretical work on a similar thing. "Oh," I said, "we should, like, collaborate." From that initial conversation we were able to produce a

paper, I think, is of significant import to the nanocomposite community. I also spent much time with Matthew "Will" Eibling in Prof. Saven's lab. Will synthesized a unique, metal-binding peptide that we thought we could use to link the gold nanorods together reversibly. The project started out pretty rough and it was difficult to get any positive results, but because of Will's brilliant insights, we were able to make the project work extremely well.

I would be remiss if I did not thank all of my groupmates. Mike Hore laid the foundation for some of the work I produced in the thesis and for that I am thankful. Also, through him, I became part of the lunch tradition present since at least the time of Jamie Ford. I have continued this tradition on to this day. Matt was always there to hang out, talk, or get a drink with and he always had something interesting to say. Chia-Chun "Jim" Lin who was always down to get coffee with me, talk to me about random group stuff or life stuff, or go out from time to time. Emmabeth Parrish Vaughn was always positive and nice despite everything. She was also our resident expert on the South, which was always great for a fun conversation. Boris Rasin was always down to talk with you, even if you weren't necessarily interested. His diverse interests did make it easy to jump into conversation with and we would always talk at length about basketball, politics, or science. Nadia Krook was also always down to talk. Her and Emma make for an interesting conversational dynamic in our office and make it very lively every day, especially while I was writing my thesis. In terms of post-docs, Carme Coll-Ferrer and Hyun-Su Lee stand out. Carme was always down to talk about anything and always brought positivity and level headedness to any conversation. Hyun-Su would answer any question I had about science and would always give me good insight into any problem I brought to his attention. I would also like to thank Sangah Gam, Jihoon Choi, Martha Grady, and Prathima Nalam.

There were many friends inside and out of the department that helped me to get here today. Tom Donnelly, my oldest friend, the best man at my wedding, was always there for me when I needed him. I lived with him for a few years during my PhD. He always kept me grounded and always gave me an out to focus on something other than science. Rick Antoine, Kevin Carfagno, Manthan Gandhi, and Bevan Reitz were also always there to hang out with no matter what. Carlos Aspetti, my "partner for ten years," and I have a long history. We both went to Drexel, studied physics, studied materials science, and worked in the same lab. We are completely different people but this made us, I think, much closer friends in the end. My cohort in MSE at Penn was invaluable throughout my career. Carlos Aspetti, Mike O'Reilly, Kate Murphy, Pavan Nukala, Vicky Doan-Nguyen, and Lisa Chen comprised my cohort. We spent a lot of time together in class, in lab, and in the bar. Mike and Kate especially have been great friends to me and we always made time to hang out whenever we could, it was truly sad to see them go. In CBE, Amit Shavit, Cory Silva, and Rick Tourdot made my first year in CBE classes a lot more comfortable. Aside from my cohorts, I was lucky to become friends with many others more junior than me. Elaine Lee, Jason Reed, Rahul Agarwal, and Cathy Yang I count among my very close friends at Penn. All of us would go to the bar, go crabbing, go on random excursions. The best time was going to the Poconos for 4th of July weekend. Memories like these I will never forget. Special shout out to Jason Reed who comprises the only remaining member of the lunch group started by Jamie Ford so long ago. We still go to lunch every day at noon. All of these traditions, all of these experiences I truly cherish and have made my time at Penn something special. Shout out to Max Yavitt. Also, thanks to Jamie Ford who taught me so many things, like how to use the SEM and who was always a constant source of

encouragement and motivation. Your sunny attitude at lunch always helped me get through my day.

Finally, I should talk about the people I have dedicated this thesis to. Throughout my life especially during this time, they have given me the most support. First, my mother. My mother did not go to college right after high school. She worked in a steel mill, on the floor, not in an office. My mother is the strongest person I know. She has endured a lot of hardship, but has always come away from it, always kept moving forward. I truly admire her for this. As a single parent, she started working in Philadelphia at PECO. At the same time, she started taking college classes to earn her degree. She started when I was 9 or 10 and graduated when I graduated high school. For her to have the energy to work, go to class, and take care of me is astounding. It is a testament to her strength, her will, her resolve, her work ethic, that she was able to do all of this. She was so busy, but she was always there for me no matter what. She always helped me when I needed it, she was always there to talk. Without her example, there is no way I would be the person I am today, there is no way I would have finished the PhD. This thesis is testament to her hard work. Second, my wife. I met my wife at a random party at Penn when I was in my second year. I was so shy when I saw her that I had to have a mutual friend convince Xiaowen to talk to me. I remember drunkenly trying to woo Xiaowen with broken Chinese and whack dance skills, but eventually I prevailed and came out with her number. My goal to set up a date with her were constantly frustrated however and she rescheduled like four times at least. That eventual date must have been great, however, since we have been together ever since. Xiaowen is truly unique. Smart, beautiful, and caring, there is no one that could ever hold a candle to her. I love her so much that I married her three times! Despite her being

from a completely different country, a completely different culture, we have so many things in common and we speak the same language, despite neither of us really speaking each other's language. Travelling with her has been the best experience of my life and we have gone all over the world. Britain, France, Japan, China, Taiwan…Maine. Every place is better than the last when I am with her. Her family has been so supportive of me, especially her father. He likes me so much that when he calls he asks when I am coming back to China, but not her. Her father and mother make me so welcome I truly have a home half way across the world. Xiaowen has supported me all this time during my "permanent head damage." Always being understanding when I had to work late, when I had to work weekends, when I had to write my thesis and could therefore not do any chores. She was always proud of me and always made me feel like I was doing well even if I wasn't sure of that myself. She was always there to love me, care for me, and support me. She always got me through the toughest times during the PhD. This thesis certainly would not have been completed without her support. Regardless of what happens after I leave Penn, I know I will have a good life as long as I am with Xiaowen. 我愛你.

ABSTRACT

Surface Chemistry Mediated Assembly of Polymer-Grafted Nanorods in Solution and Polymer Matrices

Robert Charles Ferrier, Jr.

Russell J. Composto

In the dissertation, I investigate ways to assemble nanorods, typically made of gold, in solution and polymer matrices by controlling surface chemistry. Gold nanorods were anisotropically functionalized with polymer on the side and alkane dithiol on the end causing the gold nanorods to spontaneously assemble in solution. The assembly could be tuned by controlling the incubation time which affected the solution absorbance due to plasmon coupling. Linked gold nanorods were cast in polymer thin films and their optical properties were imparted to the film. This anisotropic functionalization method was utilized to placed DNA or peptides on the ends of the gold nanorods allowing for reversibly assembly. In the case of DNA, assembly was reversed upon heating and could be tuned by controlling the concentration of the complimentary DNA strand. In the case of the peptide, assembly was triggered by the presence of Zn^{2+} ions and could be reversed by adding in a chelater. Anisotropic modification of the nanorods could also be used to assemble organic semiconductors around the nanorods at specific facets. Here, organic semiconductors rhodamine-B, 5(6)-carboxyfluorescein, and cyanine-3 were assembled onto the surface of gold nanorods. By tuning the surface chemistry the organic semiconductors would assemble around the nanorods in different ways which resulted in unique optical properties. The dispersion of PMMA-grafted mesoscopic iron-oxide rods in polymer matrices was

studied by varying the PMMA brush molecular weight (N) polymer matrix molecular weight (P), and polymer matrix type. Here, we found that the ratio of P/N and matrix type had little effect on dispersion of iron-oxide mesorods. N was found to be the main factor that determined dispersion, which is attributed to the large size of the mesorods. Long PS and short PMMA brushes were grafted to gold nanorod surfaces and the dispersion of this system in PS and PMMA was investigated by controlling matrix molecular weight. We found that the gold nanorods would disperse in PS matrices 24 times larger than the grafted brush, while in PMMA matrices the nanorods would aggregate. SCFT calculations revealed that the good dispersion is most likely due to the collapse of the short PMMA brush and the enthalpic penalty for the collapse of the PS brush onto the PMMA brush. Finally, PS-grafted gold nanorods were assembled in liquid crystals. Assembly was tuned by controlling temperature and liquid crystal defect structure in the presence of micropillar arrays. The assembly of the nanorods resulted in changes in characteristic absorbance peaks of over 100 nm. From these studies, we are able to predict and control the assembly of nanorods in both solution and polymer matrices allowing us to fine-tune optical properties.

TABLE OF CONTENTS

LIST OF TABLES

LIST OF ILLUSTRATIONS

Chapter 1 Introduction

Mastery over the assembly of nanoparticles is of the utmost importance for the fabrication of novel devices for sensing, energy harvesting, cloaking, as well as a host of others. A large range of parameters will have major implications in the final properties achieved upon the assembly of the particles. Material type grants access to optical (*e.g.* Au, CdSe), magnetic (*e.g.* Fe_3O_4), and thermoelectric (*e.g.* Si), properties, to name a few. Physical characteristics, such as size and shape, dictate the strength and range of these properties. For instance, Fe_3O_4 particles will lose their superparamagnetic properties as their size increases. As another example, gold nanorods will have vastly different optical properties from their spherical cousins. Finally, separation distance between assembled particles will influence total properties of the assembly, where this effect is intertwined with the material type and size. For example, when gold spheres plasmonically couple, the strength of the coupling decays exponentially as separation increases. Therefore, control over the material, shape, size, and separation of the particles is paramount to tune the properties of the assembly.

Extant nanoparticle chemistry dictates the possible range of parameters that can be tuned simultaneously. While isotropic particles (*e.g.*, spheres) of a vast array of materials are well studied, more exotic shapes (*e.g.*, rods, wires, pyramids, cubes) have only recently been synthesized with the ease and reproducibility to allow scientists beyond those inorganic chemists to study them. As such, anisotropic particles have opened up new realms of properties both with individual particles and with assemblies of particles. Furthermore, due

to their inherent anisotropy, these particles allow for facile surface chemistry control at individual facets, which, in turn, allows for unique nanostructures to be formed by bottom-up type assembly. Of course, surface chemistry dictates 1) dispersion state in various solvents / matrices, 2) type of assembly (*e.g.*, end-to-end or side-by-side), and 3) separation distance between particles, which all significantly affect final properties. In this section, I will discuss the synthesis routes for gold nanoparticles and nanorods, surface modification techniques, how to achieve property control, and how to assemble particles in solution and solid matrices, with a particular focus on gold nanorods.

1.1 Gold Nanorod Synthesis

Spherical metal-nanoparticles have been utilized for centuries to create beautiful hues in decorative pieces, particularly stained glass. The Lycurgus cup

Figure **1.1**), the oldest such decorative piece, contains a small amount of gold and silver nanoparticles probably formed by finely grinding gold and silver dust.(Freestone, Meeks et al. 2007) At this time, the 4th century *anno domini*, the ancient artificers crafting this piece had no real control over the size and shape of the minute particles used. As such, the remaining pieces from this era display wildly different properties than the Lycurgus cup. However, the process of making this stained glass developed over time such that repeatable colors could be achieved, while the nanoparticle synthesis remained in its infancy.

Figure 1.1 The Lycurgus cup being lit from behind. The red color is due to the presence of metal nanoparticles within the glass. Image taken from (Freestone, Meeks et al. 2007).

Centuries later, chemists have gained adroit control of not only the size, but also of the shape of nanoparticles of a wide variety of materials. Spherical nanoparticles made of iron oxide(Ozaki and Matijević 1985), silica(Stöber, Fink et al. 1968), cadmium sulfide(Petit, Lixon et al. 1990), and gold(Faraday 1857) have been synthesized for decades. As synthesis processes became better, control over the size became more exact and reproducible such that monodisperse spherical particles are easily achievable for each of these materials. From these synthesis studies came the ability to create new shapes of nanoparticles; moving away from spheres to more anisotropic and/or exotic shapes such as rods(Jana, Gearheart et al. 2001, Peng, Dong et al. 2002, Liu and Zeng 2003), cubes(Skrabalak, Au et al. 2007), wires(Sun and Xia 2002, Tuan, Lee et al. 2005),

pyramids(Guha, Kar et al. 2004, Herring, AbouZeid et al. 2011), plates(Zhang, Li et al. 2011), and stars(Pandian Senthil, Isabel et al. 2008). Contemporaneously, the synthesis processes for these shapes is being improved such that the ease of control of the syntheses becomes similar to spherical synthesis. Gold nanoparticles, in particular, have received significant attention due to their unique optical properties.

The modern synthesis of colloidal gold is relatively old. In 1857, Michael Faraday described the dispersion of "diffused gold" as a "beautiful ruby fluid." His description of the synthesis is telling:(Faraday 1857)

> *If a pint or two of the weak solution of gold* [chloride] *before described be put into a* ***very clean*** *glass bottle, a drop of the solution of phosphorous in sulphide* (sic) *of carbon added and the whole well shaken together, it immediately changes in appearance, becomes red, and being left for six or twelve hours, forms the ruby fluid required; too much sulphide* (sic) *and phosphorous should not be added, for the reduced gold then tends to clot about the portions.*

The method Faraday described some 160 years ago is still used today to produce gold nanoparticles. For instance, Mirkin and co-workers add trisodium citrate dihydrate (replacing Faraday's phosphorus) to a solution of chloroauric acid ("chloride of gold") under heavy stirring ("well shaken") to produce a deep red solution of spherical gold nanoparticles.(McFarland, Haynes et al. 2004) Many other solution syntheses of gold nanoparticles have been reported, but all bear striking resemblance to the method described by Faraday.

Gold nanoparticles provide the seeds from which gold nanorods blossom. The first synthesis of gold nanorods was described by Esumi *et al.* in a 1995 paper.(Esumi, Matsuhisa et al. 1995) Here, the authors UV irradiated a solution of hexadecyltrimethylammonium chloride (HTAC), a cationic surfactant, and chloroauric acid, which produced rod shaped gold nanoparticles. Later, in 1997, Yu *et al.*(Yu, Chang et al. 1997) produced gold nanorods via an electrochemical method. In 2001, Jana *et al.*(Jana, Gearheart et al. 2001) described the wet chemical synthesis of gold nanorods using a seed-mediated growth method. First, spherical gold particles (*ca.* 3.5 nm) (seeds) are produced by reducing gold chloride with sodium borohydride in the presence of tri-sodium citrate. Next, gold chloride, cetrimonium bromide (CTAB), a cationic surfactant, and ascorbic acid are added to the seed solution and gold nanorods are produced with celerity. **Figure 1.2** shows representative SEM image of gold nanorods from the synthesis described above as well as a cartoon of the surfactant structure. Future syntheses incorporate silver nitrate into the seed synthesis(Sau and Murphy 2004), an additional surfactant(Nikoobakht and El-Sayed 2003), and salicylic or benzoic acids(Ye, Jin et al. 2012) to produce a wide range of nanorod sizes with a high degree of monodispersity.

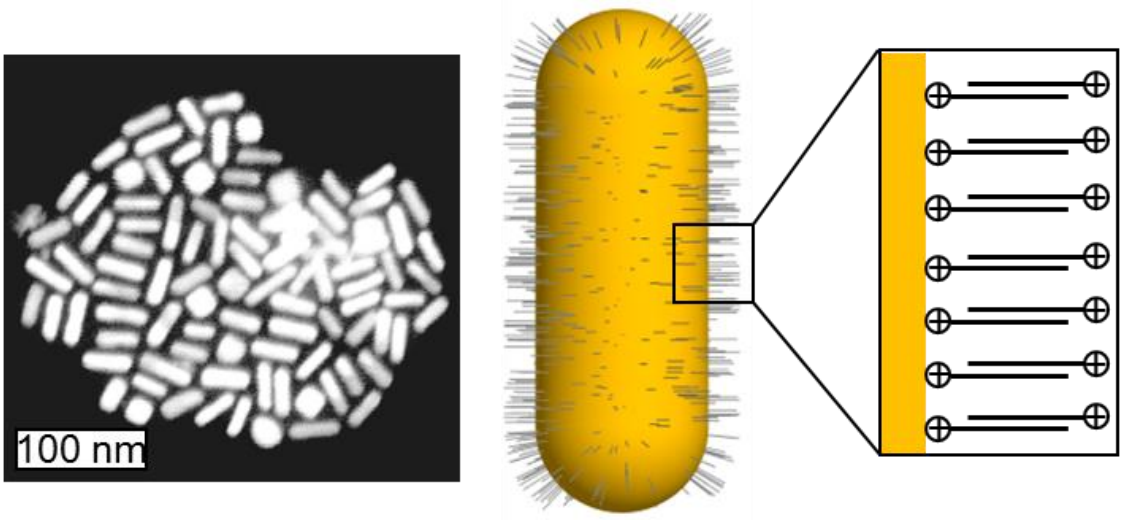

Figure 1.2 SEM image of as-synthesized gold nanorods cast onto a Si wafer. Cartoon of gold nanorods with blow up of CTAB cationic surfactant layer present on gold nanorods. Note that the CTAB forms a bi-layer in water.

1.2 Optical Properties

Metal nanoparticles have interesting optical properties. In the previous section, I mentioned that Faraday found the colloidal gold to be a "beautiful ruby" color. The Lycurgus cup, an opaque green under ambient light, shines a ruby red when illuminated from the inside. The ruby color of both the solution and the cup are due to the same phenomenon: localized surface plasmons. Surface plasmons occur when an electromagnetic field interacts with conduction band electrons leading to the coherent oscillation of electrons, which results in a strong absorption, the wavelength of which depends upon the size and shape of the nanoparticle. **Figure 1.3** shows a cartoon illustrating the plasmon resonance effect. The plasmon phenomenon is due to the size of the particle; individual gold atoms and bulk gold do not display plasmon resonance.

Mie(Mie 1908) first described the size-dependent scattering of spherical particles that had been noted by Faraday.

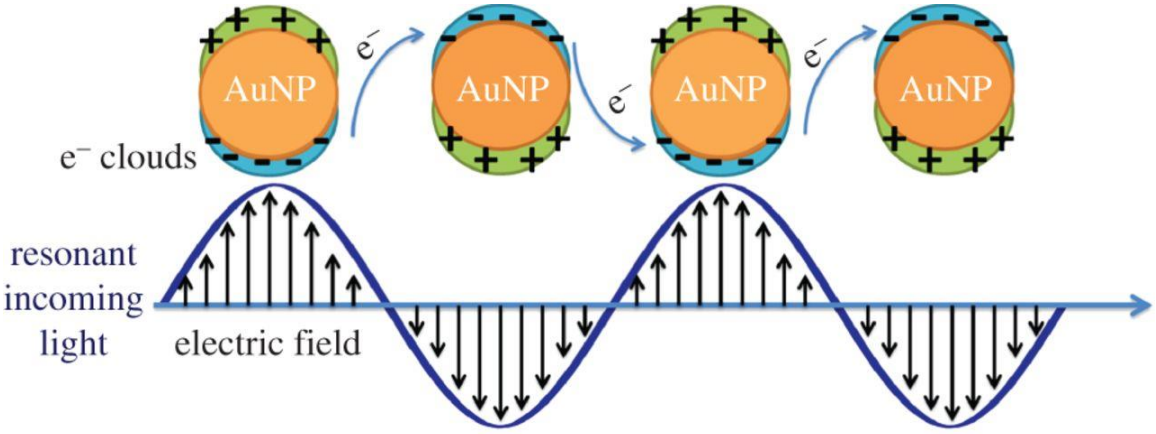

Figure 1.3 Illustration of surface plasmons in the presence of resonant incident light. Figure reproduced from (Yasun, Kang et al. 2013).

Gold nanorods have two absorbance bands due to plasmon resonance that arise from their shape.(Sharma, Park et al. 2009) Free electron oscillations can occur on both the long and short axis of the gold nanorods. The transverse surface plamon resonance peak (TSPR) is due to the electron oscillations on the diameter of the nanorods while the longitudinal surface plasmon resonance peak (LSPR) is due to electron oscillations along the length of the nanorods. The LSPR occurs at a higher wavelength than the TSPR and both peaks are affected by the physical dimension of the nanorods. As aspect ratio (L/D) increases, the LSPR peak strongly red-shifts while the TSPR undergoes a slight blue-shift, as can be seen in **Figure 1.4**.

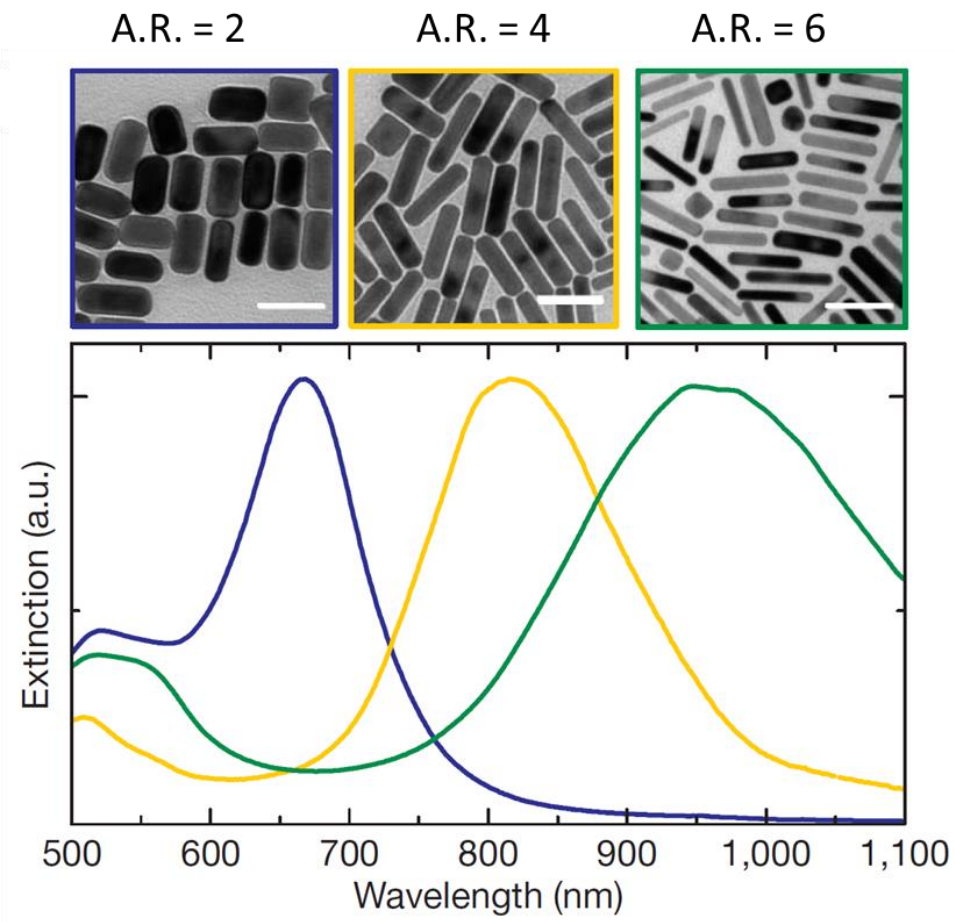

Figure 1.4 SEM image of aspect ratio (A.R.) 2 (blue), 4 (yellow), and 6 (green) and their respective extinction spectra. As A.R. is increased the LSPR peak undergoes a red-shift. All scale bars are 100 nm. Figure reproduced from (Junxi, Lide et al. 2012).

Gold nanorod absorbance is affected by inter-rod spacing and orientation. A dispersion of gold nanorods will behave, plasmonically, like an ensemble average of the individual nanorods that make up the dispersion. However, when the nanorods are brought close together, the oscillations of the surface electrons of one nanorod impinge upon those of an adjacent nanorod, which results in a significant change in the absorbance. This phenomenon is known as plasmon coupling. Plasmon coupling in gold nanorods has been

studied theoretically and experimentally by El-Sayed(Jain, Eustis et al. 2006), Link(Slaughter, Wu et al. 2010), Funston and Mulvaney(Funston, Novo et al. 2009), and Thomas.(Kumar, Wei et al. 2013) The absolute effect of plasmon coupling on the optical properties depends on the separation distance between the nanorods, the angle between the nanorods, and the number of nanorods in the assembly. Simply, a red-shift in the LSPR peak will occur when nanorods are aligned end-to-end (*i.e.* longer rod), while a blue-shift in the LSPR peak will occur when nanorods are aligned side-by-side (*i.e.* thicker rod). The angle dependence is a bit less straight-forward, but two nanorods at 90 degrees will have a LSPR peak somewhere between the LSPR peak of two nanorods end-to-end and two nanorods side-by-side. As the gap between the nanorods decreases, the shift in the LSPR band will be more dramatic, whether it be a blue or red-shift. Finally, increasing the number of nanorods in the assembly will enhance the shift even more, but with diminishing returns at higher rod number. **Figure 1.5** shows the scattering of chains of gold nanorods linked end-to-end as well as scattering when two nanorods are at different angles to each other. Therefore, the optical properties of a dispersion of gold nanorods can be significantly tuned through assembly.

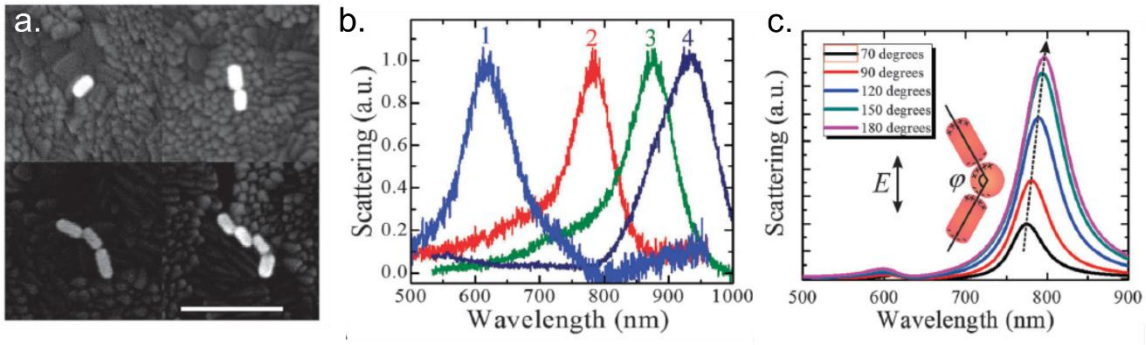

Figure 1.5 SEM images of gold nanorod chains (a) and their respective scattering (b). As the number of nanorods in a chain is increased the scattering red-shifts. (c) shows the effect of angle between the nanorods. The LSPR peak red-shifts as the angle becomes closer to 180 degrees. Scale bar is 250 nm. Figure reproduced from (Kumar, Wei et al. 2013).

Gold nanorods excited by light near their SPR peak will display significantly enhanced electric fields. Liu et al.(Liu, Guyot-Sionnest et al. 2007) studied the field enhancement around gold particles by finite difference time domain methods of different shapes: spheres, spheroids, rods, and bipyramids. They found that while spheres enhanced the field six-fold, gold rods enhanced the field more than 1000-fold with the strongest enhancement around the ends. This field enhancement is useful for Raman spectroscopy, where the Raman signal is proportional to the electric field to the power of 4. Raman spectroscopy is used to detect molecules and, when coupled with surfaces that enhance the signal, is deemed surface enhanced Raman spectroscopy (SERS). As such, gold nanorods have recently been utilized in SERS studies. El-Sayed and co-workers(Nikoobakht, Wang et al. 2002) found that dispersed gold nanorods enhanced the Raman scattering of various analytes by 10^3-10^4-fold. In a later study(Nikoobakht and El-Sayed 2003), they found that aggregated gold nanorods enhanced the Raman signal even more than dispersed nanorods. The added enhancement could be explained by plasmon coupling. Just like single nanorods enhance the electric field at their tips, nanorods that are close enough to plasmon couple enhance the electric field in the gap between. The enhancement depends upon the orientation and separation distance, with nanorods assembled end-to-end leading to the highest enhancements. For example, Kumacheva and co-workers(Lee, Andrade et al. 2011)

reported enhancement of the Raman signal of an analyte by linking gold nanorods end-to-end, as seen in **Figure 1.6**. They found that the more nanorods in the chain, the more enhanced the signal, due to the increased plasmon coupling.

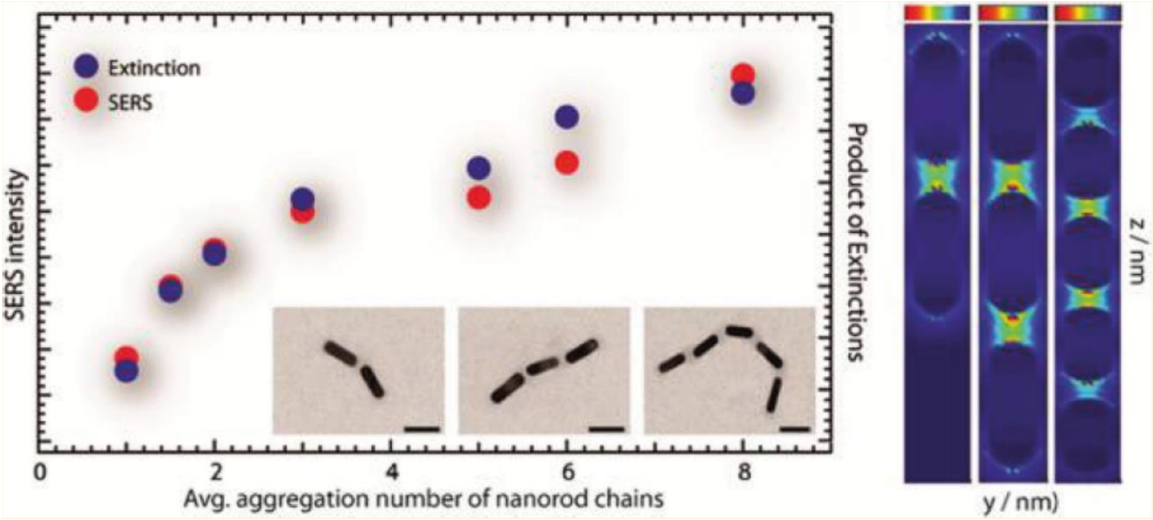

Figure 1.6 The plot on the left shows how extinction and SERS enhancement changes as a function of number of nanorods per chain. The plot on the right is a heat map of the electric field for chains of 2, 3, and 5 nanorods. Warmer colors indicate larger field strengths. In the gap between nanorods field is significantly enhanced. Scale bars are 40 nm. Figure reproduced from (Lee, Andrade et al. 2011).

Gold nanorods can affect the fluorescence of adjacent materials. Fluorescence occurs when the electron in the excited orbital is paired to the second electron in the ground-state orbital and the excited electron returns to the ground state through emission of a photon.(Lakowicz 2007) The fluorescence of a molecule can be quenched or enhanced depending upon the molecule's proximity to the gold nanorod surface. Orrit and co-workers(Khatua, Paulo et al. 2014) studied the fluorescence of crystal violet, a weakly fluorescent molecule, in the presence of gold nanorods. They found that the fluorescence

of the crystal violet increased 1000s-fold when the SPR peak was close to the excitation wavelength, as can be seen in **Figure 1.7**a and b. The enhancement is due to the SPR effect and the enhancement of the electric fields surrounding the gold nanorods. Li et al.(Li, Qian et al. 2009) studied the fluorescence of quantum dots bound to gold nanorods as a function of separation distance. They found that the emission of the quantum dots was completely quenched out to a separation distance of 5 nm, as can be seen in **Figure 1.7**c. The quenching in this case is due to a Förster resonance energy transfer (FRET) between the quantum dot and the gold nanorod. Therefore, the adaptability of the gold nanorod for either quenching or enhancement of emission can be utilized for sensing applications.

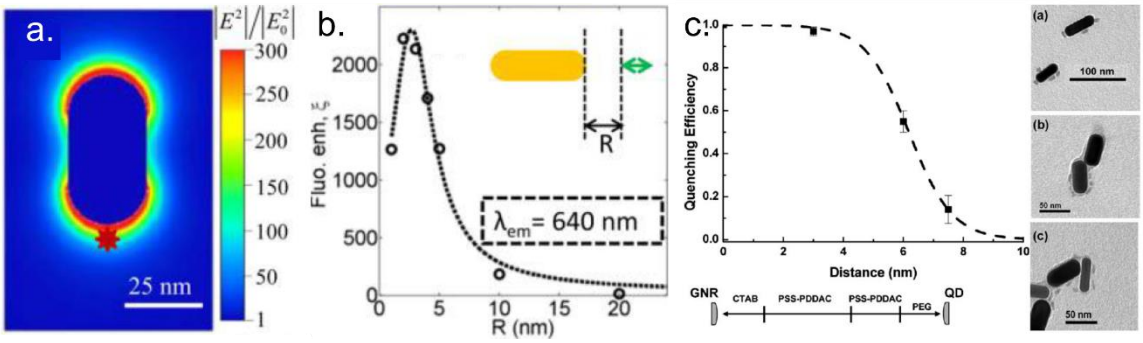

Figure 1.7 Gold nanorods can both enhance and quench fluorescence emission of an analyte depending on the proximity to and position of the analyte relative to the gold nanorod. a. FDTD simulation of the enhanced electric around a gold nanorod with an analyte placed at the tip (red star). B. The fluorescence enhancement of the analyte as a function of separation distance from the nanorod end. c. The fluorescence quenching of a quantum dot as a function of separation distance from the gold nanorod surface. Figures a and b reproduced from (Khatua, Paulo et al. 2014) and c reproduced from (Li, Qian et al. 2009).

1.3 Gold Nanorod Assembly

The way nanoparticles assemble in their host medium significantly affects the final properties of the dispersion. In the previous section, I discussed how the Lycurgus cup has its unique appearance due to the presence of gold and silver particles that exhibit surface plasmon resonance. Many other fragments of similar nanoparticle-laden glass have been found and these have significantly different properties than the Lycurgus cup. The difference in optical properties stems from the differences in the dispersion of the nanoparticles. Having a higher concentration of particles in the glass would bring the particles closer together which would lead to a bathochromic shift in the absorbance of the material which would make the glass appear bluer than the Lycurgus cup. Forcing gold nanorods closer together or further apart will change the final properties in a similar way. Furthermore, the host medium can be anything; liquid like a solvent such as water or toluene, solid like a polymer film, or something in between like a liquid crystal. In this section, I will discuss some of the strategies to assemble the gold nanorods in both solutions and polymer matrices.

1.3.1 The Role of CTAB

Gold nanorods typically begin their life in water. Gold nanorods are coated with CTAB, a cationic surfactant, which forms a bilayer on the surface of the nanorods, protecting the gold nanorods from aggregation. When the solvent is changed from water to something less polar like chloroform or toluene, the CTAB bilayer is disrupted(Shibu Joseph, Ipe et al. 2006), leaving the head group attracted to the surface and the alkyl tails pointing into the solvent. This weakens the general stability of the dispersion and leads to, if not aggregation of the nanorods, then reduction in the average interparticle spacing which leads

to a solution color change. Therefore, if one hopes to use the gold nanorods in a solvent (liquid or solid) other than water, steps need to be taken to replace the CTAB with a more stable interfacial agent.

The interaction between the gold nanorod surface and the cationic head of CTAB is relatively weak. The CTAB is bound electrostatically to the surface of the gold nanorods. As such, it can be easily replaced by incubating CTAB stabilized gold nanorods with a molecule having a chemical moiety that forms a stronger bond with the gold than the CTAB. The moiety of choice for gold nanorod modification is thiol (HS-). The sulfur positively interacts with the gold and forms a covalent bond. A vast array of molecules (DNA, peptides, short alkanes, synthetic polymers) with thiol groups have been synthesized and have been utilized to graft to (or from) the gold nanorods surface.

CTAB (probably) does not protect the ends of the gold nanorods. Recent publications suggest that the CTAB is bound, at least, far more densely on the sides of the nanorods than on the ends due to the "bulky" head group of the CTAB and high curvature of the nanorods "spherical" end cap, allowing for little viable real-estate for the CTAB to settle down on.(Gao, Bender et al. 2003, Park, Drummy et al. 2013) This CTAB distribution gradient can be exploited. Many researchers have utilized the lack of CTAB on nanorod ends to selectively bind molecules, leaving the CTAB layer intact on the side, which keeps the nanorods from aggregating side-by-side. The anisotropic functionalization of the gold nanorods can allow one to assemble the gold nanorods end-to-end or selectively adhere other molecules to the end caps.

Therefore, understanding the role CTAB plays in the stabilization of gold nanorods is paramount to being able to manipulate the gold nanorods surface chemistry to achieve the

particular assembly you desire. The next section will describe specific examples in the literature of how the surface chemistry can be changed to assemble gold nanorods. First, solution assembly will be described, followed by assembly in polymer matrices.

1.3.2 Solution Assembly

The assembly of gold nanorods in solution has received careful scrutiny from the scientific community. Gold nanorods have been assembled both end-to-end or side-by-side through both isotropic and anisotropic surface modification with such diverse active ligands as polymers, short chain molecules, proteins, DNA, organic semiconductors, and chelating agents both reversibly and irreversibly. This section will elucidate the current state of the art methods for solution assembly of gold nanorods in the literature and provide some prospective on what still needs to be done. Specifically, the section will be broken up into assembly using small molecules (<100s of g/mol) and large molecules (polymers, both natural and synthetic).

1.3.2.1. Nanorod Assembly with Small Molecules

Gold nanorods can be assembled end-to-end using alkane dithiol molecules. As mentioned above, molecules with thiol moieties readily bind to the gold nanorods surface. Therefore, the easiest method to tether two nanorods together would be with a molecule with one end bound to one nanorod and the other end bound to the other nanorod. Thomas had done early work(Thomas, Barazzouk et al. 2004) with gold nanorod linking by utilizing thiol-alkylacids (*e.g.* 3-mercaptopropionoic acid) characterized by a thiol group on one end and a carboxylic acid group on the other, which would link gold nanorods through hydrogen bonding via the carboxylic acid groups. Similar experiments were performed, but with alkanedithiols.(Shibu Joseph, Ipe et al. 2006, Pramod and Thomas 2008) In this

work, alkanedithiol molecules containing or *sans* a rigid phenyl group were added to solutions of gold nanorods in 4:1::acetonitrile:water solution. Diluting the water solution with acetonitrile was necessary in order to weaken the CTAB layer such that the alkanedithiol could bind. Thomas found that chains of gold nanorods would form with either linker present, but the absorbance was far more strongly red-shifted in the case of the phenyl containing dithiol (840 nm compared to 732 nm for alkanedithiol). Furthermore, Thomas found that linking occurred by one thiol attaching to one nanorod and the other thiol attaching to the other nanorod, rather than a mechanism that involved daisy-chaining alkanedithiols together via disulfide bridges. Finally, Thomas found that changing solvents would not disrupt the linking, making the linking in this case rather robust. **Figure 1.8** shows how the absorbance spectra changed as a function of time when gold nanorods were incubated with alkanedithiol as well as a representative SEM image. Many of the ideas presented in the Thomas papers are later utilized in work presented in this thesis.

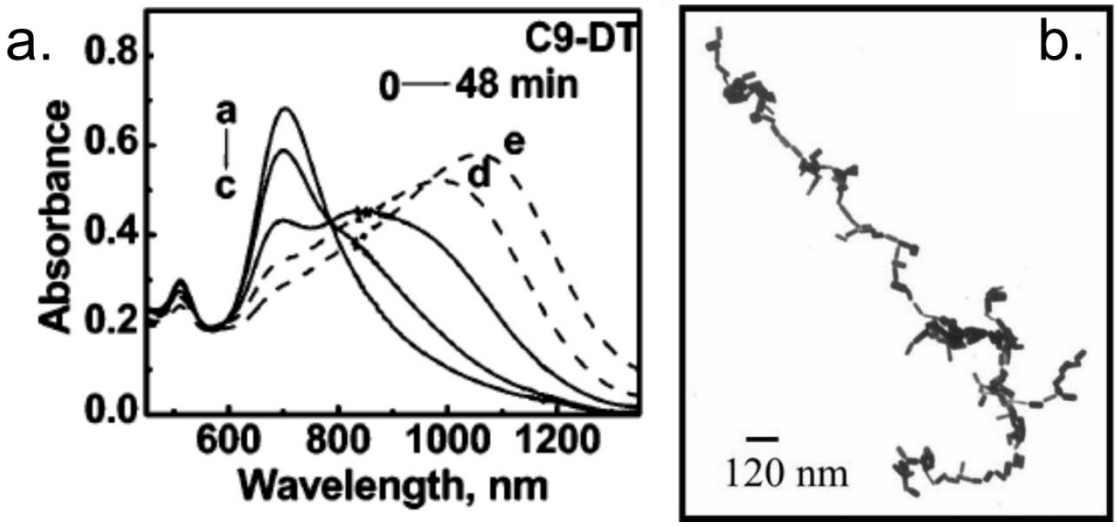

Figure 1.8 a. The absorbance spectra of gold nanorods in the presence of 1,9 nonanedithiol over time. The red shift and broadening of the LSPR peak is consistent with end-to-end

linking. b. SEM image of gold nanorods linked end-to-end by dithiol molecules. Figures reproduced from (Shibu Joseph, Ipe et al. 2006).

The small molecule cysteine has also been frequently used to assemble gold nanorods together end-to-end. Thomas and co-workers first used cysteine to link gold nanorods together.(Sudeep, Joseph et al. 2005) In this work, Thomas incubates gold nanorods in solution with cysteine, glutathione, and other alpha-amino acids and studies their assembly. In this case, only the glutathione and cysteine cause the gold nanorods to assemble, which Thomas hypothesizes is due to the zwitterionic moieties in conjunction with the thiol present on these molecules. Essentially, the thiol binds to the gold nanorod surface and the nanorods are linked together through a "two-point electrostatic interaction" between the positively charged amino group and the negatively charged carboxylic acid group. Sethi and co-workers(Sethi, Joung et al. 2009) took this study even further to elucidate the linking mechanism of the cysteine. Sethi investigated how the molecular moieties present in the linker affected the assembly of gold nanorods. Specifically, cysteine (thiol, carboxylic acid, amine), 3-mercaptopropinoic acid (thiol, carboxylic acid), and cysteamine (thiol, amine) was incubated with gold nanorods at different solution pH and the time evolution of the absorbance was captured. Here it was determined that cysteine would not link nanorods while in its zwitterionic form, precluding the hypothesis that a "two-point electrostatic interaction" would bridge the nanorods. It was suggested, rather, that the positively charged amine would link the nanorods, resulting in assembly. Finally, using cysteine, Sun et al.(Sun, Ni et al. 2008) showed the reversible assembly of gold nanorods

by increasing (assembly) and then decreasing (disassembly) the solution pH, as can be seen in **Figure 1.9**.

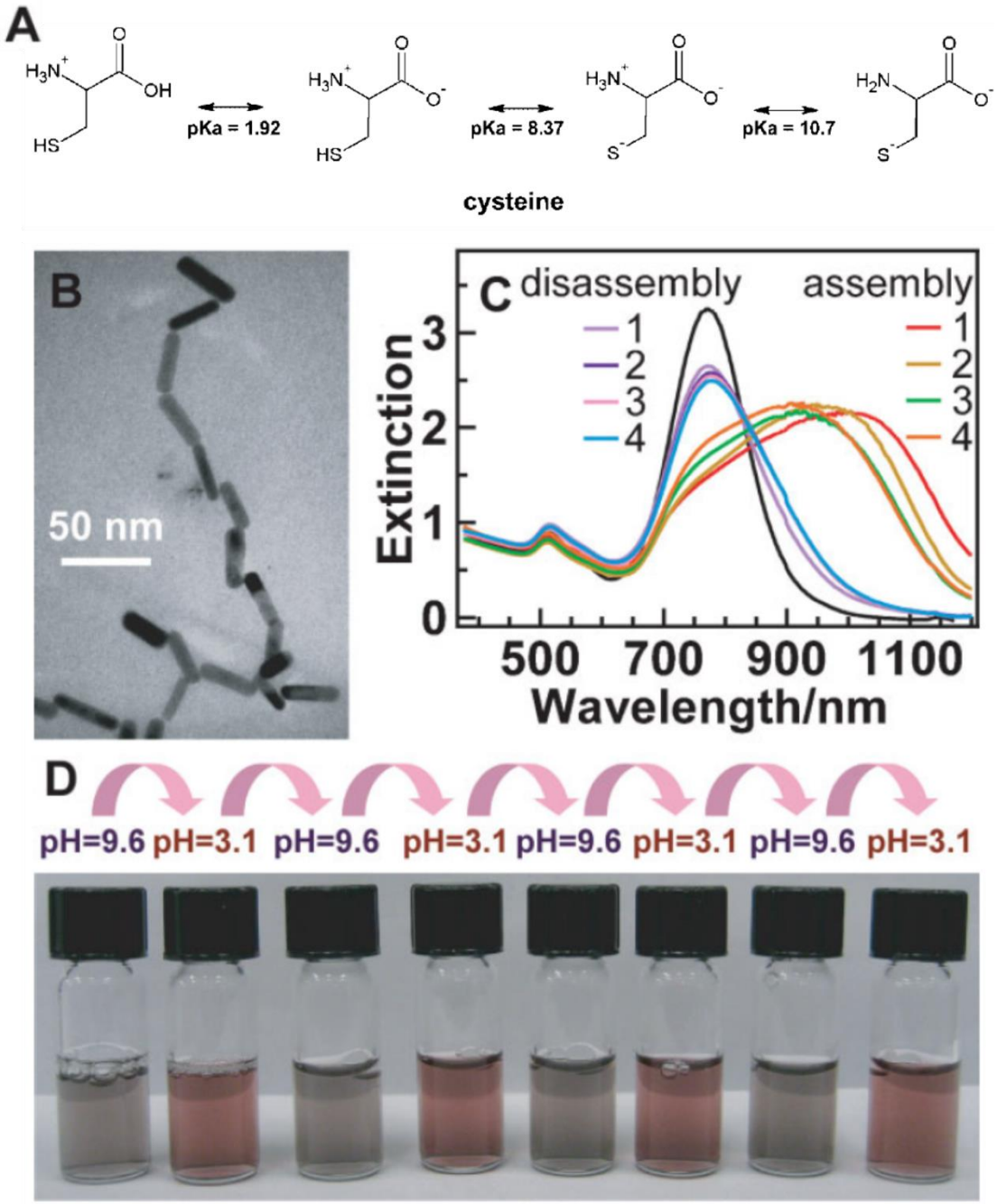

Figure 1.9 a. Cysteine charge group changes as pH is changed. b. SEM image of gold nanorods linked with cysteine. c. Absorbance spectra of gold nanorods linked with cysteine

at high pH and unlinked at low pH. The LSPR peak broadens and red-shifts when gold nanorods are linked and blue-shifts when the gold nanorods are unlinked. d. Vials containing linked (purple) and unlinked (red) gold nanorods in the presence of cysteine. The picture emphasizes the stark change in color upon linking. Figure a reproduced from (Sethi, Joung et al. 2009) while the rest were reproduced from (Sun, Ni et al. 2008).

Other small molecules (aside from cysteine and alkane dithiol which are the most germane to this thesis) have been utilized to assemble gold nanorods. Quan Li and co-workers(Ma, Urbas et al. 2012) used 4, 15-Bis(4-sulfanatophenyl)porphyrin, an organic semiconductor, to assemble gold nanorods. The negatively charged sulfate group in the organic semiconductor bound electrostatically to the CTAB encapsulating the gold nanorods. The assembly caused a significant change in the fluorescent properties of the dispersion, which could be tuned through concentration control of the organic semiconductor. Sreeprasad et al.(Sreeprasad and Pradeep 2011) used ethylenediaminetetraaceticacid (EDTA), a chelater, to reversibly assemble gold nanorods. EDTA was found to bridge gold nanorods by first forming a monolayer on the CTAB, due to EDTA's negative charge, and then hydrogen bonding with other adjacent EDTA molecules, effectively assembling the gold nanorods. Assembly was reversed by adding in a metal ion, in this case Pb(II) which the EDTA would complex with, disassembling the gold nanorods. Finally, the authors found that the enhancement of the Raman signal would decrease as a function of metal ion added. Lastly, Wang et al.(Wang, DePrince et al. 2010) drove assembly of AuNRs end-capped with undecanethiol by adding increasing amounts of water (a bad solvent for the undecanethiol). They compared the dynamics of assembly

at various added water compositions with end-linking performed with undecanedithiol and mercaptoundecanoic acid. They found that assembly with dithiol did not change much, assembly with mercaptoundecanoic acid was slowed at high water content, and assembly with the monothiol was accelerated at higher water content.

1.3.2.2. Nanorod Assembly with Large Molecules

Polymers have been used to assemble gold nanorods in solution. The Kumacheva group has published paper(Nie, Fava et al. 2007), after paper(Nie, Fava et al. 2008), after paper(Liu, Resetco et al. 2012), after paper(Lee, Andrade et al. 2011), after paper(Liu, Ahmed et al. 2013) that describe the assembly of gold nanorods typically end-grafted with polystyrene. The process by which assembly occurs is quite simple and very similar to the work by Wang *et al.* with undecanethiol. Kumacheva and co-workers(Nie, Fava et al. 2007, Nie, Fava et al. 2008) selectively modified gold nanorod ends with polystyrene by placing a concentrated aliquot of gold nanorods in water into a THF solution containing thiol-polystyrene. The molecular weight of the polystyrene end-grafts was varied to control separation distance and assembly type. Gold nanorods were then assembled by titrating in water, which causes the polystyrene brush to collapse and drives assembly end-to-end, as shown in **Figure 1.10**. The exact structure of the assembly was dependent on both the water concentration and the polystyrene molecular weight where chains, bundles, bundled chains, and rings were observed, each with distinct optical properties. They extended this in a later paper(Liu, Ahmed et al. 2013) to be used as a "plasmonic counter" whereby the "degree of polymerization" of the nanorods could be backed out via the extinction spectra of the assemblies. Finally, Kumacheva and co-workers(Lee, Andrade et al. 2011) showed

that the gold nanorod assemblies could be used in detection of small molecules via solution surface enhanced Raman spectroscopy.

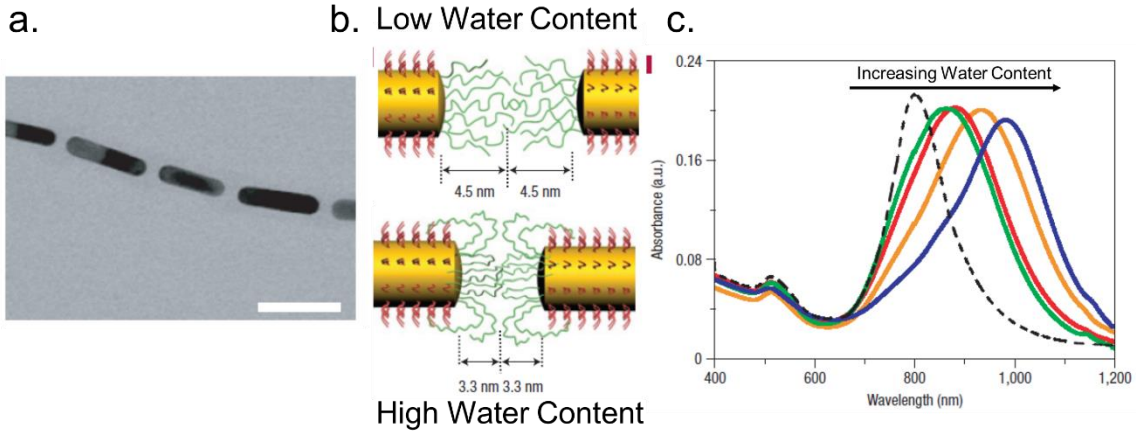

Figure 1.10 a. TEM image of end-to-end assembled gold nanorods. b. Cartoon depicting PS brush in low (top) and high (bottom) water content. Water is a poor solvent for PS and so collapses the brush driving end-to-end assembly. c. Absorbance spectra of gold nanorods at increasing water content. As water content is increased the LSPR red-shifts indicative of an increasing number of nanorods per chain. Scale bar is 50 nm. Figure reproduced from reference (Nie, Fava et al. 2007).

DNA has also been utilized to assemble gold nanorods in solution. DNA makes for great linker material due it its specificity in binding, ease of modification, and reversibility through denaturation via heat or salt. DNA as a component in assembly schemes for nanoparticles is not new. This idea was brought to the forefront separately by Alivisatos(Alivisatos, Johnsson et al. 1996) and Mirkin(Mirkin, Letsinger et al. 1996) where gold nanoparticles were controllably and reversibly crystalized using grafted DNA strands. Since then, DNA has become increasingly intertwined with nanoparticle assembly

spurred on by theoretical work on DNA folding(Seeman 1982) leading to DNA origami(Rothemund 2006), which has been used to create unique structures involving spherical gold nanoparticles.(Ding, Deng et al. 2010, Hung, Micheel et al. 2010) In the realm of gold nanorod assembly, DNA has been criminally under-utilized. A 2001 communication by Dujardin *et al.*(Dujardin, Hsin et al. 2001) described the homogeneous grafting of DNA to the gold nanorods, followed by addition of a free DNA strand that bridged two grafted strands, resulting in aggregation. Heating the assembly above 60°C resulted in the disassembly of the DNA driven agglomeration which was evidenced by the shift in the absorbance spectrum. More recently, two works have utilized DNA to assemble gold nanorods very effectively. Oleg Gang and co-workers(Vial, Nykypanchuk et al. 2013) grafted DNA strands to the sides of gold nanorods and assembled them side-by-side through the addition of a bridging DNA strand. The length of the bridging DNA was tuned to control the spacing between the gold nanorods. They studied the dynamics of assembly of these ribbon like structures using in-situ SAXS and absorbance spectroscopy. In a paper released the same year, Zhao *et al.*(Zhao, Zhang et al. 2013) grafted a self-complimentary disulfide DNA specifically to the ends of gold nanorods. Assembly was then triggered by changing the solution pH from 8.0 to 5.0, effectively end-linking the gold nanords which resulted in a bathochromic shift in the LSPR peak. They were then able to de-link the nanorods by bringing the pH back up to 8.0 and they cycled this multiple times with little loss in linking efficacy denoted by similar peak shifts.

Peptides and proteins have also been used in the assembly of gold nanorods in solution. Like DNA, peptides / proteins possess a similarly facile and tunable synthesis and possess

binding specificity making them attractive as linker molecules. The original protein used in gold nanorod linking is streptavidin due to its high affinity to bind biotin, better known as vitamin B_7. Murphy and co-workers(Caswell, Wilson et al. 2003) end-grafted biotin to gold nanorods via a thiol linkage and simply added streptavidin into solution, which immediately lead to assembly of the nanorods, both side-by-side and end-to-end. The gold nanorods did not assemble in the absence of either biotin or streptavidin. Jain et al.(Jain, Roodbeen et al. 2012) employed an oligopeptide to assemble gold nanorods. Here, they used oligomeric glycine flanked by cysteine molecules to link gold nanorods together. They also employed the same molecule but with propargyl in the middle such that modification could take place on the alkyne moiety to further direct properties. They found that assembly proceeded in a step-wise fashion marked by an increasing red-shift and broadening in the absorbance.

1.3.3 Polymer Matrix Assembly

The controlled assembly of nanoscopic fillers in polymer matrices is a burgeoning field. Previously, scientists sought ways to incorporate functional particles into polymeric materials in a well dispersed manner. For instance, the hulls and wings of the Boeing 787 Dreamliner are infused with carbon fiber to reinforce the aircraft while reducing overall weight.(Hale 2006) Furthermore, carbon nanotubes have been added to tennis rackets and bike frames. In each of these cases, the filler was well-dispersed within the host matrix so that properties would be uniform throughout. However, I have shown in previous sections that unique properties can be achieved by controllably assembling particles in a specific way. Certain applications, such as a reusable platform for Raman spectroscopy, necessitate the controlled aggregation of the particles within the polymer. Therefore, it is important to

understand both how to achieve uniform dispersion of particles in polymer matrices as well as controlled assembly.

Nanoparticles can be dispersed in polymer matrices by grafting polymer brushes to their surface. In a dispersion of particles, particle-solvent interactions play a large role in determining whether the dispersion is stable. These interactions can be mitigated by the particle surface chemistry; if grafted ligands "like" the solvent they will be solvated and will keep the particles dispersed (e.g. through steric repulsion), if the ligands do not like the solvent they collapse and the particles will aggregate. Similarly, nanoparticle dispersion in polymer matrices will depend upon the matrix-brush interaction. The favorability of interaction between two polymers is characterized by the Flory-Huggins interaction parameter (χ); If two polymers have a $\chi < 0$, they favorably interact, while if they have a $\chi > 0$ they negatively interact, where $\chi = 0$ is a neutral interaction. Favorable brush-matrix interactions are helpful in dispersing nanoparticles, but are not the only factors that affect dispersion. Entropy plays a big role, as can be expected from such large molecules, as well as particle shape.

For polymer brushes chemically similar to the matrix, chain entropy is the main determining factor in dispersion. As matrix chain size increases, there is an increasing entropic penalty for matrix interdigitation into the brush layer, which can result in depletion of the matrix chains from between the nanorods, leading to aggregation of the nanorods by depletion-attraction. The depletion of the matrix chains from the brush is called the "dry brush regime" while the interdigitation of the matrix in the brush is termed the "wet brush regime." Shull(Shull 1994) studied, by self-consistent field theory, end-grafted polymer brushes in a chemically identical polymer matrix. Shull found that as the ratio (α) of the

degree of polymerization of the matrix chains (P) to the degree of polymerization of the brush chains (N) increased, the matrix became expelled from the brush layer.

Particle shape affects the value of the wet to dry brush transition. Kim and Green(Kim and Green 2010) studied the dispersion of polystyrene grafted gold nanoparticles in polystyrene matrices of various molecular weights. Here, they determined that the ratio (α) of the index polymerization of the matrix (P) to the index of polymerization of the brush (N) was the major determining factor in the dispersion state. Specifically, they found that at $\alpha > 3$ the spheres would aggregate, while at $\alpha < 3$ the spheres would be dispersed. The transition from dispersed to aggregated is ill-defined and many other studies have found α of 4 and 5. A more in-depth overview of this topic can be found in a review by Green.(Green 2011) Hore et al.(Hore, Frischknecht et al. 2012) performed a similar study to Kim and Green, but with gold nanorods. Here, they found that the gold nanorods would disperse if $\alpha < 2$, while aggregation would occur at $\alpha > 2$, as can be seen in **Figure 1.11**. The reason for the difference between the dispersion of spheres and rods is due to the difference in shape, namely the curvature. Spheres are more curved than rods, which causes the polymer brushes to splay out giving room for larger matrix chains to interdigitate and wet the brush.

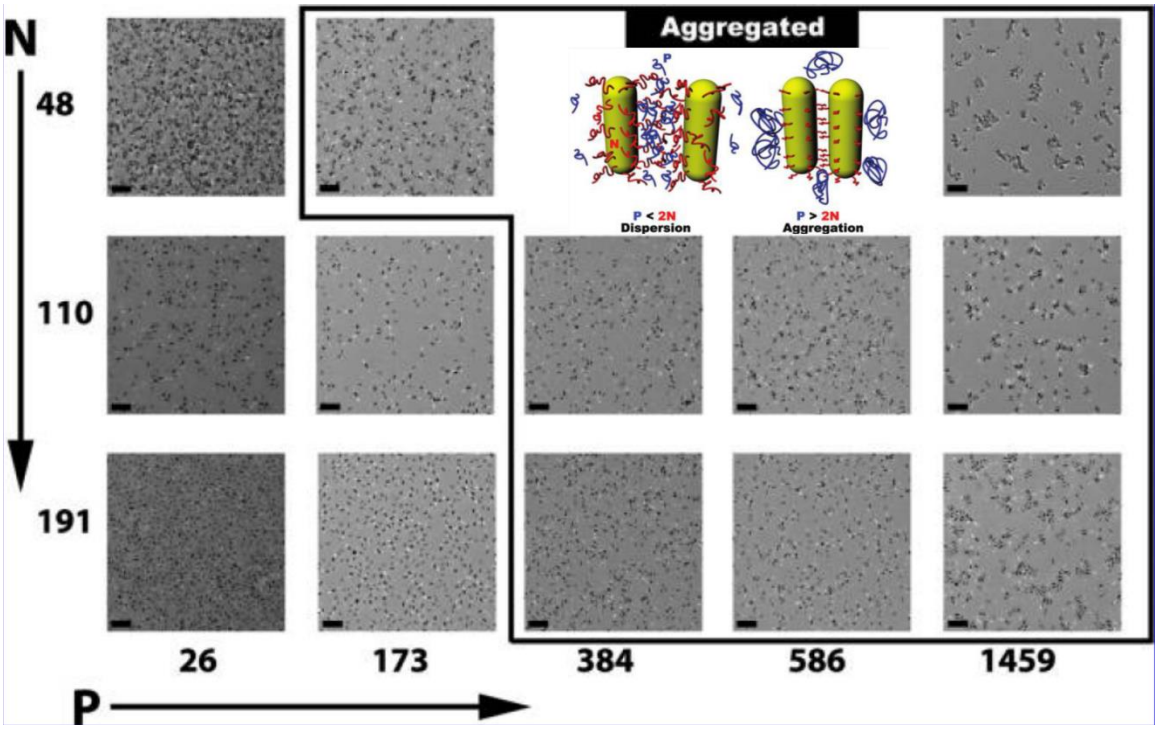

Figure 1.11 TEM images of gold nanorods in polymer matrices at various brush (N) and matrix (P) index of polymerization. If P>2N the nanorods will aggregate, while if P < 2N the nanorods will remain dispersion. Scale bars are 200 nm. Figure reproduced from reference (Hore, Frischknecht et al. 2012).

Favorable brush / matrix interactions improve the dispersion of nanoparticles. Hore and Composto(Hore and Composto 2010) investigated the dispersion of gold nanorods grafted with poly(ethylene oxide) in poly(ethyelene oxide) and poly(methyl methacrylate) matrices. The authors found that poly(ethylene oxide) grafted gold nanorods would disperse very well in high molecular weight (*i.e.* $\alpha > 2$) poly(methyl methacrylate) matrices, while they would aggregate in high molecular height poly(ethylene oxide) matrices. The gold nanorods remained dispersed in poly(methyl metacrylate) matrices even at high vol% (*ca.* 10 v%). Poly(methyl methacrylate) has a weakly favorable interaction

with poly(ethylene oxide) (*i.e.* $\chi < 0$).(Rubinstein and Colby 2003) Therefore, the enthalpic contribution due to the favorable interaction between the brush and the matrix can help to overcome the entropic contribution even when it would typically lead to a dry brush in the athermal case.

Recently, systems in which the grafted chains are bidisperse have been investigated in order to help tune the interactions of the particles within the polymer matrix.(Rungta, Natarajan et al. 2012, Li, Tao et al. 2013) Using two different lengths for the grafted chains offers a wider parameter space to optimize dispersion or particle-particle spacing. For example, Li et al. indicate that a high grafting density of short chains can prevent core-to-core interactions while a lower grafting density of longer chains can still allow for penetration of the matrix chains into the brush of the grafted chains. More generally, Jayaraman has shown in a series of theoretical PRISM studies(Nair, Wentzel et al. 2011, Martin, Dodd et al. 2013, Martin, McKinney et al. 2013) that polydispersity in grafted chain length improves the miscibility of grafted particles and the polymer matrix due to the longer chains causing steric hindrance at larger inter-particle distances while the reduction in monomer crowding still allows the matrix chains to wet the grafted brush layer.

The dispersion state of particles in polymer matrices affects the properties of the composite. So far in this section, I have discussed the factors that affect the dispersion of nanoparticles in polymer matrices. However, in some instances, controlled aggregation of the nanorods would be useful to affect the properties of the nanocomposite. Green and co-workers(Chen and Green 2010) embedded polymer grafted gold nanoparticles in a fluorescent polymer. They found that with a shorter brush, the particles are closer together and more aggregated and thus quench the fluorescence of the polymer more. Hore and

Composto(Hore and Composto 2010) observed a blue-shift in the LSPR peak when the nanorods aggregated in their polymer thin films. Winey and co-workers(White, Mutiso et al. 2010) studied the conductivity of silver nanowire polymer composites. They found that as the loading of nanowires increased, the conductivity increased significantly due to nanowire network formation. These few examples illustrate the need to develop more robust methods to control nanorod assembly in polymer matrices for future, novel devices.

1.4 Dissertation Outline

The dissertation presented herein can be best described as a collection of short stories sharing a common theme, rather than a novel. Think Dubliners as opposed to Ulysses, to reference Joyce. The theme explored is gold nanorod surface chemistry and how that affects their assembly in various media. Specifically, the surface chemistry is modified either isotropically or anisotropically with small molecules or polymers such that assembly can proceed depending upon the relevant medium. Assembly can occur in either liquid (*e.g.* water or toluene) or solid (*e.g.* polymer matrices). In solvents, small molecules are used to assemble the gold nanorods end-to-end to control their plasmonic properties. Nanorod assembly in solvents is achieved both in an irreversible and reversible fashion, which adds dynamicity to the assembly. In polymer matrices, grafted polymers are used to affect the dispersion of gold nanorods. One or more polymer brushes are grafted onto the surface of the gold nanorods and they are placed in polymer thin films which are compatible or incompatible with one or more of the brushes, leading to assembly or dispersion. Assembly of the gold nanorods is largely characterized by spectroscopy and electron microscopy methods, in particular UV/Visible/NIR spectroscopy or scanning transmission electron microscopy, respectively.

The dissertation is split into two sections based on the medium in which the nanorod assembly takes place. Chapters 2-5, which comprise section I, will discuss nanorod assembly in solution while chapters 6-8, which comprise section II, will discuss nanorod assembly in a matrix, and chapter 9 will provide a summary and possible future directions. Chapter 2 explores how to irreversibly end-link gold nanorods by anistropically modifying them and casting them into polymer thin films. Chapter 3 describes how to reversibly end-link gold nanorods by tethering a *de novo* designed metal binding peptide. Chapter 4 discusses how to reversibly end-link gold nanorods using end-grafted DNA. Chapter 5 describes how anisotropic modification of the gold nanorod surface can be used to selectively bind organic semiconductors to control optical properties. Chapter 6 explores the factors that affect the dispersion of mesoscopic iron-oxide nanorods in a polymer matrices. In chapter 7, the effect of grafting two different polymer brushes to gold nanorods and the effect on the nanorods dispersion in a polymer matrix is studied. Chapter 8 describes tuning optical properties of gold nanorod/liquid crystal composites by engineering liquid crystal defect zones around micro pillar arrays. Finally, chapter 9 explores the future directions the research presented in this dissertation can take.

Chapter 2 Gold Nanorod Linking to Control Plasmonic Properties in Solution and Polymer Nanocomposites

2.1 Abstract

A novel, solution-based method is presented to prepare bi-functional gold nanorods (B-NRs), assemble B-NRs end-to-end in various solvents, and disperse linked B-NRs in a polymer matrix. The B-NRs have poly(ethylene glycol) grafted along its long axis and cysteine adsorbed to its ends. By controlling cysteine coverage, bi-functional ligands or polymer can be end-grafted to the AuNRs. Here, two dithiol ligands (C6DT and C9DT) are used to link the B-NRs in organic solvents. With increasing incubation time, the nanorod chain length increases linearly as the longitudinal surface plasmon resonance shifts towards lower adsorption wavelengths (i.e., red shift). Analogous to step-growth polymerization, the polydispersity in chain length also increases. Upon adding polyethylene glycol or poly(methyl methacrylate) to chloroform solution with linked B-NR, the nanorod chains are shown to retain end-to-end linking upon spin casting into PEO or PMMA films. Using quartz crystal microbalance with dissipation (QCM-D), the mechanism of nanorod linking is investigated on planar gold surfaces. At sub-monolayer coverage of cysteine, C6DT molecules can insert between cysteines and reach an areal density of 3.4 molecules per nm^2. To mimic the linking of Au NRs, this planar surface is exposed to cysteine-coated Au nanoparticles, which graft at 7 NPs per μm^2. This solution-based method to prepare, assemble and disperse Au nanorods is applicable to other nanorod systems (e.g., CdSe) and presents a new strategy to assemble anisotropic particles in organic solvents and polymer coatings.

2.2 Introduction

Controllably assembled plasmonic nanoparticles hold promise as the functional components for a tunable sensing platform, such as one based upon surface enhanced Raman spectroscopy (SERS)(Nikoobakht and El-Sayed 2003, Qian, Li et al. 2009)[, 2] as well as optical polarizers(Brian, Sami et al. 2005, Zhang, Liu et al. 2008), and antennae.(MerleinJorg, Kahl et al. 2008) In addition to their facile synthesis(Nikoobakht and El-Sayed 2003, Sau and Murphy 2004), gold nanorods (AuNRs) are particularly attractive for these applications because particle anisotropy as well as AuNR spacing and orientation impart assemblies of AuNRs with unique optical properties.(Funston, Novo et al. 2009) AuNRs have been assembled in both side-by-side and end-to-end alignments by modifying the surface with small linker molecules(Caswell, Wilson et al. 2003, Chang, Wu et al. 2005, Sudeep, Joseph et al. 2005, Shibu Joseph, Ipe et al. 2006, Sethi, Joung et al. 2009) or polymers(Nie, Fava et al. 2007, Hore, Frischknecht et al. 2012) and/or by adjusting solvent conditions.(Sun, Ni et al. 2008) Whereas these approaches achieve some control over spacing, orientation, and, therefore, optical properties of the AuNRs, these strategies are restricted to water or mixed water / organic solvent solutions, thereby limiting possible device fabrication processing. Furthermore, the full potential of assembled AuNRs requires casting them into a processable medium, such as a polymer, that produces well-dispersed AuNRs. Although individual AuNRs have been cast in polymer matrices in random orientations,(Hore and Composto 2012) they have yet to be assembled as discrete chains and dispersed within a polymer matrix. The aim of this research is to develop a strategy to control the end-to-end assembly of AuNRs in a variety of solvents and demonstrate that AuNR chaining can be retained upon casting nanocomposite films. By

tuning the aspect ratio, polymer-grafted nanorods have been predicted to reconfigurably self-assemble into superstructures with nano-sized patterns(Nguyen and Glotzer 2010) offering the possibility of assisting or eschewing traditional lithography and contemporary nano-printing techniques in the fabrication of precise nano-scale devices.(Chanda, Shigeta et al. 2011) Because this is a general strategy, new, flexible devices can be designed by incorporating rod-like particles of variable compositions with the desired function into processable films, thereby establishing a new class of materials with tunable properties based on metal-nanorod/polymer nanocomposites.

Previous work by our group focused on dispersing AuNRs in polymers by grafting a polymer brush that is either chemically similar or exhibits a favorable interaction with the matrix.(Hore and Composto 2010, Hore and Composto 2012, Hore, Frischknecht et al. 2012) The optical properties of the AuNRs are imparted to the polymer film and can be tuned by controlling the local assembly and orientation of the AuNRs. In this work, we present a novel, solution-based method to synthesize bi-functional gold nanorods (B-NRs), assemble them end-to-end in a wide variety of solvents, and disperse the linked B-NRs within a polymer matrix. This strategy takes advantage of the facet dependent surface chemistries of AuNRs that allows for tuning rod-solvent or rod-matrix interactions and opening up new media (i.e., organic) for solubilizing the AuNRs. Furthermore, by exploiting the weak attraction between cysteine and the end of the AuNR, the AuNRs are assembled and dissembled by simply changing solvent and have tunable end grafting that allows for the addition of a functional ligand or polymer between cysteine molecules. By choosing a dithiol ligand, the end-to-end assembly of AuNRs in a wide array of organic solvents and, for the first time, in polymer matrices is demonstrated. Using discrete dipole

approximation (DDA) calculations and UV/Visible spectroscopy, the optical properties, in solution and polymer matrices, are finely tuned by controlling the linker length, B-NR chain length and polydispersity. Finally, quartz crystal microbalance with dissipation (QCM-D) is used to determine the role of the cysteine and dithiol in the linking mechanism that chains AuNRs together.

2.3 Experimental Section

2.3.1 Linked B-NR Preparation

Reagents used in the synthesis were purchased from Sigma-Aldrich and used as received. Polymers were used as received and obtained from Polymer Source, Inc., unless otherwise noted. Three 40 mL solutions of CTAB coated gold nanorods in DI water are synthesized by a seed-mediated growth method as outlined elsewhere.(Nikoobakht and El-Sayed 2003, Sau and Murphy 2004, Hore and Composto 2012) Excess CTAB is removed through three washing cycles consisting of centrifugation (20 min at 8,000 RPM, Eppendorf 5804) followed by replacement of the supernatant with approximately 40 mL of Milli-Q water. Following the washing steps, the three nanorod solutions are combined and concentrated in 40 mL of water, providing a stock solution of concentrated AuNRs.

End linking is performed by centrifuging 5 mL of the stock solution, removing the supernatant, and combining with 9 mL of a 400 mM NaCl solution. Three 3 mL aliquots are taken from the solution, combined with 30 μL of a 2 mM L-cysteine solution, and left overnight to end-link.

Upon completion of the previous reaction, the solutions are sonicated for several seconds to re-disperse the AuNRs. End-linked AuNRs are then functionalized with 5 kg/mol poly(ethylene glycol) methyl ether thiol (Sigma Aldrich) by adding 30 mg of the polymer

to the solutions of end-linked nanorods, centrifuging for 20 minutes, and replacing the supernatant with 3 mL of methanol or ethanol. Two additional washing steps are performed, and precipitate dispersed in chloroform. Using a similar procedure, we found a PEO grafting density of 0.5 chains/nm^2 on homogeneously grafted AuNRs.(Frischknecht, Hore et al. 2013)

Dithiol and monothiol functionalization was performed by preparing a stock solution of diluted di/monothiol ligand containing 50 μL of dithiol to 5 mL of chloroform. 100 μL of this stock solution is then added to the solution containing the B-NRs. For kinetics experiments, 1/10th the concentration of linker as above was used. Samples were prepared for SEM by spincasting at 3k RPM onto a silicon wafer and SEM images were taken on a JEOL 7500F HRSEM. Dithiol functionalization has successfully been performed in a variety of solvents including methanol, ethanol, MEK, and chloroform. In order to use these other solvents, a simple solvent exchange is performed in a similar manner as above. UV/Vis spectroscopy was done at each step with a Cary 5000 UV-Vis-NIR system.

Cysteine-coated Gold Nanosphere Synthesis. Gold nanospheres of diameter 16 ± 2.8 nm are synthesized following a procedure as laid out by McFarland *et al.* with no alterations.(McFarland, Haynes et al. 2004) Once the spheres are prepared, 5 mL of the solution centrifuged and the supernatant discarded. The concentrated gold particles are then added to 3 mL solution of a 400 mM NaCl solution. 10 μL of 2mM cysteine is then added. The solution is left overnight. Finally, a solvent exchange is performed by centrifuging the solution and replacing the supernatant with 40 mL of ethanol.

2.3.2 Thin Film Preparation

A solution containing the linked B-NRs is first solvent exchanged to chloroform. Once in Chloroform, 1.0 wt% of 7.8 kg/mol PEO or 2.1kg/mol PMMA is then added to this solution and dissolved. Finally, this solution is spin-cast directly onto a Si wafer at 3000 RPM for imaging and drop cast onto a glass slide to measure optical absorption.

2.3.3 QCM-D Experiments

The QCM-D measurement is based on the resonance frequency change of a vibrating quartz crystal, a piezoelectric material, when mass is deposited on it. The deposited mass, Δm, has a relationship with the frequency change, Δf, according to the Sauerbrey equation,(Sauerbrey 1959, Höök, Kasemo et al. 2001, Vogt, Lin et al. 2004, Jhon, Bhat et al. 2006, Lee and Penn 2008)

$$\Delta m = -C\frac{\Delta f_n}{n}$$

where C is the mass sensitivity constant (C = 17.7 ng·cm^{-2}·Hz^{-1} for an AT-cut, 5 MHz crystal) and n is the vibrational mode number (n = 1, 3, 5, ...). In addition, the dissipation change, ΔD_n , which is a measure of the loss of energy stored in a vibration cycle, indicates the physical characteristics of the deposited layer such as viscosity, elasticity, and so on. If ΔD_n is less than 2.0 x 10^{-6} and the plots of Δf_n /n under several modes are superimposed, the layer is an elastic film. The physical properties (mass and thickness) of the elastic layer can be calculated using the Sauerbrey equation.(Höök, Kasemo et al. 2001, Vogt, Lin et al. 2004) On the contrary, if ΔDn is more than 2.0 x10^{-6} and the plots of Δf_n /n are not superimposed, the layer is viscoelastic. The physical properties (thickness, shear modulus, and viscosity) of the viscoelastic layer can be estimated by fitting between the QCM-D experimental data (Δf_n /n (n = 1, 3, 5, ...) and ΔD_n) and a Voigt-based viscoelastic model

incorporated in Q-Sense software Q-Tools.(Höök, Kasemo et al. 2001, Jhon, Bhat et al. 2006, Lee and Penn 2008)

Stock solutions of C6DT, cysteine, and cysteine-capped Au nanospheres (C-AuNPs) in ethanol are prepared. Briefly, 10 μL of C6DT is added to 40 mL of ethanol, 100 μL of 2mM cysteine is added to another 40 mL of ethanol, and preparation of the C-AuNP stock solution is described above. An E4 QCM instrument (Q-Sense Inc., Gothenburg, Sweden) was used to monitor the binding of cysteine, C6DT, and C-AuNPs to Gold-coated QCM sensor crystals. Prepared solutions were pumped by peristaltic pump at a rate of 20 μL/min through a flow cell containing the sensor crystal. The temperature of the system was fixed at 21 °C.

2.3.4 DDA Calculations

Discrete dipole approximation (DDA) calculations were performed to determine the extinction efficiencies of dimers and tetramers of AuNRs (42 nm x 12 nm) immersed in a polystyrene matrix as a function of the interparticle separation and wavelength using DDSCAT 7.1 compiled with Open MP support.(Draine and Flatau 1994, Draine and Flatau 2010) The extinction efficiency (Q_{ext}) is the sum of the scattering and absorption efficiencies, Q_{sca} and Q_{abs}, respectively. The criterion for accuracy within 5% is that $|m|kd < 0.05$, where m is the complex refractive index, k is the wavenumber, and d is the effective particle size. For our calculations, the gold is embedded in a matrix with average refractive index of 1.55. Dielectric data were obtained from Weaver *et al.(Weaver and Fachinformationszentrum Energie)* and corrected for surface damping due to collisions of electrons with the surface of the nanorods.(Funston, Novo et al. 2009, Ungureanu,

Rayavarapu et al. 2009) The extinction efficiencies were determined by taking the average value for light polarized parallel and perpendicular to the length of the nanorods.

2.4 Results and Discussion

2.4.1 Functionalization and Assembly of B-NRs in Solution and Polymer Matrices

Figure 2.1 shows the four steps to prepare and end-to-end link the bi-functional AuNRs (B-NRs). The CTAB-coated AuNRs are synthesized by methods discussed elsewhere.(Nikoobakht and El-Sayed 2003, Sau and Murphy 2004, Hore and Composto 2010) First, the ends of the CTAB-coated AuNRs are modified by cysteine which links the AuNRs in water as shown in step 1. In step 2, the B-NRs are formed by replacing the CTAB along the sides of the AuNRs by a thiol-end functionalized poly(ethylene oxide) brush (HS-PEO). In step 3, the aqueous solution is exchanged with an organic solvent, resulting in the delinking of the B-NRs, and, in step 4, the B-NRs in organic solvent are linked together by end-attached alkane dithiol molecules (DT). Details of each step are described next.

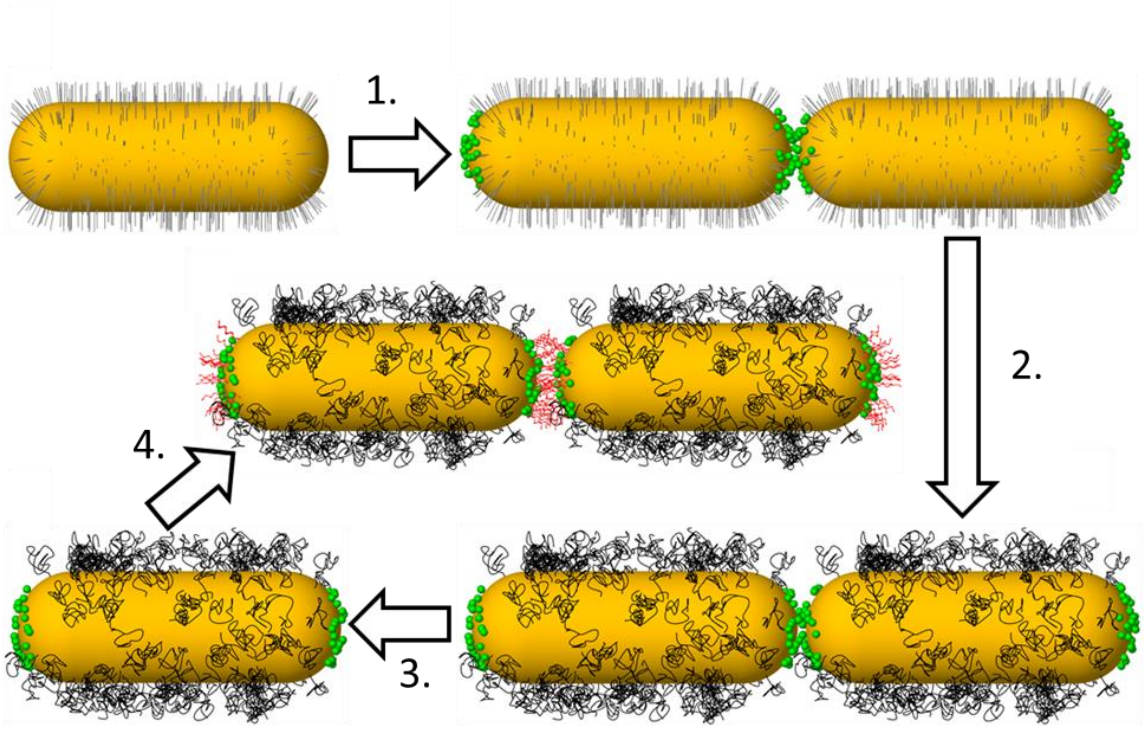

Figure 2.1 Synthesis proceeds clock-wise from the top left. CTAB-coated AuNRs are linked with cysteine (Step 1.). CTAB is replaced with HS-PEO (Step 2.) to facilitate transfer to non-aqueous solvents. A solvent exchange from water to methanol is performed (Step 3.), which de-links the B-NRs and frees up surface binding sites to allow for further end-functionalization. B-NRs are then linked with DT molecules in an organic solvent (*e.g.* chloroform) (Step 4.) and chains of B-NRs can then be transferred to polymer films via simple techniques such as spin-casting.

Figure 2.2a shows a representative SEM image of CTAB-coated AuNRs, which have a length and diameter of 39.1 ± 5.1 nm and 12.5 ± 1.4 nm, respectively, and an aspect ratio (AR) of 3.1. **Figure 2.2**b shows the UV/Vis spectrum of these AuNRs in water. The

longitudinal surface plasmon resonance (LSPR) peak wavelength is 707 nm, consistent with the literature for AuNRs with AR 3.1.(Link, Mohamed et al. 1999) The transverse surface plasmon resonance (TSPR), determined by the AuNR diameter, is observed at 536 nm.

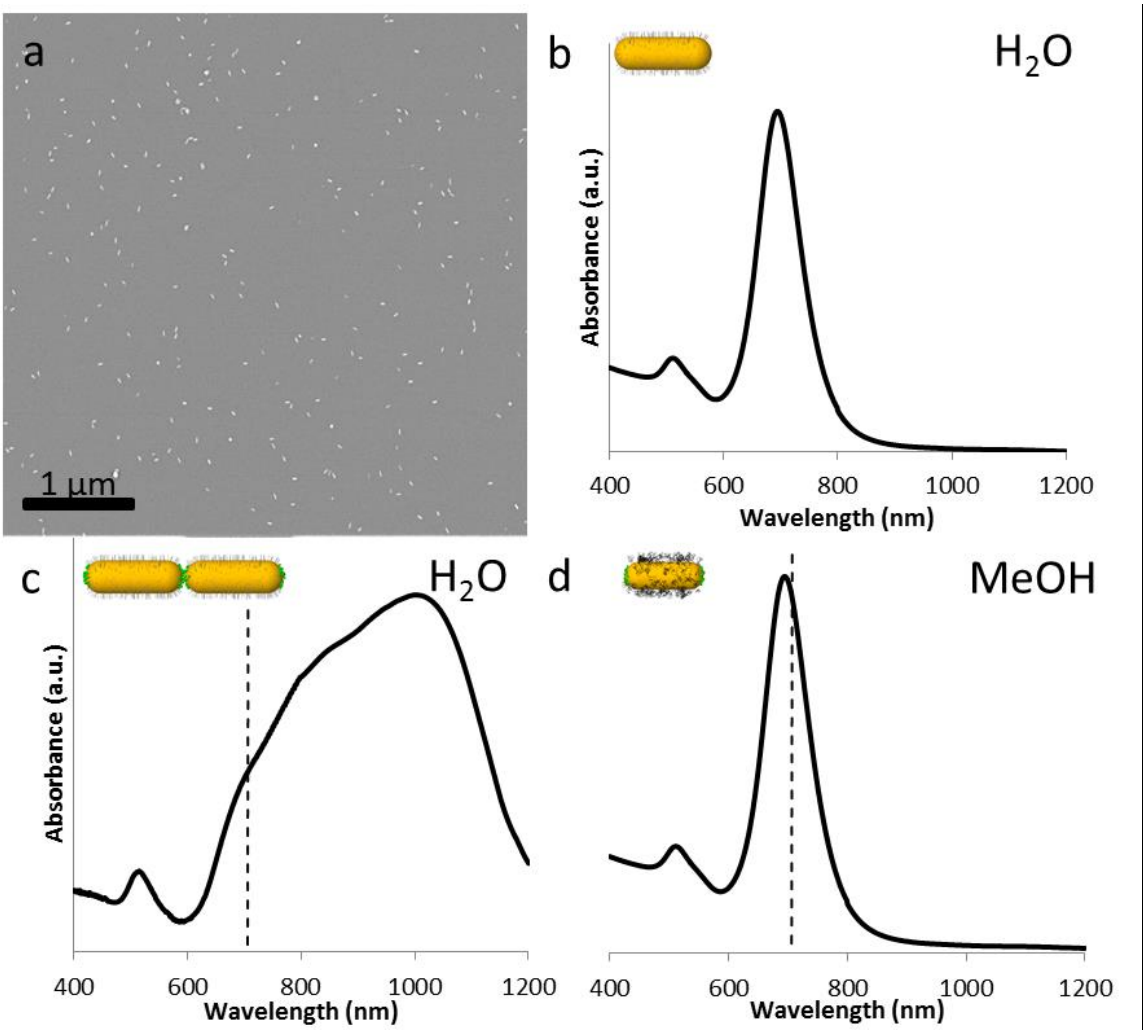

Figure 2.2 (a) Representative scanning electron microscope (SEM) image of AuNRs spin-cast from water onto a silicon substrate. The AuNRs are 39 nm long by 12.5 nm in diameter, which results in an aspect ratio of approximately 3.1. This aspect ratio is consistent with the LSPR peak of 707 nm seen in the UV/Vis spectra (b). Linking with cysteine results in a strong red-shift and broadening in the LSPR band, shifting the peak to 1024 nm as can

be seen in spectra (c), where the dotted line shows the unlinked peak position. The spectra returns to the discrete AuNR case after the CTAB on the side of the AuNR is replaced with 5 kg/mol HS-PEO and the solution is solvent exchanged to methanol with a peak position of 694 nm (d), nearly identical to the discrete AuNRs in water. The small blue shift is most likely due to a change in the index between water and methanol ($n_{H2O} > n_{MeOH}$).(Link, Mohamed et al. 1999, Chen, Kou et al. 2008)

The CTAB-coated rods are then linked with cysteine, an amino acid, (**Figure 2.1**, step 1) using a modified procedure from the literature.(Sethi, Joung et al. 2009) Whereas CTAB inhibits attachment along the side of the AuNR, cysteine binds to the ends of the AuNRs via the thiol moiety. Cysteine is thought to link AuNRs together either by hydrogen bonding(Ni, Mosquera et al. 2010) or because of its free amino group, the cysteine can link the AuNRs together via an electrostatic interaction.(Sethi, Joung et al. 2009) Regardless of linking mechanism, further modification at the ends of the AuNRs is suppressed. **Figure 2.3** are representative SEM images of the cysteine linked AuNRs. Upon linking, **Figure 2.2**c shows that the LSPR peak broadens and undergoes a strong red-shift to 1024 nm compared to the CTAB-coated AuNRs (dashed line). This red-shift is due to increased plasmon coupling between the AuNRs, whereas the broadening results from both increased coupling and convolution of LSPR peaks from individual, pairs, triads, etc. of AuNRs. This strong red-shift, broadening, and peak location are consistent with literature values for cysteine linked AuNRs.(Sethi, Joung et al. 2009)

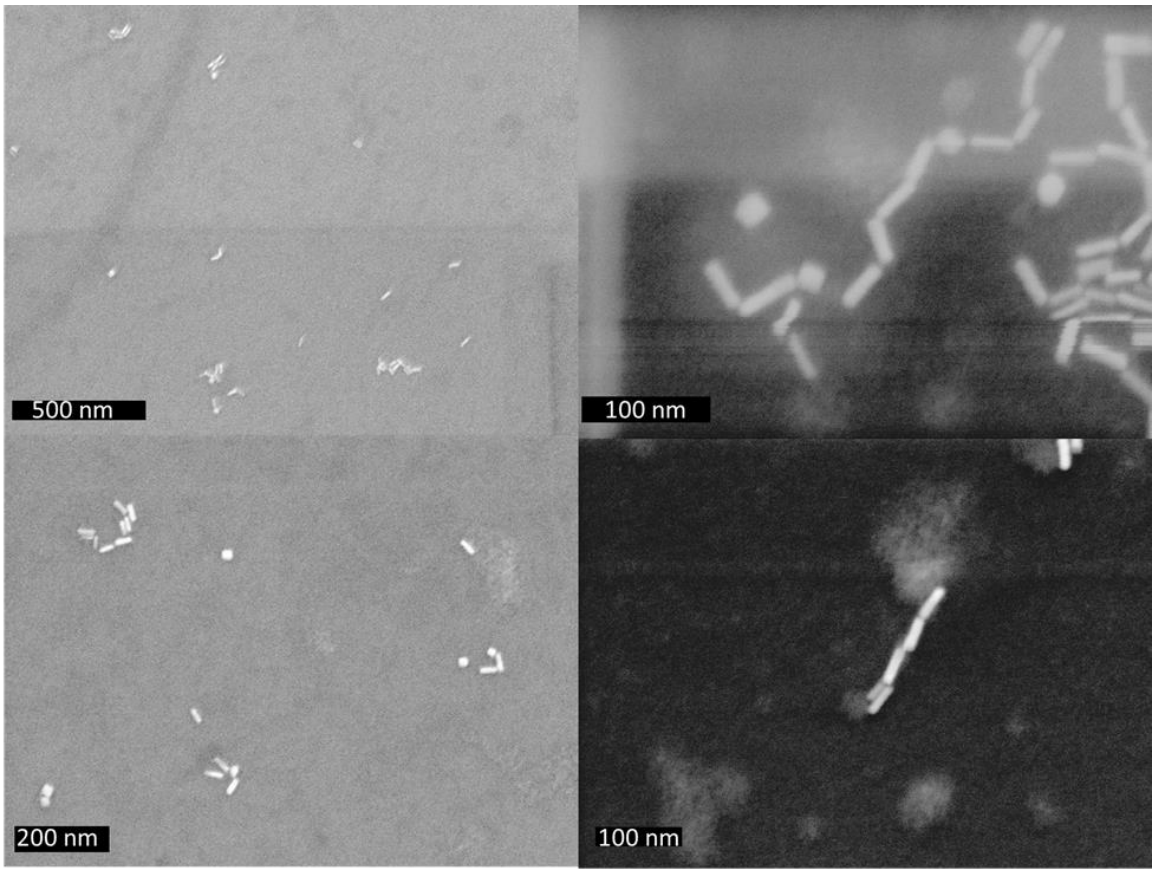

Figure 2.3 Scanning electron micrographs of AuNRs end-linked with cysteine. Samples were drop cast from water.

Because the ends of AuNRs are protected, a thiol-terminated polymer can be introduced to selectively replace CTAB molecules along the side of the AuNR as shown in **Figure 2.1**, step 2. In this study, the CTAB is replaced by a hydrophilic polymer brush, HS-PEO with a molecular weight of 5 kg/mol in aqueous solution. Brush molecular weight is a tunable parameter and assemblies have been demonstrated utilizing a HS-PEO brush with a larger molecular weight of 10 kg/mol. In step 3 of **Figure 2.1** the solvent is exchanged from water to methanol or ethanol, resulting in the de-linking of the AuNRs denoted by the blue shift of the LSPR peak to 694 nm as shown in **Figure 2.2**d. The small blue shift,

relative to isolated AuNRs in water, occurs due to the lower index of refraction of methanol versus water. Nevertheless, the peak position of dispersed AuNRs in methanol is very similar to that observed for the CTAB-coated AuNRs in water denoted by the dotted line in **Figure 2.2**d and the solid line in **Figure 2.2**b. Merely replacing the CTAB with 5K HS-PEO results in a small red-shift ca. 5 nm in the LSPR peak position as can be seen in **Figure 2.4**.

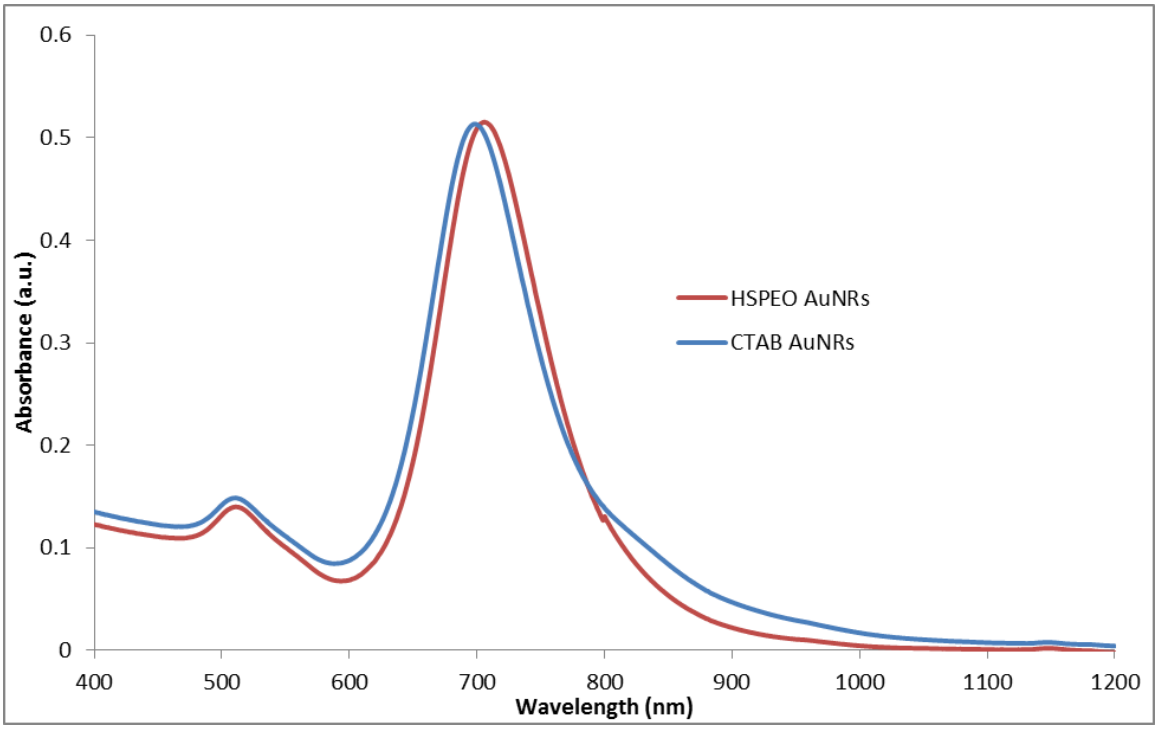

Figure 2.4 Absorbance spectra of AuNRs before (blue curve) and after (red curve) replacement of CTAB surfactant layer with 5K HSPEO. A 5nm red shift can be seen after CTAB is replaced with a homogeneous PEO layer.

Due to their hydrophilic PEO side and cysteine ends, B-NRs are a versatile building block for hierarchical assembly, in part because the B-NRs disperse in solvents that dissolve PEO. In particular, the B-NRs are adaptable for further end-functionalization.

Dithiol (DT) molecules have been used to link CTAB-coated AuNRs in mixed aqueous / organic solvents.(Shibu Joseph, Ipe et al. 2006) In the present study, 1,6 hexanedithiol (C6DT) and 1,9 nonanedithiol (C9DT) are attached to the ends of the B-NRs (**Figure 2.1**, step 4) to demonstrate control over the end-to-end separation and optical properties of linked B-NRs in solutions and films. **Figure 2.5**a, b, and c show SEM images of unlinked B-NRs and B-NRs incubated with C6DT and C9DT, respectively, for three hours, deposited on silicon. The UV/Vis spectra for the dispersed, C6DT linked and C9DT linked B-NRs in solution are given in Figures 2e to 2g, respectively. For the dispersed B-NRs, the LSPR peak is at 716 nm. (*c.f.* **Figure 2.2**b, **Figure 2.2**d). Upon adding C6DT and C9DT, the peak red-shifts to 878 nm and 789 nm, respectively, and broadens, consistent with end-linking. This UV-Vis behavior is supported by the SEM images in **Figure 2.5**b and **Figure 2.5**c which show chains with an average number of B-NRs of 5.5 ± 2.2 and 3.0 ± 1.2 rods per chain for C6DT and C9DT, respectively. Systematic studies of linker length on chaining of B-NRs are needed to understand difference in chain length between C6DT and C9DT linked B-NRs. To determine if linking is possible without the dithiols, B-NRs are also incubated with an alkane monothiol, 1-octanethiol, for 24 h. Relative to dispersed B-NRs, **Figure 2.5**h shows that the LSPR peak undergoes a small blue shift from 716 to 699 nm and slightly broadens. The SEM images in **Figure 2.5**d show that the B-NRs are mainly isolated with a few pairs of side-by-side B-NRs, which accounts for the small blue-shift in **Figure 2.5**h.

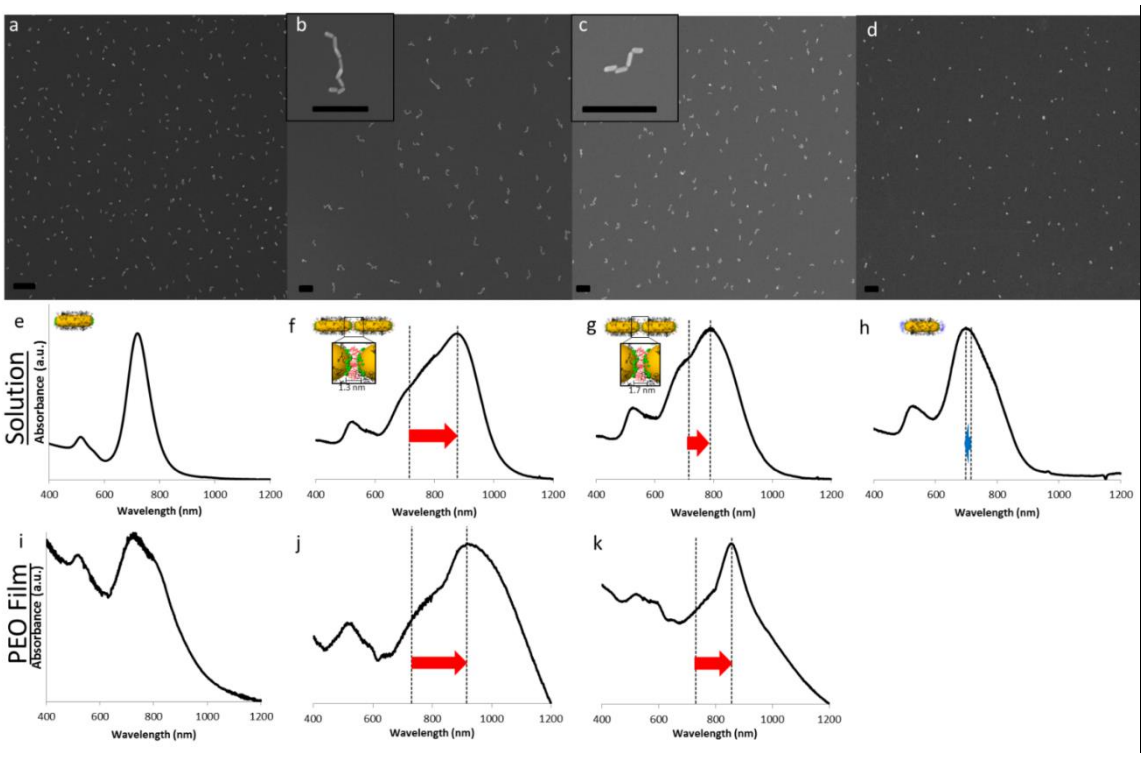

Figure 2.5 Representative SEM images of B-NRs unlinked (a), linked with C6DT (b), linked with C9DT (c), and incubated with 1-octanethiol (d) (all scale bars are 250 nm). B-NRs are well dispersed in the unlinked case (a) and the 1-octanethiol case (d) whereas in the linked cases (b and c) chains of end-linked B-NRs can be clearly seen. UV/Vis spectroscopy was performed on solutions of unlinked B-NRs (e), B-NRs linked with C6DT (f) and C9DT (g), and B-NRs incubated with 1-octanethiol (h). A strong red-shift and LSPR peak broadening is seen for linked B-NRs (f and g) as compared to the discrete case (e), while B-NRs incubated with 1-octanethiol exhibit a small blue-shift. UV/Visible spectroscopy was also performed on PEO films of B-NRs unlinked (i) and linked with C6DT (j) and C9DT (k). Spectra from the films compare favorably with those taken in solution.

Polymer nanocomposite films containing end-to-end linked B-NRs in a PEO matrix were prepared by mixing the B-NRs with C6DT or C9DT in an organic solvent containing 1wt% PEO (7.8 kg/mol), incubating for 3 hours to allow linking of B-NRs, and finally drop-casting the solution onto glass slides. For comparison, a solution of unlinked B-NRs in an organic solvent containing 1 wt% PEO was also drop-cast onto a glass slide. **Figure 2.5**i-k show the absorbance spectra for films containing unlinked B-NRs, B-NRs linked by C6DT, and B-NRs linked by C9DT, respectively. For the unlinked B-NR system, the LSPR peak position is 731 nm. This small red-shift relative to the solution case (*c.f.* **Figure 2.5**e, 716 nm) is attributed to the change in refractive index and/or some aggregation of B-NRs upon drying. In contrast, relative to the unlinked B-NR system, the LSPR peak positions undergo a significant red-shift to 916 nm and 857 nm for the C6DT and C9DT linked B-NR systems, respectively. **Table 2.1** summarizes the absorbance peak positions at each step during the surface modification and linking process. LSPR peak positions in PEO films are similar to those found in solution suggesting that the linking in solution is retained in the drop-cast film.

Table 2.1 LSPR Peak Positions of unlinked and linked AuNRs

Surface Functionalization	Solvent or Polymer	LSPR Peak (nm)
CTAB	H_2O	707
Cysteine	H_2O	1024
HS-PEO	Methanol	694
HS-PEO	$CHCl_3$	716
1-octanethiol	$CHCl_3$	699
C6DT	$CHCl_3$	878
C9DT	$CHCl_3$	789
HS-PEO	PEO	731
C6DT	PEO	916
C9DT	PEO	857

2.4.2 Inter-rod Spacing, B-NR Chain Length, and Optical Properties

To interpret the experimental results, the extinction efficiencies (Q_{ext}) and LSPR peak position of end-to-end aligned AuNRs were determined from discrete dipole approximation (DDA) calculations. **Figure 2.6**a shows Q_{ext} for pairs of AuNRs (42 nm x 12nm, AR = 3.5) at separations of 100, 10, and 1 nm, as well as Q_{ext} for a tetramer having an equal spacing of 1 nm. At a separation of 100 nm (red), plasmonic coupling between AuNRs is weak because the gap is much greater than the nanorod size. Thus, the LSPR peak position is sharp and located at 844 nm, consistent with the aspect ratio of 3.5. As the gap between pairs decreases, **Figure 2.6**a shows that the LSPR peak red-shifts to 880 nm and 959 nm for separations of 10 nm (blue) and 1 nm (black), respectively. The LSPR peaks also broaden as the gap decreases. For the tetramer at 1 nm separation (black dashed), **Figure 2.6**a shows that the LSPR peak position undergoes a very strong red-shift to 1064 nm as well as further broadening, compared to discrete AuNRs (red). This strong

red-shift and broadening is attributed to increased coupling as the number of "linked" AuNRs increases.

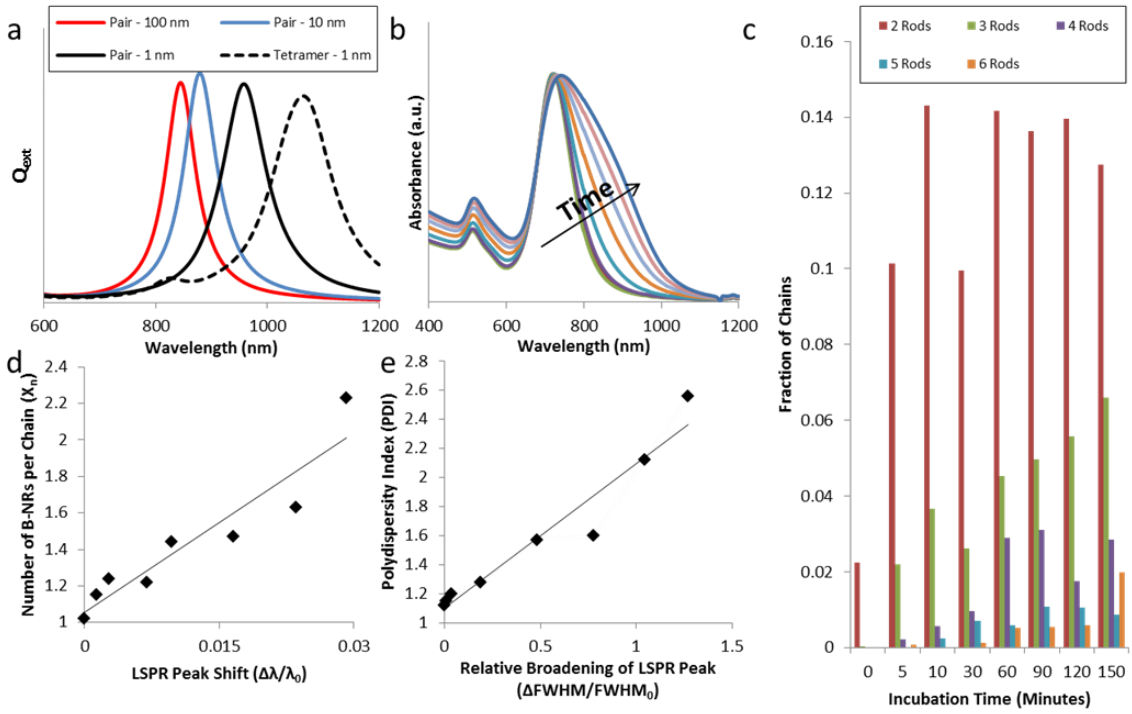

Figure 2.6 (a) DDA calculations for end-linked rods in a polymer matrix. Calculations were performed for pairs of rods at end-to-end separation distances of 100 nm, 10 nm, and 1 nm and for a tetramer of rods at 1 nm. As the distance decreases, the LSPR peak red-shifts and broadens. B-NRs were incubated with C6DT and absorbance spectra were taken at various time points (b). The LSPR peak red-shifts and broadens as a function of time. This solution was cast in a PMMA film at the same time points as the UV/Vis data and chain length was analyzed (c). As incubation time increases, the average number of B-NRs per chain (X_n) also increases. X_n is correlated with LSPR peak shift (d) which is consistent with DDA calculations. Polydispersity in chain size (PDI) also increases with incubation

time and this is correlated with the relative broadening of the LSPR peak (e). The trendlines in d and e serve as guides to the eye.

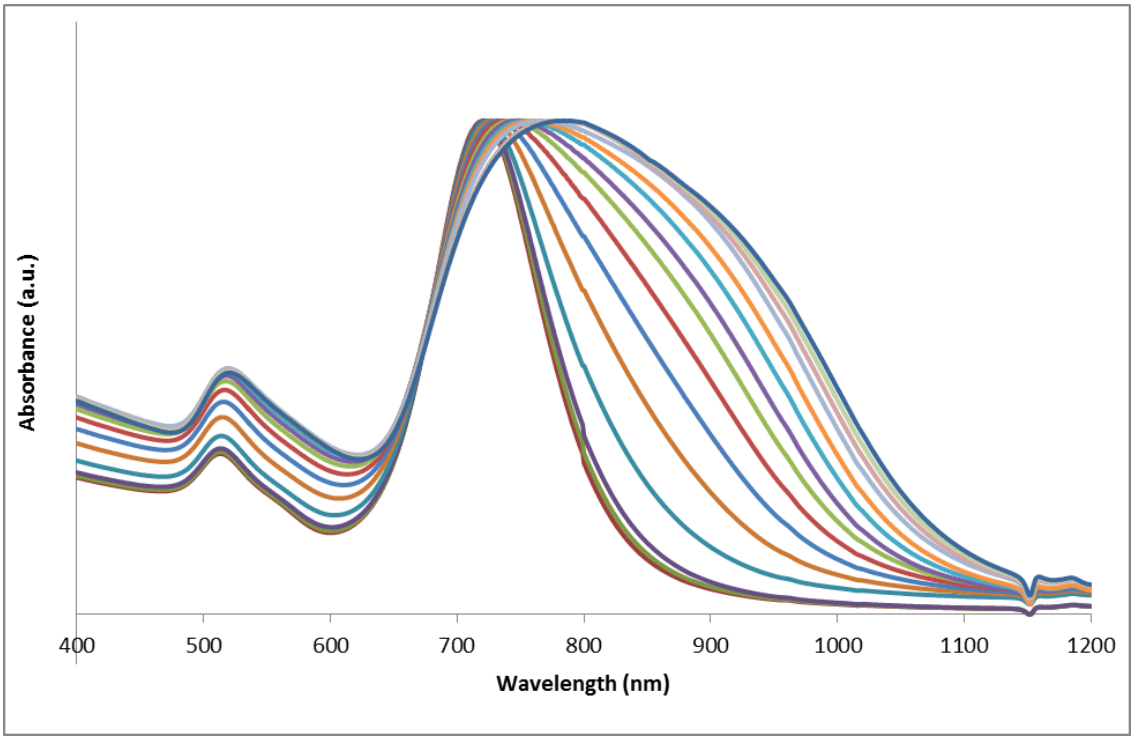

Figure 2.7 UV/Vis spectra for B-NRs linked with 1,6 hexanedithiol in chloroform at different incubation times. Curves shown are for 0, 5, 10, and 30 minutes incubation, followed by curves every 30 minutes (*i.e.* 60 minutes, 90 minutes, *etc.*) up to 6 hours. As time increases, the LSPR peak red-shifts and broadens, consistent with linking.

These DDA calculations support the experimental studies of the LSPR peak shifts and broadening reported in **Figure 2.5** and **Table 2.1**. The DDA calculations show a stronger shift between discrete rods and the tetramer case, 220 nm, as compared with discrete B-NRs and those linked with C6DT, 162 nm, despite a similar average chain size (5.5 B-NRs per chain). This discrepancy is resolved by realizing that the distance between B-NRs

linked with C9DT is almost twice the gap size in the DDA calculation, 1.7 nm compared with 1 nm, resulting in weaker coupling between the B-NRs and a smaller shift.(Funston, Novo et al. 2009) Furthermore, DDA calculations assume that rods are perfectly parallel to each other, whereas in the films, the B-NRs are not perfectly aligned because the linker (*i.e.*, -CH_2- units) is flexible and rods interacting at angles exhibit weaker longitudinal plasmon coupling.(Funston, Novo et al. 2009, Shao, Woo et al. 2010) This comparison illustrates the sensitivity of optical properties to small changes in linker length and stiffness and suggests a simple route to fine tune the extinction. For example, by replacing the flexible alkane with a stiff phenyl backbone, end-to-end alignment between B-NRs would increase and correspondingly a larger red-shift would result.

Absorbance spectra in solution predict the assembly of AuNRs after casting into films. B-NRs were linked by incubating in chloroform containing C6DT and poly(methyl methacrylate) (PMMA). PMMA (2.1 kg/mol) was chosen as a matrix to demonstrate that matrix polymers in addition to PEO (**Figure 2.5**) are possible. A lower concentration of C6DT, as compared with our previous experiments, was chosen to decrease the reaction kinetics to more precisely analyze the linking behavior of B-NRs. Absorbance spectra from the solution were acquired as a function of incubation time and plotted in **Figure 2.7**. After incubating the B-NRs with C6DT for a range of times, films were spin cast from these solutions and then imaged by SEM to correlate the LSPR peak shift and relative broadening with the number and polydispersity of linked B-NRs. **Figure 2.6**b shows selected absorbance spectra from the solutions that were used to cast films. **Figure 2.6**c shows that the fraction of pairs, triads, *etc.* of B-NRs increases as incubation time increases, in qualitative agreement with the increasing LSPR peak position red–shift (*c.f.* **Figure 2.6**b)

and DDA calculations (*c.f.* **Figure 2.6**a). For example, after 90 minutes, the percentage of individual B-NRs has decreased to 76%, whereas the pairs and triad fraction has increased to 14% and 5%, respectively. **Figure 2.6**d shows that the number averaged B-NRs per chain (X_n) increases linearly plotted against the LSPR peak shift toward the red, consistent with literature.(Liu, Ahmed et al. 2013) **Figure 2.6**e shows that the polydispersity index (PDI) of linked B-NRs increases with time, consistent with a step-growth polymerization mechanism where a wide variety of chain sizes will be present at any given time due to the independence of 'monomer' (*i.e.* B-NRs in this case) reactivity from chain size.(Odian 2004, Liu, Nie et al. 2010) This increase in PDI correlates with an increase in the FWHM of the LSPR peak that results from the overlap of individual peaks due to pairs, triads, tetramers, *etc*. In conclusion, these studies show that the LSPR in polymer nanocomposites can be varied by controlling inter-rod spacing between B-NRs (peak position), B-NR X_n (peak position and breadth) and B-NR PDI (peak breadth). By tailoring nanorod linking, a novel route towards tuning the optical properties of polymer nanocomposite films has been demonstrated here.

2.4.3 Mechanism for AuNR Assembly

To understand and better control the assembly of B-NRs, the mechanism for linking B-NRs end-functionalized with dithiol molecules was investigated using QCM-D. In step 1 of **Figure 2.1**, the ends of the AuNRs are modified with cysteine resulting in linking. In this step, the addition of salt screens the self-interaction between the carboxylic and amine groups on the cysteine molecules. Upon solvent exchanging from water to methanol (step 2), the electrostatic interaction weakens and the soluble salt concentration decreases, resulting in a delinking of AuNRs. A corresponding decrease in the grafting density of the

cysteine allows for subsequent attachment of DT molecules at the ends of the AuNRs. However, the cysteine grafting density is sufficient to allow only one end of the DT to attach (*i.e.*, no loops form). Because it is longer than the short cysteine, the DT molecule can extend its free SH group to bind with the end of a neighboring AuNR. As incubation time increases, the number of end-to-end linked AuNRs increases as previously observed in **Figure 2.6**b.

QCM-D is an in-situ method for quantifying the coverage of molecules or particles. The resonance frequency of the quartz crystal substrate decreases as molecules/particles adsorb from the surrounding fluid onto the surface. For elastic layers, this frequency change is related to mass uptake using the Sauerbrey equation. To mimic the functionalization of the end of the AuNR, a gold-coated QCM-D crystal was exposed to the treatments described in **Figure 2.1**. First, the assembly of elastic layers of cysteine and C6DT on the gold-coated crystal was investigated. A monolayer of cysteine was measured and found to have an areal density of 1.94 molecules/nm^2, consistent with the literature.(Zhang, Chi et al. 2000) The areal density of C6DT on the gold crystal was found to be only 0.16 molecules/nm^2, significantly lower than 4.7 molecules/nm^2 reported for alkane monothiols.(Strong and Whitesides 1988) This sub-monolayer coverage indicates that both ends of C6DT can bind to the gold surface, limiting further attachment of C6DT.(Leung, Gerstenberg et al. 2000)

The mechanism of linking was investigated by exposing the planar gold-coated crystal to the scheme in **Figure 2.8**a, which mimics the steps to link AuNRs depicted in **Figure 2.1**. First, after an exposure time of 40 minutes and rinsing, cysteine is bound to the gold-coated crystal at a surface coverage of about 50%, similar to the coverage on the ends of AuNRs after delinking. **Figure 2.8**b shows the areal mass determined from the QCM

frequency (**Figure 2.9**) using the Sauerbrey equation, where the white and gray regions represent the elastic adlayers of cysteine and cysteine/dithiol, and the viscoelastic adlayer of the AuNPs grafted to the cysteine/dithiol layer. After rinsing to remove loosely bound molecules, the areal density of cysteine is 1.12 molecules/nm^2, about half a monolayer. Upon exposing the sub-monolayer of cysteine to C6DT, the mass increases rapidly and then more slowly after ~ 100 minutes, reaching an areal density of 3.4 C6DT molecules/nm^2 after rinsing. Compared to the areal density of C6DT molecules grafted directly to gold, the cysteine primed surface allows for nearly a 2000% increase, suggesting that cysteine directs C6DT to only end attach rather than form a loop on the gold surface. However, this grafting density is about 30% less than literature values for similarly lengths of alkane monothiols,[25] consistent with cysteine blocking surface sites.

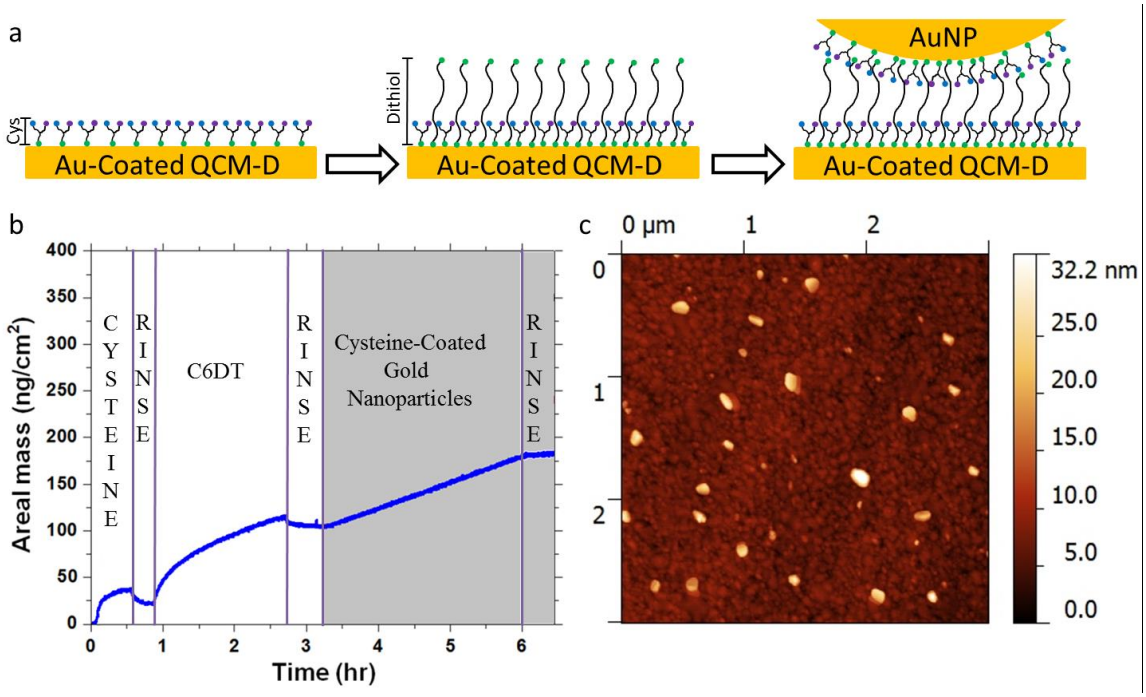

Figure 2.8 (a) Cartoon depicting each step in QCM-D experiments. A gold QCM-D crystal is first coated with a sub-monolayer of cysteine (cys), followed by C6DT, which binds at

interstitial sites between cysteine molecules. Cysteine coated gold nanoparticles (16 nm in diameter) then bind to the gold substrate via C6DT that "stands up." Figure (b) details the change in areal mass as calculated from the change in frequency of the 7^{th} mode at each step in the QCM-D experiment detailed in scheme (a). Binding events are characterized by an increase in the areal mass. Rinsing steps were done to remove physically bound molecules. Cysteine bound at a density of 1.12 chains/nm^2, while C6DT bound at 3.4 chain/nm^2. Cysteine-coated gold nanoparticles were calculated to bind at 18.5 NPs/μm^2. AFM was performed (c) on the QCM-D crystal and particles with an average feature height of 18.2 +/- 5 nm were bound at an areal density of 7 +/- 3 NPs/μm^2.

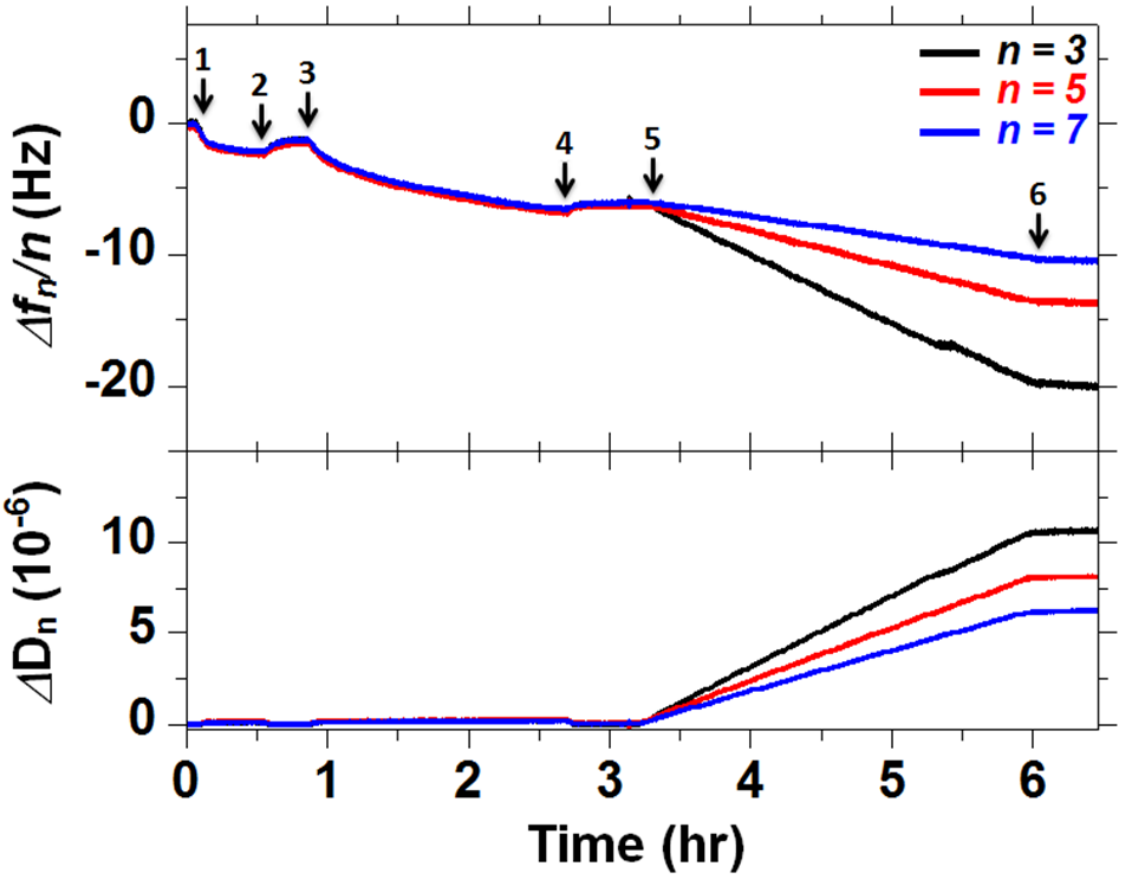

Figure 2.9 Traces of (top) $\Delta f_n/n$ (n= *3, 5, 7*) and (bottom) ΔD_n versus time for formation of cysteine sub-monolayer, followed by formation of 1,6 hexanedithiol/cysteine layer and subsequent nanoparticle grafting. Arrows 1, 2, 3, 4, 5, and 6 represent the exposure of cysteine solution, rinsing with ethanol, the exposure of 1,6 hexanedithiol solution, rinsing with ethanol, the exposure of nano-particle (~16 nm) solution, and rinsing with ethanol, respectively.

To mimic step 4 in **Figure 2.1**, the planar gold crystal surface is functionalized with a mixture of cysteine and C6DT and then exposed to cysteine-coated spherical AuNPs (16 nm in diameter) for approximately three hours as described in **Figure 2.8**a. Because they

are tethered to the crystal, the AuNP layer is viscoelastic as evidenced by the splitting of the harmonics and increase in dissipation shown in **Figure 2.9**. For comparison, the cysteine and cysteine/C6DT layers show overlapping harmonics and negligible splitting consistent with an elastic solid. To limit overestimating the NR mass when applying the Sauerbrey equation to viscoelastic films, the harmonic with the lowest dissipation value (n=7, *c.f.* **Figure 2.9**) was used to determine the areal mass and NP areal density at long times, namely 160ng / cm^2 and 18.5 NPs/μm^2, respectively. For a random closed packed arrangement of non-interacting, spherical, monodisperse AuNPs, the maximum areal density is about 2500 NPs/μm^2. Thus, the QCM-D measurements indicate a AuNP coverage about 1% of the ideal maximum packing.

AFM was used to verify the AuNP coverage determined by QCM-D. **Figure 2.8**c shows a topography image (3 μm x 3 μm) of the same surface used in the QCM-D experiments described in **Figure 2.8**b. The isolated high features (white) are about 1 mm apart and have a height of 18 ± 5 nm. This height is consistent with the diameter measured by SEM, 16 nm. For comparison, an AFM image of a neat gold-coated QCM-D crystal was also measured and found to be featureless, **Figure 2.10**. The areal coverage of AuNPs is 7 ± 3 NPs /μm^2. Given the sparse coverage and resulting error, the direct space AFM results are in agreement with the more sensitive measurement by QCM-D. To summarize, based upon the QCM-D and AFM results, after an initial sub-monolayer of cysteine forms on the Au surface, C6DT is able to insert itself into the cysteine layer and bind by one end to the gold surface. Moreover, because the cysteine blocks the C6DT from forming a loop on the surface, a free thiol end extending from the surface can bind with a neighboring AuNP in solution or, in the case of AuNRs, link together nanorods.

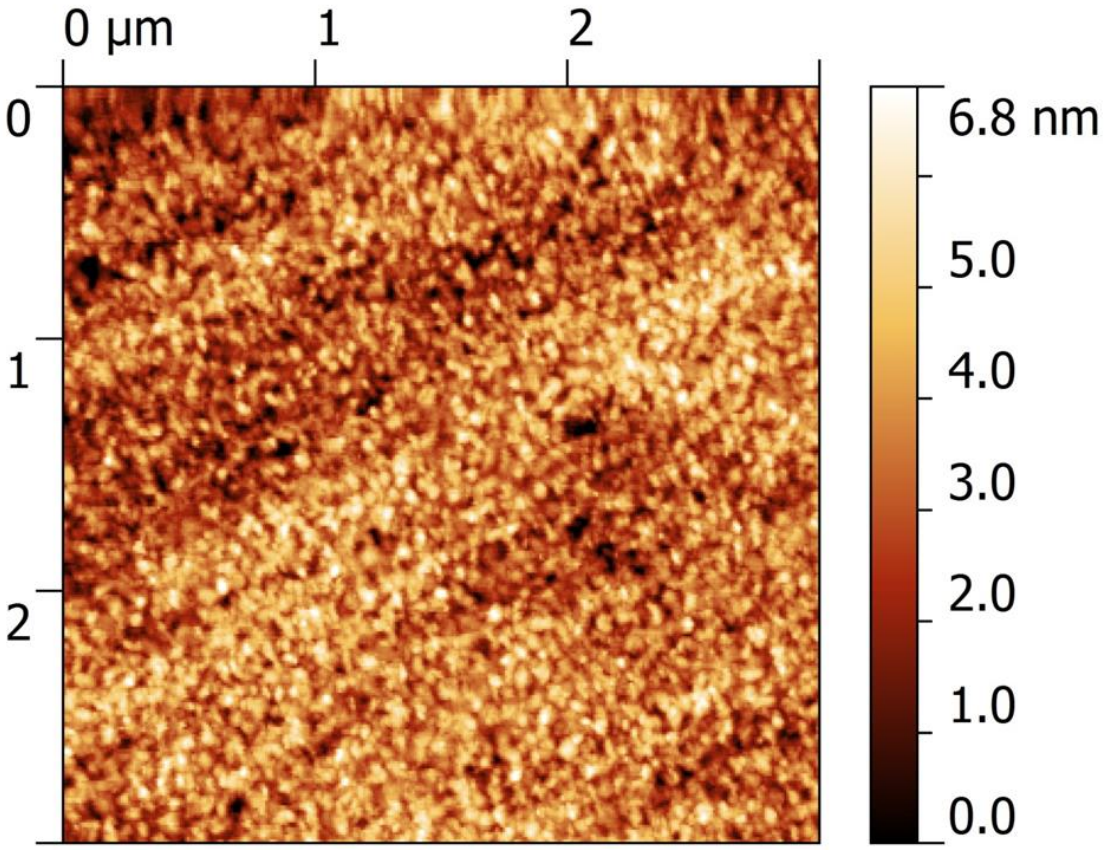

Figure 2.10 Topography AFM image of neat QCM-D crystal showing no features.

2.5 Conclusions

Herein, we have demonstrated a robust method to synthesize B-NRs, link end-to-end with DT molecules, and disperse, while linked, in a PEO or PMMA matrix. Using a combination of methods including DDA, UV/Vis, and SEM, the chain length, inter-rod distance, and chain polydispersity are shown to affect the optical properties of the nanocomposite films. Through UV/Vis and QCM-D experiments, the mechanism for B-NRs to be further modified with thiolated molecules has been elucidated. Namely, one end of the DT inserts into the cysteine adlayer on the end of the B-NR and bonds with the end of the B-NR leaving a free thiol to bond with the end of a neighboring B-NR. The links

between B-NRs are retained in various solvents and even persist after spin coating solutions to create a polymer nanocomposite film. The UV/Vis studies show that the LSPR peak shift is consistent with those predicted by DDA calculations for end-to-end pairs and tetramers of AuNRs at various separation distances. By changing the length of the linker and incubation time, absorption can be tuned both in solution and, for the first time, in a polymer matrix. This latter ability is particularly important because the gap directly determines the strength of plasmonic coupling. By understanding the mechanism that controls linking of B-NRs, side-by-side assembly is also possible by selecting different end and side group molecules, to further tune absorption. Using liquid crystal molecules on the ends, the gap between nanorods can itself become functional and impart additional liquid crystal properties superimposed on those of the metallic nanorods. The anisotropic surface chemistry examined in this study can be expanded to other nanometric "building blocks" to create unique nanostructures such as controlling the faces of attachment for nanocubes.(Gao, Arya et al. 2012) Thus, the advances in understanding how to direct the assembly of complex particles within a polymer can now be applied to create novel optical, electronic, and sensory devices.

Chapter 3 DNA-Gold Nanorod Polymers

In Collaboration with Drs. Guillaume Gines, Patrice Rannou, Didier Gasparutto, and Brigitte Pépin-Donat (INAC/CEA/CNRS, France)

3.1 Abstract

In this work, we controllably link gold nanorods using end-grafted DNA (DNA-NRs). Gold nanorods are end-grafted with one of two complimentary DNA strands (A-DNA and B-DNA) and combined with water to make solutions of A-DNA-NRs and B-DNA-NRs. By adding B-DNA-NRs to a reservoir of A-DNA-NRs, the DNA-NRs are linked through DNA hybridization. The degree of linking or "polymerization" (X_n), which depends upon the amount of B-DNA-NRs added to the A-DNA-NR reservoir, and the X_n follows the Carothers' equation describing step growth polymerization. Finite difference time domain simulations are performed to determine the longitudinal surface plasmon resonance (LSPR) peak as a function of X_n, which is compared to the experimentally determined LSPR peaks. Finally, the "polymers" are characterized by electron microscopy to determine the experimental X_n, which matches up very well with the X_n calculated from Carothers' equation. This procedure can be extended to controllably polymerize nanorods of two disparate materials (*e.g.* gold and CdSe) for further property control.

3.2 Introduction

The utilization of metal nanoparticles as robust sensing platforms has received significant interest from the scientific community. Gold nanorods (AuNRs) are particularly attractive for sensing applications due to their facile synthesis(Nikoobakht and El-Sayed 2003, Sau and Murphy 2004), assembly dependent optical properties(Funston, Novo et al. 2009, Hore and Composto 2010, Ferrier, Lee et al. 2014), and ease of functionalization. AuNRs are characterized by two absorbance peaks, the longitudinal surface plasmon resonance peak (LSPR), based on the AuNR length, and the transverse surface plasmon resonance peak (TSPR), based on the AuNR diameter. SPR peaks are affected, not only by the physical characteristics of individual AuNRs, but also by the assembly of the AuNRs; assembling AuNRs end-to-end will cause a bathochromic shift in the LSPR, while assembling side-by-side will cause a hypsochromic shift in the LSPR. Furthermore, the end-to-end assembly of AuNRs results in the generation of "hot-spots" in the gaps between AuNRs. In these hot-spots, the electric field is significantly enhanced, making AuNRs useful for surface enhanced Raman spectroscopy (SERS).(Nikoobakht and El-Sayed 2003, Lee, Andrade et al. 2011) Optical property changes can, therefore, be used to probe the assembly of the AuNRs.

Anisotropically functionalized AuNRs can be linked end-to-end to control the optical properties. Many schemes to link nanorods have been developed. Thomas and co-workers(Shibu Joseph, Ipe et al. 2006) used alkanedithiol molecules to link nanorods end-to-end. Sethi *et al.*(Sethi, Joung et al. 2009) used cysteine to link gold nanorods and Sun *et al.*(Sun, Ni et al. 2008) showed this cysteine linkage could be reversed by tuning the solution pH. Kumacheva and co-workers(Nie, Fava et al. 2007, Nie, Fava et al. 2008) end-

assembled gold nanorods by grafting polystyrene to the end of AuNRs and titrating in water, a poor solvent for polystyrene, to trigger assembly. However, while gold nanorods can be controllably assembled end-to-end, all of the assembly schemes mentioned above lack a specificity in assembly and facile control over the gap distance. That is to say, if one wants to assemble two different materials in a specific order, at a precise distance, the methods above cannot accomplish this.

DNA can be used to reversibly and specifically assemble nanoparticles. DNA is typically thought of as a building block for life, allowing complex biological structures to be synthesized from the information coded in a base pair sequence. However, DNA has also been used as a building block for inorganic matter. Alivisatos(Alivisatos, Johnsson et al. 1996) and Mirkin(Mirkin, Letsinger et al. 1996) first demonstrated this ability independently from one another by assembling 3D structures of DNA grafted gold nanoparticles (AuNPs). Since then, techniques such as DNA origami(Rothemund 2006) have evolved to allow precisely controlled 3D structures of AuNPs in a wide variety of shapes.(Sharma, Chhabra et al. 2009, Ding, Deng et al. 2010, Gu, Chao et al. 2010) DNA has been used to reversibly assemble AuNRs. Djuardin *et al.*(Dujardin, Hsin et al. 2001) first demonstrated the assembly of AuNRs with DNA; they functionalized strands of DNA to AuNRs, and added in a free DNA strand with a sequence that would bridge two grafter DNA strands .and then hybridized the DNA. The LSPR peak underwent a hypsochromic shift as a function of DNA linker concentration. More recently, Zhao *et al.(Zhao, Zhang et al. 2013)* demonstrated that AuNRs can be reversibly assembled end-to-end through DNA hybridization. Here, Zhao *et al.* grafted self-complimentary DNA strands selectively to the ends of the AuNRs. Upon hybridization the AuNRs linked end-to-end resulting in a strong

bathochromic shift in the LSPR peak position, which could be reversed by heating the solution above the DNA melting temperature. Therefore, they were able to turn the shift on and off. However, because the DNA used was self-complimentary, little control over the strength of the shift was achieved and specificity was not demonstrated.

In this work, we present a method for precisely tuning the optical properties of DNA end-grafted bi-functional gold nanorods (DNA-NRs) solutions by controllably linking DNA-NRs by hybridization. Hybridization of DNA-NRs can be thought of as monomers linking by covalent bond and, therefore, we can consider this a "polymerization." One batch of DNA-NRs is functionalized with A-DNA and another batch is functionalized with complimentary B-DNA. The solutions were then mixed at a controlled ratio of A-DNA-NRs to B-DNA-NRs such that the degree of polymerization (X_n) can be tuned, thereby controlling the final optical properties. Optical properties were probed with both UV/Visible spectroscopy. Upon increasing the ratio of B-DNA-NRs in a reservoir of A-DNA-NRs a bathochromic shift in the LSPR peak was observed. The chain length of the NR polymers was predicted by applying Carothers' equation for step-growth polymerization. Finite difference time domain (FDTD) simulations were performed to calculate the LSPR peak position at various X_n, which was compared to the experimentally determined LSPR peak positions and were used to predict experimental X_n. The X_n and DNA-NR gap distance determined by SEM was found to be in good agreement with the calculated values. Specifically, the spacing of the DNA-NRs polymers was found to be ca. 2.6 nm (*c.f.* 3 nm with FDTD) and the X_n was found to be 2.1 (*c.f.* 2.2 with Carothers' equation). Therefore, we have demonstrated that we can polymerize two different batches

of DNA-NRs which we could then extend to the polymerization of nanorods consisting of two different materials (*e.g.* gold and CdSe) ala block co-polymer.

3.3 Experimental Procedure

All reagents were purchased from Sigma-Aldrich, unless otherwise specified.

3.3.1 DNA-NR Preparation

Two complimentary DNA strands end-functionalized with thiol were purchased from Eurogentech and purified through HPLC prior to use. The sequences are A-DNA: 5'-HS-C_6-TCG-GAT-ACC-CAA-GGA-3' and B-DNA: 5'-HS-C_6-TCC-TTG-GGT-ATC-CGA-3'. Bi-finctional gold nanorods (BNRs) were synthesized as described elsewhere.(Ferrier, Lee et al. 2014) Briefly, BNRs consist of AuNRs with the long axis grafted with 5000 g/mol thiol end functionalized poly(ethylene oxide) (HS-PEO), where the ends of the AuNRs are functionalized with a sub-monolayer of cysteine. The BNRs used in this study were 38 +/- 3.4 nm in length by 12.3 +/- 1.6 nm in diameter. Two identical, stock solutions of BNRs, A and B, were prepared with a volume of 200 µL (0.8 nM). A-DNA was added to stock solution A at a final concentration of 170 nM, while B-DNA was added to stock solution B at the same final concentration. DNA / BNR solutions were incubated overnight followed by purification via centrifugation (to remove excess DNA) and a solvent exchange to 10 mM PBS buffer. The final stock solution volume was 500 µL. Solutions were characterized by UV/Visible spectroscopy (HP851A) before DNA incubation, after DNA incubation, and after solvent exchange to PBS buffer.

3.3.2 DNA-NR "Polymerization" Preparation

DNA-NRs were linked via DNA hybridization by adding a small volume of stock solution B to stock solution A, heating above the T_m of DNA, and quenching to room temperature. First, 5% of stock solution B was added to A (now solution AB) and this solution was allowed to incubate overnight. Next, solutions AB and B were heated to 50 °C for 3 minutes and then quenched to room temperature. UV/Visible spectroscopy was performed on both solutions to determine if linking had occurred. Solution AB was also drop-cast onto Si wafers for SEM imaging (JEOL7500F). Finally, this procedure was repeated for final of %B added: 12.5% and 37.5%.

3.3.3 Finite-Difference Time Domain (FDTD) Calculations

Lumerical (v. 8.11.318) was used for FDTD simulations. AuNRs were simulated by creating a cylinder with spherical end caps. The AuNRs were 39 nm in length by 12 nm in diameter. The simulation box was fit to surround the AuNRs with a cubic mesh size of 0.8 nm. Conform_0 was used to estimate properties in partially filled meshes. Incident light was directed perpendicular to the AuNRs and polarized along the long axis of the AuNRs to calculate the LSPR peak absorbance between 600 and 1200 nm.

3.4 Results and Discussion

Thiol-ssDNA was grafted selectively to the ends of bi-functional gold nanorods (BNRs). BNRs consist of poly(ethylene oxide) (M_n = 5000 g/mol) grafted sides and cysteine grafted ends and were prepared as described elsewhere.(Ferrier, Lee et al. 2014) The two complimentary DNA strands (A and B) both consist of a 15-mer sequence with a 6 carbon spacer and a thiol end group at the 5' end. The BNR solution was divided into two sets at

identical concentration of 0.8 nM. The A-DNA was added to one set and the B-DNA was added to the second set each at a concentration of 170 nM. The solutions were purified by centrifugation to remove free DNA and exchanged to 10 mM PBS. **Figure 3.1** shows the absorbance spectra of the BNRs before and after incubation with A and B DNA. The absorbance spectrum for the NRs before and after functionalization remains the same with an LSPR peak position of 738 nm.

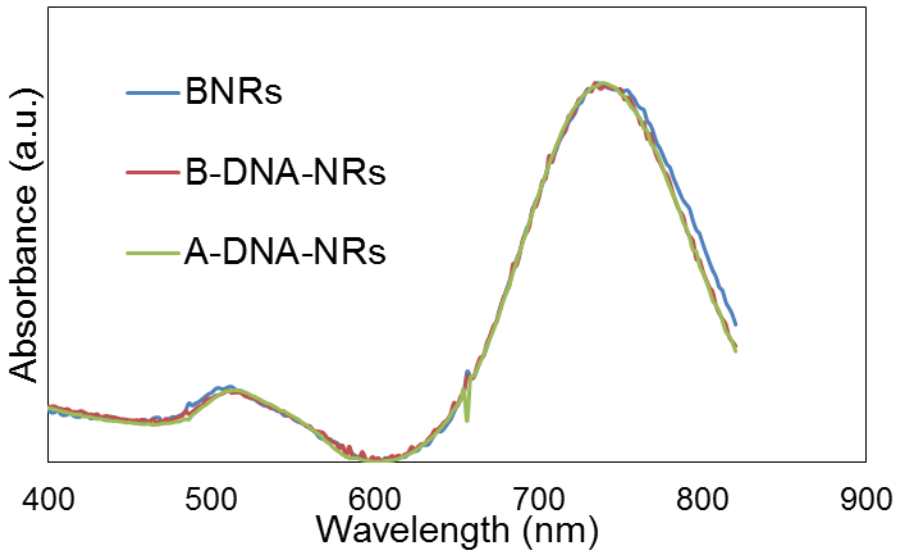

Figure 3.1 Absorbance spectra of BNRs (blue), B-DNA-NRs (red) and A-DNA-NRs (green). There is no change in optical properties after end-grafting of DNA.

The polymerization of DNA-NRs was studied upon varying the number of B-DNA-NRs in a reservoir of A-DNA-NRs. A-DNA-NRs cannot link to each other and can only link via complimentary strands on B-DNA-NRs. Therefore, a small amount of B-DNANRs was added to the reservoir of A-DNA-NRs and hybridization was allowed to occur by heating the solution above the T_m of DNA to 50 °C for 3 minutes. Heating is required to disrupt intra-DNA hydrogen bonding and therefore allow hybridization to more easily occur. The

amount of B-DNA-NRs added was: 5%, 12.5%, 25% and 37.5% of the total B-DNA-NRs solution volume. **Figure 3.2** contains the absorbance spectra of the solution after polymerization. The LSPR peak red-shifts and broadens as the number of B-DNA-NRs is increased. Specifically, the LSPR peak position is located at 738 nm for 0% B-DNA-NRs and shifts to a final position of 816 nm for 37.5% B-DNA-NRs. It should be noted that the spectrometer could only detect absorbance up to 820 nm. The red-shift and broadening is consistent with end-to-end linking of the DNA-NRs.

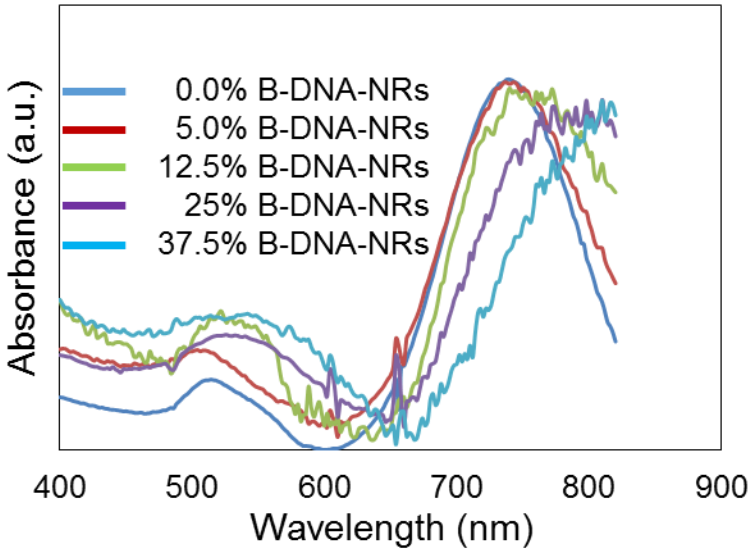

Figure 3.2 Absorbance spectra of DNA-NRs at increasing amounts of B-DNA-NRs added. As the number of B-DNA-NRs is increased, the LSPR peak undergoes a red-shift and broadening consistent with end-to-end linking.

The effect of heating on the DNA-NRs was investigated by UV/Visible spectroscopy. Polymerization can only occur if both types of DNA-NRs coexist in solution. To determine if self-hybridization could occur a pure B-DNA-NR solution was heated under the same conditions as the A- and B-DNA-NR mixture. **Figure 3.3** is the absorbance spectrum of

the B-DNA-NRs before and after one, two, and three heating/cooling cycles. There is a small hypsochromic shift (*ca.* 2 nm) in the LSPR peak position upon first heating the B-DNA-NR solution. Previous studies by our group have shown that heating AuNRs in polymer melts can reshape the AuNRs at high enough temperature.(Liu, Mills et al. 2009) To test reshaping at 50 °C and multiple heatings, the B-DNA-NR solution was heated and cooled. No change is observed in the LSPR peak position across multiple heating cycles. Therefore, heating neither causes polymerization alone, nor reshapes the DNA-NRs.

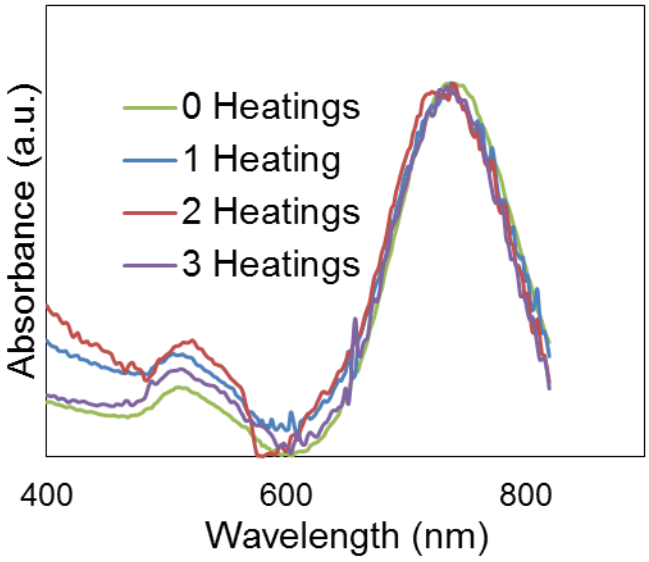

Figure 3.3 Absorbance spectra of pure B-DNA-NRs after 0 to 3 heating/cooling cycles at 50 C to room temperature. There is little to no change in the LSPR peak as the temperature is cycled indicating no reshaping of the DNA-NRs and no linking of the DNA-NRs.

The linking or "polymerization" of DNA-NRs can be studied in the context of traditional step-growth polymerization. One can think of the hybridization of complimentary strands of DNA to link DNA-NRs as a step-growth polymerization involving two different bi-functional monomers (A-A and B-B). When A-A is in excess, polymerization will proceed

by A-A binding to B-B such that chains form as 3A-A + B-B -> A-A-B-B-A-A +A-A such that B-B is fully exhausted. Adding more B-B to the solution will further increase the chain length in a similar manner. The stoichiometric ratio (r) is the ratio of B-B monomers to A-A monomers and is always less than or equal to 1. The number-averaged degree of polymerization was defined by Carothers as $X_n = 1+r/(1+r-2rp)$ where p is the extent of reaction. When there is 100% conversion (*i.e.* p=1), $X_n = (1+r)/(1-r)$. For the DNA-NR reactions, r is the percent of the B-DNA-NRs added.(Allcock and Lampe 1981, Odian 2004) Therefore, we can calculate X_n for each number of B-DNA-NR present. **Figure 3.4** is a plot of calculated Xn as a function of r for r values corresponding to the experimental system. The plot shows that at the largest amount of B-DNA-NRs (*i.e.* r = 0.375) X_n is 2.2, which suggests that an average chain should have 2.2 DNA-NRs.

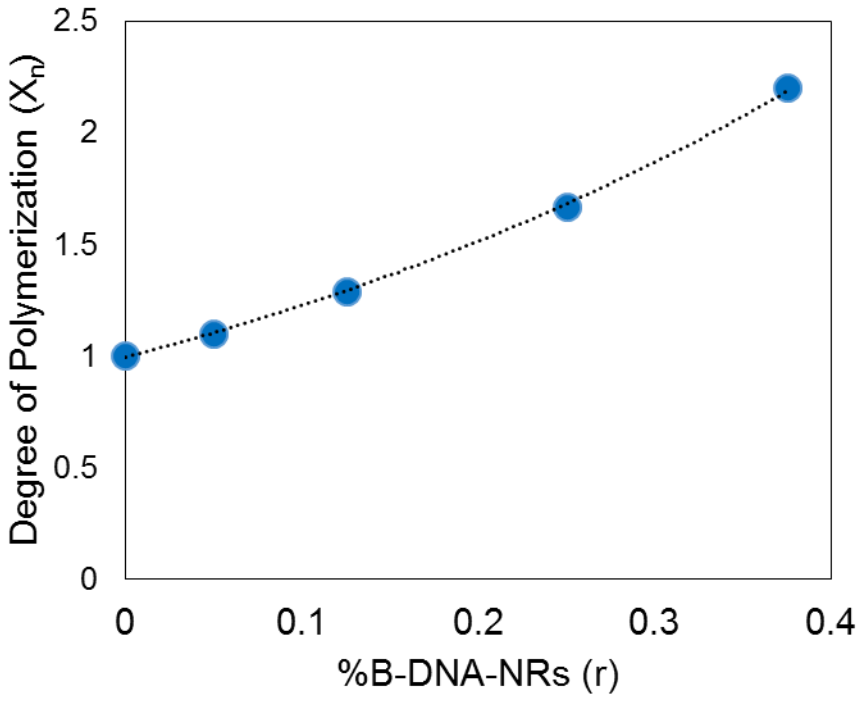

Figure 3.4 The degree of polymerization as a function of B-DNA-NRs added to a solution of A-DNA-NRs as calculated using Carothers' equation.

To probe whether the absorbance spectra is consistent with the predicted chain length (i.e. **Figure 3.4**), finite difference time domain (FDTD) calculations were performed on end-to-end linked chains of DNA-NRs in water. Here, we chose the AuNRs to be aligned linearly end-to-end in chains of 1, 2, 3, and 4 NRs. **Figure 3.5** contains the absorption cross-section spectra for monomer, dimer, trimer, and tetramer species of NRs at 3 nm separation distance. The calculated and experimental LSPR peak for the monomer (*i.e.* $X_n = 1$) are in good agreement with the LSPR peaks located at 734 nm and 738 nm, respectively. The LSPR peak undergoes a bathochromic shift from 734 nm to 803 nm, 835 nm, and 855 nm for the dimer, trimer, and tetramer, respectively. Note that the increase in LSPR peak position becomes weaker as X_n increases. The end-to-end spacing was also varied for nanorod assemblies and spacings of 2 nm, 3 nm, 4 nm, 5 nm, and 6 nm were investigated. The simulation at 2 nm was only done for dimers. The other separation distances were analyzed in the same way. **Figure 3.6** shows how the LSPR peak position in the simulations changes as a function of X_n and separation distance (circles). Also plotted in **Figure 3.6** is the experimental LSPR peak position at calculated values of X_n (red squares). The experimental absorbance closely follows the calculated absorbance for the separation distance between 2 and 3 nm. The spacing between two NRs due to the hybridized DNA strands located at the apex of the NR is *ca.* 5.5 nm. The spacing suggested by the absorbance behavior (*ca.* 3 nm) is less possibly because strands off the NR apex can hybridize, resulting in a smaller gap.

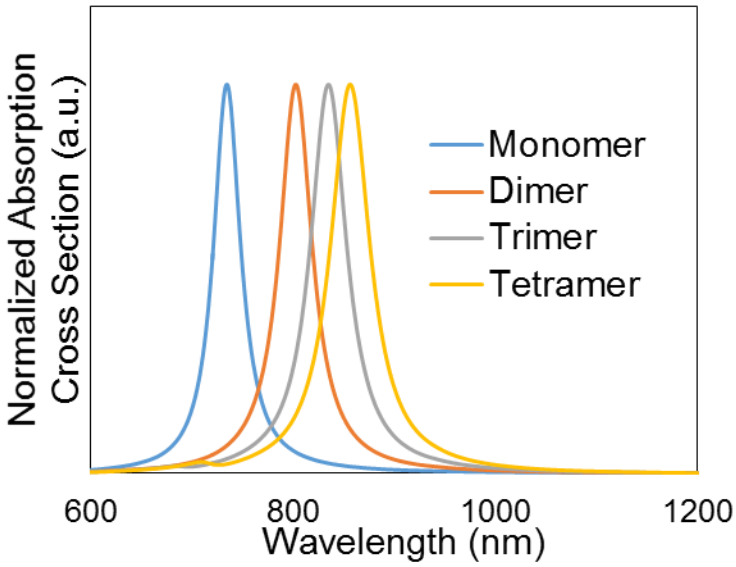

Figure 3.5 Simulated normalized absorption cross section versus wavelength for monomer, dimer, trimer, and tetramer DNA-NRs with a separation distance of 3 nm. The NRs are end-to-end aligned linearly. As the degree of polymerization increases, the LSPR absorption peak also increases (i.e. red-shifts).

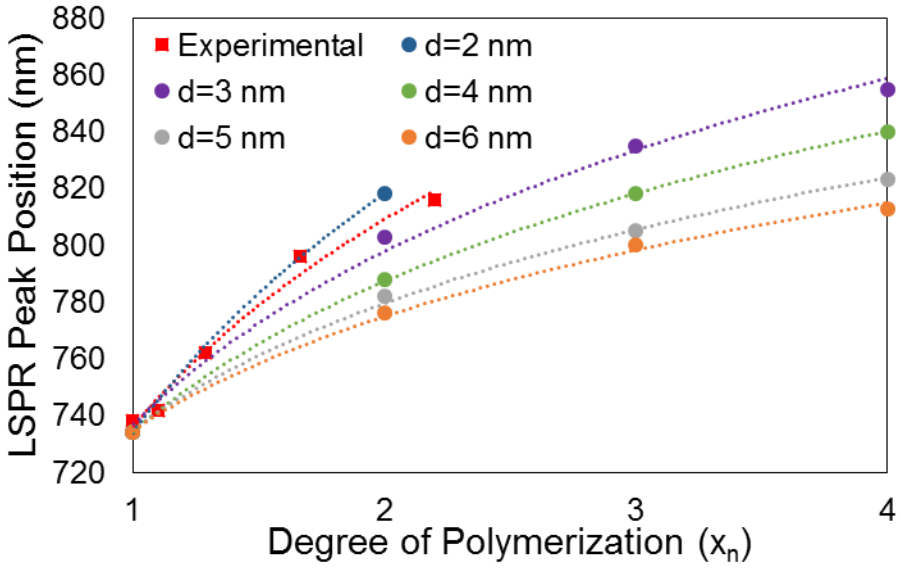

Figure 3.6 LSPR peak position versus degree of polymerization for simulated and experimental DNA-NR polymers. The separation distance for dimers, trimers, and tetramers was varied from 2 nm to 6 nm, and the data is denoted with circles. The data in red squares is from experiments. The plot shows that the DNA-NRs most closely follow the simulated DNA-NRs with separation distance of between 2 nm and 3 nm. Trend-lines are added to guide the eyes.

The linking of DNA-NRs was directly studied using scanning electron microscopy (SEM). **Figure 3.7** shows SEM images of DNA-NRs after linking or "polymerization" in the presence of 5% (a) and 37.5% (b) B-DNA-NRs. As B-DNA-NRs are increased, the polymerized DNA-NR chains increase in length. In **Figure 3.7**a, very few of the DNA-NRs are paired, while, in **Figure 3.7**b many of the DNA-NRs are linked into chains. Chains are highlighted by red circles. Chains appear collapsed due to drying effects upon casting DNA-NRs from PBS onto silicon. The separation distance between linked DNA-NRs was determined to be 2.6 nm +/- 0.2 nm, which is consistent with the separation distance predicted from the FDTD simulations. Cluster analysis was performed on the SEM images of each sample to quantify the assembly of DNA-NRs, as shown in **Figure 3.8**. As the amount of B-DNA-NRs increases, the number of individual DNA-NRs decreases while populations of multiple DNA-NRs per chain increase. From this data, the X_n at each B% (*i.e.* r) was calculated and plotted, in **Figure 3.9**, against the values calculated from Carothers' equation (*c.f.* **Figure 3.4**). There is good agreement between the calculated and the experimentally obtained values of X_n at each r.

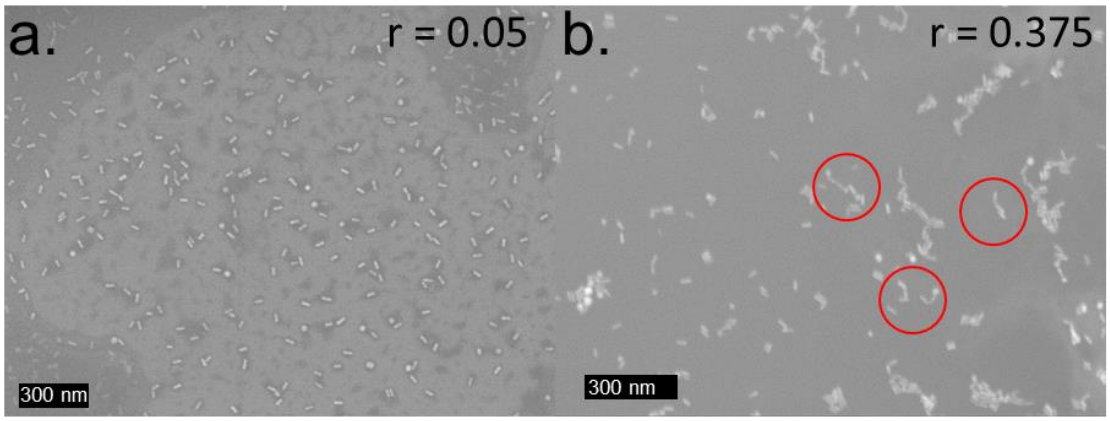

Figure 3.7 SEM images of DNA-NRs with 5% of B-DNA-NRs (a) and 37.5% B-DNA-NRs (b). The degree of polymerization increases significantly as the amount of B-DNA-NRs is increased.

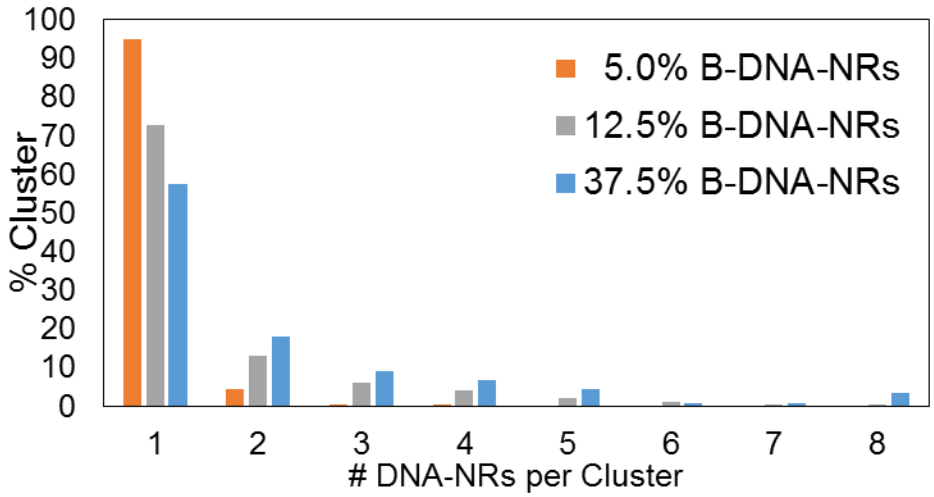

Figure 3.8 Cluster analysis performed on SEM images of 5% (orange), 12.5% (gray), and 37.5% (blue) B-DNA-NRs. The percent of individual DNA-NRs significantly decreases when larger amounts of B-DNA-NRs are present.

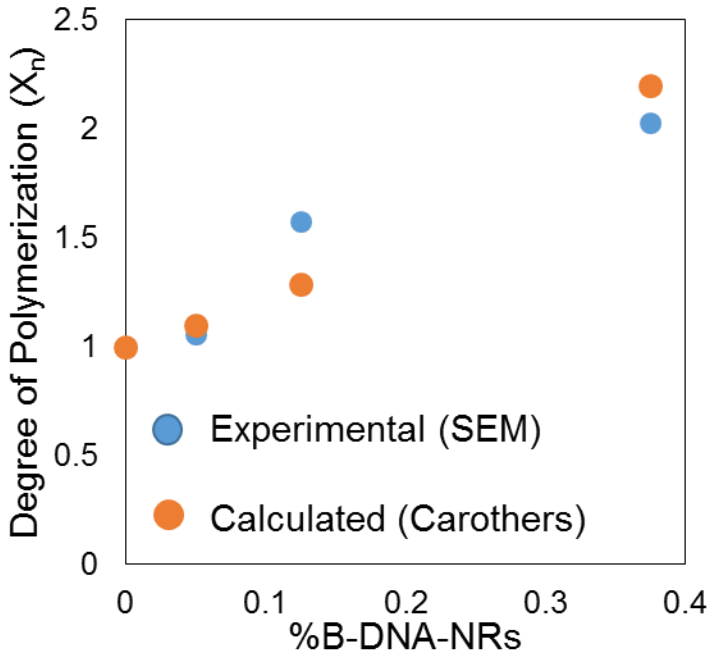

Figure 3.9 Calculated (orange) and experimental (blue) degree of polymerization values. The experimental values are close but slightly lower than the theoretically determined values probably due to a lack of full conversion of B-DNA-NRs at higher r.

3.5 **Conclusions**

Herein, we have demonstrated control over the assembly of DNA tethered AuNRs, and thereby the optical properties, by tuning the ratio of A-DNA-NRs to B-DNA-NRs. While holding A-DNA-NRs concentration fixed, a strong red-shift and broadening is observed in the LSPR band as the percentage of B-DNA-NRs in solution increases, consistent with A- and B-DNA-NRs linking. The chain length at each ratio of A- to B-DNA-NRs was predicted by Carothers' equation, which gave a maximum chain length of 2.2 DNA-NRs at percentage of B-DNA-NRs of 37.5%. FDTD simulations were performed on DNA-NRs at various separation distances and X_n. When FDTD simulation data was compared with

experimental absorbance spectra coupled with the chain length prediction, we found the DNA-NR separation distance should be *ca.* 3 nm. Characterization of each sample with SEM reveals chains of DNA-NRs with a separation distance of 2.6 nm, consistent with that predicted by FDTD. The observed chain length increases with increasing B-DNA-NR to a maximum of 2.1 DNA-NRs per chain, consistent with the predicted value from Carothers' equation. Further studies are needed for larger r values, especially those closer to unity. This method allows for the synthesis of other types of nanorod polymers. For instance, two different types of nanorods can be used to form a nanorod co-polymer or a more complex DNA sequence can be used to form star or bottle brush nanorod polymers. Each polymer offers a different set of optical properties thereby enabling one to choose the correct polymer architecture for a given application.

Chapter 4 Directed Reversible Linking of Gold Nanorods via a Computationally Designed, Metal-binding Peptide

In Collaboration with Matthew "Will" Eibling of Prof. Jeffery G. Saven's Group (Penn)

4.1 Abstract

A highly specific method to reversibly assemble gold nanorods (AuNRs) end-functionalized with a *de novo* designed metal-binding peptide is presented. A peptide (P), which was designed *in silico* to specifically bind Zn^{2+}, is end-grafted to AuNRs (PNRs). PNRs are assembled by adding Zn^{2+} to the PNR solution. Assembly is reversed by adding in an equimolar quantity of a chelater, EDTA. Assembly is found to only occur when Zn^{2+} is added and does not occur in the presence of other 2+ ions. Finally, the Zn^{2+} concentration dependence on the assembly is investigated and we find that the PNR absorbance peak undergoes a bathochromic shift from 760nm to 976 nm as Zn^{2+} concentration increases. For diagnostic applications, the peak shift can be used to determine the unknown Zn^{2+} concentration. Therefore, we have demonstrated a unique, AuNR biosensor that selectively detects Zn^{2+} in solution. This work can be further extended to detect other metal-ions or small molecules through precise, *de novo* peptide design.

4.2 Introduction

The utilization of metal nanoparticles as robust sensing platforms has received significant interest from the scientific community. Gold nanorods (AuNRs) are particularly attractive for sensing applications due to their facile synthesis(Nikoobakht and El-Sayed 2003, Sau and Murphy 2004), assembly dependent optical properties(Funston, Novo et al. 2009, Hore and Composto 2010, Ferrier, Lee et al. 2014), and ease of functionalization. AuNRs are characterized by two absorbance peaks, the longitudinal surface plasmon resonance peak (LSPR), based on the AuNR length, and the transverse surface plasmon resonance peak (TSPR), based on the AuNR diameter. SPR peaks are affected, not only by the physical characteristics of individual AuNRs, but also by the assembly of the AuNRs; assembling AuNRs end-to-end will cause a bathochromic shift in the LSPR, while assembling side-by-side will cause a hypsochromic shift in the LSPR. Optical property changes can, therefore, be used to probe the assembly of the AuNRs.

AuNRs can be used to detect additives in solution through analysis of the change in solution optical properties, making AuNRs attractive as sensors. AuNRs have been utilized to sense alkanedithiols(Shibu Joseph, Ipe et al. 2006), chelating agents(Sreeprasad and Pradeep 2011), and chromophores(Ma, Urbas et al. 2012). The presence of these molecules in an AuNR solution triggers assembly of the AuNRs via specific or non-specific interactions. For example, Thomas and co-workers(Shibu Joseph, Ipe et al. 2006) assembled AuNRs with alkanedithiol molecules which linked AuNRs together via Au-thiol bonds. The shift in the LSPR peak was found to be proportional to the alkanedithiol concentration. Li and co-workers(Ma, Urbas et al. 2012) showed that AuNRs assemble in the presence of a negatively charged porphyrin molecule due to electrostatic interactions.

Again, optical property changes were tied to the concentration of the porphyrin. While detection of these molecules by way of AuNR assembly is clear-cut in the cases above, AuNRs would assemble in the same way with the addition of any dithiol or symmetrically charged molecule, with little or no differentiation between them. Furthermore, in most cases, the assembly of the AuNRs occurred irreversibly, so the AuNRs could not be re-used in their sensing capacity.

Depending on their surface chemistry, assembly of AuNRs can be triggered to reversibly assemble through changes in the solution environment. AuNRs have been assembled end-to-end or side-by-side by changing pH(Sun, Ni et al. 2008, Zhao, Zhang et al. 2013), salt content(Sethi, Joung et al. 2009), and organic solvent content(Nie, Fava et al. 2007). For instance, Kumacheva and co-workers(Nie, Fava et al. 2007) assembled AuNRs end-to-end by grafting a polystyrene brush selectively to the ends of the AuNRs and modulating the water to dimethylformamide ratio. Zhao *et al.(Zhao, Zhang et al. 2013)* reversibly assembled AuNRs end-to-end by end-grafting selfhybridizing DNA to the ends of AuNRs and adjusting the pH to encourage or discourage DNA hybridization. While AuNRs have been reversibly assembled by changing environment, reversible assembly of AuNRs has not been demonstrated in the presence of a specific additive. Therefore, the ideal AuNR sensor would assemble in the presence of a specific trigger, reverse assembly quickly with little loss in efficacy, and be able to be redesigned to respond to other triggers.

In this work, we present the reversible assembly of AuNRs triggered by the addition of a specific metal ion. The specific assembly of the AuNRs was accomplished by end-grafting a peptide. While peptides have been used to assemble AuNRs before(Huang, Koria et al. 2008, Jain, Roodbeen et al. 2012), we utilized a *de novo* designed peptide which

specifically binds Zn^{2+}. AuNR assembly in the presence of Zn^{2+} was characterized via UV/Visible spectroscopy and SEM. The AuNR assemblies were easily and quickly reversed with the addition of a chelating agent, returning the AuNRs back to their dispersed state where they could be re-linked by reading Zn^{2+}. Other 2+ ions, such as Ca^{2+}, were also investigated, but resulted in no linking of the AuNRs. Finally, the Zn^{2+} concentration dependent optical properties of the AuNR solution was investigated and we found that as Zn^{2+} concentration increased, the LSPR peak position underwent a strong bathochromic shift from 760 nm to 976 nm. Therefore, we have demonstrated the precise assembly of AuNRs in the presence of a specific metal ion. This method can be generalized to other metal ion additives as well, through *de novo* design of the peptide.

4.3 Results and Discussion

Gold nanorods (AuNRs) were synthesized via a seed-mediated growth method. The synthesis procedure is outlined elsewhere.(Nikoobakht and El-Sayed 2003, Sau and Murphy 2004, Ferrier, Lee et al. 2014) After synthesis, three 40 mL solutions of AuNRs were centrifuged to separate AuNRs from impurities, the supernatant was removed, and the AuNR aliquots were combined to form a concentrated AuNR stock solution. The AuNRs were then characterized with UV/Visible spectroscopy (Varian Cary 5000) and SEM (Jeol 7500F). **Figure 4.1** is the (a) absorbance spectrum of AuNRs in water and (b) an SEM image of the as-synthesized AuNRs drop cast on a Si wafer. The AuNR absorbance is characterized by a longitudinal surface plasmon resonance (LSPR) peak at 760 nm and a transverse surface plasmon resonance peak (TSPR) at 512 nm. Analysis of AuNR SEM

images reveals AuNRs that are 35 nm long by 12 nm in diameter, which is consistent with the observed absorbance spectrum.

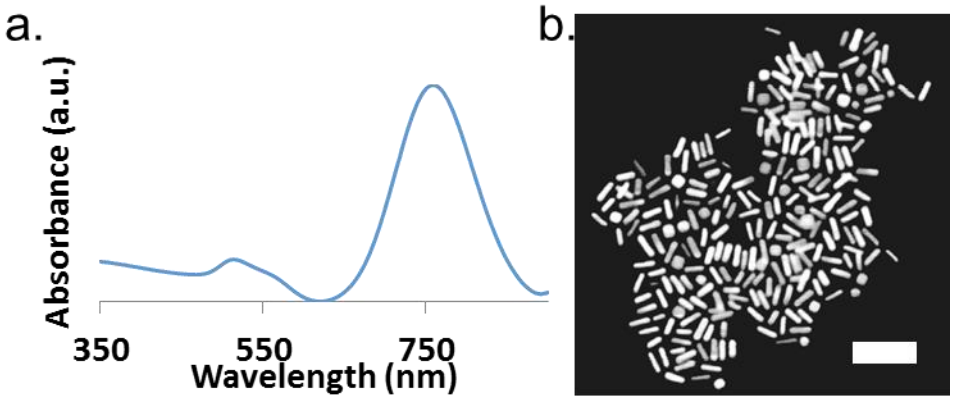

Figure 4.1 (a) The absorbance spectrum of as-synthesized AuNRs in DI H_2O. The LSPR peak position is found to be at 760 nm. (b) A representative SEM image of the as-synthesized AuNRs. Analysis of SEM images reveals AuNRs that are 35 nm in length by 12 nm in diameter. The scale bar is 100 nm.

A metal-binding peptide was designed *de novo* and synthesized. We wanted to create a peptide system which could control distance between multiple objects in solution, with the ability to turn on or off the association by adding or removing a metal ion. To this end, design was carried out by utilizing an ensemble of idealized 35-residue, dimeric, D_2 symmetric anti-parallel coiled-coil structures which were generated using the coiled-coil builder plugin for VMD. For each structure in the ensemble, a bis-his zinc binding site(Krantz and Sosnick 2001) was constructed by placing histidine residues at symmetric positions on opposing helices in the coiled-coil. From this, the ideal peptide structure to bind Zn^{2+} ions was determined. The final peptide design contains 5 Zn^{2+} binding sites to achieve a cooperative "switch-like" behavior over a small Zn^{2+} concentration range.

Figure 4.2 displays the binding behavior and the sequence of the as designed peptide. Two peptides will undergo a coil to helix transition with the two helices bridged by Zn^{2+} if 1) they come together in an anti-parallel fashion and 2) the concentration of Zn^{2+} is high enough. If the peptides are not anti-parallel, the binding geometry is not ideal and binding will not occur. Zn^{2+} ions stabilize the helix structure and the helical structure can be disrupted by removing the Zn^{2+} ions with a chelater, resulting in a disassociation of the bound peptides. Peptide sequences were synthesized via solid phase peptide synthesis on Rink-Amide resin at 100 micromole scale using a Liberty-1 microwave peptide synthesizer. The purity was determined via analytical HPLC to be >95%, and the molecular mass was determined via matrix assisted laser desorption ionization time of flight mass spectrometry (MALDI-TOF-MS).

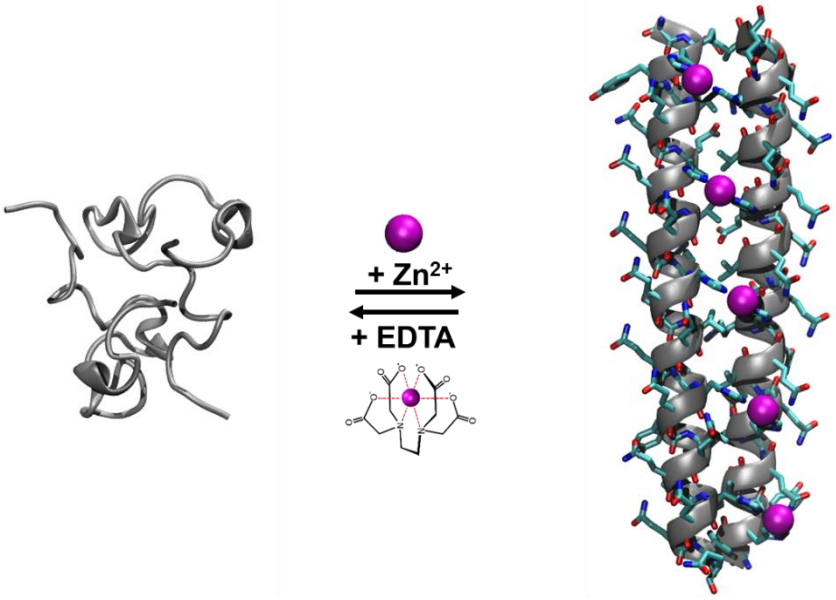

Figure 4.2 (top) Peptide coil to helix transition induced by Zn^{2+} and reversed by a chelater (EDTA). (bottom) Sequence of the as-designed peptide with a 4 residue linker terminated by cysteine.

AuNRs were end-functionalized with a metal-biding peptide. A Zn^{2+} binding peptide was designed *de novo*, *in silico* and synthesized. The peptide features a cysteine end-cap, which allows it to bind specifically to the ends of the AuNRs via the thiol moiety.(Sun, Ni et al. 2008, Sethi, Joung et al. 2009) AuNRs (2.7 nM) were mixed with the peptide (2.7 μM) in DI H_2O and incubated overnight at 32°C under mixing. The peptide AuNR (PNR) solution was centrifuged to remove free peptide and exchanged to a 100 mM CTAB / 10mM MOPS buffer. The absorbance spectrum of the final, purified solution was acquired via UV/Visible spectroscopy and can be seen in **Figure 4.3**a. The LSPR peak position was found to be at 766 nm, very similar to the non-functionalized AuNRs and indicative of good dispersion. SEM was also performed on a drop-cast PNR sample dried on a Si wafer. A representative SEM image can be seen in **Figure 4.3**b. The SEM reveals the PNRs are well dispersed.

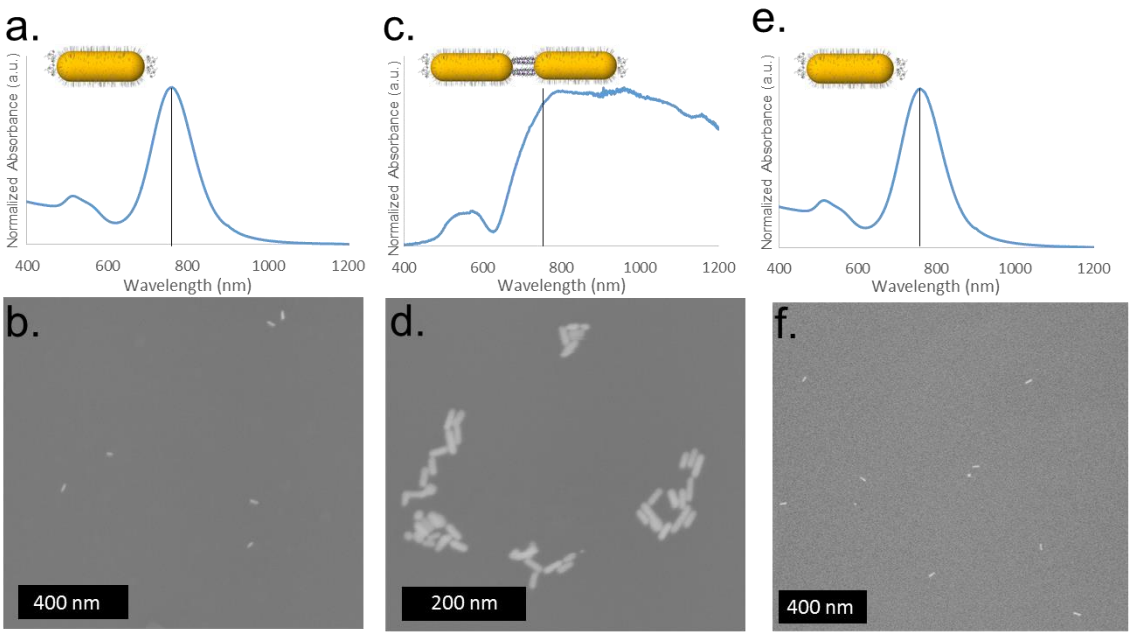

Figure 4.3 Normalized absorbance spectra and corresponding SEM image of PNRs before addition of Zn^{2+} (a,b), after addition of 250 µM Zn^{2+} (c,d), and after addition of 250 µM EDTA (e,f). Before the addition of Zn^{2+}, the PNRs are well dispersed with LSPR peak at 766 nm. Adding Zn^{2+} causes the PNRs to link, which causes the LSPR to undergo a broadening and bathochromic shift to 960 nm. Adding EDTA causes the PNRs to revert to their dispersed state which is characterized by a hypsochromic shift in the LSPR to 764 nm. The line on the absorbance spectra (a,c,e) indicates the peak position of the dispersed PNR LSPR peak (*e.g.* 766 nm).

PNRs were end-linked by adding free Zn^{2+} ions to the solution. $ZnSO_4$ (250 µM) was added to the PNR solution and mixed overnight to allow linking. The solution underwent a color change from the red wine color of the dispersed PNRs to a blue color with a precipitate forming at the bottom of the vial, indicative of assembly. The absorbance of the

linked-PNR solution can be seen in **Figure 4.3**c. Upon linking the LSPR undergoes a significant broadening and bathochromic shift from 760 nm to 960 nm, consistent with linking. Linked PNRs were further characterized by SEM. A representative SEM image can be seen in **Figure 4.3**d. The SEM reveals the PNRs form chains with 10 or more PNRs per chain. The polydispersity in the chain length results in the broadening of the LSPR peak. Due to drying effects, chains are bundled rather than elongated.

PNRs were de-linked by adding a chelating agent, ethylenediaminetetraacetic acid (EDTA), to the PNR solution. EDTA was added to the solution of linked-PNRs in an equimolar quantity to the $ZnSO_4$ (*i.e.* 250 μM) to promote full reversal of linking. The de-linking process occurs with much celerity and the PNRs are de-linked in under 40 seconds with some slight shaking. A movie of the de-linking process was recorded (supplemental) with stills of the movie comprising **Figure 4.4**. **Figure 4.4**a is the juxtaposition of the unlinked (left cuvette) and linked (right cuvette) PNR solution. The linked solution is much bluer in color than the unlinked solution which is a red-wine color. The EDTA is then added via pipette (**Figure 4.4**b) at 9 seconds into the movie. The linked PNR cuvette is shaken by hand in **Figure 4.4**c and the PNR solution returns to the red-wine color of dispersed PNRs in **Figure 4.4**d. De-linking is characterized by a color change from blue to red-wine coupled with the dissolution of the previously formed precipitate. The absorbance spectrum of the de-linked PNRs can be seen in **Figure 4.3**e. The LSPR undergoes a significant hypsochromic shift from 960 nm to 764 nm. A juxtaposition of the absorbance spectra prior to linking and after de-linking reveals they are the same, indicating a full reversal of the linking process. De-linked PNRs were further characterized by SEM and a

representative SEM image can be seen in **Figure 4.3**f. The SEM reveals the PNRs are no longer linked and are fully dispersed.

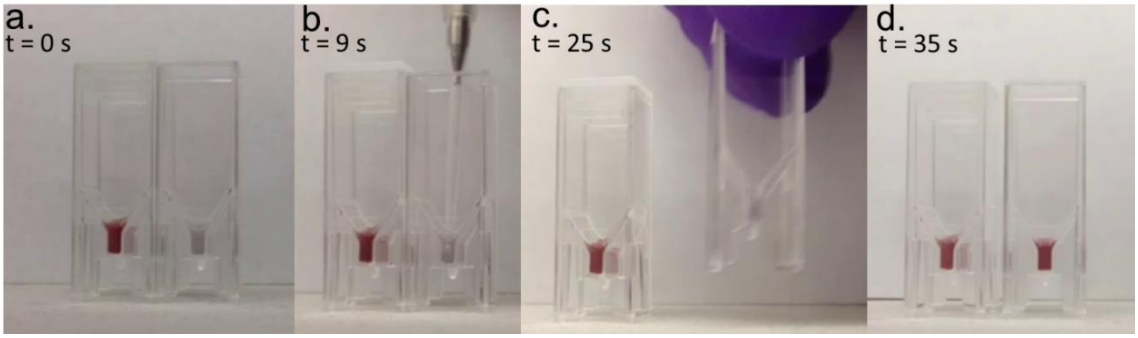

Figure 4.4 Still images from a movie, which can be viewed in supplemental, that shows the speed and ease with which the PNRs are de-linked. (a) Still of the juxtaposition of the dispersed (left cuvette) and linked (right cuvette) PNR solutions. The linked PNR solution is noticeably bluer than the unlinked PNR solution which is red-wine in color. (b) EDTA is added to linked PNR solution via pipette. (c) Cuvette containing EDTA / linked PNR solution is shaken for a few seconds. (d) Juxtaposition of the previously unlinked (left cuvette) and previously linked (right cuvette) after addition of EDTA and shaking.

PNR linking occurs most efficiently upon addition of Zn^{2+} ions. The linking experiment presented above was repeated, but with Ca^{2+} ions instead of Zn^{2+} ions in solution. The PNR solution was incubated with Ca^{2+} for 72 hours. No color change was observed; the solution remained the red-wine color consistent with dispersed PNRs. The absorbance spectrum of the PNR and Ca^{2+} solution was acquired and can be seen in **Figure 4.5**. The LSPR peak position remained at 764 nm, which is the same as for the PNRs with no metal ions. An equimolar quantity of EDTA (*i.e.* 250 μM) was then added and mixed for 24 hours. The absorbance spectrum for this solution was acquired and can also be seen in **Figure 4.5**. The

absorbance spectrum for the Ca^{2+} and EDTA case is identical to the case of just the Ca^{2+}, meaning no assembly or disassembly of the PNRs has taken place. As a final control, 250 µM of EDTA was added to a solution of unlinked PNRs that had not been exposed to Ca^{2+} previously and the resulting absorbance spectrum can be seen in **Figure 4.5**. The absorbance is identical to the unlinked PNR case, which means EDTA itself does not trigger assembly. While EDTA has been used to assemble AuNRs previously(Sreeprasad and Pradeep 2011), we observe no assembly with EDTA most likely due to the salt in the buffer solution screening out EDTA-CTAB electrostatic interactions. Similar experiments were performed on the pure peptide over a wide range of metal ions. In these experiments, the peptide bound Zn^{2+} at least 1000 times more efficiently than any other metal ions studied. Therefore, the peptide specifically and efficiently binds Zn^{2+}.

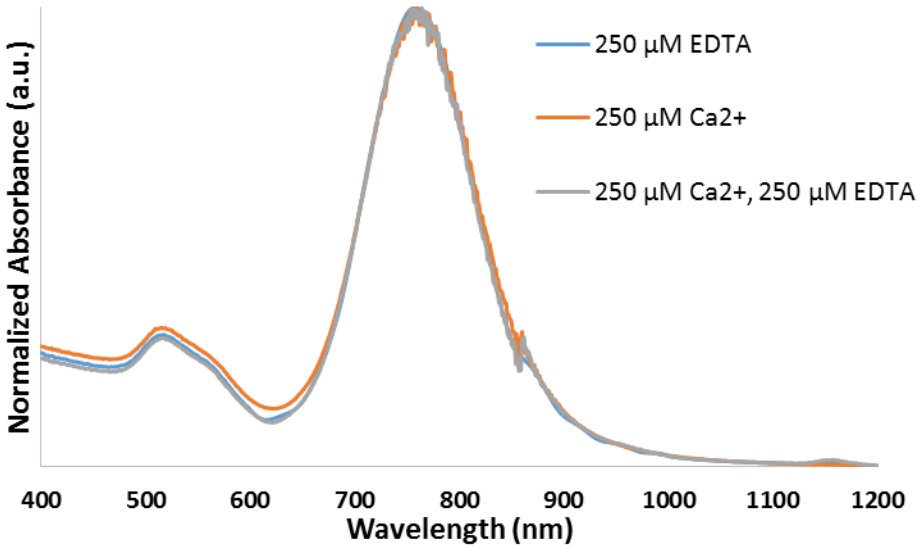

Figure 4.5 Absorbance spectra of PNRs with 250 µM EDTA (blue), 250 µM Ca^{2+} (orange), and 250 µM of Ca^{2+} and 250 µM of EDTA (gray). None of the combinations of additives

causes the PNRs to link which is evident by the LSPR peak staying constant at 764 nm, consistent with well-dispersed PNRs.

The effect of Zn^{2+} concentration on the optical properties of the PNR solutions was investigated. Zn^{2+} was added to PNR solutions at concentrations of 0, 50, 75, 90, 125, 175, 200, 225, and 250 µM. Assembly was allowed to occur over 48 hours under mixing. The 48 hour time point was chosen to allow equilibration for all concentrations of Zn^{2+}. The absorbance spectra of all solutions were acquired and selected spectra can be seen in **Figure 4.6**a. As Zn^{2+} concentration increases beyond 50 µM, the LSPR peak undergoes a bathochromic shift from 760 nm (0-50 µM) to 976 nm (175 µM) and broadens, consistent with linking. The LSPR peak position was plotted as a function of Zn^{2+} concentration in **Figure 4.6**b. The plot shows linking begins to occur after a critical concentration, 50 µM, is reached and increases linearly until plateauing at 976 nm (175 µM). This assembly behavior is consistent with the cooperative binding mechanism present in the peptide.

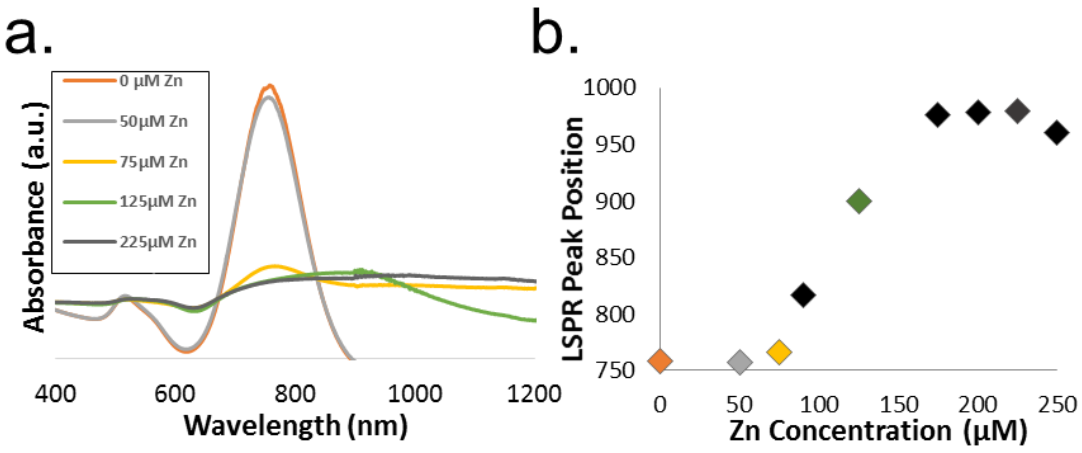

Figure 4.6 (a) Selected absorbance spectra of PNRs incubated with 0, 50, 75, 125, and 225 µM of Zn^{2+}. As the Zn^{2+} concentration is increased, the LSPR peak strength at 760 nm

significantly decreases as the LSPR peak undergoes a broadening and bathochromic shift. The shift at high Zn^{2+} concentration is captured in (b) which is the LSPR peak position at each Zn^{2+} concentration. The LSPR peak begins to shift after 50 μM of Zn^{2+} is added and continues shifting roughly linearly until 175 μM of Zn^{2+} is added, after which the peak position plateaus at 976 nm.

4.4 Conclusions

We have demonstrated, for the first time, the reversible assembly of PNRs end-grafted with a metal binding peptide. The unique binding mechanism of the peptide allows for controlled assembly of the PNRs to take place by tuning Zn^{2+} concentration, which allows for the 'dialing in' of the solution optical properties. We have also demonstrated the full reversibility of the assembly, allowing the PNRs to be assembled again in the presence of Zn^{2+} making this system an effective, specific, and reusable biosensor. The controlled linking of the PNRs can be used tune the optical properties for use in surface enhanced Raman spectroscopy. Furthermore, this proof of concept system opens the door for highly specific biosensors moving forward. This system was designed, *de novo*, to bind a particular metal ion, Zn^{2+}. We can envision the ability to sense other metal ions by precisely designing peptides *in silico*.

Chapter 5 Tuning Optical Properties of Functionalized Gold Nanorods through Controlled Interactions with Organic Semiconductors

In Collaboration with Drs. Guillaume Gines, Patrice Rannou, Didier Gasparutto, and Brigitte Pépin-Donat (INAC/CEA/CNRS, France)

5.1 Abstract

In this chapter, a novel nano-hybrid assembly consisting of gold nanorods (AuNRs) and organic semiconductors (OSCs) to tune optical properties is presented. OSCs are bound to specific areas of the AuNRs (*e.g.* end or side) by controlling the surface chemistry of the AuNRs. AuNRs are anisotropically functionalized with CTAB, cysteine, poly(ethylene oxide) (PEO) and / or DNA. Rhodamine-B (RhB), 5,6 carboxyfluorescein (CF), or cyanine3 (Cy3) are incubated with the anisotropically functionalized AuNRs. The resulting optical properties of the dispersed AuNRs are characterized via steady-state UV-Vis absorption and photoluminescence (PL) spectroscopies as a function of OSC concentration. We found that CF and RhB adsorb to the AuNR differently depending on the AuNR surface chemistry which results in unique optical properties of the assembly. The unique spectra were used to determine the interaction between the OSC and the AuNR. Finally, we found that attaching Cy3 specifically to the ends of the AuNR via a DNA tether results in a larger emission quenching process than when Cy3 is not attached. This method of nano-hybrid assembly can be extended to other metal nanostructures and OSCs. Its generic nature qualifies it as new methodology to precisely assemble nano- and molecular objects with controlled (opto)electronic properties.

5.2 Introduction

The precise (self-)assembly of molecular components and nano-objects is essential for the realization of nanodevices with unique properties. It constitutes one of the foremost challenges in nanotechnology today. To date, much work has focused on the directed self-assembly of individual metal-nanoparticles (NPs) into organized structures, such as chains(Kang, Erickson et al. 2005, Zhang and Wang 2008, Schreiber, Huber et al. 2015) and vesicles(Nie, Fava et al. 2007, Hu, Wu et al. 2012), to tune their properties thanks to a diverse tool-kit allowing for the anisotropic functionalization of NPs. The anisotropic surface chemistry can be exploited to self-assemble molecular components at precise locations on the particle to create unique nanoarchitectures. Gold nanorods (AuNRs) are particularly attractive for use as a component in nano-hybrid assemblies. AuNRs possess size and assembly dependent optical properties which have found use in cancer therapy(Huang, El-Sayed et al. 2006), biosensing(Zijlstra, Paulo et al. 2012), surface enhanced Raman spectroscopy (SERS)(Nikoobakht and El-Sayed 2003, Qian, Li et al. 2009), and solar cells(Lee, Park et al. 2009, Xu, Kyaw et al. 2013) applications. Furthermore, AuNRs can be anisotropically functionalized. AuNRs have been anisotropically functionalized with functional ligands such as cysteine(Sethi, Joung et al. 2009), DNA(Zhao, Zhang et al. 2013), polymers(Liu, Ahmed et al. 2013, Ferrier, Lee et al. 2014), and alkanes(Shibu Joseph, Ipe et al. 2006). The diverse array of functional groups allows for broad control over surface chemistry, surface charge, and ligand length along particular facets of the AuNRs.

Organic semiconductors (OSCs) are also attractive and smart components for nano-hybrid assembly. OSCs, such as rhodamine-B (RhB) and 5,6 Carboxyfluorescein (CF), are

used in a wide-variety of applications such as sensors(Imsick, Acharya et al. 2013, Wang, Yan et al. 2014), imaging(Robertson, Bunel et al. 2013, Yu, Li et al. 2014), and solar cells(Yang, Chen et al. 2015) due to their fluorescent properties. OSC fluorescence intensity and wavelength are tied to their concentration, charge, and complexation, which can be characterized through simple spectroscopic techniques. Donor/Acceptor (D/A) complexes can formed when OSCs interact with an electron acceptor, like AuNRs, resulting in the quenching of the emission of the OSC. The quenching process is D/A separation distance dependent, with smaller distances typically resulting in a larger emission quenching.(Zhang, Marocico et al. 2012, Abadeer, Brennan et al. 2014) OSCs have been homogeneously assembled on the surface of AuNRs in the past (Gabudean, Focsan et al. 2012, Ma, Urbas et al. 2012, Abadeer, Brennan et al. 2014), but not, to the authors' knowledge, with control over the particular area of the AuNR (*e.g.* end or side) that the OSC is bound to. Furthermore, anisotropy in the AuNR surface coating would allow for precise tuning of the optical properties; OSCs of a particular chemistry would be directed to a particular ligand bound to a particular area of the AuNR paving roads to robust biosensing activity and biosensors with high specificity.

In this work, we control the optical properties of AuNR/OSC dispersions by the directed self-assembly of OSCs onto particular areas of the AuNR by taking advantage of the AuNR surface chemistry. RhB, CF, and Cyanine3 (Cy3) are chosen as representative donor OSC for AuNRs due to their absorbance and emission spanning over different parts of the visible spectrum, different chemical moieties/charge, and for their water solubility. AuNRs are synthesized with a wide variety of surface chemistries, both homogeneous and anisotropic, to program the AuNR / OSC interactions. Specifically, four different AuNR chemistries

are studied: CTAB-coated (CTAB-NRs), CTAB side-coated with cysteine end-caps (Cys-NRs), PEO side-coated with cysteine end-caps (Bi-NRs), and PEO-side coated with DNA end caps (DNA-NRs). The OSC/NR complexes are characterized by steady-state UV-Visible absorption and photoluminescence (PL) spectroscopies which allow us to glean how the OSCs self-assemble on the AuNR surface. CF and RhB are used investigate how optical properties of the OSC / NR dispersion evolve with OSC concentration. Cy3 tethered to single-stranded DNA (ssDNA) is used to show how specific interactions, like DNA-DNA, can be used to program the directed self-assembly of OSCs to specific areas of the AuNRs. We find that CF binds preferentially to CTAB and, at high concentrations, to cysteine end-caps as manifested by the quenching of its PL emission. RhB binds to CTAB-coated AuNRs as well as PEO-coated AuNRs, resulting in a concentration dependent quenching of the emission of RhB. Finally, we found that attaching cy3 specifically to the ends of the AuNR via a DNA tether results in a larger emission quenching process than when Cy3 is not attached. Therefore, we show interactions can be precisely dialed in by controlling AuNR surface chemistry, which, at present, allows for a versatile biosensor and, in the future, is one step towards bottom-up prepared precise nano-devices.

5.3 Experimental Methods

5.3.1 NR Synthesis and Functionalization

Reagents used in the experiments were obtained from Sigma-Aldrich and used as received unless otherwise noted. Fifteen base pairs single-stranded-DNA (ssDNA) were purchased from Eurogentec and purified through HPLC prior to use. Cyanine3-DNA (Cy3) was synthesized as detailed elsewhere.(Gines, Saint-Pierre et al. 2014) Three 40 mL solutions of cetrimonium bromide (CTAB) coated gold nanorods in DI water were

synthesized by a seed-mediated growth method as outlined elsewhere.(Nikoobakht and El-Sayed 2003, Sau and Murphy 2004, Ferrier, Lee et al. 2014) Excess CTAB was removed through two washing cycles consisting of centrifugation (20 min at 8,000 RPM, Eppendorf 5804) followed by replacement of the supernatant with approximately 40 mL of Milli-Q water. Following the washing steps, the three AuNR solutions were combined and concentrated in 40 mL of water, providing a stock solution of concentrated CTAB-NRs.

End-linking with cysteine was performed by centrifuging 5 mL of the stock solution, removing the supernatant, and combining with 9 mL of a 400 mM NaCl solution.(Sethi, Joung et al. 2009, Ferrier, Lee et al. 2014) Three 3 mL aliquots were taken from the solution, combined with 30 μL of a 2 mM L-cysteine solution, and left overnight to end-link. For cysteine NR (Cys-NR) studies, after end-linking, NRs were sonicated for several seconds to re-disperse the NRs and were centrifuged for 20 minutes, the supernatant removed and replaced with DI water. This was done to remove the salt and de-link the Cys-NRs.

Upon completion of the cysteine end-linking, the solutions were sonicated for several seconds to re-disperse the NRs. End-linked NRs are then functionalized with 5 kg/mol poly(ethylene glycol) methyl ether thiol (PEO) by adding 30 mg of the polymer to the solutions of end-linked NRs, centrifuging for 20 minutes, and replacing the supernatant with 3 mL of DI water. Two additional washing steps were performed, and the precipitate were dispersed in DI water. These bi-functional NRs (Bi-NRs) consist of cysteine end-caps and a PEO side brush.(Ferrier, Lee et al. 2014)

Two different sets of DNA end-functionalized Bi-NRs (DNA-NRs) were prepared. The first set, consisting of ssDNA-SH, was prepared by incubating a 1.5 nM solution of Bi-

NRs with a 32 nM solution of ssDNA-SH (sequence: 5'-HS-C_6-TCG-GAT-ACC-CAA-GGA-3') overnight in DI water. The solution was then centrifuged at 8000 RPM and the supernatant removed and replaced with 10 mM PBS buffer. The washing step was performed two more times to ensure no free DNA was left. The second set of DNA-NRs consisted of ssDNA-SH (sequence above) hybridized to a Cyanine3-DNA (Cy3-DNA) probe (sequence: 5'-Cy3-GTC-TCC-TTG-GGT-ATC-CGA-TGT-3'). Cy3-DNA was hybridized to ssDNA-SH by heating to 60°C for 2 minutes and then cooling to room temperature. Hybridized Cy3-DNA (32 pmol) was then incubated with Bi-NRs.

5.3.2 UV-Vis Absorbance Studies

Steady state UV-Vis absorption spectra were recorded using a (Hewlett Packard) HP8451A Diode Array Detector spectrometer and (Hellma) Quartz QX cuvette with a 1 mm light path. Samples were prepared for UV-Vis absorbance studies by first placing 500 µL of NR or DI water sample into the quartz cuvettes. After the spectrum with no OSC was acquired, a small volume of a stock solution of RhB (525 µM) or CF (110 µM) was added to the initial 500 µL solution and the spectrum was acquired. This procedure was repeated for stock OSC volumes of: 5 µL, 13 µL, 25 µL, 37 µL, 50 µL, 75 µL, 100 µL, 150 µL, 200 µL, and 250 µL.

Three samples were prepared for Cy3-DNA studies: Cy3-DNA in 10 mM PBS, Cy3-DNA in 10 mM PBS with Bi-NRs, Cy3-DNA hybridized to thiol-ssDNA in 10 mM PBS with Bi-NRs. In all cases, 32 pmol of Cy3-DNA is added to 500 µL of solution.

5.3.3 Photoluminescence (PL) Studies

Steady-state PL emission spectra were recorded using a (Hitachi) F-4500 fluorescence spectrometer at a scanning rate of 60 nm/min and (Hellma) Quartz QS semi-micro cuvettes with a 1 cm light path. Samples were prepared for PL emission studies by first placing 500 μL of NR or DI water sample into a quartz cuvettes. After the spectrum with no OSC was acquired, a small volume of a stock solution of RhB or CF was added to the initial 500 μL solution and the spectrum was acquired. This procedure was repeated for stock OSC volumes of: 5 μL, 13 μL, 25 μL, 37 μL, 50 μL, 75 μL, 100 μL, 150 μL, 200 μL, and 250 μL.

Three samples were prepared for Cy3-DNA studies: Cy3-DNA in 10 mM PBS, Cy3-DNA in 10 mM PBS with Bi-NRs, Cy3-DNA hybridized to thiol-ssDNA in 10 mM PBS with Bi-NRs. In all cases, 32 pmol of Cy3-DNA is added to 500 μL of solution.

5.4 Results and Discussion

5.4.1 5,6-Carboxyfluoroscein and Nanorods

The 5,6-carboxyfluorescein (CF) organic semiconductor (OSC) was chosen to elucidate the role gold nanorod (AuNR) surface chemistry plays in tuning OSC/NR interactions and their optical properties. As displayed in **Figure 5.1**a, the structure of CF consists of a xanthene core functionalized with a phenyl ring with two carboxylic groups. The carboxylic groups are both deprotonated in DI water(Aschi, D'Archivio et al. 2008), giving CF a net negative charge. The optical properties of CF were first characterized by steady-state UV-Vis absorption and photoluminescent (PL) spectroscopies as a function of CF concentration. Specifically, CF, at volumes up to 250 μL, was added to 500 μL of DI water. **Figure 5.1**b shows the steady-state UV-Vis absorption spectra acquired for CF volumes of

5, 13, 25, 38, 50, 75, 100, 150, 200, and 250 µL. The absorbance spectra obtained are typical for a true molecular solution of CF and show CF's vibronic structure. CF absorbance is characterized by an absorption band with a maximum at 482 nm which increases in intensity as a function of CF volume added. Figure 1c is the corresponding PL emission spectra acquired for the same CF volumes. CF emission is characterized by an emission band showing a maximum at 514 nm which increases as a function of CF volume added.

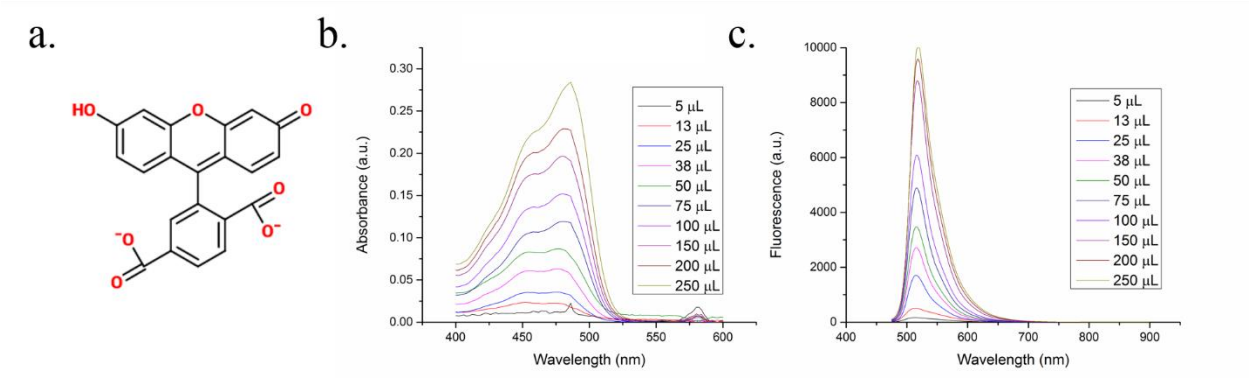

Figure 5.1 Chemical structure of CF in DI water (a). Absorbance spectra (b) and emission spectra (c) of CF. Both absorbance and emission increase at increasing concentration of CF.

The absorbance of AuNRs with a variety of surface chemistries was studied by steady-state UV-Vis absorption spectroscopy as a function of the CF concentration. Specifically, CF, at volumes up to 250 µL, was added to 500 µL of DI water containing CTAB coated gold nanorods (CTAB-NRs), cysteine end functionalized gold nanorods (Cys-NRs), and bi-functional nanorods (Bi-NRs). A cartoon of the various proposed AuNR surface chemistries investigated can be seen in **Figure 5.2**. Steady-state UV-Vis absorption spectra

were acquired for each sample at CF volumes of 0, 5, 13, 25, 38, 50, 75, 100, 150, 200, and 250 μL. **Figure 5.3** is the absorption spectra for CTAB-NRs (a and d), Cys-NRs (b and e), and Bi-NRs (c and f). For clarity, the spectra are presented for wavelengths domains ranging from 400 nm to 600 nm (a-c), and from 600 nm to 820 nm (d-f). In **Figure 5.3**a-c, the absorbance band due to CF is subtracted from each experiment at the same CF volume so that the enhanced absorption contribution due to the AuNRs can be highlighted. For CTAB-NRs, **Figure 5.3**a shows that the transverse surface plasmon resonance (TSPR) band is subjected to a small, but measurable hypsochromic shift of *ca*. 4 nm (*i.e.* from 512 nm to 508 nm) and increases from an absorbance of 0.1 to 0.52 as CF concentration increases. **Figure 5.3**b shows a similar trend for Cys-NRs. Here, the TSPR band undergoes a hypsochromic shift from 512 nm to 508 nm and increases from an absorbance of 0.1 to 0.41 with CF volume until 150 μL, where the absorbance plateaus. **Figure 5.3**c shows that the UV-Vis absorbance spectra for Bi-NRs behave differently than the Cys-NRs and CTAB-NRs systems. Namely, the TSPR band undergoes a strong hypsochromic shift from 512 nm to 498 nm, whereas the peak absorbance increases only slightly from 0.06 to 0.17. The longitudinal surface plasmon resonance (LSPR) absorbance band of CTAB-NRs, shown in Figure 2d, undergoes a hypsochromic shift from 750 nm to 744 nm after adding 150 μL of CF and then undergoes a slight bathochromic shift back to 750 nm. For Cys-NRs, Figure 2e shows that the LSPR peak position does not change as CF volume increases and remains near 746 nm. The Bi-NR LSPR position undergoes a significant hypsochromic shift from 762 nm to 738 nm, and then plateaus after adding 100 μL of CF as shown in **Figure 5.3**f. For the LSPR band in all cases (**Figure 5.3**d-f), the maximum absorbance decreases to 50% of the initial height at the final volume of CF due to dilution.

Figure 5.2 Cartoon of the different proposed AuNR surface chemistries investigated

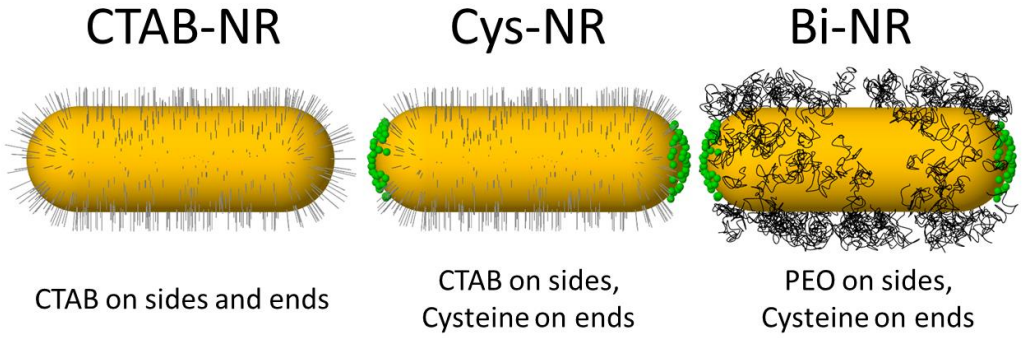

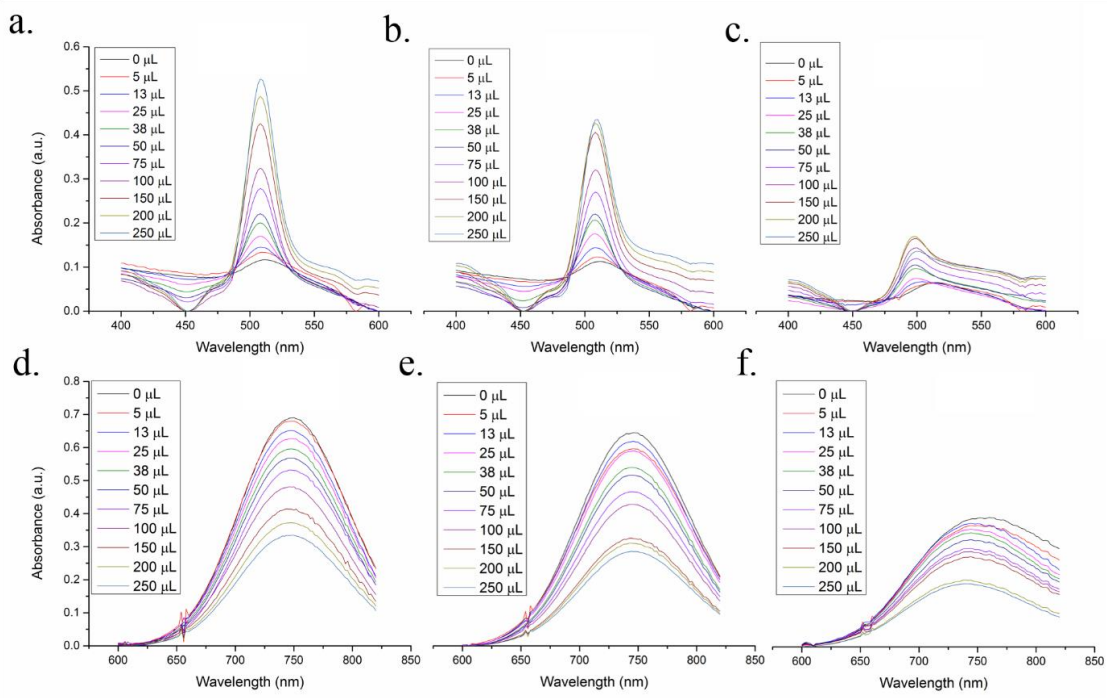

Figure 5.3 Steady-state absorbance near the AuNR TSPR for CTAB-NRs (a), Cys-NRs (b), and Bi-NRs (c). The absorbance due to CF was subtracted out for clarity. Absorbance

spectra near the AuNR LSPR for CTAB-NRs (d), Cys-NRs (e), and Bi-NRs (f) at 0 to 250 μL of CF added. Steady-State absorbance near the TSPR band increases at increased concentrations of CF for CTAB-NRs (a) and Cys-NRS (b). The absorption band for Bi-NRs (c) undergoes an hypsochromic shift of ~18 nm and increases with increasing CF concentration, but less strongly than CTAB-NRs and Cys-NRs. The absorbance of the LSPR band decreases, in all cases, by approximately 50%. No shift was seen in CTAB-NRs spectra (d), a small hypsochromic shift of 6 nm is seen in Cys-NRs spectra (e), and an hypsochromic shift of *ca.* 25 nm was seen in Bi-NRs spectra (f) at increased CF concentration.

The PL emission of dispersion containing CF and AuNRs was studied by PL spectroscopy as a function of CF volume. CF, at volumes up to 250 μL, was added to 500 μL of DI water containing CTAB-NRs, Cys-NRs, Bi-NRs, and CTAB. PL emission spectra were acquired with an excitation wavelength λ_{exc} of 450 nm for each sample at CF volumes commensurate with UV-Vis absorption experiments and can be seen in **Figure 5.4**. For CTAB-NRs (a), the maximum of the emission band is located at 524 nm and is quenched by *ca.* ~70% compared to the pure CF case (*c.f.* **Figure 5.1**b). The maximum of the emission band for Cys-NRs (b) is localized at 528 nm and, like CTAB-NRs, is significantly quenched (~80%) compared to pure CF. The emission plateaus after 50 μL of CF is added and begins to decrease after 100 μL is added. The maximum of the emission bands for Bi-NRs (c) and CTAB (d) occur at 514 nm and 527 nm, respectively. In both cases, the band strength increases as the CF volume increases in the same way as pure CF. All samples

exhibit a bathochromic-shift of the maximum of their emission band by *ca.* 5 nm as the CF volume increases from 0 to 250 µL.

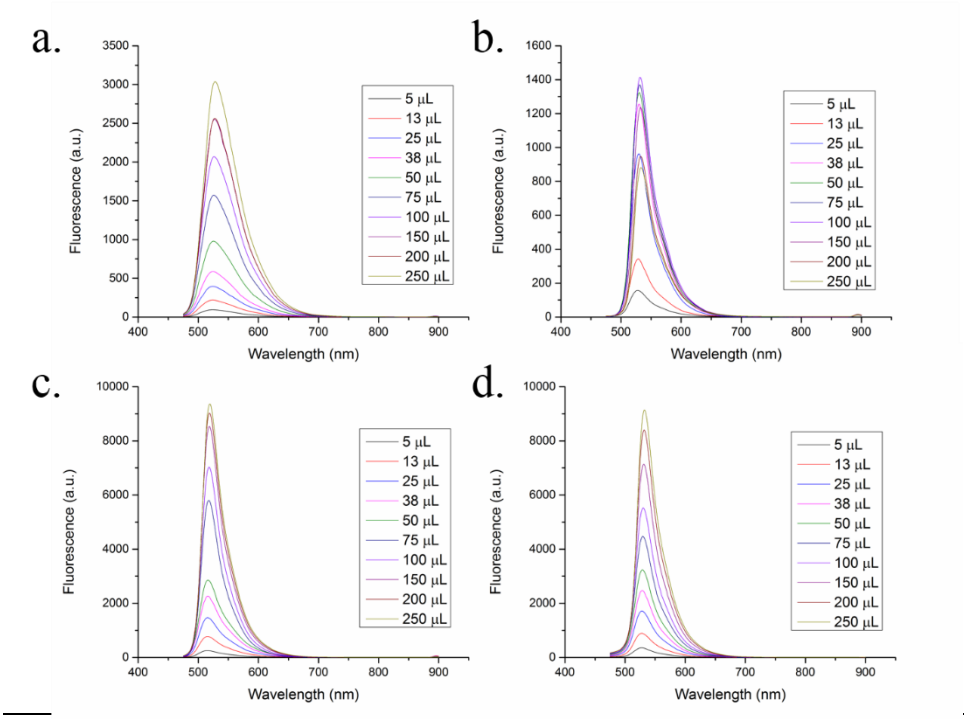

Figure 5.4 Steady-state PL emission spectra for CTAB-NRs (a), Cys-NRs (b), Bi-NRs (c), and CTAB (d) at increasing volume of CF. Bi-NRs (c) and CTAB (d) show no quenching compared to neat CF (*c.f.* figure 1b). CTAB-NRs (a) and Cys-NRs (b) show significant quenching of 70% and 70-90%, respectively, compared to neat CF. Cys-NRs show additional quenching after 100 µL of CF was added.

CF can adsorb to the CTAB on the NR surface by an attractive electrostatic interaction. Whereas CTAB was present on the surface of both CTAB-NRs and Cys-NRs, this surfactant is not on the Bi-NRs. Correspondingly, the CTAB-NRs and Cys-NRs dispersions showed a strong quenching (>70%) of the emission, whereas Bi-NRs did not (*i.e.*, compare **Figure 5.4**a and b with c). In DI water, CF contains two deprotonated

carboxylic acid groups, which can be electrostatically attracted towards the ammonium end group on CTAB. Further evidence of the interaction between CTAB and CF can be seen in the absorbance band. **Figure 5.5** shows the normalized absorbance of CTAB-NRs, Bi-NRs, Cys-NRs, and pure CF at the same CF concentration, namely 250 µL of CF. The CF absorbance band undergoes a bathochromic shift from 486 nm for pure CF to 508 nm in the presence of CTAB-NRs and Cys-NRs. The bathochromic shift to 508 nm is consistent with the carboxylic moiety interacting with the ammonium in the CTAB.(Bonizzoni, Long et al. 2012) Furthermore, CTAB-NRs have been previously shown to bind to SAMs with exposed carboxylic acid groups.(Gole, Orendorff et al. 2004) Therefore, CF binds to CTAB present on the NRs, which affects their optical properties.

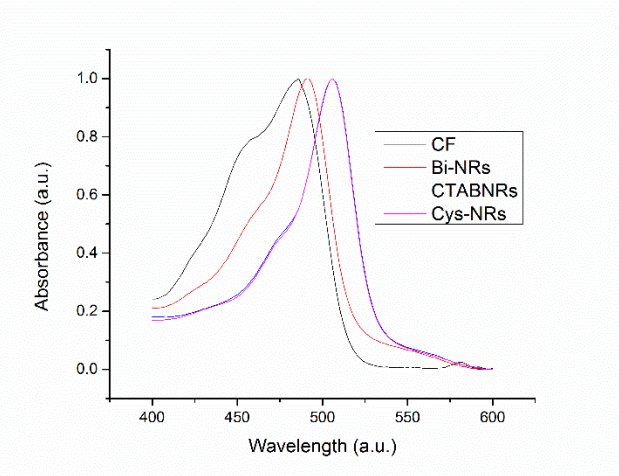

Figure 5.5 Normalized UV-Vis absorbance spectra of neat CF, CTAB-NRs, Cys-NRs, and Bi-NRs at 250 µL of CF added. Neat CF solutions exhibit a characteristic absorbance band at 486 nm. CF solutions containing Cys-NRs and CTAB-NRs exhibit a bathochromic shift, compared to neat CF, by *ca.* 32 nm to 508 nm. CF solutions containing Bi-NRs exhibit a small bathochromic shift of ca. 5 nm to 491 nm.

The quenching of CF emission is attributed to an energy transfer between the excited CF and nearby AuNR. CF binding to CTAB does not cause, by itself, quenching of the CF emission, unlike what is observed by Bonizonni *et al*.(Bonizzoni, Long et al. 2012) When CF is added to a solution of CTAB, there is no change in intensity of the PL emission compared to the pure CF case (*c.f.* **Figure 5.1**c and **Figure 5.4**d). However, a bathochromic shift is observed in the absorbance spectra, as shown in **Figure 5.6**, indicating that the interaction between free CTAB and CF is similar to bound CTAB and CF. Bound CF would be separated from the AuNR surface by the CTAB layer which would place it approximately 2 nm from the AuNR surface. There is also a spectral overlap between the AuNR absorbance and CF emission. Therefore, a Förster resonance energy transfer (FRET) could take place between the excited CF, as the donor, and the AuNR, as the acceptor, causing a quenching of the emission band of the OSC for dispersions containing Cys-NRs and CTAB-NRs.

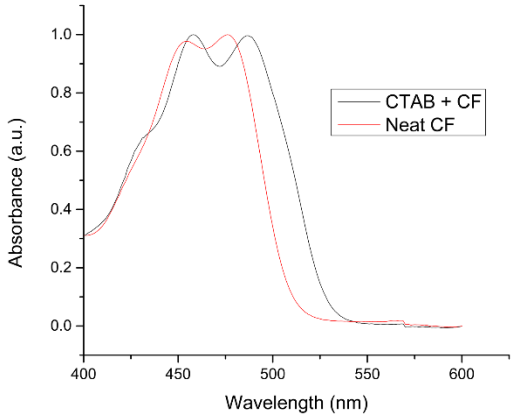

Figure 5.6 Normalized absorbance spectra of pure CF and CF with free CTAB. The maximum of the absorbance band undergoes a bathochromic shift from 478 nm to 488 nm upon addition of CTAB.

CF emission and absorbance spectra exhibit subtly different behavior depending on whether CF is mixed with CTAB-NRs or Cys-NRs. **Figure 5.7**a displays the peak absorbance intensity for neat CF, CTAB-NRs, and Cys-NRs. For CF incubated with CTAB-NRs, the absorbance band intensity increases monotonically as CF concentration increases. Contrariwise, the band intensity for CF incubated with Cys-NRs increases in magnitude only until a CF concentration of 150 μL, after which the intensity reaches a plateau. The difference in absorbance band behavior indicates that the interaction between the CF and the NRs changes after 150 μL is added. Examining the PL emission spectra reveals further details of the CF/NR interaction. **Figure 5.7**b shows the intensity of the PL emission band for neat CF, CTAB-NRs, and Cys-NRs. For CTAB-NRs, emission follows the same trends seen in the pure CF case except for the quenched emission; namely, as CF concentration increases, PL emission intensity increases linearly, until reaching a plateau after 100 μL. The PL emission of CF is quenched by a constant 70% +/- 5% for all CF concentrations when incubated with CTAB-NRs. For Cys-NRs, the PL emission of CF rapidly plateaus at 50 μL and begins to decrease after 100 μL, ultimately leading to a 90% quenching of its emission. These observations indicate that the mechanism for quenching emission from CF in the presence of Cys-NRs is unique from the CTAB-NRs case.

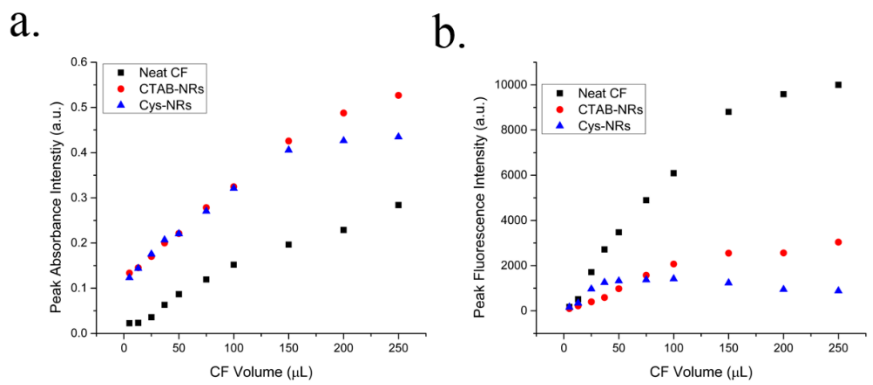

Figure 5.7 Peak absorbance intensity (a) and peak fluorescence intensity (b) for CF, CTAB-NRs, and Cys-NRs.

The different optical properties of CF incubated with CTAB-NRs and Cys-NRs can be attributed to NR surface charge and chemistry. **Figure 5.8** illustrates how AuNR surface chemistry impacts the interaction between CF and CTAB-NRs or Cys-NRs. For CTAB-NRs (top row), bound and unbound CF molecules are in equilibrium at all concentrations of CF. CF binding to CTAB reduces CF-CF interactions, which is counterbalanced by an increase in steric repulsion due to crowding on the surface of the NR. As more CF is added to the solution, the CF molecules partition between the NR surface and the solution, which is why quenching is constant for all CF concentrations. For Cys-NRs (bottom row), the CF behaves qualitatively similar, whereby there is a competition between CF adsorbing to the CTAB covering the NR and free CF. However, above a critical concentration, rather than continuing to pack along the side of the NR, CF begins to bind to cysteine at the ends of the NR through an H-bonding interaction. At low concentrations, CF binding to the ends is initially frustrated by the electrostatic repulsion from the carboxylic moiety on cysteine,

but at higher CF concentrations the driving force to charge stabilization overcomes this electrostatic repulsion, leading to binding of CF at the ends and a strong quenching of emission. The true nature of the (energy or electronic) transfer between the donor and acceptor of these AuNR/CF assemblies remains uncertain to date. The PL emission quenching could be due to FRET, but, because of the relatively short length of the cysteine (< 7 Å) and the lack of change in absorbance spectra, the mechanism may be Dexter electron transfer (DET) instead. The transfer mechanism could be elucidated through future experiments by ultra-fast time-resolved PL spectroscopic studies. For the Bi-NRs, there is no quenching of the CF emission despite cysteine being present on the ends of the NRs. In this case, there is no CTAB in solution, which means cysteine self-interactions dominate (*i.e.* dimers form through H-bonding interactions in between COOH and NH_2 groups) (Sethi, Joung et al. 2009), limiting any possible CF binding.

Figure 5.8 Cartoon illustrating concentration and surface chemistry effect of CF binding to NRs.

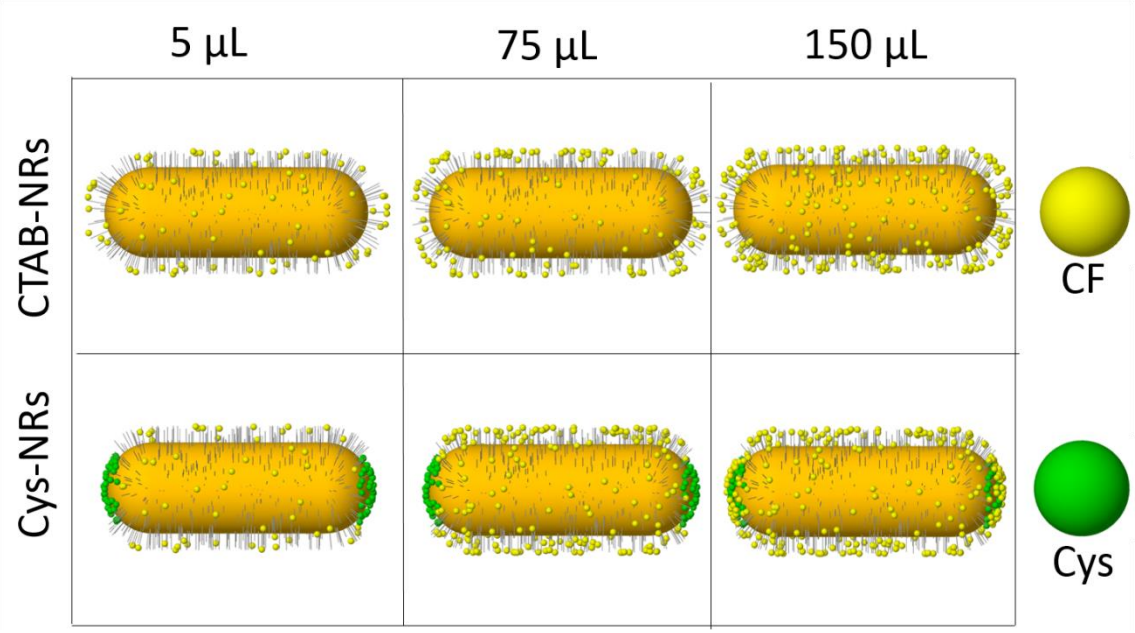

5.4.2 Rhodamine-B and Nanorods

Another OSC, Rhodamine-B (RhB), was chosen to further elucidate the role OSC structure plays in tuning OSC/NR interactions and optical properties. RhB has a similar structure to CF (**Figure 5.9**a), except the xanthene is terminated by a quaternary ammonium, providing a positive charge. The ammonium, combined with the deprotonated carboxylic acid group also present, makes RhB net charge zwitterionic in DI water. The optical properties of RhB were characterized by steady-state UV-Vis absorption and PL spectroscopies as a function of RhB volume added. Specifically, RhB, at volumes up to 250 µL, is added to 500 µL of DI water. **Figure 5.9**b is the steady-state UV-Vis absorption spectra acquired for RhB volumes of 5, 13, 25, 38, 50, 75, 100, 150, 200, and 250 µL. The

absorbance spectra obtained are typical for RhB and are characterized by a band with a maximum at 554 nm and a shoulder at 520 nm, both of which increase in intensity with increasing RhB volume. **Figure 5.9**c shows the PL emission spectra acquired for the same RhB volumes as in the steady-state UV-Vis absorption measurements. RhB PL emission is characterized by a band with a maximum at 573 nm which increases until 38 µL of RhB added and then monotonically decreases in intensity. The RhB emission band also undergoes a bathochromic shift from 574 nm to 582 nm as a function of increased RhB volume. The loss in intensity and bathochromic shift is due to fluorescence reabsorption and is typical for RhB. (Wurth, Grabolle et al. 2013)

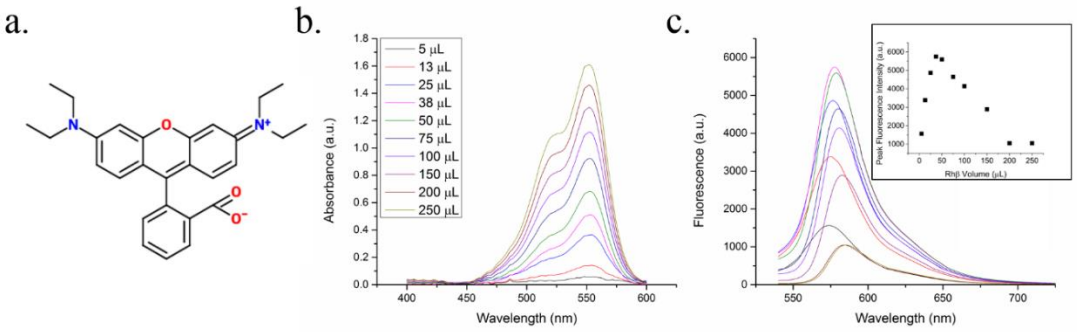

Figure 5.9 Chemical structure of RhB in DI water (a). Absorbance spectra (b) and PL emission spectra (c) of RhB. Absorbance increases as a function of RhB volume added. Fluorescence initially increases as a function of RhB volume added and then decreases and undergoes a bathochromic shift. The inset in (c) is the peak fluorescence intensity as a function of RhB volume, which clearly shows the increase and subsequent decrease in intensity at higher RhB volumes.

The absorbance of AuNRs with a variety of surface chemistries was studied by steady-state UV-Vis absorption spectoscopy as a function of the RhB concentration. Specifically RhB, at volumes up to 250 μL, is added to 500 μL of DI water containing CTAB-NRs or Bi-NRs. Absorbance spectra were acquired for each sample at 0, 5, 13, 25, 38, 50, 75, 100, 150, 200, and 250 μL of RhB volume added. **Figure 5.10** shows the absorbance spectra for CTAB-NRs (a and c) and Bi-NRs (b and d). For clarity, spectra are separated in two parts: absorbance at wavelengths between 400 nm and 600 nm and between 600 nm and 820 nm in the region of the TSPR (a and b) and of the LSPR (c and d), respectively. In figures 8a and 8b, the absorbance due to RhB is subtracted at each RhB volume to elucidate the difference in absorbance between the pure RhB and RhB with NRs. The TSPR band for CTAB-NRs (a) experiences a large bathochromic shift of *ca.* 40 nm from 510 nm to 550 nm after RhB is added and continues to shift to 560 nm with increasing RhB concentration. The TSPR band linearly increases in intensity as a function of RhB concentration. For Bi-NRs (b), the TSPR band position and strength remain approximately constant across all RhB volumes. The LSPR peak position remains approximately constant for both CTAB-NRs (c) and Bi-NRs (d) at 746 nm and 752 nm, respectively and decreases to 50% of the initial height due to dilution.

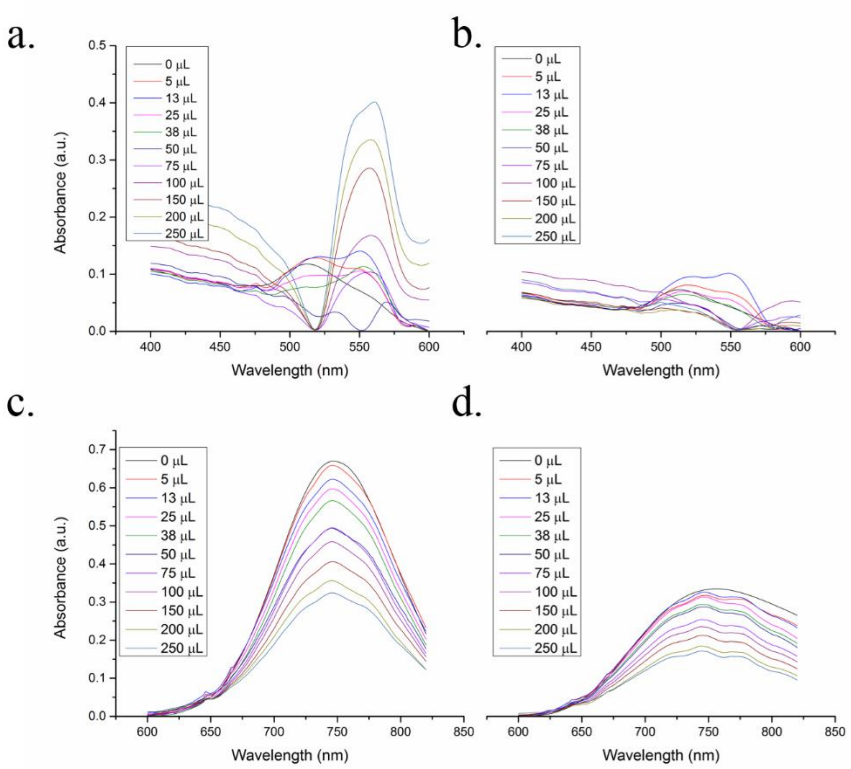

Figure 5.10 Absorbance spectra near the AuNR TSPR for CTAB-NRs (a) and Bi-NRs (b) at 0 to 250 µL of RhB added. The absorbance due to Rh-B was subtracted out for clarity. The absorbance peak for CTAB-NRs undergoes a 30 nm bathochromic shift and increases as a function of Rh-B volume added. The absorbance band for Bi-NRs undergoes no change at increased RhB volume. Absorbance spectra near the AuNR LSPR for CTAB-NRs (c), and Bi-NRs (d) at 0 to 250 µL of Rh-B added. The absorbance bands for CTAB-NRs and Bi-NRs decrease as function of Rh-B volume added. Bi-NR absorbance and LSPR absorbance peak also undergoes a small hypsochromic shift of 10 nm.

The PL emission of solutions of RhB and various additives was studied by steady-state PL spectroscopy as a function of RhB volume. RhB, at volumes up to 250 µL, was added

to 500 µL of DI water containing solutions of CTAB-NRs, Bi-NRs, and CTAB. PL emission spectra were acquired with an excitation wavelength $\lambda_{exc.}$ of 520 nm for each sample at RhB volumes commensurate with absorbance measurements and can be seen in **Figure 5.11**. The PL emission spectra of RhB with CTAB-NRs (a) and Bi-NRs (b) both exhibit quenching of the emission band at 574 nm when compared with pure RhB (*c.f.* **Figure 5.9**c). However, for solutions containing CTAB (c), RhB emission experiences a nearly two-fold enhancement compared with pure RhB. The emission band for all samples are subjected to a bathochromic shift of *ca.* 14 nm as a function of RhB volume

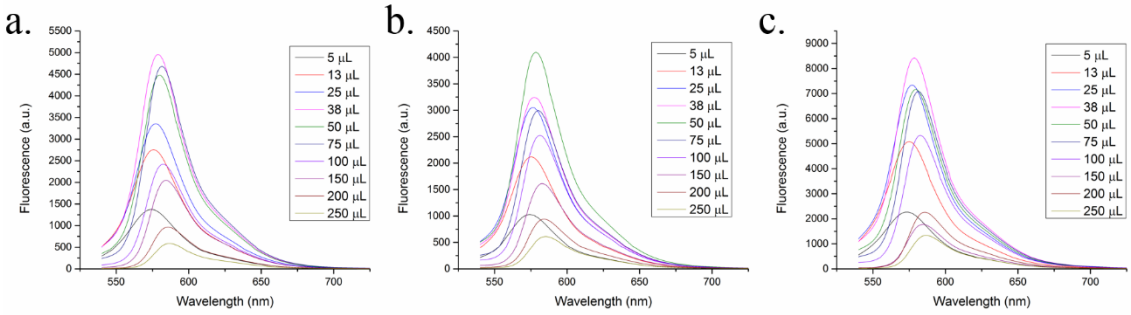

Figure 5.11 PL emission spectra of CTAB-NRs (a), Bi-NRs (b), and CTAB (c) at increasing volumes of RhB. For all samples, the PL emission band increases monotonically until 38 µL (a, c) or 50 µL (b) is added and then decreases as a function of Rh-B volume added. The PL emission band also undergoes a bathochromic shift in all cases. The PL emission is slightly quenched in both the CTAB-NRs and Bi-NRs case compared to neat Rh-B. The PL is enhanced in the CTAB case due to free CTAB protecting the Rh-B from aggregating and self-quenching.

The presence of CTAB mitigates RhB self-quenching. RhB aggregates in solution at concentrations above 10^{-5} M (Arbeloa, Ojeda et al. 1989), resulting in the quenching of its PL emission (*cf.* **Figure 5.9**c) and an increase in the relative intensity of a shoulder present in its absorbance spectra (*cf.* **Figure 5.12**). (López Arbeloa and Ruiz Ojeda 1982, Arbeloa, Ojeda et al. 1989, Wurth, Grabolle et al. 2013) CTAB acts as a surfactant for RhB, limiting aggregation and, thereby, limiting quenching, resulting in an enhancement of fluorescence compared with the neat RhB case (*cf.* **Figure 5.9**a and **Figure 5.11**c). The absorbance peak for the CTAB-NRs case (*cf.* **Figure 5.10**a) increases as a function of RhB concentration and undergoes a bathochromic shift, much like in the case of CF, implying that the RhB is binding to the CTAB on the side of the CTAB-NRs. Furthermore, the relative increase in the shoulder intensity is not present in the absorbance spectra for CTAB-NRs (*cf.* **Figure 5.13**), indicating less aggregation of RhB. The RhB/CTAB interaction is further supported by analyzing the PL emission spectra. As shown in **Figure 5.11**a, CTAB-NRs quench the RhB emission by *ca.* 41% compared to neat RhB when the emission enhancement due to the presence of CTAB is taken into account. Quenching is not due to RhB aggregation, like in the pure RhB case, but is due to the proximity of the RhB to the CTAB-NR surface allowing for Förster or Dexter transfer between the RhB excited state and the CTAB-NR.

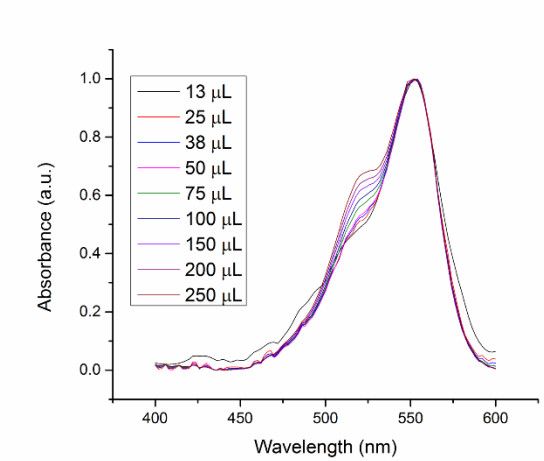

Figure 5.12 Normalized absorbance spectra for RhB. The shoulder at 512 nm increases in relative intensity as a function of RhB volume added, which is indicative of RhB aggregation.

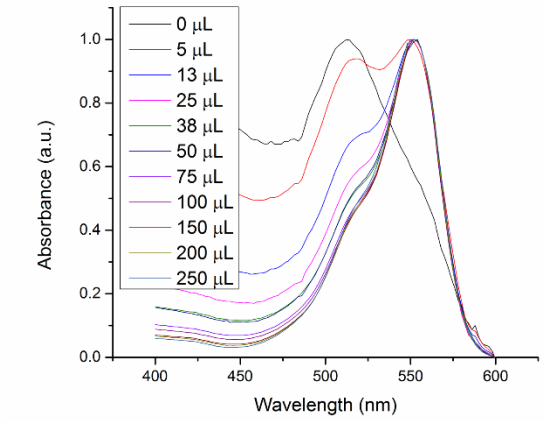

Figure 5.13 Normalized absorbance spectra for CTAB-NRs. The shoulder at 512 nm is suppressed as a function of RhB volume added, indicating RhB is well-dispersed.

RhB binds to the cysteine at the ends of the Bi-NRs, resulting in the quenching of its emission. Unlike the CTAB and CTAB-NRs systems, the Bi-NR solution has no free

CTAB and therefore RhB can form large aggregates in solution. Such aggregates result in self-quenching, which is evident upon direct comparison of the normalized absorbance spectra for Bi-NRs and pure RhB (*c.f.* **Figure 5.14**). In both cases, the raised shoulder indicates RhB aggregation. Furthermore, the relative intensity of the shoulder compared to the peak is the same in both cases indicating similar aggregation behavior. However, the PL emission spectra for the Bi-NRs exhibits 35% more quenching than for neat RhB. Therefore, this calls for a secondary mode of quenching. Both RhB and cysteine are zwitterionic in DI water. (López Arbeloa and Ruiz Ojeda 1982) Therefore, RhB can bind to the cysteine via an H-bonding interaction. The PL emission quench in the Bi-NRs case is similar in strength to the quenching phenomenon seen in the CTAB-NRs case. The cysteine is physically smaller than CTAB, so the RhB is closer to the AuNR and should, therefore, be subjected to a stronger quenching. However, cysteine covers only about 25% of the AuNRs assuming cysteine covers 50% of the end-caps.(Ferrier, Lee et al. 2014) Therefore, less RhB molecules are quenched, but those that are quenched are quenched more strongly for the Bi-NRs than for the CTAB-NRs. Considering that the RhB is aggregating the same way in both the neat RhB and Bi-NRs cases, there is only a small percentage of the RhB binding to the cysteine. The quenching mechanism is probably the same as seen in the Cys-NRs with CF samples due to the strength of the quenching and the lack of change in absorbance spectra as a function of RhB concentration. Again, the exact mechanism could be further elucidated in future experiments by employing ultra-fast time-resolved PL spectroscopy. Finally, as way of an illustrative summary of this section, **Figure 5.15** is a cartoon depicting how we hypothesize RhB interacts with the CTAB-NRs and Bi-NRs.

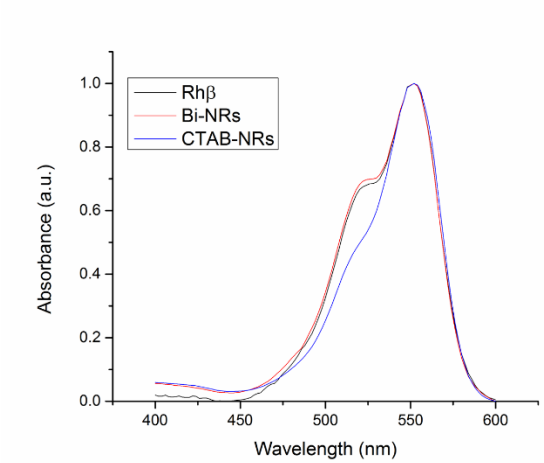

Figure 5.14 Normalized absorbance spectra for neat RhB, Bi-NRs, and CTAB-NRs at 250 μL of RhB added. The relative intensity of the shoulder at 512 nm is similar in both the neat RhB and Bi-NRs case, but is significantly suppressed in the CTAB-NRs case.

Figure 5.15 Cartoon depicting RhB interaction with CTAB-NRs and Bi-NRs

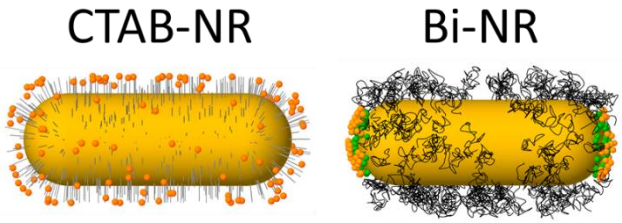

5.4.3 Cyanine3 and DNA-NRs

OSCs can be self-assembled with AuNRs by taking advantage of specific interactions. So far, we have shown that OSCs self-assemble on AuNR surfaces via non-specific interactions, which allows for some control over the optical properties of the assembly. However, being able to precisely tune donor /acceptor distance and binding trigger will allow for more robust control over these nano-hybrid assemblies. One way to achieve both control over the distance and assembly mechanism is to utilize single stranded and double

stranded DNA (ssDNA and dsDNA) upon specific hybridization. In this study, we end-functionalize Bi-NRs with ssDNA (DNA-NRs) and investigate how the optical properties of a DNA-OSC probe change when the probe is unattached or attached to the end of the DNA-NR. The DNA-OSC used is cyanine3 (Cy3) which is attached to 5' end of a 15-mer ssDNA. The DNA is attached to the Bi-NR end via a thiol-C_6 on the 5' end of a 15-mer ssDNA strand, which is complimentary to the Cy3.

The absorbance and emission of DNA-NR / Cy3 assemblies were studied by steady-state UV-Vis absorption and PL spectroscopies, respectively. **Figure 5.16**a is the absorbance spectra of neat Cy3 (black), free Cy3 and DNA-NRs (red), Cy3 hybridized to DNA-NRs (blue). The absorbance spectra of Cy3 is not resolvable due to the low concentration. The absorbance spectra of the DNA-NRs with free or attached Cy3 are the same; both overlap with each other and display peak positions consistent with absorbance of the NRs. **Figure 5.16**b is the PL emission spectra of Cy3 (black), free Cy3 and DNA-NRs (red), Cy3 hybridized to DNA-NRs (blue). The PL emission of neat Cy3 is characterized by a band with a maximum at 566 nm. This characteristic emission band does not shift with the addition of DNA-NRs or after hybridization. However, Cy3 emission is significantly quenched when DNA-NRs are present; Cy3 emission is quenched *ca.* 50% when not hybridized to the DNA-NR and *ca.* 75% when hybridized to the DNA-NR. The emission is quenched even when Cy3 is unattached to the DNA-NR because of non-specific interactions between the DNA on the NR and the Cy3. However, the quenching phenomenon is stronger in the hybridized Cy3 case due to the strong, specific interaction between the DNA strands. Therefore, we have shown that specific interactions can be used to more completely bind OSCs to NR surfaces allowing for tighter control over the optical

properties. Furthermore, as donor/acceptor distance can be finely tuned with dsDNA containing different number of base pairs, this pave the way towards further dial-in optical properties of AuNR/OSC nano-assemblies.

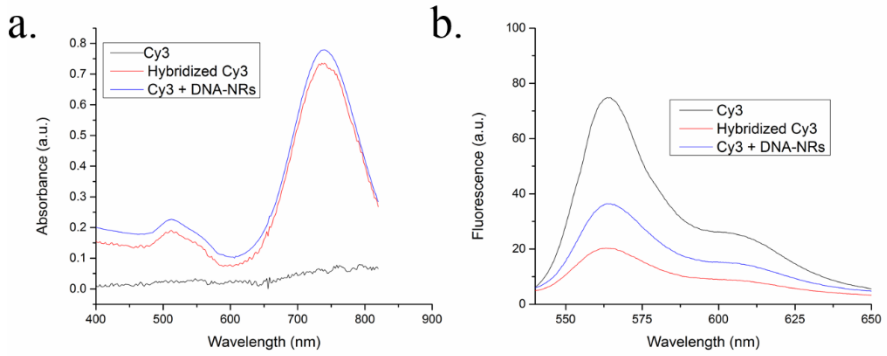

Figure 5.16 (a) Absorbance spectra of DNA-NRs with free Cy3-DNA (black) and Cy3-DNA hybridized to DNA-NR end (red). (b) Emission spectra of free Cy3-DNA (black), free Cy3-DNA + DNA-NRs (blue), and Cy3-DNA hybridized to DNA-NR end (red).

5.5 Conclusions

Energy or electron transfers in between OSCs and AuNRs depend on both the chemical structure and functional groups of the OSC and the surface chemistry of the AuNR. The nature of OSC/NR interactions can be gleaned through the change in the optical properties (*i.e.* UV-Vis absorbance and PL emission) as OSCs are added to solutions containing AuNRs of various surface chemistries. OSCs bound to the AuNRs exhibited a reduced fluorescence due to the AuNR acting as an acceptor for OSC playing the role of donor. We found that CF could be bound homogeneously to the AuNR with a constant emission quench (CTAB-NRs), to the sides and ends of the NR depending on concentration (Cys-NRs), or not at all (Bi-NRs). RhB could be bound homogeneously to the AuNR (CTAB-

NRs) or to the ends of the AuNR (Bi-NRs). OSC binding was characterized by both UV-Vis absorption and PL emission spectroscopies which allowed us to glean the OSC position on the AuNR. We found that the presence of free surfactant can facilitate OSC binding to specific sections of the AuNRs. Finally, we showed that OSCs could be tethered preferentially to the ends of AuNRs via specific DNA interactions and that this led to a more efficient OSC binding, as evidenced by an increased quenching of the fluorescence of the OSC. Therefore, we have demonstrated that one can precisely control the adsorption of OSCs to the surface of NRs by controlling NR surface chemistry, free surfactant, OSC concentration, and OSC charge groups. These studies show how nano-hybrid structures and optoelectronic properties can be created and tuned though directed self-assembly. At present, our study shows that AuNRs allows for versatile biosensors and, in the future, is one step towards bottom-up prepared precise nano-devices.

Chapter 6 Dispersion of PMMA-grafted, Mesoscopic Iron-oxide Rods in Polymer Thin Films

In Collaboration with Yun Huang of Prof. Kohji Ohno's Group (Kyoto University)

6.1 Abstract

In this work, we investigate the parameters that affect the dispersion of polymer grafted mesoscopic iron-oxide rods (FeMRs) in polymer matrices. FeMRs (181 nm long by 34 nm in diameter) are grafted with poly(methyl methacrylate) (PMMA) at three different brush molecular weights: 3.7 kg/mol, 32 kg/mol, and 160 kg/mol. Each FeMR sample was cast in a polymer thin film consisting of either PMMA or poly(ethylene oxide) (PEO) each at molecular weight much higher or much lower than the brush molecular weight. We find that the FeMRs with 160 kg/mol brush disperse in all matrices while the FeMRs with 32 kg/mol and 3.7 kg/mol brush aggregate in all matrices. We perform simple free energy calculations, taking into account steric repulsion from the brush and van der Waal's attraction between FeMRs. We find that there is a barrier for aggregation for the FeMRs with the largest brush, while there is no barrier for the other FeMRs. Therefore, for these mesoscopic particles the brush size is the main factor that determines the dispersion state in polymer matrices with athermal or weakly attractive brush-matrix interactions. With this insight, we now understand the mechanisms that affect dispersion in polymer matrices of mesoscopic particles and can therefore design systems with well-dispersed mesoscopic particles.

6.2 Introduction

Polymer nanocomposites (PNCs) have found a broad range of uses in a wide variety of fields owing to their ease in processability and vast array of potential properties. PNCs consist of a polymer matrix that is host to a nanosized filler material. Many different types of filler material have been used ranging from metal and non-metal nanoparticles (NPs)(Bakueva, Musikhin et al. 2003, Mbhele, Salemane et al. 2003, Corbierre, Cameron et al. 2005, Oh and Green 2009, Gam, Corlu et al. 2011), carbon nanotubes(Mitchell, Bahr et al. 2002, Park, Ounaies et al. 2002, Du, Scogna et al. 2004), and clays(Krishnamoorti and Giannelis 1997, Fornes, Yoon et al. 2001). Utilizing various filler materials has resulted in PNCs with unique optical(Bakueva, Musikhin et al. 2003, Hore and Composto 2010), magnetic(Hong, Li et al. 2004, Xu, Ohno et al. 2009), electrical(Du, Scogna et al. 2004, White, Vora et al. 2011), and sensing properties(Ma, Ali et al. 2006), depending on the material used. The fillers used have typically been nanometric (less than 100 nm) or colloidal (greater than 1 μm) in size scale. Little work has been done on mesoscopic filler particles, those between 100 nm and 1 μm.

The dispersion of the filler material within the host matrix also plays a significant role in the final properties of the PNC. White *et al.* have shown that PNCs containing silver nanowires have vastly different electrical properties depending on whether a majority of nanowires are close to or far from each other.(White, Vora et al. 2011) Similarly, Hore *et al.*(Hore, Frischknecht et al. 2012) showed that the dispersion of gold nanorods in a polymer matrix would shift the absorption wavelength of the PNC. Understanding how to control the tendency of the filler to disperse or aggregate allows one to tune the overall properties of the PNC and therefore has vast implications in a broad range of fields.

One strategy to disperse NPs in a polymer matrix is to graft a polymer brush compatible with the matrix to the surface of the NP. For example, Kim and Green(Kim and Green 2010) studied the dispersion of spherical gold nanoparticles coated with a PS brush layer in a PS polymer matrix. The degree of polymerization of the brush (N) relative to that of the matrix (P) determined whether or not the particles would disperse. The authors found that at $\alpha = P/N > 3$ the matrix chains are excluded from the brush layer, causing the brush to collapse (dry regime). When $\alpha < 3$, the matrix chains were small enough to penetrate the brush layer, causing the brush to splay out (wet regime). Hore et al.(Hore, Frischknecht et al. 2012) studied the effects of the brush/matrix interaction on the dispersion of AuNRs. The authors found that a transition from wet to dry would occur at $\alpha > 2$, and, by exploiting this, were able to disperse PS-coated AuNRs in PS thin films. While the above studies, and many others(Corbierre, Cameron et al. 2005, Srivastava, Agarwal et al. 2012, Sunday, Ilavsky et al. 2012), focused on NPs that are 10s of nms in size, no studies have looked at the effect of the polymer brush and matrix on the dispersion of NPs 100s of nm in size.

In this work we attempt to elucidate the factors that affect the dispersion of our model material, PMMA-grafted, mesoscopic, iron oxide rods (FeMRs) in polymer thin films. PMMA brushes of various sizes were grafted from the surface of the FeMRs via surface-initiated atom transfer radical polymerization (SI-ATRP). The PMMA brush molecular weight (M_n) was varied from 3.7 kg/mol to 160 kg/mol in order to determine the effect of brush size on dispersion of the FeMRs. The polymer matrix was chosen to either be PMMA or PEO. Whereas the PMMA brush PMMA matrix is athermal, the PEO matrix has a weak, favorable interaction (*i.e.* small negative χ) with PMMA, which may enhance dispersion of PMMA grafted FeMRs in PEO. Finally, the matrix index of polymerization (P) was

chosen such that for every brush index of polymerization (N), one matrix would wet the brush (P/N <2) while the other would dry the brush (P/N>2). FeMR dispersion within the films was studied with transmission electron microscopy (TEM). The FeMRs grafted with the largest brush (M_n = 160 kg/mol) fully dispersed, in both PMMA and PEO matrices, independent of P. Free energy calculations reveal that the only non-negligible forces acting on the FeMRs are steric repulsion due to brush-brush repulsion and van der Waal's attraction between the mesoscale iron-oxide mesorods. This work helps to understand the role particle size plays in dispersion of nanoparticles in polymer matrices.

6.3 Results and Discussion

Poly(methyl methacrylate) (PMMA) brushes were grafted from the FeMR surface. FeMRs were synthesized using methods discussed elsewhere.(Zocher and Heller 1929, Watson, Cardell et al. 1962, Huang, Ishige et al. 2015) Three samples of FeMRs were prepared, each with different molecular weight (M_n) brushes of PMMA polymerized from the FeMR surface via atom transfer radical polymerization (ATRP).(Huang, Ishige et al. 2015) The brush M_n were 3.7 kg/mol, 32 kg/mol, and 160 kg/mol, where the degree of polymerization of the brush (N) = 37, 320, and 1600, respectively. The grafting density was *ca.* 0.3 chains/nm^2 and was nearly constant across all M_n.(Huang, Ishige et al. 2015) The M_n were chosen such that dispersion could be studied across a broad range of brush / matrix combinations.. Specifically, as the brush M_n is increased, the FeMRs should be more likely to disperse in a wider range of matrix M_n. Additionally, controlling the brush M_n allows one to control the minimum separation distance, which is important for tuning the properties of the nanocomposite films. **Figure 6.1** is a representative TEM image of the

synthesized FeMRs with a 160 kg/mol brush. FeMRs were determined to be 181 +/- 16 nm in length with a diameter of 34 +/- 3 nm.

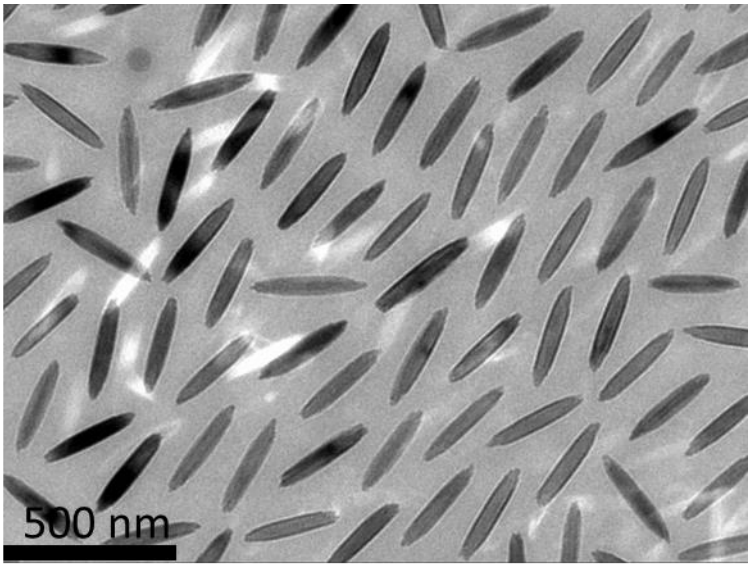

Figure 6.1 Representative TEM image of FeMRs drop cast from solution onto a TEM grid. This particular image is of the FeMRs with 160 kg/mol PMMA brush. The FeMRs are 181 +/- 16 nm in length with a diameter of 34 +/- 3 nm.

FeMRs were cast in polymer thin films. FeMRs (0.1 wt%) and PMMA or PEO (1.0 wt%) were dispersed in toluene. PMMA and PEO were chosen due to their unique interaction with the PMMA brush. For the PMMA matrix, the brush matrix interaction is nearly athermal (*i.e.* $\chi \approx 0$) and therefore the brush regime (*e.g.* wet or dry) is expected to depend strongly on the ratio (α) of the degree of polymerization of the matrix (P) relative to the brush (N), such that α=P/N. However, for the PEO matrix, the PMMA brush has a weak, favorable interaction with PEO (*i.e.* $\chi < 0$), which should loosen the α requirement and allow the FeMRs to disperse in a broader range of PEO P. FeMR dispersion dependence on α was probed, for each matrix type and brush M_n, by choosing a matrix M_n

such that $\alpha > 2$ (dry) or $\alpha < 2$ (wet). In total, 11 solutions were prepared and they are summarized in **Table 6.1**. The solutions were then spin-cast onto silicon nitride membranes at 2000 RPM. The thickness of these films was determined by ellipsometry, by casting in the same manner on a Si wafer, and was uniformly between 1 and 2 rod diameters in thickness. This was done to ensure that rods were confined in two-dimensions. The volume fraction of the FeMRs was approximately 5 vol% in all films prepared.

Table 6.1 Summary of Samples Prepared.

PMMA-FeMR Brush (M_n)	Matrix Type	Matrix M_n (P)
3.7 kg/mol	PMMA	1.1 kg/mol (11)
3.7 kg/mol	PMMA	37 kg/mol (370)
3.7 kg/mol	PEO	7.8 kg/mol (176)
32 kg/mol	PMMA	1.1 kg/mol (11)
32 kg/mol	PMMA	77 kg/mol (770)
32 kg/mol	PEO	5.4 kg/mol (122)
32 kg/mol	PEO	102 kg/mol (2317)
160 kg/mol	PMMA	77 kg/mol (770)
160 kg/mol	PMMA	290 kg/mol (2900)
160 kg/mol	PEO	102 kg/mol (2317)
160 kg/mol	PEO	400 kg/mol (9090)

The dispersion state of the prepared films was studied by transmission electron microscopy (TEM). Representative TEM images from six of the samples can be seen in **Figure 6.2**. **Figure 6.2**a and **Figure 6.2**d show the FeMRs with the largest M_n brush (160

kg/mol) in 77 kg/mol PMMA and 102 kg/mol PEO, respectively. For the 160 kg/mol brush, the FeMRs were found to be dispersed across all matrix types and P with no side-by-side aggregation. Contrariwise, the FeMRs with the shorter grafted brushes, 32 kg/mol and 3.7 kg/mol, formed small aggregates across all matrix types and matrix M_n. The 32 kg/mol brush FeMRs in 77 kg/mol PMMA and 102 kg/mol PEO can be seen in **Figure 6.2**b and **Figure 6.2**e, respectively, and the 3.7 kg/mol brush FeMRs in 7.8 kg/mol PMMA and PEO 37 kg/mol can be seen in **Figure 6.2**c and **Figure 6.2**f, respectively. In each of these cases, the FeMRs aggregate side-by-side. The aggregate size does not appear to change much between samples, in that the FeMRs aggregate similarly in PMMA as in PEO.

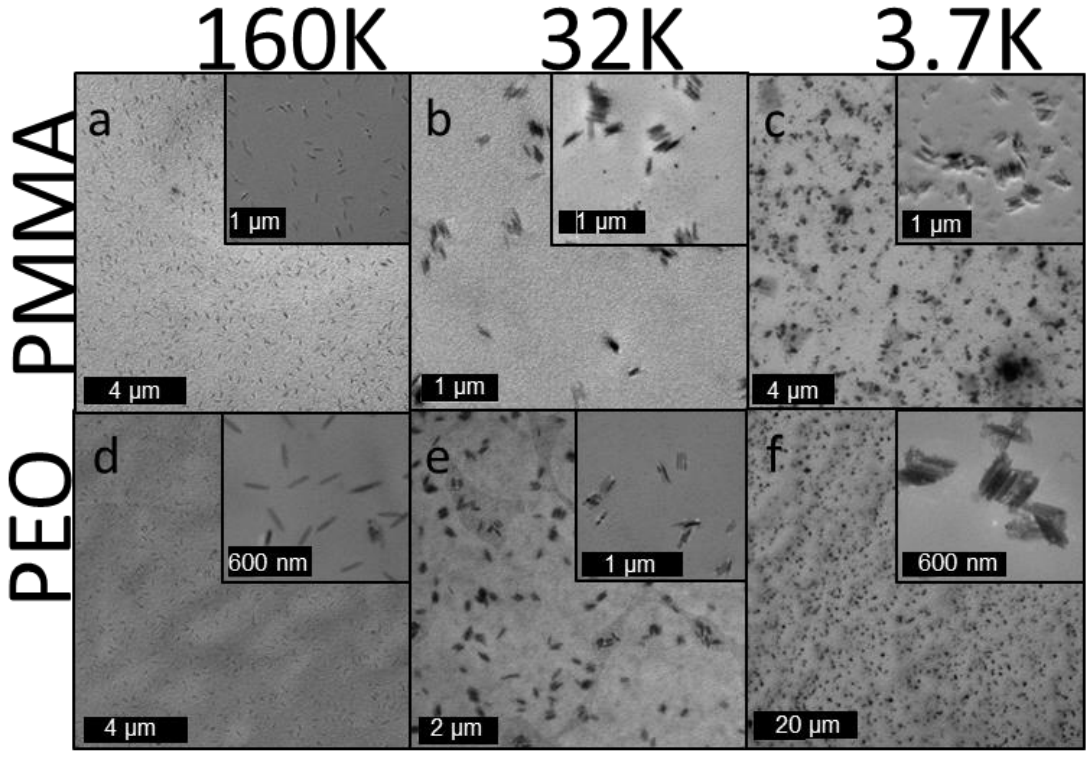

Figure 6.2 Representative TEM images FeMRs in thin films of PMMA (top row) and PEO (bottom row). The FeMRs with 160 kg/mol brush (a, d) dispersed well in across all matrices and matrix P. The FeMRs with 32 kg/mol brush (b, e) and 3.7 kg/mol brush (c, f) aggregated across all matrices and matrix P. Insets show a close up of the FeMRs.

Cluster analysis was performed to quantify the dispersion of the 32 kg/mol and 3.7 kg/mol FeMR samples. **Figure 6.3** shows the fraction of individual FeMRs present at each matrix P. In all cases, individual FeMRs comprised less than 36% of the sample, corresponding to an aggregated case. Previous studies with gold nanorods have shown that an $\alpha < 2$ leads to good dispersion.(Hore, Frischknecht et al. 2012) However, we do not observe such a trend. For example, for 3.7 kg/mol (N=37) FeMRs, in P=11 ($\alpha = 0.3$) 11% of the sample is individual FeMRs, while in P = 370 ($\alpha = 10$), 17% of the sample is individual FeMRs. From the nanorod studies, we would expect the FeMRs to disperse in P=11 and aggregate in P=370, but both cases are aggregated. Even at the larger brush size of 32 kg/mol (N=320) aggregation is still present; Individual FeMRs make up 36% of the sample in P = 11 (α=0.03) matrix and 10% of the sample in P=770 (α=2.4) matrix. Again, one would expect dispersion for the P=11 matrix and aggregation for the P=770 matrix, but both systems are aggregated. Previous studies also suggest that PEO-grafted nanroods will disperse very well in PMMA matrices at α up to 30 due to the weak, favorable interaction between PEO and PMMA.(Hore and Composto 2010) However, for the FeMRs, the PEO matrix does not enhance dispersion. The 3.7 kg/mol and 32 kg/mol brush FeMRs aggregate in all PEO matrices investigated. The aggregation of the 3.7 kg/mol and 32 kg/mol brush FeMRs, coupled with the good dispersion of the 160 kg/mol FeMRs across

all PMMA and PEO matrices suggests that brush M_n is the dominant factor in determining the dispersion of the FeMRs. However, our group has shown that both α and enthalpy affect the dispersion state for nanorods. The main difference between the two systems is the length scale of the rods studied, which could account for the discrepency.

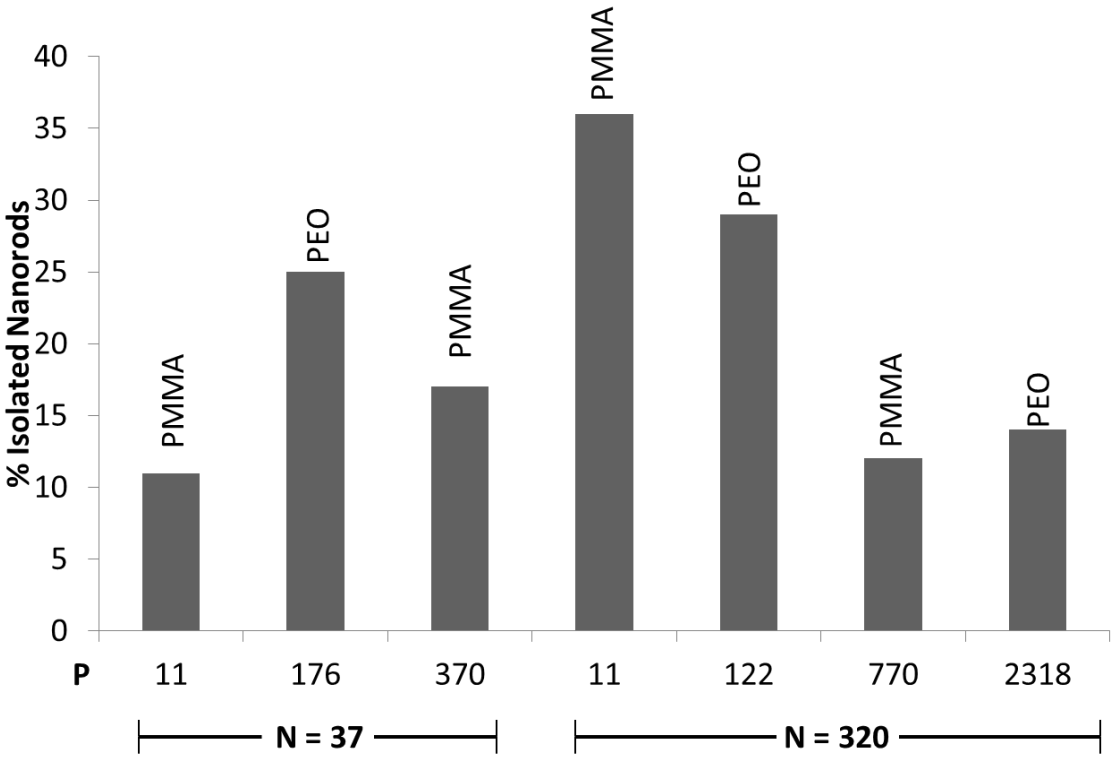

Figure 6.3 Percentage of isolated FeMRs in samples that are qualitatively determined to be aggregated by visual inspection of TEM images, namely those samples containing FeMRs with brush Mn = 3.7 kg/mol (N=37) and 32 kg/mol (N=320). At most, 36% of the FeMRs are isolated, much lower than the criteria for dispersion which is >90%.

Free energy calculations were performed to better understand the thermodynamic factors that determine FeMR aggregation. For nanorods, van der Waal's attraction had a limited effect on aggregation due to their relatively small length size. However, FeMRs are much larger than the nanorods and, therefore, it is conceivable that van der Waal's attraction would be a more significant factor for aggregation. The van der waal's free energy (Fv) can be calculated for two FeMRs separated by a gap D. To simplify the system, the FeMRs were treated like flat, iron-oxide plates. For two parallel plates, the Van der Waals interaction energy per unit area is given by:

$$F_v = \frac{-A}{12D^2}$$

where A is the Hamaker constant of the material, R is the radius of the rod and D is the separation distance between the two plates.(Israelachvili 1985) In the case of the FeMRs with a polymer brush in between, A is defined by the following equation:

$$A = (\sqrt{A_{11}} - \sqrt{A_{22}})^2$$

where A_{11} is the Hamaker constant of the FeMRs and A_{22} is the Hamaker constant of the polymer brush. The Hamaker constants were taken from the literature and for Iron oxide A_{11} is $6.8*10^{-20}$ J(Faure, Salazar-Alvarez et al. 2011) and for PMMA A_{22} is $2.32*10^{-19}$J. (Burke 2012)

The other major contribution to the free energy is the steric repulsion due to the interaction of adjacent brushes. The free energy can be calculated using analytical Self-Consistent Field analysis as put forth by Milner.(Milner 1988, Milner, Witten et al. 1988, MILNER 1991) The free energy per unit area as a function of brush height is given by:

$$F_s(u) = \frac{5}{9} f_0 \left(\frac{1}{u} + u^2 - u^5 \right)$$

where u is defined as u≡ h/h_0 with h and h_0 being the compressed and uncompressed polymer brush heights, respectively. Here, h is also equal to D/2 when the brush is compressed. The free energy of the uncompressed brush, f_0, and the height of the uncompressed brush are defined as:

$$f_0 = \frac{9}{10} N \sigma^{\frac{5}{3}} w^{\frac{2}{3}} \left(\frac{\pi^2}{12} \right)^{\frac{1}{3}} v^{\frac{1}{3}}$$

$$h_0 = \left(\frac{12}{\pi^2} \right)^{\frac{1}{3}} N \sigma^{\frac{1}{3}} w^{\frac{1}{3}} v^{-\frac{1}{3}}$$

where N is the index of polymerization, σ is the grafting density, w is the excluded volume parameter, and v is inversely proportional to the square of the radius of gyration. It should be noted that F_s assumes a brush that is strongly stretched and, therefore, may overestimate the compressed brush contribution to the free energy as compared with a real brush (*e.g.* dry brush).

The total free energy (F_{tot}) was calculated by summing the contribution due to F_v and F_s. F_{tot} was calculated at plate separations between 0.1 and 100 nm for N = 1600 (M_n = 160 kg/mol), 320 (M_n = 32 kg/mol), and 37 (M_n = 3.7 kg/mol). The results of this calculation were plotted as free energy in units of k_BT versus D (nm) in **Figure 6.4**. For N = 37 and 320 (**Figure 6.4**a and **Figure 6.4**b respectively), the free energy is always negative, implying that the Van der Waals force overcomes the steric repulsion due to brush compression at all separation distances, leading to aggregation. Note that at a separation of 20 nm the attraction is about -10 k_BT. Contrariwise, for N=1600 (**Figure 6.4**c), a primary

minimum occurs at a separation of *ca.* 40 nm, with a large potential barrier at closer separations, leading to dispersion. This separation distance is roughly in agreement with the observed minimum separation distance within the films (*ca.* 60 nm). These results are consistent with our experimental observations of the FeMRs in thin films. Calculations were also performed utilizing an additional electrostatic interaction free energy with no effect on the results. Furthermore, an additional medium of PEO was factored into the Van der Waal's free energy calculation through an additional Hamaker constant, again with no change to the results. Therefore, the dominant factor that leads to aggregation is the strength van der Waal's attraction between two rods.

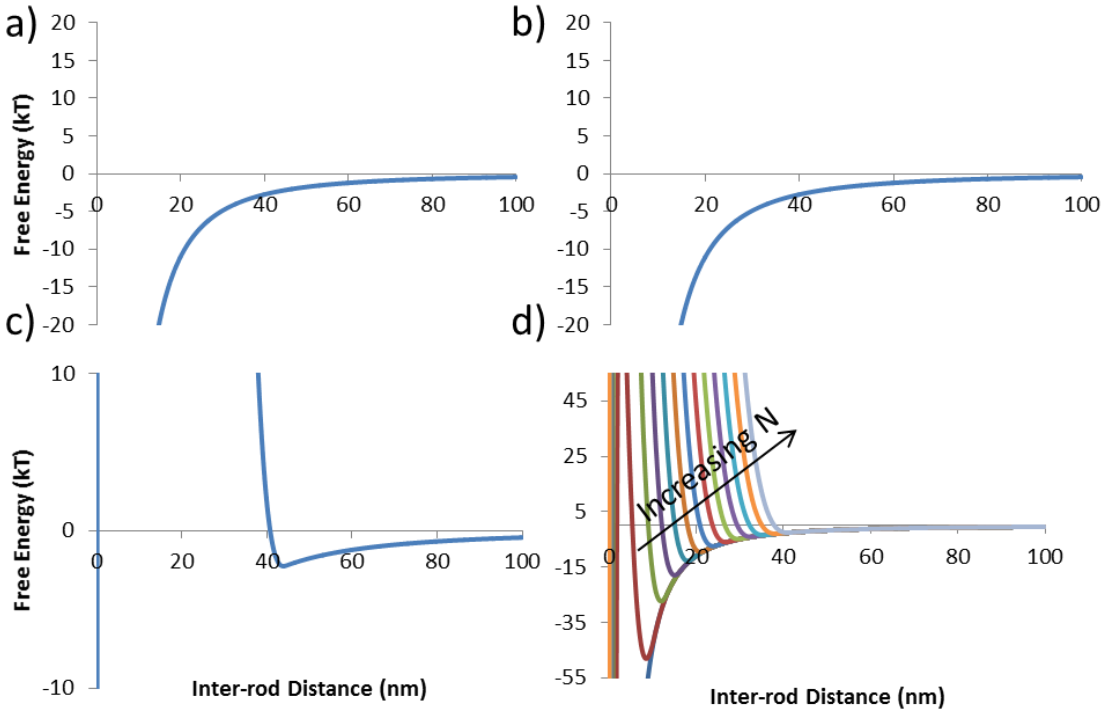

Figure 6.4 Free energy calculations for FeMRs with grafted polymer brushes the same size as those in our experimental studies (a-c) and brushes between N = 300 and N = 1200 (d) as a function of separation distance. The free energy in figures a and b (N = 37 and N =

320, respectively) are always negative implying that the FeMRs are largely attracted to one another and will tend toward aggregation, which is in agreement with experimental observations. The free energy in c (N=1600) has a primary minima and then a large energy barrier implying that the rods are repulsive. The location of the minima (*ca.* 40 nm) is roughly consistent with observed separation distance of the rods (*ca.* 60 nm). Figure d shows that FeMRs with N > 600 should be dispersed.

Additional free energy calculations were performed to determine the window for dispersion. The free energy calculations were done in the same manner as above for N = 300, 400, 500, 600, 700, 800, 900, 1000, 1100, and 1200. The result of these calculations can be seen in **Figure 6.4d** where free energy in units of k_BT is plotted vs. D in units of nm. The well depth becomes shallower and shifts to higher D as N increases, consistent with the repulsion due to the brush becoming stronger. The well depth commensurate with aggregation is not perfectly defined. From our previous studies with nanorods, aggregation was found to occur when the free energy was at least less than -5 k_BT.(Hore, Frischknecht et al. 2012) Here, we select a value of -15 k_BT as our criteria for aggregation. In this case, a N less than 700 will result in aggregation. Furthermore, these calculations show that one of our experimental systems that aggregated (N=320) is close to an N calculated as being dispersed. These rods aggregated regardless of favorable matrix conditions, despite being close to a region of dispersion. Therefore, for these mesoscale rods, the range of N where brush wetting would significantly affect dispersion is narrow.

To more easily elucidate the trends, a dispersion map of the experimental results is plotted in **Figure 6.5**. The line P=2N is plotted on this map to emphasize the divergence of

our data from previous studies where P > 2N indicated aggregation.(Hore, Frischknecht et al. 2012) Here the green data represent the aggregated systems and the red data represent the dispersed systems. Circles are used for PEO matrices, while squares are used for PMMA matrices, with filled symbols corresponding to experiments while open symbols correspond to calculations. There is no correlation between the dispersion state and α, or the dispersion state and matrix type. Dispersion of the FeMRs did not change across three orders of magnitude of P at each M_n. The reasons that only the brush M_n matters in the dispersion of FeMRs are still unclear. The key, we think, is due to the size of the rods. At low M_n, the rods are so large that their van der Waal's force overcomes the steric repulsion due to the brush regardless of regime. Furthermore, the calculations assume a strongly stretched brush, so being 'wet' will do no more to stabilize the dispersion than what was assumed in the calculations, which is most likely why we see aggregation at low M_n even in PEO. At high M_n, the brush provides enough steric repulsion such that aggregation due to van der Waal's attraction is prevented. Small angle neutron scattering (SANS) measurements could be performed on the PNCs to more fully elucidate the brush behavior in each of the samples presented here.(Hore, Ford et al. 2013) Finally, more sophisticated numerical methods such as potential of mean force calculations performed via self-consistent field theory would aid in the understanding of the aggregation mechanism in this system.

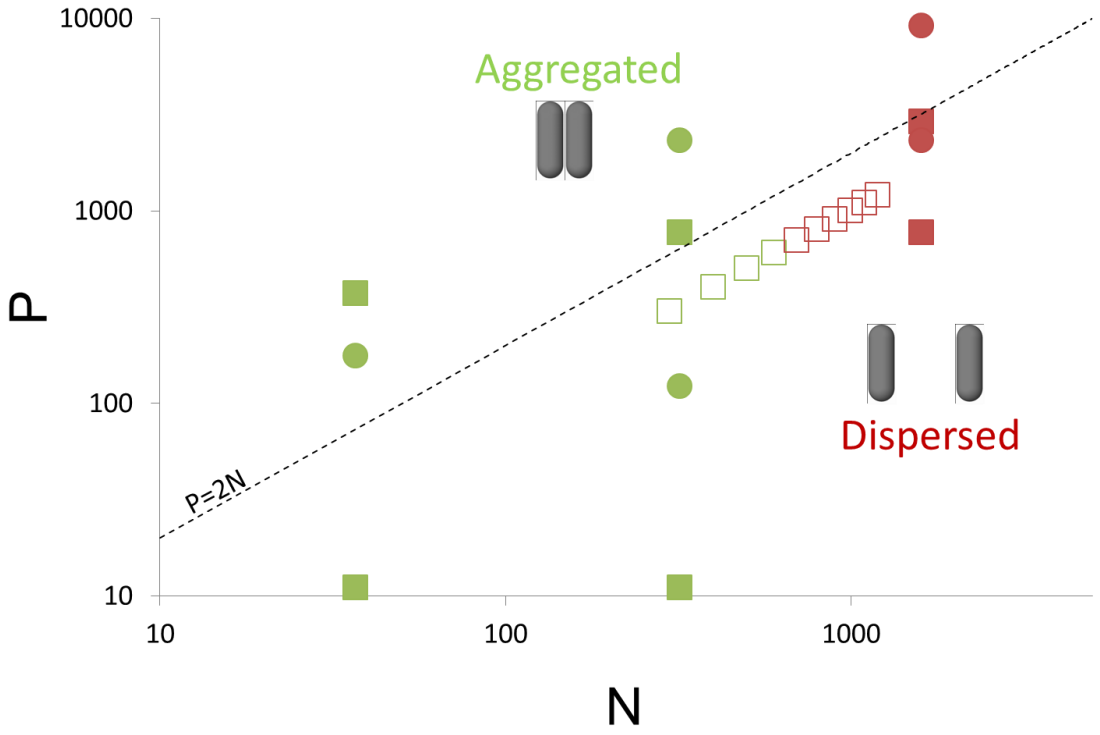

Figure 6.5 Phase map P vs. N of all experimental and calculated samples. The line P=2N is plotted to show the divergence of our data from previous studies.(Hore, Frischknecht et al. 2012) Green markers are aggregated samples, red markers are dispersed samples, squares are FeMRs in a PMMA matrix, circles are FeMRs in a PEO matrix, unfilled markers are the calculated samples. While P does not play a role in the calculations, P was set equal to N to place the calculations on this plot.

6.4 Conclusions

In this work, we have systematically studied the factors that affect the dispersion of 'mesoscopic' PMMA grafted FeMRs in PMMA and PEO matrices. Namely, we explored the effect of matrix P, brush M_n, and matrix type on the dispersion state of FeMRs. For these FeMRs, the brush M_n determined whether the rods dispersed and neither enthalpy

nor matrix P played a role. Free energy calculations were performed to further understand this phenomena. The free energy calculations are consistent with the experimental results that were attained and show that, for FeMRs, only the brush M_n affects the dispersion as the steric repulsion of the brush must overcome the van der Waal's attraction between the rods. Furthermore, these calculations show that the range of M_n where the matrix P is important is narrow; The FeMRs will either disperse or aggregate regardless of whether the brush is wet or dry. Thus, the dominant factor that matters in dispersion of the mesoscopic FeMRs is the brush M_n.

This work is the first to explore the factors that affect the dispersion of mesoscopic polymer grafted anisotropic particles in polymer matrices. The results of this work, namely that brush M_n is the dominant factor in the dispersion of mesoscale rods, can be applied to other similarly sized or larger particles of other materials. Simple free energy calculations can also be used to predict dispersion properties of large particlesas a function of brush M_n. Interesting further studies could look at the effect grafting density on the dispersion mesoscale rods.

Chapter 7 Engineering the Assembly of Gold Nanorods in Polymer Matrices

In Collaboration with Jason Koski of Prof. Robert A. Riggleman's Group (Penn)

7.1 Abstract

In this work we investigate, both experimentally and through hybrid particle/self-consistent field theoretic (hSCFT) calculations, the dispersion state of gold nanorods (AuNRs) grafted with homopolymer, bidispersed, or mixed polymer brushes. AuNRs are grafted with 11.5 kg/mol PS (HNRs), 11.5 kg/mol PS and 5.3 kg/mol PS (BNRs), or 11.5 kg/mol PS and 5K poly(methyl methacrylate) (PMMA) (MBNRs) and cast in PS or PMMA films consisting of short to very long chains compared to the grafted brush. We further investigated the MBNR systems by varying the length of the PS brush. Overall, we find that the MBNRs dispersed markedly better than the other brush types (HNRs or BNRs) in PS matrices. We utilize hSCFT calculations, in particular potential of mean force (PMF) and brush profile calculations, to elucidate the thermodynamics of these systems. The PMFs and brush profiles exhibit similar trends for the BNRs and MBNRs where the short grafted chain forces the longer grafted chain away from the AuNR surface and promotes wetting by the matrix chains.The hSCFT calculations demonstrated qualitative trends consistent with the aggregation observed for AuNRs in PMMA matrices. Therefore, we have demonstrated that MBNR dispersion in polymer matrices is enhanced compared to the HNR and BNR cases, which extends the dispersion window for new combinations of nanorods and polymers.

7.2 Introduction

The incorporation of nanoparticles in a polymer matrix has received considerable attention due to the promising combination of the processability of polymers and the wide range of functionalities that nanoparticles have to offer. In many applications, the homogeneous dispersion of nanoparticles in the polymer matrix is paramount in achieving the desired material properties. These enhanced properties can include improved tensile(Balazs, Emrick et al. 2006, Liu, Jia et al. 2014, Ma, Yu et al. 2014) strength or ionic conductivity.(Giannelis 1996, Johan, Shy et al. 2011, Tan and Johan 2011) Unfortunately, nanoparticles tend to aggregate in a polymer matrix based on favorable van der Waals forces with other nanoparticles or depletion interactions where the polymers gain conformational entropy by exiting the space between the particles. A common approach to help combat the nanoparticles from aggregating is to graft polymer chains onto the surface of the nanoparticle.(Green 2011, Srivastava, Agarwal et al. 2012, Kumar, Jouault et al. 2013) In principle, the grafted chains help repel the particles as they approach one another due to the added steric hindrance between the grafted chains. Nevertheless, in certain conditions, the added steric hindrance between the grafted chains is not enough to keep the particles dispersed in the polymer matrix. However, in these conditions, grafting polymer chains onto the surface of a nanoparticle provides a unique route to control the spacing between aggregated nanoparticles, which can have a significant impact on the material's optical properties.(Hore and Composto 2012, Hore, Frischknecht et al. 2012) Specifically, it has been shown that the spacing between gold nanorods in polymer thin films affects the resulting UV absorbance spectrum, which has important implications in plasmonic devices,

such as a creating a tunable platform for surface enhanced Raman spectroscopy.(Ferrier, Lee et al. 2014)

For grafted nanoparticles in a polymer matrix, the most studied system is the case where the grafted chains are monodisperse in length and chemically identical to the matrix chains.(Kumar, Jouault et al. 2013) In these "athermal" systems, it is has been established that the relative degree of polymerization of the matrix (P) to the grafted chains (N) plays a primary role in whether the nanoparticles disperse or aggregate, which is typically denoted as α, where $\alpha = P/N$. When the matrix chains are short in comparison to the grafted chains ($\alpha < 2$), the matrix chains are able to penetrate or "wet" the brush, which allows for the nanoparticles to remain dispersed in the matrix. On the other hand, when the matrix chains are long relative to the grafted chains ($\alpha > 2$), the matrix chains are unable to penetrate the brush and the brush is said to be "dry", and the particles aggregate. This is often referred to as the wet-to-dry transition, which can equivalently be thought of as the dispersed-to-aggregated transition. Numerous studies,(Akcora, Liu et al. 2009, Green 2011, Hore and Composto 2012, Hore, Frischknecht et al. 2012, Srivastava, Agarwal et al. 2012, Srivastava, Agarwal et al. 2012, Sunday, Ilavsky et al. 2012, Frischknecht, Hore et al. 2013, Kumar, Jouault et al. 2013, Chao, Hagberg et al. 2014, Ferrier, Lee et al. 2014) both experimentally and theoretically, have demonstrated that in a high grafting density regime, where the particle core-core interactions are minimal, that α is critical in the dispersion or aggregation of particles. However, at very high grafting densities, the matrix may be unable to penetrate the brush based on monomer crowding near the surface of the particle. As a result, it is unclear that simply relying on working in a low α regime is

enough to keep the nanoparticles dispersed in addition to the fact that this also limits the range of usable matrix or grafted chain lengths.

Recently, systems in which the grafted chains are bidisperse in length and chemically similar have been investigated in order to help tune the interactions of the particles within the polymer matrix.(Rungta, Natarajan et al. 2012, Li, Tao et al. 2013) Using two different lengths for the grafted chains offers a wider parameter space to optimize dispersion or particle-particle spacing. For example, Li *et al.*(Li, Tao et al. 2013) indicate that a high grafting density of short chains can prevent core-to-core interactions while a lower grafting density of longer chains can still allow for penetration of the matrix chains into the brush of the grafted chains. More generally, Jayaraman has shown in a series of hybrid polymer reference interaction site model (PRISM) – Monte Carlo (MC) studies(Nair, Wentzel et al. 2011, Martin, Dodd et al. 2013, Martin, McKinney et al. 2013) that polydispersity in grafted chain length improves the miscibility of grafted particles and the polymer matrix due to the shorter chains preventing core-to-core interactions while also pushing out and stretching the longer chains. This, in-turn, leads to steric hindrance at larger inter-particle distances while also allowing the matrix chains to penetrate the brush layer due the reduced monomer density near the surface of the particle.

Nanoparticles that are grafted with chains that are monodisperse in length, but are chemically distinct have very recently begun to receive attention. Kim *et al.*(Kim, Kim et al. 2015) investigated the brush profiles of polystyrene (PS) and poly(methyl methacrylate) (PMMA) grafted gold nanospheres in a good solvent. They found that the grafted chains phase separated with increasing molecular weight though the mechanism remains unclear. To our knowledge, nanoparticles grafted with chains that are bidisperse in length and

chemically distinct have not been investigated. A global understanding of the effect of the polydispersity in chain length and chemical heterogeneity of grafted polymer chains can significantly increase the number of tunable parameters to help control the dispersion or aggregation of nanoparticles in polymer thin films. Furthermore, the wider range of tunable parameters could potentially allow for fine-tuning the spacing between nanoparticles on very small length scales, which would have exciting implications in the degree of control of optical properties in polymer thin films.

In this paper, we present a controlled study at which we characterize the dispersion or aggregation of gold nanorods that are grafted with chains that are monodisperse in length and chemically similar, chains that are bidisperse in length and chemically similar, and chains that are bidisperse in length and chemically distinct. Interestingly, we find that both the dispersity in chain length and chemical heterogeneity of the grafted chains has significant implications on the resulting macroscopic optical properties which we quantify based on the dispersed or aggregated nature of the gold nanorods. Specifically, the gold nanoroads grafted with chains that are bidisperse in length and chemically distinct exhibit the best dispersion when the longer chains are chemically similar to the matrix, even in conditions of very high α. As a result, we further investigate the dispersity in chain length for the case where the chemical brushes are distinct. Lastly, to provide further insight, hybrid particle/self-consistent field theory (hSCFT) calculations are used to help quantify the particle-to-particle interactions as well as the particle's interaction with the matrix chains through potential of mean force curves and brush profiles, respectively.

7.3 Computational Methods

7.3.1 Model Details

We implemented a hybrid particle-field approach(Sides, Kim et al. 2006, Hickey, Koski et al. 2014, Koski, Chao et al. 2015) where we define discrete grafted nanoparticles within a polymer matrix. The polymer chains are modeled as discrete Gaussian chains with statistical segment size of polymer, b, where the "A" matrix chains have $N_{A,M}$ discretization points while the grafted "A" and "B" chains have $N_{A,G}$ and $N_{B,G}$ discretization points, respectively. The particle density of the "A" matrix chains is given by

$$\hat{\rho}_{A,M}(\mathbf{r}) = \sum_{i=1}^{n_{A,M}} \sum_{i=j}^{N_{A,M}} \delta(\mathbf{r} - \mathbf{r_{i,j}}) \tag{1}$$

and similarly, the grafted "A" and "B" chains are defined as

$$\hat{\rho}_{A,G}(\mathbf{r}) = \sum_{i=1}^{n_{A,G}} \sum_{i=j}^{N_{A,G}} \delta(\mathbf{r} - \mathbf{r_{i,j}}) \tag{2}$$

$$\hat{\rho}_{B,G}(\mathbf{r}) = \sum_{i=1}^{n_{B,G}} \sum_{i=j}^{N_{B,G}} \delta(\mathbf{r} - \mathbf{r_{i,j}}) \tag{3}$$

where $n_{A,M}$, $n_{A,G}$, and $n_{B,G}$ are the number of "A" matrix chains, "A" grafted chains, and "B" grafted chains, respectively.

The particles in our system are incorporated as cavity functions that exclude the polymer chains from entering the core of the particle. The nanoparticle density is defined as

$$\hat{\rho}_P(\mathbf{r}) = \sum_{i=1}^{n_P} \Gamma(|\mathbf{r} - \mathbf{r_i}|) \tag{4}$$

while the functional form of Γ is given as

$$\Gamma(\mathbf{r}) = \frac{\rho_0}{2}\mathrm{erfc}\left(\frac{\mathbf{r} - \mathrm{R_P}}{\xi}\right) \tag{5}$$

where R_p is the radius of the particle, ρ_0 is the total system density, and ξ is the length scale at which the particle density goes smoothly from ρ_0 in the particle core to 0 at the outside surface of the particle. The particle(s) location is defined explicitly in the simulation and do(es) not change over the course of the calculation.

The statistical segments of the polymer chain are connected with a Gaussian bonding potential

$$\beta U_0 = \sum_{i=1}^{n_{A,M}} \sum_{i=j}^{N_{A,M}-1} \frac{3(|\mathbf{r_{i,j}} - \mathbf{r_{i,j+1}}|)^2}{2b^2} \tag{6}$$

while the enthalpic interactions between the "A" and "B" components are governed by a simple local interaction of the form

$$\beta U_1 = \frac{\chi}{\rho_0}\int d\mathbf{r}\hat{\rho}_A(\mathbf{r})\hat{\rho}_B(\mathbf{r}) \tag{7}$$

where $\hat{\rho}_A = \hat{\rho}_{A,M} + \hat{\rho}_{A,G}$, $\hat{\rho}_B = \hat{\rho}_{B,G}$, and χ is the Flory parameter governing the strength of interaction between the "A" and "B" components. Lastly, we assume our model is incompressible by implementing the condition that at every point in the simulation box, the total density must equal ρ_0. This is given by

$$\delta[\hat{\rho}_+(\mathbf{r}) - \rho_0] \tag{8}$$

where $\hat{\rho}_+ = \hat{\rho}_{A,M} + \hat{\rho}_{A,G} + \hat{\rho}_{B,G}$.

Using Hubbard-Stratonovich transformations, a hybrid particle-field based partition function is given by

$$\mathcal{Z} = z_0 \int \mathcal{D}w_+ \int \mathcal{D}w_- \int d\mathbf{r}^{n_P} e^{-\mathcal{H}(\mathbf{r}^{n_P};[w_+,w_-])} \tag{9}$$

where z_0 contains numerical prefactors (*e.g.* thermal de Broglie wavelength) that are not important in the calculations considered in this work. The effective Hamiltonian is given by

$$\mathcal{H}(\mathbf{r}^{n_P};[w_+,w_-]) = \int d\mathbf{r} \left[\frac{\rho_0}{\chi} w_-(\mathbf{r})^2 - i w_+(\mathbf{r})\{\rho_0 - \hat{\rho}_P(\mathbf{r})\}\right] \tag{10}$$
$$-n_{A,M} \ln Q_{A,M} - n_{A,G} \int d\mathbf{r}\, \sigma(\mathbf{r}) \ln q_{A,G}(\mathbf{r}) - n_{B,G} \int d\mathbf{r}\, \sigma(\mathbf{r}) \ln q_{B,G}(\mathbf{r})$$

where $Q_{A,M}$, $q_{A,G}(r)$, and $q_{B,G}(r)$ are the partition functions of a single "A" matrix chain, "A" grafted chain, and "B" grafted chain, respectively. $\sigma(r)$ is the distribution of graft sites on the surface of the nanoparticles for the grafted chains.

The partition function and density operators of the polymer chains are calculated from the chain propagators, q, which are generated from iterating the Chapman-Kolmogorov equation

$$q(j+1,\mathbf{r}) = e^{-w_K(\mathbf{r})} \int d\mathbf{r}\, \Phi(\mathbf{r}-\mathbf{r}') q(j,\mathbf{r}) \tag{11}$$

The partition function of the "A" matrix chains are calculated from the following equation

$$Q_{A,M} = \frac{1}{V} \int d\mathbf{r}\, q(N_{A,M},\mathbf{r}) \tag{12}$$

where V is the total volume of the system while the segment density is calculated by

$$\rho_{A,M}(\mathbf{r}) = \frac{n_{A,M}}{V Q_{A,M}} \sum_{j=0}^{N_{A,M}} q(j,\mathbf{r}) e^{+w_{A,M}(\mathbf{r})} q(N_{A,M}-j,\mathbf{r}) \tag{13}$$

where the initial condition for the "A" matrix chains is given by $q_{A,M}(0, \mathbf{r}) = e^{-w_{A,M}(\mathbf{r})}$. Similar to the "A" matrix chains, the free ends of both the "A" and "B" grafted chains have initial condition $q_{K,G}(0, \mathbf{r}) = e^{-w_{K,G}(\mathbf{r})}$. The partition functions of the grafted chains are defined as $q_{K,G} = q_{K,G}(N_{K,G}, \mathbf{r})$, where K = "A" or "B". As shown in our previous work [27] in modeling mixed brush grafted nanoparticles, the initial condition for the grafted ends of the grafted chains are defined from a grafting site distribution, $\sigma(\mathbf{r})$, that is homogeneous distributed around the explicit particles given by

$$\sigma(\mathbf{r}) = \frac{1}{\sigma_0} \exp\left[-\left(\frac{|\mathbf{r}^{n_P}| - R_P - \xi}{\xi}\right)^2\right] \tag{14}$$

where σ_0 is a normalization prefactor defined such that $\int d\mathbf{r}\, \sigma(\mathbf{r}) = 1$. From this definition, the complimentary chain propagator of the grafted chains, $q^{\dagger}_{K,G}$ has initial condition

$$q^{\dagger}_{K,G}(0, \mathbf{r}) = \frac{\sigma(\mathbf{r})}{q_{K,G}(N_{K,G}, \mathbf{r})} \exp[-w_{K,G}(\mathbf{r})] \tag{15}$$

The initial condition of the complimentary propagator effectively forces the grafted end of the grafted chains to be placed at the surface of the particle. Finally, the segment density of the grafted chains is given by

$$\rho_{K,G}(\mathbf{r}) = n_{K,G} \sum_{j=0}^{N_{K,G}} q(j, \mathbf{r}) e^{+w_{K,G}(\mathbf{r})} q(N_{K,G} - j, \mathbf{r}) \tag{16}$$

7.3.2 Potential of Mean Force Curves

We generated potential of mean force curves using the aforementioned model by using 2D hSCFT calculations and varying the inter-particle distance of two explicit mixed brush grafted particles. Under the mean-field approximation, the Helmholtz free energy is equal to the effective Hamiltonian to within a constant. As a result, calculating the Hamiltonian

of the system at a given inter-particle distance and subtracting the Hamiltonian at a large inter-particle distance where the two particles do not interact (assumed to be 30b in all cases) gives the free energy as a function of inter-particle distance. An important note is that because the calculations were run in 2D, the free energy is actually a free energy per length, which we denote as $\Omega(\mathbf{r})$. The 2D calculations ignore the particles rotational degrees of freedom, curvature effects near the ends of the nanorods, and it is assumed that the nanorods primarily arrange themselves side-by-side.

The calculations were conducted in a 30.612b x 60b box with 75 x 147 grid points in the respective direction. Simulation parameters were chosen such that grafting density, σ, Rp/Rg, and χ matched the experimental system. Specifically, $\sigma = 0.5$ chains / statistical segment length, Rp / Rg ≈ 0.33, and $\chi = 0.15$ with $\chi / \rho_0 = 0.0375$. It should also be noted that under the mean-field approximation, the relative length scales of the polymer chains and particles is what is important rather than the absolute length scales. The number of chains grafted onto the particles was held constant across all simulations. In generating the potential of mean force curves, the degree of polymerization of the matrix chains was varied from 4, 8, 16, 32, 64, and 128 while several combinations of the grafted chain lengths (ranging from 5 to 32) and chemistries were tested. The most relevant results to the experiments are presented in the Results section.

7.3.3 Brush Profiles

Brush profiles of the grafted chains were generated by defining a single explicit particle in the center of the box and calculating the local volume fraction of the grafted chains as a function of the radial distance from the center of the particle. A 40b x 40b box was used

with 81 x 81 grid points. The same grafting density, Rp/Rg, and χ values were used as in the PMF calculations and remained constant across all simulations. The matrix chain lengths tested were 4 and 256 while several combinations of grafted chain lengths (ranging from 5 to 32) and chemistries were tested. The most relevant results to the experiments are presented in the Results section. For clarity, the profiles are labeled as PS or PMMA rather than "A" or "B" to more easily be compared with the experiments.

7.4 Experimental Methods

All reagents were purchased from Sigma-Aldrich unless otherwise noted. Thiolated polymers were purchased from Polymer Source Inc.

7.4.1 AuNR Synthesis and Functionalization

AuNRs are synthesized as reported elsewhere.(Nikoobakht and El-Sayed 2003, Sau and Murphy 2004, Hore and Composto 2010, Ferrier, Lee et al. 2014) AuNRs were functionalized with thiolated polymers by first preparing a solution containing the thiolated polymer in tetrahydofuran (THF). Thiolated polymers were added in equimolar quantities so that the number of each polymer chain in solution would be constant. Next, the AuNRs in water were centrifuged down and the supernatant removed. The concentrated AuNR aliquot was then injected into the THF / polymer solution under heavy stirring. The thiolated polymers were allowed to incubate with the AuNRs in THF overnight. Finally, the now functionalized AuNRs were centrifugated and the supernatant was removed and replaced with toluene. The centrifugation and solvent replacement was repeated a total of three times to remove free thiol polymer from solution. In the case of the 15 kg/mol PMMA, 5.3 kg/mol PS functionalized AuNRs, the toluene was replaced with methyl ethyl

ketone (MEK), with all other steps being the same. MEK was used instead of toluene due to the AuNRs aggregated in toluene solution, which was characterized by increased solution turbidity and a blue shift in the absorbance peak position.

7.4.2 Thin Film Preparation

Polymer thin films were prepared by adding 0.7 to 0.4 mg of free polymer to 100 μL of AuNR solution in toluene or MEK. The free polymer was allowed to dissolve and then 20 μL of the polymer / AuNR solution was spin cast at 2000 RPM onto a Si wafer for SEM imaging or onto a glass coverslip for UV/Vis spectroscopy. The samples were allowed to dry overnight prior to any imaging or spectroscopy. Films cast from MEK were noticeably less homogeneous than films cast from toluene for both PS and PMMA.

7.4.3 Thin Film Characterization

Thin film PNCs were analyzed by both SEM and UV/Visible spectroscopy. SEM was performed on a JEOL7500F in low angle backscatter (LABE) mode. UV/Visible spectroscopy was performed on a Cary 5000 UV-Visible-NIR spectrometer.

7.4.4 SEM Image Analysis

SEM images were analyzed using ImageJ image analysis software (v.1.45S). Prior to analysis of the particle area, images were first thresholded such that the AuNRs were able to be recognized by the software. The result of this analysis was then further analyzed in a spreadsheet where the results were binned by area where a range of areas were equal to 1, 2, 3…etc. AuNRs. This analysis resulted in the final bar graphs constituting the cluster analysis. The radial distribution function (RDF) was calculated in a similar manner as above. First, the image was thresholded so the AuNRs could be recognized. Next, a macro

was run in ImageJ that finds the centers of the AuNRs and calculates the RDF. Finally, the result of the macro was presented with no further modification.

7.5 Experimental Results

7.5.1 Effect of Brush Type on Dispersion of Polymer Grafted AuNRs in Polymer Thin Films

Gold nanorods (AuNRs) were grafted with three different types of polymer brush. The AuNRs were grafted with 11.5 kg/mol polystyrene (PS) (PS brush index of polymerization (N_{PS})=110), a mixture of 11.5 kg/mol PS and 5.3 kg/mol PS (N_{PS}=51), and a mixture of 11.5 kg/mol PS and 5 kg/mol poly(methylmethacrylate) (PMMA) (N_{PMMA}=50), which will be referred to as homopolymer AuNRs (HNRs), homopolymer bidispersed AuNRs (BNRs), and chemically mixed bidispersed AuNRs (MBNRs), respectively. Functionalization with PS and PMMA brushes was confirmed via FTIR (**Figure 7.1**). In the MBNRs case, the grafting density was estimated from quartz crystal microbalance with dissipation (QCM-D) experiments to be 0.24 chains / nm^2 for PS and 0.31 chains / nm^2 for PMMA. **Figure 7.2** details the different brush cases. **Figure 7.3** is the absorbance spectra and an SEM image for each AuNR type acquired in toluene. The HNR and BNR LSPR peak position are both at 743 nm, while the MBNR LSPR peak position is at 753 nm. SEM images were analyzed to determine the physical characteristics of all AuNR samples. MBNRs were determined to be 43.8 +/- 6.6 nm in length and 15.5 +/- 4.4 nm in diameter, while BNRs and HNRs were determined to be 37.8 +/- 6.2 nm in length and 14.08 +/- 4.6 nm in diameter. The NRs are different dimensions due to the variability in the synthesis.

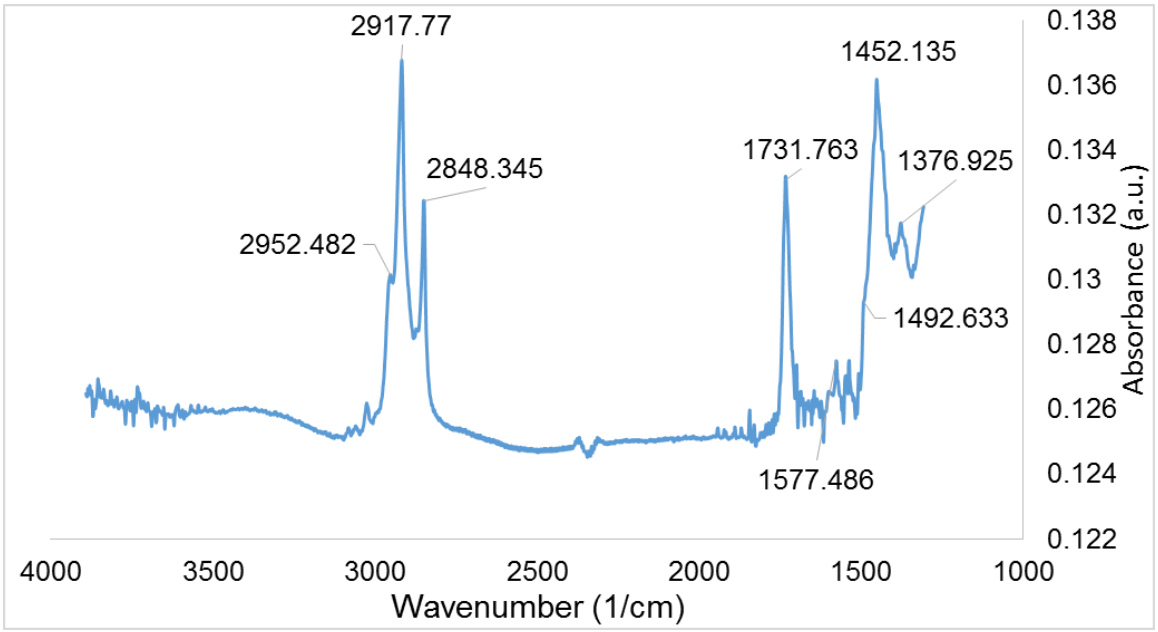

Figure 7.1 FTIR spectra taken from MBNR solution drop-cast onto a silicon wafer. Peaks at wavenumbers 2917, 2848, 1577, and 1492 (shoulder) correspond to polystyrene brush.(Chalmers and Griffiths 2002) Peaks at wavenumbers 2952 (shoulder), 1731, 1452, and 1376 correspond to the PMMA brush.(Duan, Zhang et al. 2008)

Figure 7.2 Cartoon of AuNRs Studied

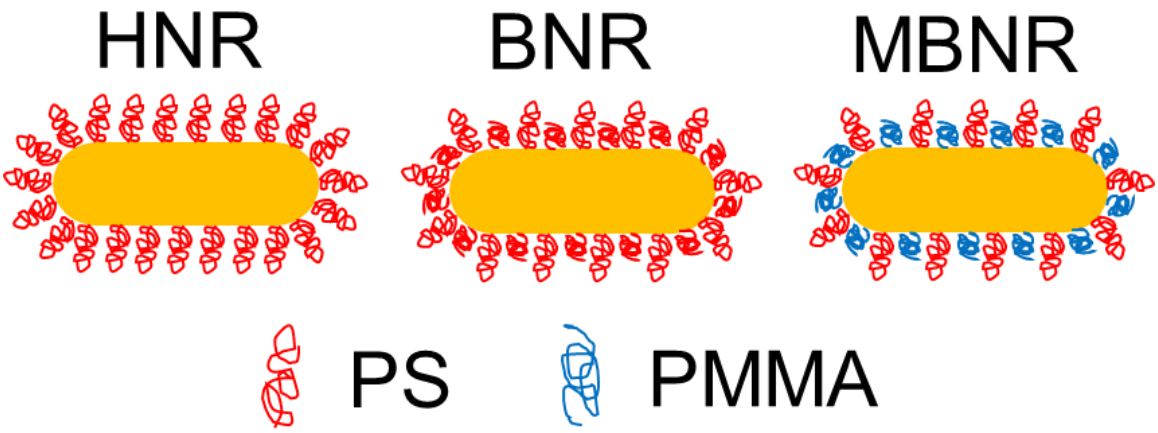

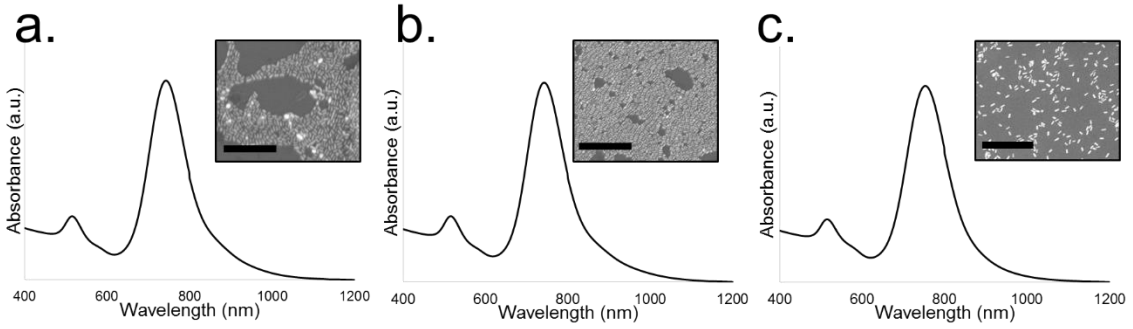

Figure 7.3 Absorbance spectra (a-c) and SEM images (insets) for HNRs (a), BNRs (b) and MBNRs (c) in toluene. HNRs and BNRs each have a LSPR peak at 743 nm, while MBNRs have a LSPR peak at 753 nm. The HNRs and BNRs are each 37.8 +/- 6.2 nm in length by 14.1 +/- 4.6 nm in diameter. The MBNRs are 43.8 +/- 6.6 nm in length and 15.5 +/- 4.4 nm in diameter. Scale bars for SEM images are 500 nm.

Each type of AuNR was cast in a thin film of PS or PMMA at various matrix polymer molecular weights (M_n). Specifically, matrix M_n investigated were: 1.7 kg/mol (PS matrix index of polymerization (P_{PS}) = 16), 5.78 kg/mol (P_{PS} = 55), 90 kg/mol (P_{PS} = 865), and 270 kg/mol (P_{PS} = 2596) PS, and 1.1 kg/mol (P_{PMMA} = 11), 17 kg/mol (P_{PMMA} = 170), 77 kg/mol (P_{PMMA} = 770), and 336 kg/mol (P_{PMMA} = 3360) PMMA. All films were cast from toluene onto a silicon wafer (for SEM) and glass cover slip (for absorbance). Representative SEM images for HNRs (demarcated by green box), BNRs (demarcated by blue box), and MBNRs (demarcated by red box) in matrices of 1.7 kg/mol PS (a,c,e), 270 kg/mol PS (b,d,f), 1.1 kg/mol PMMA (g,i,k), and 336 kg/mol PMMA (h,j,l) can be found in **Figure 7.4**. SEM images for the other matrix M_n can be found in **Figure 7.5**. It should be noted that the vol% of the MBNRs (~10%) is greater than the vol% for the HNRs and BNRs (~5%). All AuNR types appear dispersed in 1.7 kg/mol PS (a, c, e). Both HNRs and

BNRs appear aggregated in 270 kg/mol (b and d, respectively). Aggregation for these cases is also seen in the 90 kg/mol PS matrix (**Figure 7.5**). Contrariwise, the MBNRs disperse well in 270 kg/mol PS (f) matrix and, in fact, *the MBNRs appear well dispersed at all PS matrix* M_n. All AuNR types disperse in 1.1 kg/mol PMMA (g, i, k) and aggregate in 336 kg/mol PMMA (h, j, l). Aggregation begins at PMMA matrix M_n of 17 kg/mol and is also present in the 77 kg/mol PMMA matrix (**Figure 7.5**). However, for BNRs and MBNRs, AuNR aggregation in the 17 kg/mol PMMA matrix is noticeably less than for the HNRs. Therefore, a quantitative method to identify the conditions of AuNR dispersion is important.

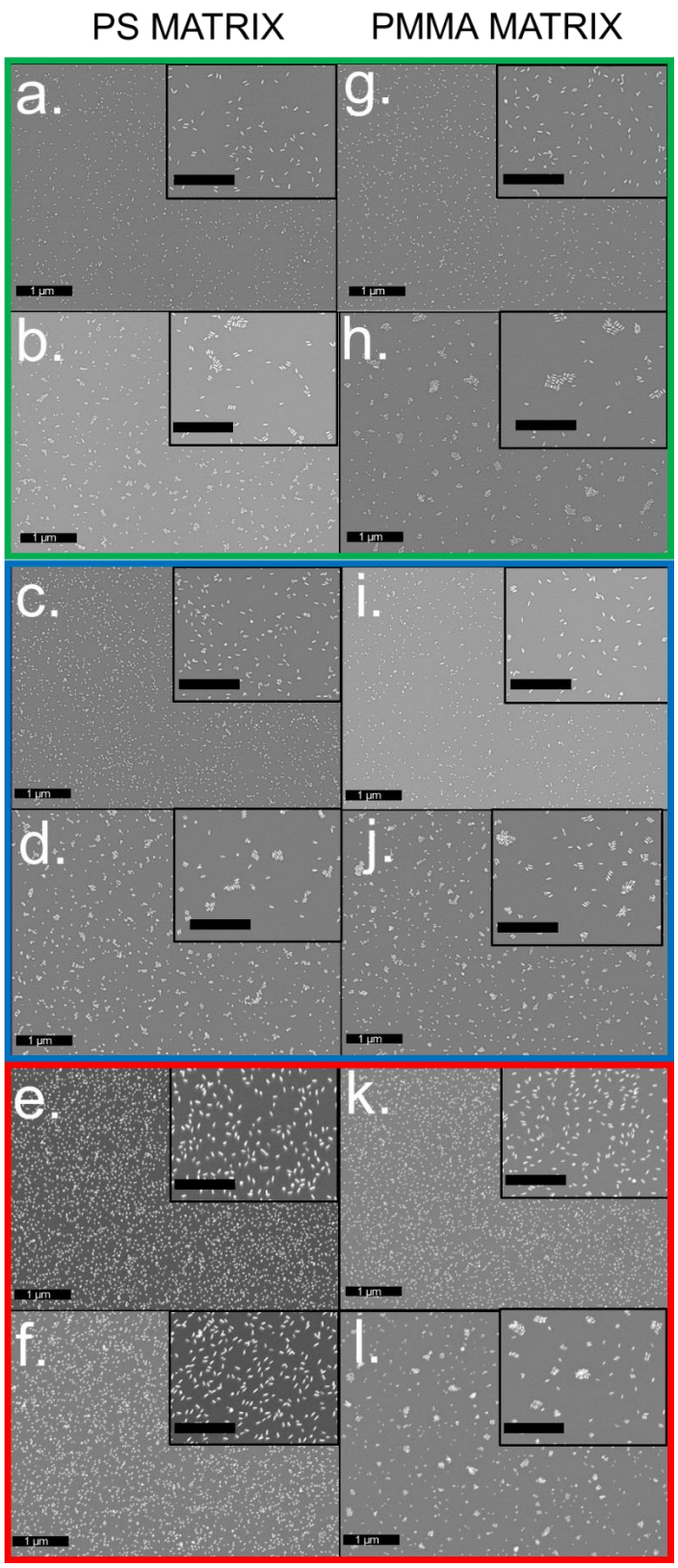
PS MATRIX
PMMA MATRIX
a.
g.
b.
h.
c.
i.
d.
j.
e.
k.
f.
l.

Figure 7.4 SEM images of AuNR systems in various polymer matrices. The left column (a-f) are AuNRs in PS matrices, while the right column (g-l) are AuNRs in PMMA matrices. For each AuNR system, the lowest (1.7 kg/mol for PS, 1.1 kg/mol for PMMA) and highest (270 kg/mol for PS, 336 kg/mol for PMMA) matrix M_n are presented. The images demarcated by green are for the HNRs system, by blue are the BNRs system, and by red are the MBNRs system. In PS matrices, the HNRs and BNRs go from dispersed to aggregated as the matrix M_n is changed from low to high (a to b and c to d, respectively), whereas the MBNRs remain dispersed even at high M_n (compare e and f). In PMMA, all systems behave similarly and aggregate as the matrix M_n is changed from low to high (compare g to h, i to j, and k to l). Inset scale bars are 500 nm.

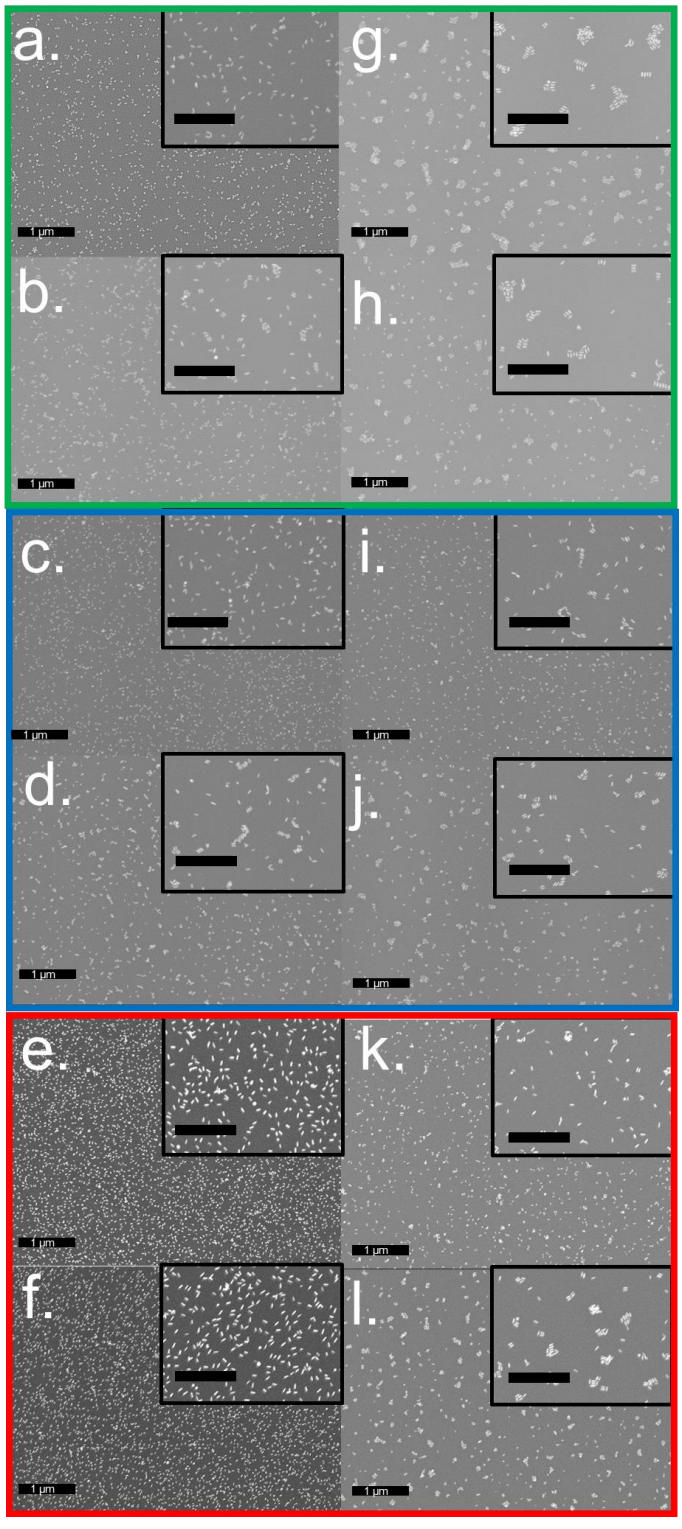
a.
g.
b.
h.
c.
i.
d.
j.
e.
k.
f.
l.

Figure 7.5 SEM images of HNRs (a,b, g,h), BNRs (c,d,i,j), and MBNRs (e,f,k,l) in PS (left column) and PMMA (right column). PS M_n = 5.78kg/mol (a,c,e) and 90 kg/mol (b,d,f). PMMA M_n = 17 kg/mol (g,i,k) and 77 kg/mol (h,j,l).

The dispersion state of the AuNR composites is quantified through cluster analysis of SEM images. A criteria for determining whether a system is dispersed or aggregated must be defined. Dispersion is quantified by analyzing the cluster size of the AuNRs in the polymer matrices. **Figure 7.6** plots the percentage of clusters that contains 1 through 8 plus AuNRs for each brush type, matrix type, and matrix M_n. From the cluster analysis, we define a "dispersed" (D) system as containing more than 80% individual AuNRs, a "semi-dispersed" (D/A) system as having between 60% and 80% individual AuNRs, and an "aggregated" (A) system as having less than 60% individual AuNRs. As an example, the percent of individual MBNRs in PMMA matrices with M_n = 1.1 kg/mol, 17 kg/mol, and 77 kg/mol are 90% (D), 73% (D/A), and 51% (A), respectively. For the PS matrices, the dispersion behavior of the HNRs (a) and BNRs (b) is similar; namely, for M_n = 5.78 kg/mol the individual AuNRs is 85%, whereas for M_n = 90 kg/mol , the percent decreases to 50% due to aggregation. For MBNRs (c), on the other hand, the percent of individual AuNRs is greater than 85% in all PS matrices. In the PMMA matrices, the HNRs (d) exhibit different behavior than the BNRs (e) and MBNRs (f). Specifically, HNRs aggregate much more strongly than the other systems in PMMA with M_n 17 kg/mol and above. In 17 kg/mol PMMA, individual HNRs decrease to 29% from 90% in 1.1 kg/mol PMMA, while individual BNRs and MBNRs decrease to only 72% and 73%, respectively, from 82% and 90%, respectively. The percentage of individual HNRs remain low in 77 kg/mol and 336

kg/mol PMMA at 15% and 24%, respectively. Again, BNRs and MBNRs, remain significantly more dispersed (still aggregated) than the HNRs in 77 kg/mol and 336 kg/mol PMMA at 54% and 58% individual HNRs, respectively, and 47% and 52% individual MBNRs, respectively. **Table 7.1** summarizes the dispersion states of all systems. To summarize, the HNRs and BNRs behave similarly in PS, while the MBNRs disperse very well in all M_n of PS. In PMMA, the BNRs and MBNRs behave similarly, while the HNRs aggregate very strongly. The dispersion behavior of these systems will be interpreted using self-consistent field theoretic (SCFT) calculations later in this paper.

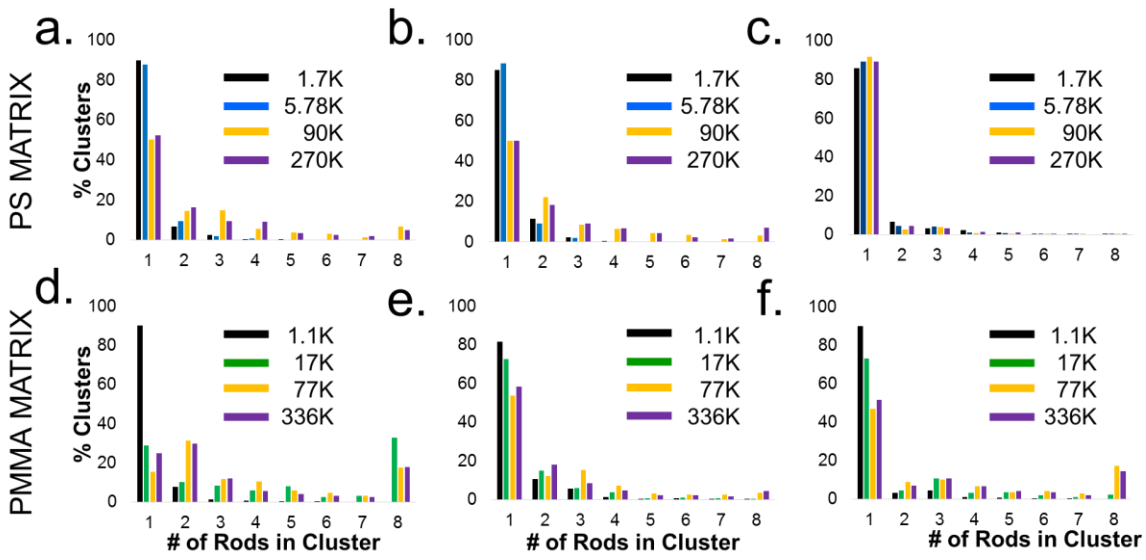

Figure 7.6 Cluster analysis for PS matrices (top row) containing HNRs (a), BNRs (b), and MBNRs (c) and for PMMA matrices (bottom row) containing HNRs (d), BNRs (e), and MBNRs (f). The HNRs and BNRs behave similarly in PS; at high matrix M_n both AuNR systems aggregated. However, the MBNRs remain highly dispersed. The BNRs and MBNRs behave similarly in PMMA; at higher matrix M_n the percent of individual AuNRs

decreases to *ca.* 50%. The HNRs strongly aggregate in PMMA with individual AuNRs making up only *ca.* 20% at higher matrix M_n.

Table 7.1 Summary of Dispersion States for Each System Studied

PS (M_n)	HNRs	BNRs	MBNRs
1.7 kg/mol	D	D	D
5.78 kg/mol	D	D	D
90K kg/mol	A	A	D
270 kg/mol	A	A	D

PMMA (M_n)	HNRs	BNRs	MBNRs
1.1 kg/mol	D	D	D
17 kg/mol	A	D/A	D/A
77 kg/mol	A	A	A
336 kg/mol	A	A	A

To further quantify the aggregated and dispersed states, the radial distribution function (RDF) was calculated for each system and can be found in **Figure 7.7**. For systems with dispersed AuNRs, g(r) quickly goes to 1 over a short distance, indicating that the AuNRs are uncorrelated. For systems with aggregated AuNRs, g(r) peaks at distances commensurate with multiples of AuNR lengths or diameters. For example, the HNRs in PS have peaks in g(r) at *ca.* 21 nm (MBNR diameter + 6.5 nm) and 37 nm (MBNR length), and 40 nm (2x MBNR diameter + 11 nm). The BNRs come a bit closer and have peaks consistent with a rod-rod separation distance of 4 nm (*i.e.* MBNR diameter + 4 nm). In PMMA, all aggregated systems have inter-rod separation distances of about 4 nm.

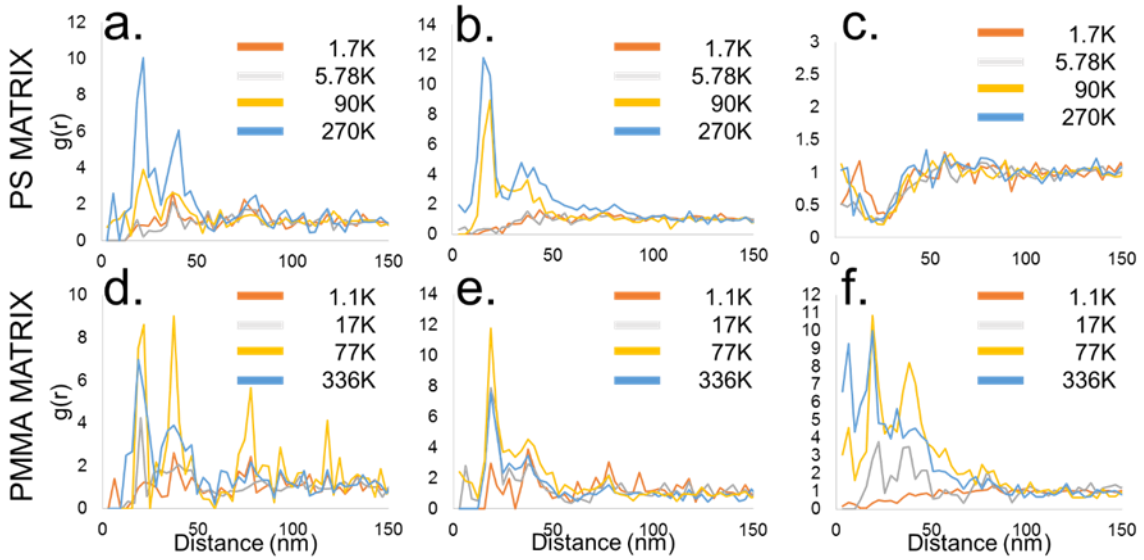

Figure 7.7 Radial distribution function (RDF) for HNRs (a,d), BNRs (b, e), and MBNRs (c,f) in PS (top row) and PMMA (bottom row). The g(r) goes to 1 for samples that are well-dispersed (e.g. c, or low M_n samples). When the AuNRs aggregate, g(r) spikes at distances commensurate with AuNR separation distances.

Absorbance spectra of all AuNR systems were acquired to investigate the correlation between optical properties and dispersion AuNRs. The absorbance of cast AuNR / polymer films represents the macroscopic average dispersion state of the AuNRs. **Figure 7.8** shows the absorbance spectra for all three AuNR brush types of films with the lowest and highest M_n for PS (top row), namely 1.7 kg/mol and 270 kg/mol , and PMMA (bottom row), namely 1.1 kg/mol and 336 kg/mol. The LSPR peak position for the HNRs in 1.7 kg/mol PS is at 757 nm, while in 270 kg/mol PS the LSPR peak position is located at 739 nm and broader than the 1.7 kg/mol case (a). The hypsochromic shift in the LSPR peak is consistent with aggregation and similar to what we have observed in similar systems in previous experiments.(Hore and Composto 2010) The LSPR peak for the BNRs system undergoes

a hypsochromic shift from 748 nm 718 nm upon increasing the Mn of PS from 1.7 kg/mol to 270 kg/mol (b). However, the LSPR peak for the MBNRs undergoes essentially no shift as M_n increases from 1.7 kg/mol PS to 270 kg/mol PS (c) with LSPR peak positions at 768 nm and 769 nm, respectively. The lack of LSPR peak shift observed in the MBNRs system is consistent with the good dispersion of AuNRs shown in SEM (*c.f.* **Figure 7.4**f). In PMMA, all systems undergo a hyspochromic shift and broadening in the LSPR peak between 1.1 kg/mol PMMA and 336 kg/mol PMMA, indicative of aggregation. The LSPR peak for HNRs (d) shifts from 740 nm to 703 nm, the LSPR peak for BNRs (e) shifts from 740 nm to 702 nm, and the LSPR peak for MBNRs (f) shifts from 734 nm to 709 nm upon increasing from 1.1 kg/mol PMMA to 336 kg/mol PMMA. **Table 7.2** summarizes the LSPR peak positions for the systems mentioned above. So far then, we have shown that the dispersion of the MBNRs is drastically different from the dispersion of HNRs and BNRs in homopolymer matrices.

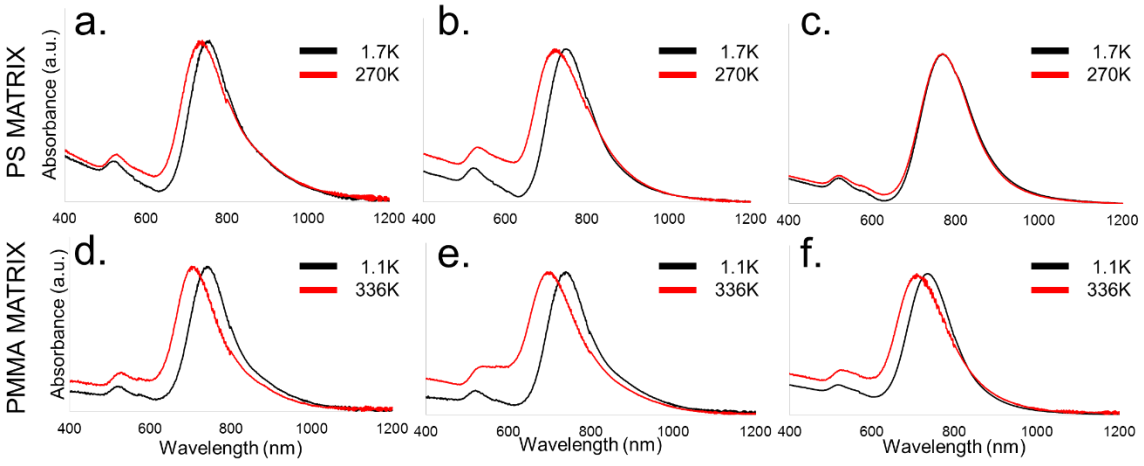

Figure 7.8 Absorbance spectra of AuNR systems taken in PS (top row) at M_n 1.7 kg/mol (black) and 270K and in PMMA (bottom row) at M_n 1.1 kg/mol and 336 kg/mol . In PS,

the LSPR peak for HNRs (a) and BNRs (b) undergoes a hyspochromic shift as M_n increases from 1.7 kg/mol to 270 kg/mol. No shift is evident in the LSPR peak for MBNRs (c), consistent with good dispersion in both systems. In PMMA, there is a hypsochromic shift in the LSPR for the HNRs (d), BNRs (e), and MBNRs (f) as M_n increases from 1.1 kg/mol to 336 kg/mol, consistent with aggregation.

Table 7.2 Summary of LSPR Peak Position for Each System Studied

MATRIX	HNRs	BNRs	MBNRS
1.7K PS	757	748	768
270K PS	739	718	769
1.1K PMMA	740	740	734
336K PMMA	703	702	709

The experiments so far have shown the tendency for MBNRs to disperse well at high matrix M_n PS, but still aggregate in PMMA at higher matrix M_n presumably due to the unfavorable enthalpic interactions between the PMMA matrix and the long PS brush. We should therefore expect a symmetric behavior where NRs grafted with long PMMA brushes and short PS will disperse in a PMMA matrix and aggregate in a PS matrix. To test this hypothesis, 15 kg/mol PMMA and 5.3 kg/mol PS brushes were grafted to AuNRs (denoted as reversed MBNRs or RMBNRs) which were then dispersed in the same PS and PMMA matrices as before. SEM images of PS and PMMA matrices at low and high M_n can be seen in **Figure 7.9**. The RMBNRs dispersed at all PMMA matrix M_n, whereas they aggregated in all PS matrices. Qualitatively, the dispersion of RMBNRs in all cases was not as good as in the MBNRs case because the RMBNRs / matrix films had to be cast from

methyl ethyl ketone (MEK). This point is explained in the experimental section. Cluster analysis was performed on the samples as in the case of the other AuNR systems. The cluster analysis confirms that for the RMBNRs in PMMA at low and high M_n that the RMBNRs are on the border between semi-dispersed and dispersed with individual AuNR percentage of 75% and 77%, respectively. For the PS matrix, the cluster analysis yields individual RMBNRs at 65% and 54% for the 1.7 kg/mol PS and 270 kg/mol PS matrices, respectively. Therefore, the trend is similar to the MBNRs system.

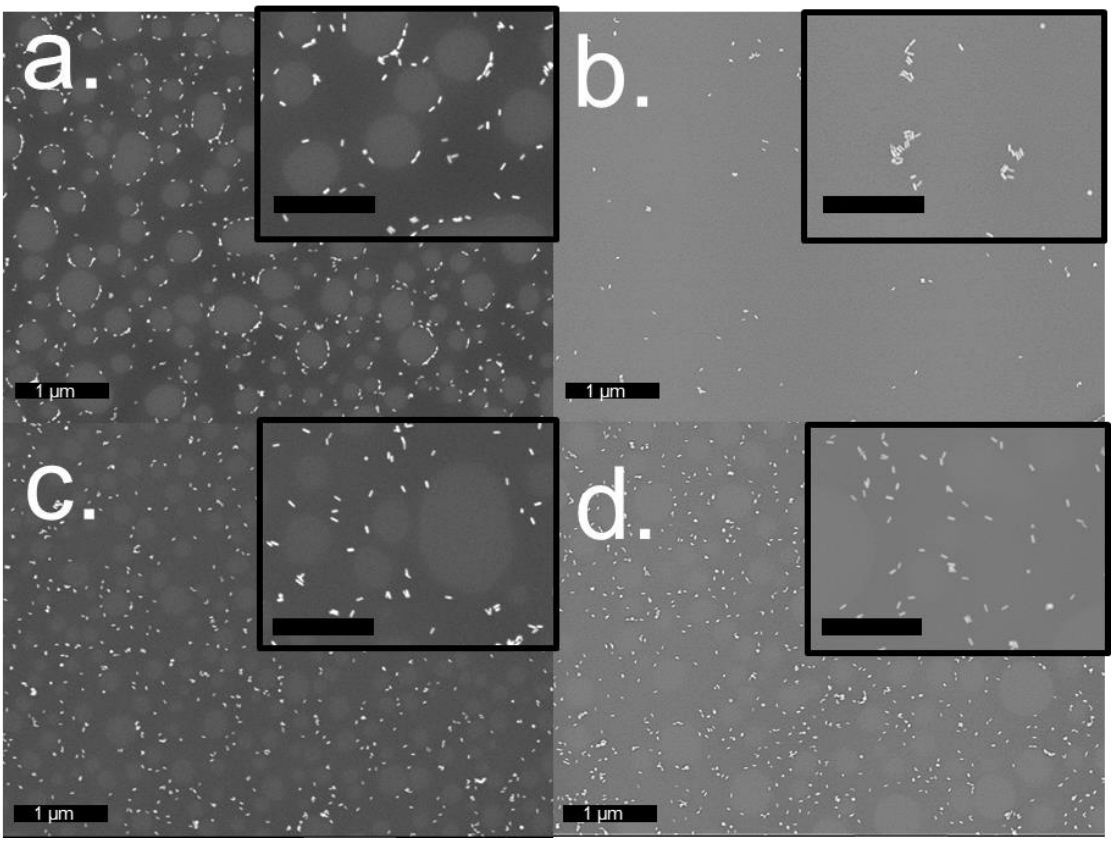

Figure 7.9 AuNRs grafted with 15 kg/mol PMMA and 5.3 kg/mol PS in PS (top row) and PMMA matrices (bottom row). In PS M_n = 1.7 kg/mol (a), AuNRs are between dispersed in aggregated, while in PS M_n = 270 kg/mol (b) the AuNRs are aggregated. In both PMMA

M_n = 1.1 kg/mol (c) and 336 kg/mol (d) the AuNRs are dispersed. The films in all cases were of poorer quality than the films prepared in the main text due to the necessity of casting them from methyl ethyl ketone. This probably leads to worse dispersion in all cases.

7.5.2 Effect of Brush Length on Dispersion of MBNRs in Polymer Thin Films

For the MBNRs, the PS brush M_n was varied to investigate the effect of brush length on the AuNR dispersion. AuNRs were grafted with 5.3 kg/mol PS and 5 kg/mol PMMA brushes (medium MBNRs or M-MBNRs) or 3 kg/mol PS and 5 kg/mol PMMA brushes (small MBNR or S-MBNRs). M-MBNRs and S-MBNRs were characterized by SEM and UV/vis spectroscopy. **Figure 7.10** contains representative SEM image and absorbance spectrum of M-MBNRs (a) and S-MBNRs (b). The LSPR peak position was 753 nm for M-MBNRs and 750 nm for S-MBNRs, similar to the LSPR peak for MBNRs of 753 nm. Both AuNRs are prepared from the same batch as the MBNRs and are, therefore, 43.8 +/- 6.6 nm in length and 15.5 +/- 4.4 nm in diameter.

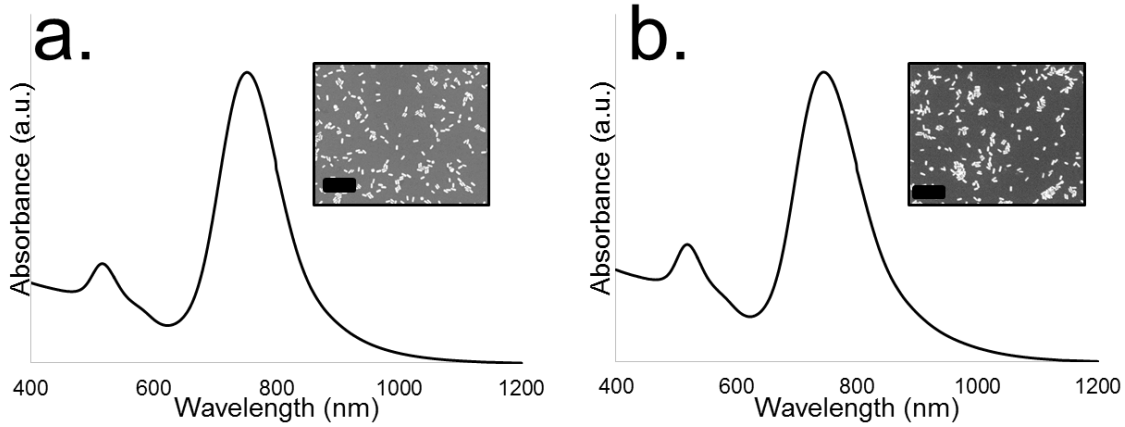

Figure 7.10 Absorbance spectra (in toluene) and SEM images of M-MBNRs (a) and S-MBNRs (b). The LSPR peak position for the M-MBNRs is 753 nm, while the LSPR peak position for S-MBNRs is 750 nm. Inset scale bars are 200 nm.

M-MBNRs and S-MBNRs were cast in polymer thin films to study their dispersion. **Figure 7.11** contains SEM images of the M-MBNRs and S-MBNRs in low and high M_n PS (left column), namely 1.7 kg/mol (a,c) and 270 kg/mol (b,d), and PMMA (right column), namely 1.1 kg/mol (e,g) and 336 kg/mol (f,h). Images pertaining to the M-MBNRs are demarcated by orange while those related to the SMBNRs are surrounded by purple. The M-MBNRs appear to be well dispersed for all PS matrix M_n, while the S-MBNRs appear to be aggregated for all PS matrix M_n. In PMMA, M-MBNRs appear to be well-dispersed in the 1.1kg/mol PMMA matrix, but appear aggregated in the higher M_n PMMA matrix. The S-MBNRs appear aggregated in all PMMA matrices.

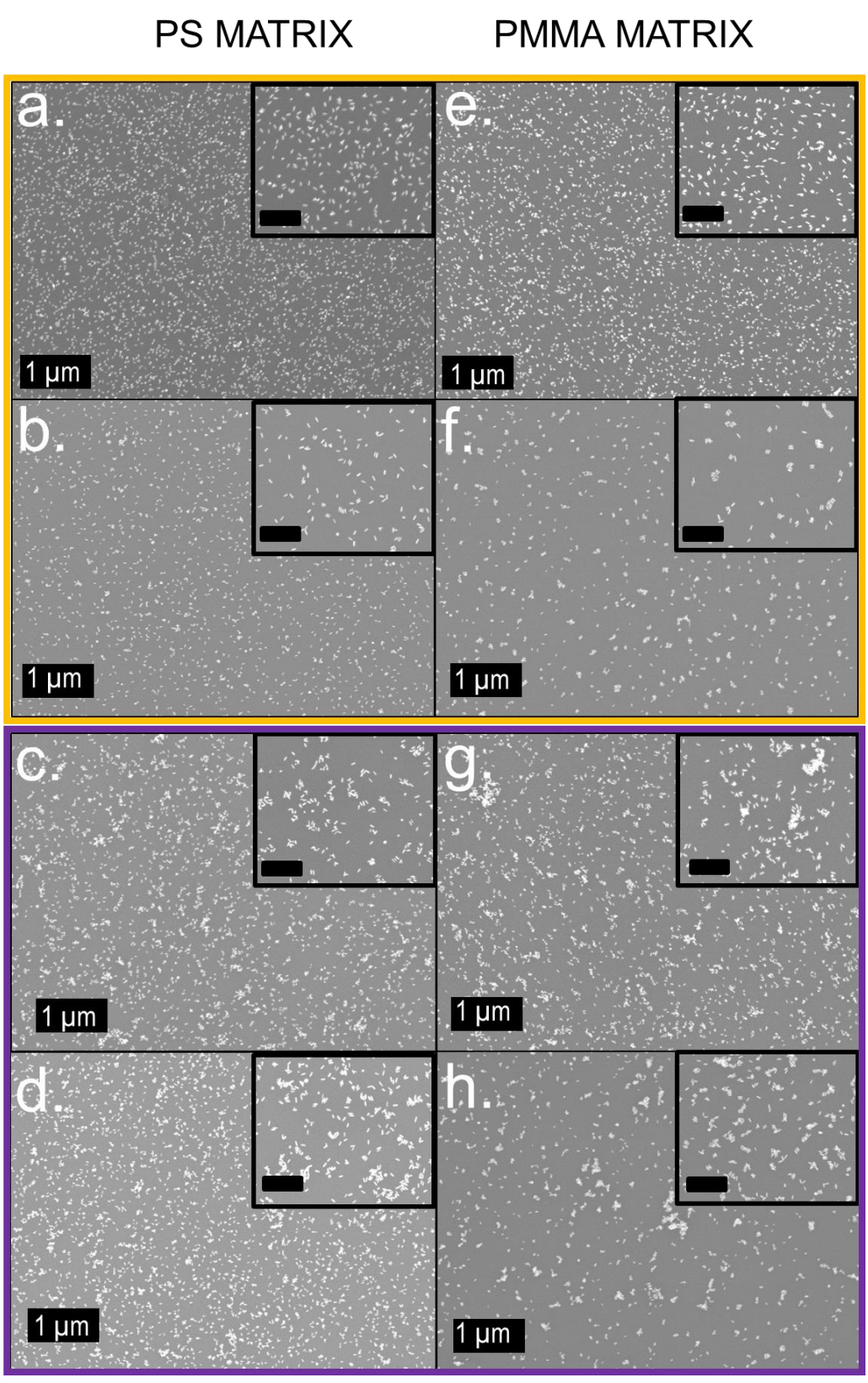
PS MATRIX
PMMA MATRIX
a.
e.
1 µm
1 µm
b.
f.
1 µm
1 µm
c.
g.
1 µm
1 µm
d.
h.
1 µm
1 µm

Figure 7.11 SEM images of AuNR systems in various polymer matrices. The left column (a-d) are AuNRs in PS matrices, while the right column (e-h) are AuNRs in PMMA matrices. For each AuNR system, the lowest (1.7 kg/mol for PS, 1.1 kg/mol for PMMA) and highest (270 kg/mol for PS, 336 kg/mol for PMMA) matrix M_n are presented. The images demarcated by orange are for the M-MBNRs system and by purple are the S-MBNRs system. In PS matrices, the M-MBNRs remain relatively dispersed between the 1.7 kg/mol (a) and 270 kg/mol (b) PS matrices, while the S-MBNRs show poor dispersion in both the 1.7 kg/mol (c) and 270 kg/mol (d) PS matrices. In PMMA matrices, the M-MBNRs go from dispersed in 1.1 kg/mol (e) to aggregated in 336 kg/mol PMMA, while the S-MBNRs remain poorly dispersed in both 1.1 kg/mol (g) and 336 kg/mol (h) PMMA. Inset scale-bars are 200 nm.

To verify the dispersion state of the M-MBNRs and S-MBNRs in polymer matrices, cluster analysis was performed on SEM images. **Figure 7.12** is the cluster analysis for both M-MBNRs and SMBNRs in all matrices. MMBNRs are dispersed in PS matrices (a). Individual M-MBNRs account for 86% 82% 84% and 77% of the AuNRs in 1.7 kg/mol, 5.78 kg/mol , 90 kg/mol , and 270 kg/mol , respectively. A juxtaposition of the cluster analysis of MBNRs (*c.f.* **Figure 7.6c**) and M-MBNRs in PS reveals that the M-MBNRs are more aggregated than the MBNRs case especially at high PS matrix M_n (*i.e.* 90 kg/mol and 270 kg/mol). M-MBNRs are generally aggregated in PMMA matrices. Individual M-MBNRs account for 80% AuNRs in 1.1 kg/mol PMMA, but this number significantly decreases to 52% in 17 kg/mol PMMA, finally reaching a nadir of 45% in 77 kg/mol PMMA and 336 kg/mol PMMA. The M-MBNRs disperse slightly more poorly than the

MBNRs in both PS and PMMA, but behave qualitatively similar. The S-MBNRs display relatively poor dispersion in all matrices compared with the M-MBNRs. The percent of individual S-MBNRs monotonically decreases from 73% to 57% as the PS M_n is increased from 1.7 kg/mol to 270 kg/mol. S-MBNR dispersion in PMMA is also poor. In a 1.1 kg/mol PMMA matrix, individual S-MBNRs account for 67% of the clusters, which quickly decreases to 53% in 17 kg/mol PMMA and then remains roughly constant for 77 kg/mol (55%) and 336 kg/mol (50%) matrices. The dispersion results for S-MBNRs and M-MBNRs are summarized in **Table 7.3**.

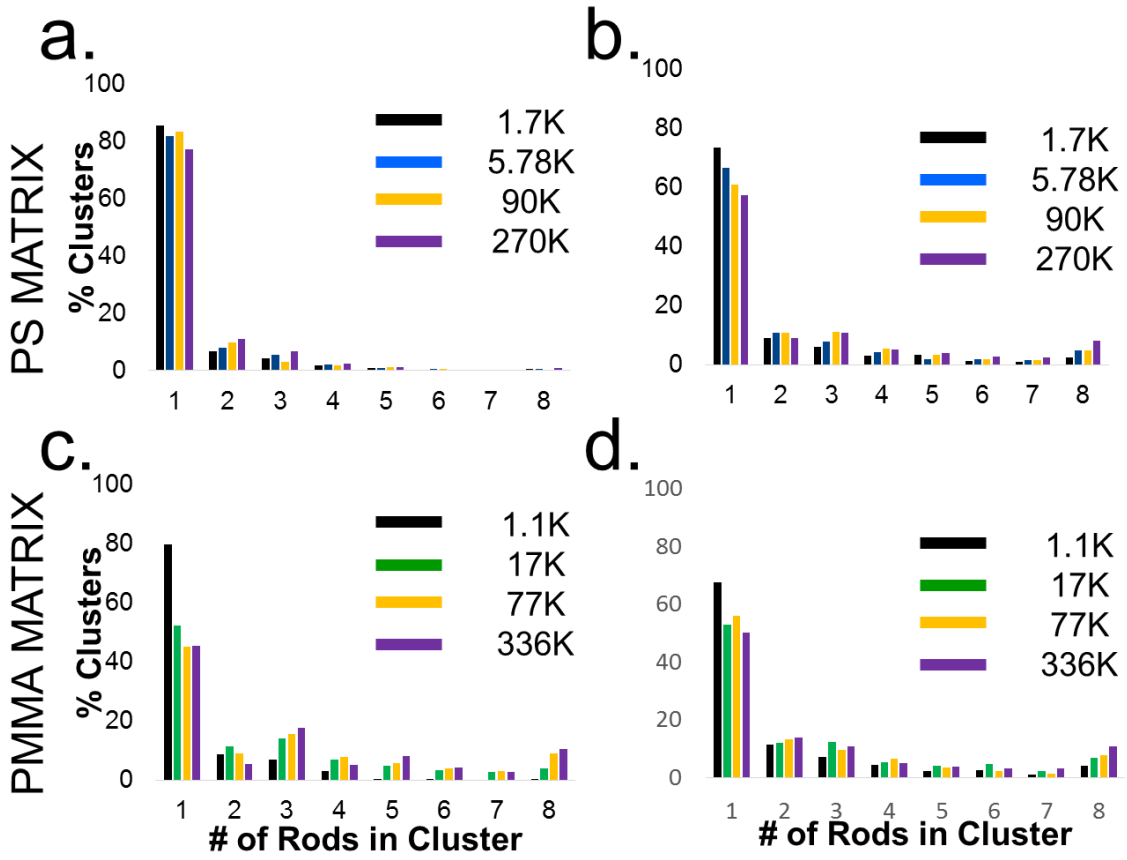

Figure 7.12 Cluster analysis in PS (top row) and PMMA (bottom row) matrices for M-MBNRs (a,c) and S-MBNRs (b,d). The MMBNRs show similar dispersion across all PS

(a) matrix M_n, while in PMMA (c) they aggregate at higher PMMA M_n. The SMBNRs display poor dispersion in both PS (b) and PMMA (d), where the percent of individual S-MBNRs decreases monotonically as M_n is increased.

Table 7.3 Summary of Dispersion State for M-MBNRs and S-MBNRs

PS (M_n)	M-MBNRs	S-MBNRs
1.7 kg/mol	D	D/A
5.78 kg/mol	D	D/A
90 kg/mol	D	A
270 kg/mol	D/A	A

PMMA (M_n)	M-MBNRs	S-MBNRs
1.1 kg/mol	D	D/A
17 kg/mol	A	A
77 kg/mol	A	A
336 kg/mol	A	A

The cluster analysis results are supported by UV/vis spectroscopy. **Figure 7.13** is the absorbance spectra of M-MBNRs in 1.7 kg/mol and 270 kg/mol PS (a) and 1.1 kg/mol and 336 kg/mol PMMA (c), and S-MBNRs in 1.7 kg/mol and 270 kg/mol PS (b) and 1.1K and 336 kg/mol PMMA (d). The LSPR peak position of the S-MBNRs remains constant as the PS M_n increases. However, the LSPR peak is noticeably broader in the 270 kg/mol PS matrix as compared with the 1.7 kg/mol PS matrix. Similarly, in PMMA, the LSPR peak does not shift between 1.1 kg/mol PMMA and 336 kg/mol PMMA. However, the LSPR peak does broaden at 336 kg/mol PMMA, similar to the PS matrix case. The absence of a shift and the broadening in the LSPR peak as the PS and PMMA M_n increases indicates that the S-MBNRs are not moving from a dispersed to aggregated state like, say, BNRs in

PS (*c.f.* **Figure 7.8**b), but are, initially, already aggregated at low M_n, and increasingly aggregate at high M_n. Therefore, the LSPR peak broadens, but does not shift. The LSPR peak position for the M-MBNRs case in PS matrices shows no shift between the low and high PS matrix M_n, which is consistent with the M-MBNRs being dispersed in all PS matrices. The LSPR peak undergoes a hypsochromic shift from 742 nm to 708 nm as PMMA M_n increases from 1.1 kg/mol to 336 kg/mol, respectively, consistent with dispersion at low M_n and aggregation at high M_n. The LSPR peak positions for S-MBNRs and M-MBNRs are summarized in **Table 7.4**.

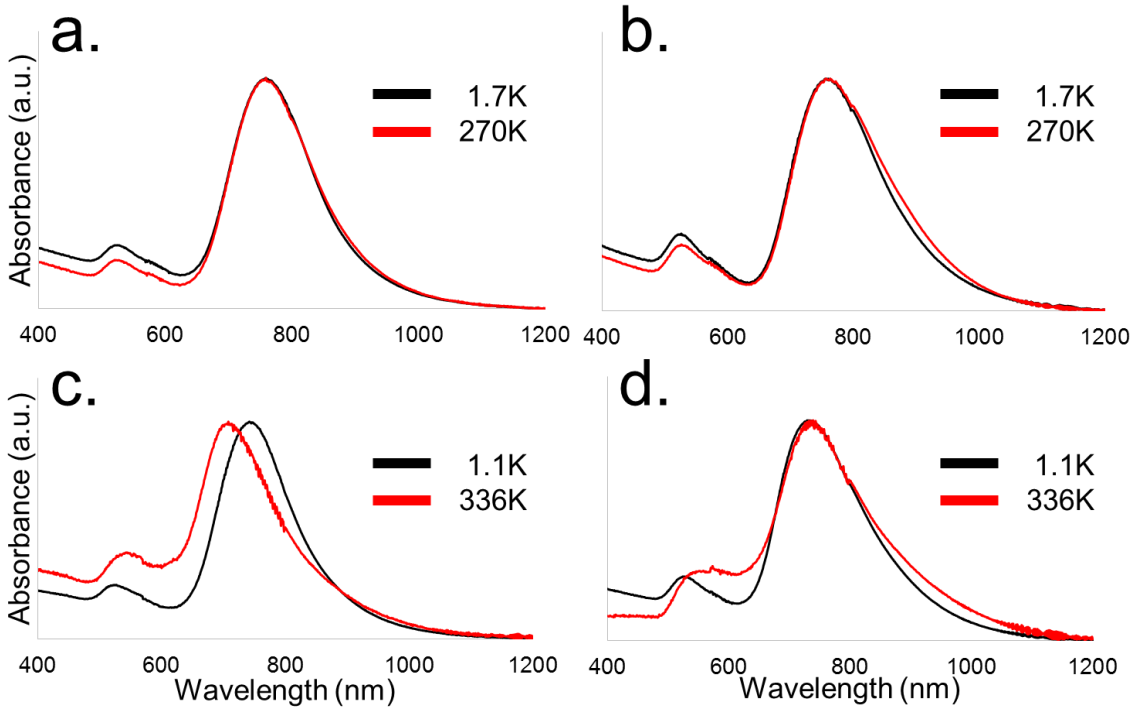

Figure 7.13 Absorbance spectra of M-MBNRs (a, c) and S-MBNRs (b,d) in PS (top row) and PMMA (bottom row). The LSPR peak does not shift at higher PS matrix M_n for M-MBNRs (a), consistent with good dispersion, but does undergo a hypsochromic shift at higher PMMA matrix M_n (c), consistent with aggregation. The LSPR peak does not shift

for S-MBNRs in either PS (b) or PMMA (d), but does broaden significantly suggesting the S-MBNRs begin poorly dispersed and aggregate more as matrix M_n is increased, resulting in broadening.

Table 7.4 Summary of LSPR Peak Position for M-MBNRs and S-MBNRs

MATRIX	M-MBNRs	S-MBNRs
1.7K PS	759	755
270K PS	759	756
1.1K PMMA	742	739
336K PMMA	708	739

7.5.3 Investigation of Dispersion Mechanism with Self-consistent Field Theory

Self-consistent field theory is used to elucidate the thermodynamic driving force that determines whether the AuNRs disperse in a homopolymer. Specifically, hSCFT was used to determine the potential of mean force (PMF) and brush profile for each AuNR brush and matrix condition. PMF calculations give insight into the relative strength of attraction between two parallel AuNRs in a polymer matrix while the brush profiles show the extent of stretching or collapse experience by the brush (or brushes) in the presence of matrix chains.

PMF calculations were performed on the systems studied experimentally. **Figure 7.14** shows the plots of free energy per unit length versus separation distance for HNRs (a,d), BNRs (b,e) and MBNRs (c,f) in PS (top row) and PMMA (bottom row). The PMF calculations in a PS matrix are qualitatively similar across all three NR systems. In each

case, the free energy per unit length is strictly positive at small P values, which indicates the AuNRs are dispersed, which is consistent with the observation that AuNRs disperse well in 1.7 kg/mol PS and 5.78 kg/mol PS. As P increases the AuNRs begin to come closer together, ultimately resulting in a small energy well of up to -0.5 kT per unit length for all graft structures at 90 kg/mol PS. Interestingly, the PMF does not explain why the HNRs and BNRs aggregated in the high PS M_n while the MBNRs remained dispersed. The MBNRs exhibit the best dispersion experimentally in PS. However, the PMFs indicate similar attractive wells for the MBNRs in comparison to BNRs at P = 90 kg/mol PS. The attractive well for the HNRs is at a greater distance simply due to there being more longer chains than in the BNRs or MBNRs. The potentials of mean force exhibit more prominent differences across the AuNR systems in PMMA matrices (d-f). Again, the free energy is positive at all separation distance for the small P case (P = 1.1k), which implies good dispersion and is consistent with all AuNR systems being well dispersed in 1.1 kg/mol PMMA experimentally. However, a deep free energy well rapidly develops as P increases for all systems. Interestingly, the free energy is more negative in the HNRs (d) case than in the BNRs (e) or MBNRs (f) cases. Specifically, at P = 77 kg/mol, the free energy reaches a nadir of nearly -6 kT per unit length for HNRs compared with only -5 kT per unit length for the BNRs and -4 kT per unit length for the MBNRs. Furthermore, the attractive well arises at a much greater separation distance in the HNRs as compared to the BNRs or MBNRs. This qualitatively mirrors the dispersion behavior of these three systems in PMMA experimentally; namely the HNRs aggregate significantly more than BNRs and MBNRs systems in PMMA (c.f. **Figure 7.6**d, e, and f).

The free energy per unit length landscape is drastically different for all AuNR systems in PMMA matrices (d-f). Again, the free energy is positive at all separation distance for P = 4, which implies good dispersion and is consistent with all AuNR systems being well dispersed in 1.1 kg/mol PMMA. However, a deep free energy well rapidly develops as P increases for all systems. Interestingly, the free energy is significantly more negative in the HNRs (d) case than in the BNRs (e) or MBNRs (f) cases. Specifically, at P = 128 (purple), the free energy reaches a nadir of approximately -11 kT per unit length for HNRs compared with only -5 kT per unit length for the other two cases. This qualitatively mirrors the dispersion behavior of these three systems in PMMA experimentally; namely the HNRs aggregate significantly more than BNRs and MBNRs systems in PMMA (*c.f.* Figure 7.6def). The distance at closest approach of the BNRs in PMMA at high P is 4 nm while it is *ca.* 3.5 nm for the BNRs and MBNRs. The distances are consistent with RDF analysis of the aggregated AuNRs systems which finds a separation distance of about 4 nm.

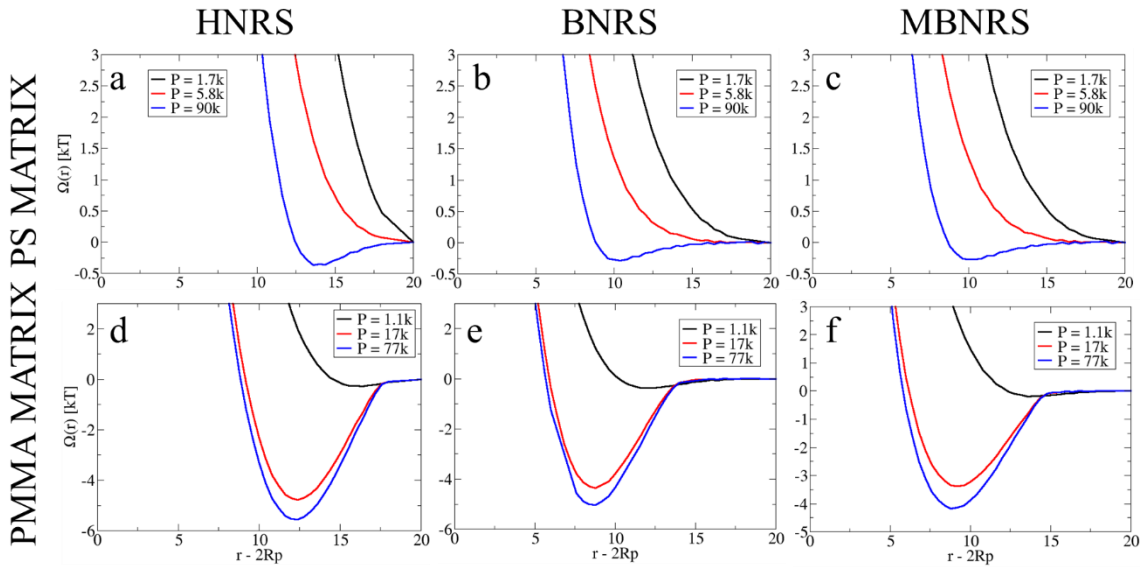

Figure 7.14 Free energy per unit length vs. separation distance in PS (top row) and PMMA (bottom row) for HNRs (a,d), BNRs (b,e), and MBNRs (c,f). For the HNRs, N = 11.5 kg/mol while for the BNRs and MBNRs, the long brush has an N = 11.5 kg/mol PS and the short brush has an N = 5.3 kg/mol PS (BNRs) or N = 5 kg/mol PMMA (MBNRs). Each curve on each plot corresponds to a different matrix chain size (P), namely P = 1.7 kg/mol (black), 5.8 kg/mol (red), and 90 kg/mol for the PS matrix calculations while P = 1.1 kg/mol (black), 17 kg/mol (red), and 77 kg/mol for the PMMA matrix calculations. In PS, HNRs (a), BNRs (b), MBNRs (c) display qualitatively similar behavior; as P is increased a free energy well is formed and deepens. However, the well is relatively shallow with a depth of up to *ca.* -0.5 kT. In PMMA, HNRs (d), BNRs (e), and MBNRs (f) all display deep wells as P is increased. However, the HNRs possess an energetic nadir of -6 kT per unit length that arises at a greater separation distance than that of BNRs and MBNRs, which have an energetic nadir of -5 and -4 kT per unit length, respectively.

Brush profile calculations were performed to further elucidate factors that could affect the dispersion state of the AuNR systems. **Figure 7.15** contains plots of total volume fraction versus distance from the AuNR surface. For HNRs (a) in PS (P = 1.7 kg/mol), the brush is well-extended into the matrix, whereas for PS (P = 90 kg/mol) the brush is significantly compressed. The brush compression is indicative of the matrix chains being expelled, which is associated with the depletion-attraction of the AuNRs and aggregation. Comparing the brush profiles for the BNRs (b) to the MBNRs (c) in PS matrix a qualitatively similar trend is observed; namely, the long grafted chain is very stretched for both systems for P = 1.7 kg/mol, extending well into the matrix. For P = 90 kg/mol, the

long brush is stretched but slight compressed in comparison to the case of P = 1.7 kg/mol. The total brush profile for both systems is almost identical at all cases. Comparing the brush profiles for both systems (*c.f.* **Figure 7.15b** and **Figure 7.15c**) reveals that the long brush is slightly more extended and the short brush is slightly more compressed in the MBNRs case as compared with the BNRs case. The additional compression of the short brush and extension of the long brush is based on the enthalpic penalty for collapse of the long PS brush due to increased contact with the short PMMA brush. While the longer chains are more extended and the short chains more compressed in the MBNRs over the BNRs, the subtle differences in the PMFs and brush profiles do not adequately explain the drastic difference in the aggregated and dispersed state of the AuNR at high M_n that is observed experimentally. This could be attributed to the 2D nature of the hSCFT calculations, disregarding many body effects, or through the use of a homogeneous grafting approximation. We suspect that the discrepancy is most likely due to our choice of holding the total grafting density constant for each NR design. Additionally, the hSCFT calculations assume that the ratio of short and long chains is the same in both the case of the BNRs and MBNRs. Lastly, the nature of hSCFT calculations provides only insight in the equilibrium state of the AuNRs and does not discern whether the experimental thin films are truly in an equilibrium or kinetically trapped state.

The grafted PS chains in every case are more compressed in PMMA (d-f) than in PS (a-c) in comparing the corresponding graft structure. The brush becomes extremely compressed in the case of the long PMMA matrix chain. For the BNRs (e) and MBNRs (f) systems in PMMA matrix, the long brush is quite extended into the matrix when P = 1.1 kg/mol, consistent with the dispersion observed experimentally. However, when P = 77

kg/mol, the long brush is significantly compressed which we suspect leads to the aggregation that is observed in the experiments. The total brush profile for the HNRs is more extended brush than for the BNRs and MBNRs in PMMA. This is consistent that the attractive well arising at a larger distance for the HNRs than in the BNRs or MBNRs and the observation that the HNRs aggregate to a larger extent than for the other two systems in PMMA.

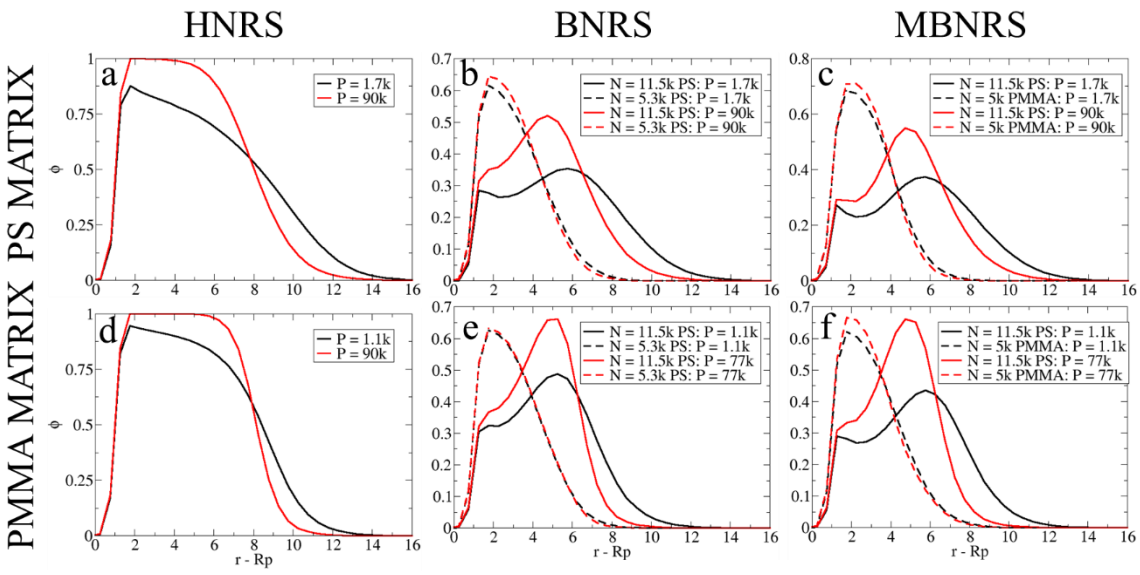

Figure 7.15 Brush profiles for HNRs (a,d), BNRs (b,e) and MBNRs (c,f) in PS (top row) and PMMA (bottom row). Each plot contains the brush profiles at two different P, namely P = 1.7 kg/mol (black) and 90 kg/mol (red) for the PS matrix and P = 1.1 kg/mol (black) and 77 kg/mol (red) for the PMMA matrix. For the HNRs, N = 11.5 kg/mol PS while for the BNRs and MBNRs, the long brush (solid) has a N = 11.5 kg/mol PS while the short brush (dashed) has a N = 5.3 kg/mol PS (BNRs) or N = 5 kg/mol (MBNRs). For HNRs, the brush is extended in P = 1.7 kg/mol PS, but is compressed in P = 90 kg/mol, while in PMMA P = 1.1 kg/mol the brush is more compressed than PS P = 1.7 kg/mol and is

extremely compressed when PMMA P = 77 kg/mol. The BNRs and MBNRs display similar brush behavior except that the short brush for MBNRs is significantly more compressed than the short brush for the BNRs, which is coupled with a slight extension of the long brush of the MBNRs compared to the BNRs.

PMF calculations were also performed on the m-MBNRs and s-MBNRs systems. In the model m-MBNRs and s-MBNRs systems the grafted PS chain length (N) is decreased from 11.5 kg.mol (Figures 10) to 5.3 kg/mol and 3 kg/mol, respectively. The PMMA N = 5 kg/mol in all cases (*i.e.* Figures 10c, 10f, and in Figure 11). **Figure 7.16** contains plots of the free energy per unit length vs. separation distance for m-MBNRs (a,c) and s-MBNRs (b,d) in PS (top row) and PMMA (bottom row). The free energy per unit length significantly decreases as P increases from 1.7 kg/mol to 90 kg/mol for m-MBNRs and s-MBNRs in PS. The deepest well is nearly -1.5 kT per unit length for m-MBNRs and -0.5 kT per unit length for s-MBNRs, both of which occur at P = 90 kg/mol. In PMMA, a similar trend is observed; the free energy is always positive for P = 1.1 kg/mol and then becomes negative (attractive) as P increases to 77 kg/mol with a nadir value of -1.0 kT per unit length for m-MBNRs and -0.5 kT per unit length for s-MBNRs, as shown in **Figure 7.16**c and **Figure 7.16**d, respectively.

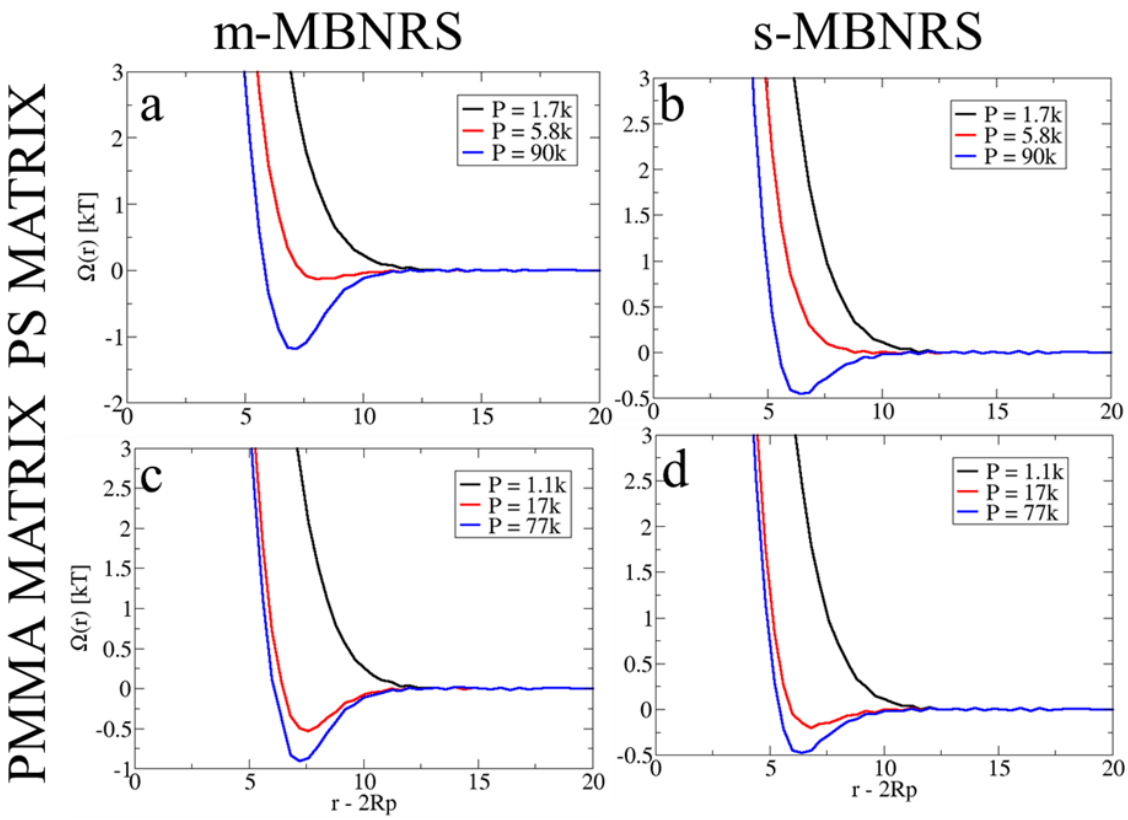

Figure 7.16 Free energy per unit length vs. separation distance plots for m-MBNRs (a,c) and s-MBNRs (b,d) in PS (top row) and PMMA (bottom row). The m-MBNRs have a PS N = 5.3 kg/mol while the s-MBNRs have a PS N = 3 kg/mol. In all cases, the PMMA N = 5 kg/mol. Each curve on each plot corresponds to a different matrix chain size (P), namely P = 1.7 kg/mol (black), 5.8 kg/mol (red), and 90 kg/mol (blue) for the PS matrix calculations while P = 1.1 kg/mol (black), 17 kg/mol (red), and 77 kg/mol (blue). m-MBNRs in PS (a) display a well depth inversely correlated to P; at high P the system achieves maximum well depth of nearly *ca.* -1.5 kT per unit length. The trend is the same in PMMA (c), but the well is a bit shallower at -1.0 kT per unit length. Similarly for s-MBNRs, in PS (b) and PMMA (d) the well depth increases with increasing P. The depth

of the well at high P is approximately -0.5 kT per unit length in both PS and PMMA matrices.

Brush profile calculations were performed to further elucidate factors that could affect the dispersion state of the m-MBNR and s-MBNR systems. **Figure 7.17**contains plots of the total volume fraction vs. distance for m-MBNRs (a, c) and s-MBNRs (b, d) in PS (top row) and PMMA (bottom row). Two matrix chain sizes were investigated for each system: P = 1.7 kg/mol and 90 kg/mol for the PS matrix and P = 1.1 kg/mol and 77 kg/mol for the PMMA matrix. For the m-MBNRs in PS with P = 1.7 kg/mol, the long brush (PS) and short brush (PMMA) are both extended. For P = 90 kg/mol, the long brush is slightly compressed, but generally extended while the short brush is compressed. The compression of the short brush and extension of the long brush could account for the good dispersion seen in the PS matrix for the m-MBNRs. In PMMA, both the long and short brush are well extended for P = 1.1 kg/mol while for P = 77 kg/mol the PS brush is quite compressed while the PMMA brush is slightly extended. For the s-MBNRs system, the brush profiles in PS and PMMA are similar. The overall narrow thickness of the brush and minimal extension is consistent with the experimentally observed aggregation across all matrix types and M_n.

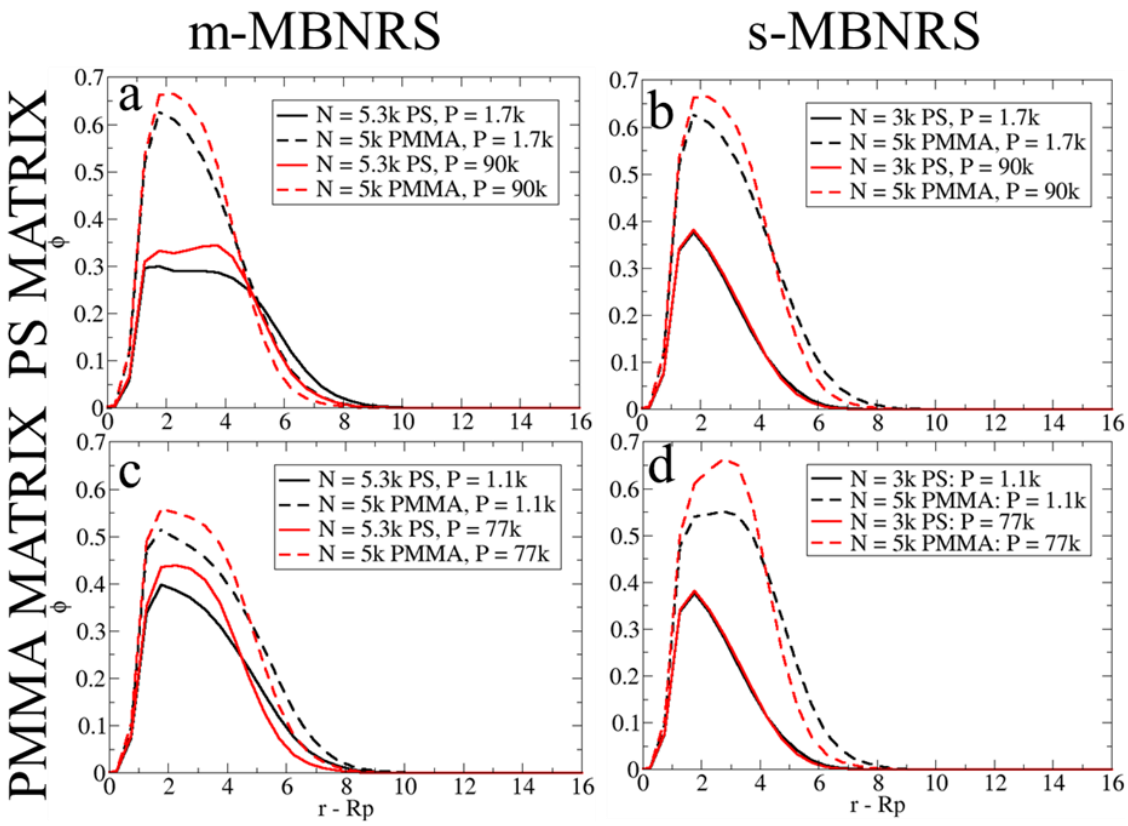

Figure 7.17 Brush profiles for m-MBNRs (a,c) and s-MBNRs (b,d) in PS (top row) and PMMA (bottom row). The m-MBNRs have a PS N = 5.3 kg/mol while the s-MBNRs have a PS N = 3 kg/mol. In all cases, the PMMA N = 5 kg/mol. The black curves represent either the case of P = 1.7 kg/mol (PS matrix) or 1.1 kg.mol (PMMA matrix) while the red curves represent the case of P = 90 kg/mol (PS matrix) or 77 kg/mol (PMMA matrix).

In every calculation shown thus far, χ, σ, and f_A remained constant. **Figure 7.18, Figure 7.19, and Figure 7.20**, show the role of χ, σ, and f_A on the PMFs and brush profiles in a P = 90kg/mol PS matrix. Increasing the χ between the short and long grafted chains leads to additional collapse of the short chains and additional extension of the longer chains, though the total brush profiles change minimally. The increase in χ also leads to almost no change

in the PMF calculations. The grafting density has a more prominent effect on both the brush profiles and the PMFs. As the grafting density is increased, the total brush profile extends further into the matrix and is reflected in the increased separation distance of the attractive wells that show up in the PMFs. Similarly, as the relative amount of long chains to short chains, f_A, is increased, the brushes once again extend further into the matrix and exhibit attractive wells in the PMFs at larger separation distances. The increase in grafting density or the relative amount of long to short chains leads to the short chains being completely shielded from the long chains as the particles approach one another. As a result, this leads to nearly no change between the case of $\chi = 0$ (BNRs) and $\chi = 0.15$ (MBNRs) in the total brush profile or PMF calculations at high σ, and f_A values. However, the additional collapse of the short chains and additional extension of the long chains remains consistent across all σ, and f_A values tested.

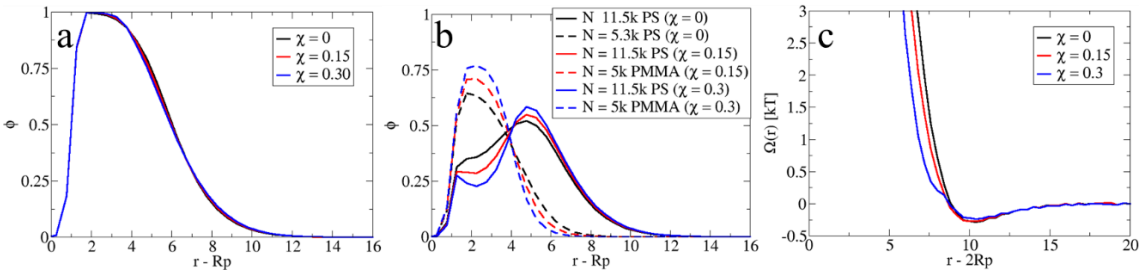

Figure 7.18 Effect of Chi on (a) total brush profile, (b) individual brush profiles, and (c) PMF calculations. P = 90 kg/mol PS while the longer graft chains have an N = 11.5 kg/mol PS and the short graft chains have an N = 5.3 kg/mol PS (χ, = 0) or N = 5 kg/mol PMMA ($\chi > 0$).

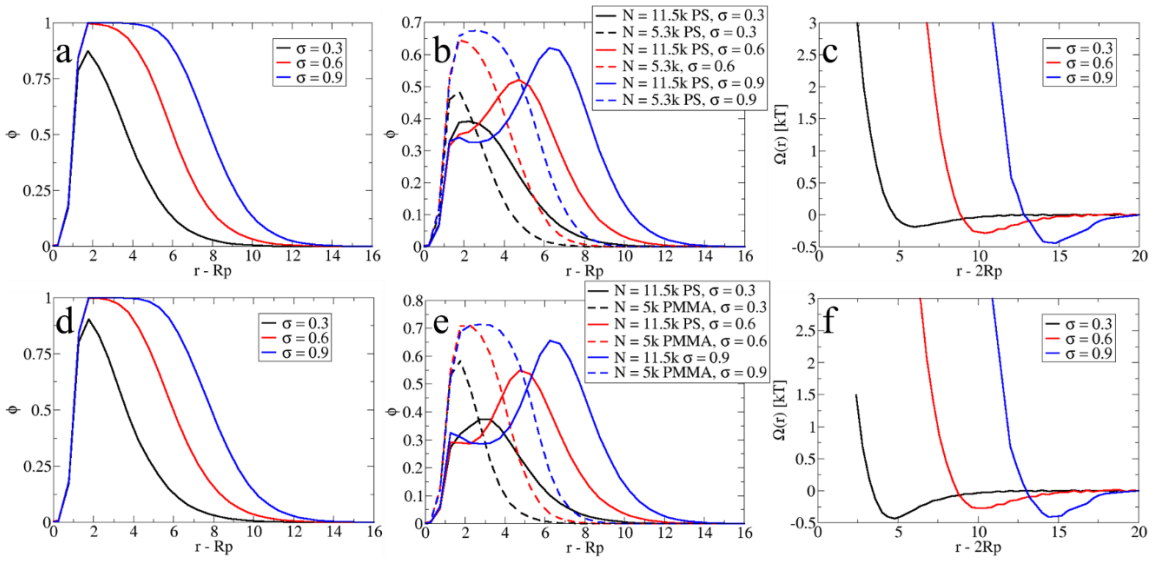

Figure 7.19 Effect of grafting density (σ) at χ of 0 (a-c) and 0.15 (d-f) on (a, d) total brush profiles, (b, e) individual brush profiles, and (c, f) PMF calculations. P = 90 kg/mol PS while the longer graft chains have an N = 11.5 kg/mol PS and the short graft chains have an N = 5.3 kg/mol PS (a-c) or N = 5 kg/mol PMMA (d-f).

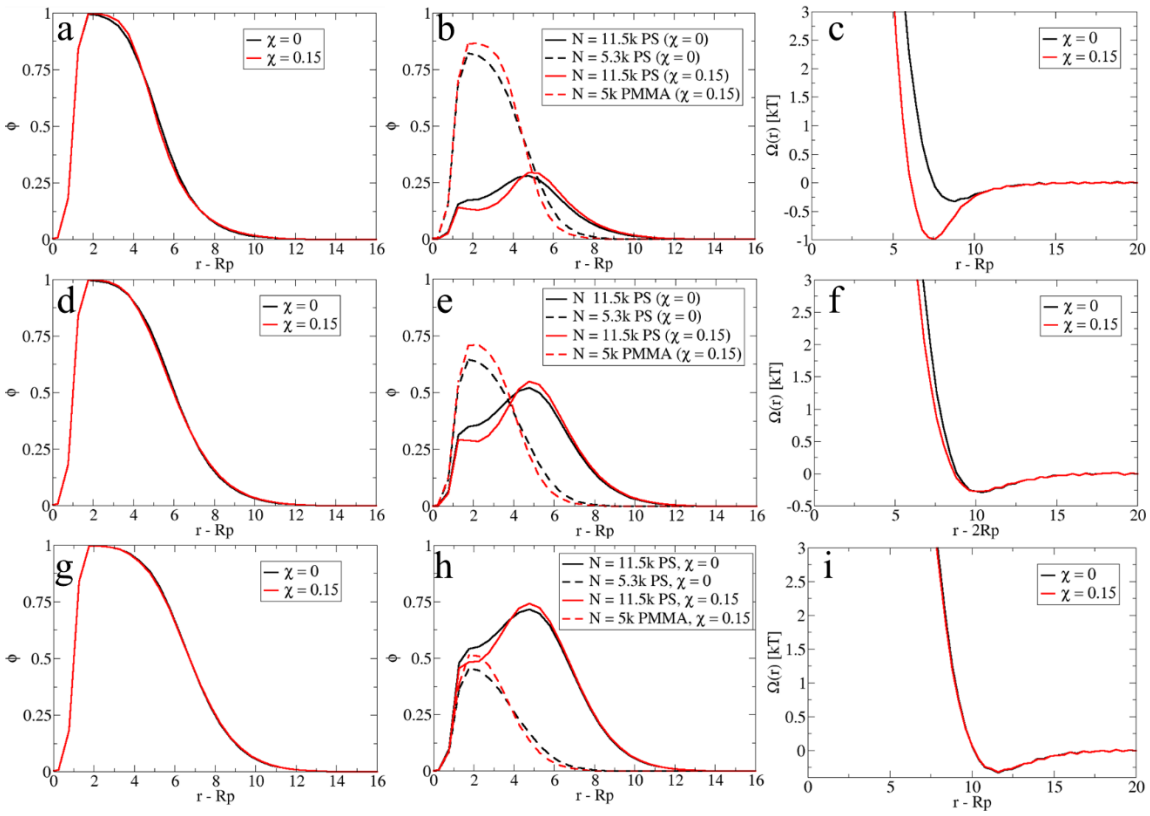

Figure 7.20 Effect of ratio of long to short chains (f_a) at different chi on (a, d, g) total brush profiles, (b, e, h) individual brush profiles, and (c, f, i) PMF calculations. f_a was chosen to be 0.2 (a-c), 0.4 (d-f), and 0.6 (g-i). P = 90 kg/mol PS while the longer graft chains have an N = 11.5 kg/mol PS and the short graft chains have an N = 5.3 kg/mol PS ($\chi = 0$) or N = 5 kg/mol PMMA ($\chi = 0.15$).

7.6 Conclusions

In this work, we have investigated the effect of brush type, brush M_n, matrix type, and matrix M_n on the dispersion of polymer grafted AuNRs. Specifically, we investigated HNRs, BNRs, and MBNRs. We found that the MBNRs dispersed much better and at higher matrix M_n in PS than the other two systems studied. In this case, the chemistry of the long

brush dictates the dispersion of the MBNRs; MBNRs with a long PS brush are well-dispersed in PS matrices, while MBNRs with a long PMMA brush are well-dispersed in PMMA matrices. The PS brush M_n was varied for the MBNRs to determine the effect on the dispersion. m-MBNRs disperse very well at high PS M_n, but not as well as the MBNRs. The s-MBNRs aggregated in every matrix due to the shortness of the brush.

SCFT calculations were performed to elucidate the thermodynamic mechanisms present that may lead to a particular dispersion state. We found that PMF calculations, which provided us with the free energy per unit length for each system, described the behavior of the AuNRs in PMMA qualitatively well, but did not well-describe the dispersion state of the MBNRs across all matrix lengths in PS. Brush profiles were utilized to investigate the behavior of the individual brushes on each AuNR system, where we found that in PS, there was additional extension of the long brush and additional compression of the short brush in the case of the MBNRs over the BNRs. However, the total brush profiles were similar and the discrepancies of the brush profiles did not lead to prominent differences in the PMF calculations. As a result, we hypothesize that the grafting density and the distribution of the chains on the surface of the AuNRs plays a prominent role in the improved dispersion from the BNRs to the MBNRs at high M_n observed experimentally. Finally, the SCFT calculations described the m-MBNRs similarly to the MBNRs; an extension of the PS brush and collapse of the PMMA brush allows for the dispersion of the m-MBNRs even at high PS M_n. For the s-MBNRs, the polymer shell encapsulating the rods is relatively small and the brush-matrix interactions do not play a large role in dispersion-aggregation mitigation. Polymer brushes that are chemically similar to the matrix have been commonly used to control dispersion by tuning the wet ($\alpha < 2$) and dry ($\alpha > 2$) brush state. Polydispersity

of these chemically similar brushes has also been used to enhance miscibility relative to the monodisperse case. The present work shows that chemically mixed brushes further expands the matrix systems that can be used to disperse AuNRs. This is important because it serves as an additional means to improving dispersion of nanoparticles within a polymer matrix and therefore allows for further tuning the controllability of the resulting material properties.

Chapter 8 Self-assembly and Actuation of Gold Nanorods in Liquid Crystals over Micropillar Arrays for Tunable Plasmon Resonance

In Collaboration with Dr. Elaine Lee and Yu Xia of Prof. Shu Yang's Group (Penn)

8.1 Abstract

Here we present a method to dynamically assemble gold nanorods in liquid crystals over micropillar arrays. Polystyrene-grafted gold nanorods (PS-AuNRs) are dispersed in a liquid crystal and the solution is placed between glass plates fabricated with epoxy pillars. The pillar geometry modulates liquid crystal defect structure. The defect structure is further controlled by tuning the temperature. As the liquid crystal / PS-AuNR solution is heated, defect rings shrink and the PS-AuNRs compress upon each other. This compression causes a hypsochromic shift in the absorbance of the system due to PS-AuNR aggregation. The absorbance changes by more than 100 nm across the temperature range investigated, an order of magnitude higher than other studies involving AuNRs and liquid crystals. The absorbance change is not present when the defect rings are not formed. Changing the aspect ratio of the pillars changes the defect ring structure formed which can be used to further tune the optical properties. Precise control over the surface properties of all the components in the system leads to reversible coupling of the PS-AuNRs and large plasmon peak shifts. This effect can be applied for enhanced and selective sensing applications.

8.2 Introduction

Control over the assembly of functional, nanostructured materials is imperative for the realization of novel nanodevices. Much work has focused on the assembly of metal-nanoparticles due to their applications in energy harvesting,(Karker, Dharmalingam et al. 2014) sensing,(Gormley, Chapman et al. 2014) metamaterials,(Young, Ross et al. 2014) and catalysis.(Zhou, Duan et al. 2014) Gold nanorods (AuNRs), in particular, have received considerable interest due to the facile synthesis of variable size and aspect ratios,(Nikoobakht and El-Sayed 2003, Sau and Murphy 2004) diverse chemistry for surface modification,(Nie, Fava et al. 2007, Sethi, Joung et al. 2009, Hore and Composto 2010, Zhao, Zhang et al. 2013, Ferrier, Lee et al. 2014) and anisotropic optical properties.(Funston, Novo et al. 2009) Collective oscillations of free electrons at the surface of metal nanoparticle surfaces interact with light to cause strong resonances in the optical region of the electromagnetic spectrum, known as localized surface plasmon resonance (LSPR). Owing to their shape, AuNRs have two such absorbance bands, a transverse mode and a longitudinal mode, which depend on the diameter and length of the AuNR, respectively. Furthermore, AuNRs have significantly enhanced electric fields near their tips, which make AuNRs attractive for use as a sensing platform based on surface enhanced Raman spectroscopy (SERS).(Nikoobakht and El-Sayed 2003, Qian, Li et al. 2009) However, in order to apply them for any optical device, it is essential to control the assemblies of AuNRs, and thus their optical properties.

The absorbance of AuNRs significantly changes when AuNRs come into close contact with each other due to plasmonic coupling. For instance, when two AuNRs come together side-by-side the absorbance band undergoes a hypsochromic (blue) shift, whereas when

two AuNRs come together end-to-end the absorbance band undergoes a bathochromic (red) shift.(Funston, Novo et al. 2009) The strength of the shift depends upon the number of AuNRs in the assembly and their spacing. AuNRs can be assembled in solutions in a controlled manner.(Nie, Fava et al. 2007, Sethi, Joung et al. 2009, Zhao, Zhang et al. 2013) However, solution assembly may not be desired in device fabrication. More recent work has shown controlled assemblies of AuNRs in polymer matrices,(Hore and Composto 2010, Ferrier, Lee et al. 2014) but the optical properties cannot be tuned once the films are cast. Therefore, a more dynamic approach, where AuNRs can be reversibly assembled and disassembled triggered by a specific stimulus, is attractive to realize the full potentials of AuNR-based nanodevices.

Liquid crystal (LC), an anisotropic soft matter, is one such promising candidate for the reversible tuning of the assemblies of AuNRs. The alignment of LCs can be controlled by surface chemistry, surface topography, or by external field. The coupling of the optical properties of AuNRs with the spontaneous order-disorder transitions of LCs upon triggering by external stimuli such as heat, light and electrical field will offer great capabilities for active plasmonic devices. This coupling can be achieved in several ways, including functionalization of AuNRs with liquid crystalline ligands, depositing an active LC layer over immobilized AuNRs, and simply mixing AuNRs with LCs. Umadevi *et al.* showed that AuNRs functionalized with a liquid crystalline ligand could be assembled into large scale aggregates with some ordering.(Umadevi, Feng et al. 2013) However, further manipulation and dynamic tuning of the optical properties was not shown. Several groups have shown that the optical properties of metallic particle arrays could be tuned by assembling LCs on top of them.(Dickson, Wurtz et al. 2008, Hsiao, Zheng et al. 2008, Hao,

Zhao et al. 2011, De Sio, Cunningham et al. 2012, De Sio, Klein et al. 2013) However, only a small shift of plasmon resonance peak (<50 nm) and a drop in peak intensity were observed upon application of an electric field. It is suggested that the change in optical properties is the result of change in the refractive index of the LC medium due, via changing the alignment of the LC molecules, rather than by the actuation of the active plasmonic particles. Liu *et al.* showed AuNRs could be directionally aligned in the nematic phase of a LC, leading to polarization-dependent optical properties of the AuNR/LC dispersion.(Liu, Tang et al. 2014, Liu, Yuan et al. 2014) However, the unique temperature-dependent properties of LCs were not further exploited to actuate the AuNRs. While these previous studies have shown the co-assembly of AuNRs and LCs, none have demonstrated direct manipulation of the optical responses of AuNRs by LC phase transitions.

Recent theoretical(Lopez-Leon, Fernandez-Nieves et al. 2011) and experimental(Senyuk, Evans et al. 2012) work has demonstrated the sequestration of individual AuNRs into the defects in ordered LC phases. However, the reversible clustering of nanoparticle ensembles to tune the plasmonic resonance has not been realized. In this work, we exploit the anisotropic thermal, optical and elastic properties of LCs to tune the clustering of AuNRs, and thereby modulating their plasmonic resonances. By exploiting the confinement of smectic-A LCs (SmA LCs) to topographically patterned pillars, we show that defects can be formed at precise locations around each pillar and tuned by varying the temperature of the system. When dispersing polystyrene (PS)-functionalized AuNRs into the LC prior to drop-casting onto the polymer pillar arrays, the AuNRs are spontaneously assembled into the defects surrounding pillars. The dimensions of the defect structure and consequently, the nanorod assembly can be altered by heating and cooling.

Accordingly, the plasmonic peaks shift with temperature. By optimizing the surface anchoring conditions (homeotropic vs. planar) and aspect ratio (AR = height/diameter) of the pillar arrays, we can maximize the plasmonic peak shift. For homeotropic anchoring epoxy pillars with an AR = 1.3, the transverse and longitudinal local surface plasmonic peak shift are ~100 and ~150 nm, respectively.

8.3 Experimental methods

8.3.1 Surface functionalization of gold nanorods with polystyrene

Three 40 mL solutions of cetyltrimethylammonium bromide (CTAB) coated AuNRs in deionized (DI) water were synthesized by a seed-mediated growth method as outlined elsewhere.(Nikoobakht and El-Sayed 2003, Sau and Murphy 2004, Ferrier, Lee et al. 2014) Excess CTAB was removed through two washing cycles consisting of centrifugation (20 min at 8,000 RPM, Eppendorf 5804) followed by replacement of the supernatant with approximately 40 mL of Milli-Q water. Following the washing steps, the three AuNR solutions were combined and concentrated in 40 mL of water, providing a stock solution of concentrated AuNRs.

The stock solution of AuNRs (9 mL, 0.4 nM) in DI water was centrifuged (20 min at 8,500 RPM, Eppendorf 5804) and the supernatant was removed so that there was only a small aliquot of concentrated AuNR solution. 30 mg of 5,300 g/mol thiol-terminated polystyrene (HSPS) (Polymer Source) was added to a solution of 10 mL THF until dissolved. Next, the AuNR aliquot was added to the THF/HSPS solution under stirring. The solution was stirred overnight and then solvent exchanged to chloroform twice to remove free HSPS. Finally, AuNRs were suspended in 1 mL of chloroform.

8.3.2 Substrate functionalization

To achieve planar anchoring, the epoxy pillars or glass cover slips were treated with UVO (Jelight, model 144AX) for 1 h and used immediately. For homeotropic anchoring substrates, silicon tetrachloride was evaporated onto the epoxy pillars or glass cover slips in a vacuum dessicator for 10 min.(Miguez, Tetreault et al. 2002) Then, the substrates were placed into a 65°C oven with water vapor for 10 min, forming a silica thin film. The substrates were then immersed into a 3 wt% ethanol solution of dimethyloctadecyl[3-(trimethoxysilyl)propyl]ammonium chloride (DMOAP) for 1 h. They were then washed with DI water 3 times and dried in a 100°C oven.

8.3.3 Assembly of gold nanorods in liquid crystals

4′-n-octyl-4-cyano-biphenyl (8CB) (Sigma Aldrich or Kingston Chemicals) was added to the chloroform solution of PS-AuNR and ultra-sonicated for dispersion. The chloroform was then evaporated using a vacuum oven at room temperature. The suspension was heated to 45°C (above the nematic-isotropic transition temperature, T_{NI}) and drop cast over the surface-treated epoxy pillars. A surface-treated glass cover slip was used to close the liquid crystal cell.

8.3.4 Characterization

Transmittance of the AuNR and PS-AuNR suspensions as synthesized were measured using the Cary 5000 UV-Vis-NIR spectrophotometer (Agilent Technologies). The LC cell was mounted on a Mettler FP82 hot stage equipped with FP 90 controller and heated at 45°C for 5 min to reach the isotropic group. It is then cooled down to 25°C at a rate of 10°C min^{-1} to form the smectic-A (SmA) phase. In parallel to the heating and cooling cycle, the LC textures were observed under the Olympus BX61 motorized optical

microscope with crossed polarizers using CellSens software. Alternatively, the transmission of the LC cell is measured using a custom-built spectrophotometer with a fiber-coupled tungsten-halogen light source and a USB4000 detector (Ocean Optics).

8.4 Optical properties of gold nanorods

The functionalization of the AuNRs with PS is detailed in **Figure 8.1a**. As-synthesized PS-AuNRs displayed two characteristic extinction bands at 512 nm (transverse band) and 727 nm (longitudinal band) in water, as can be seen in **Figure 8.1b**. The longitudinal band underwent a slight bathochromic (red) shift to 742 nm after AuNRs are functionalized with HSPS and solvent exchanged to chloroform, as seen in **Figure 8.1c**. Finally, PS-AuNRs were characterized via SEM (**Figure 8.1d**) with length of 31 ± 4 nm and diameter of 11.3 ± 1.5 nm.

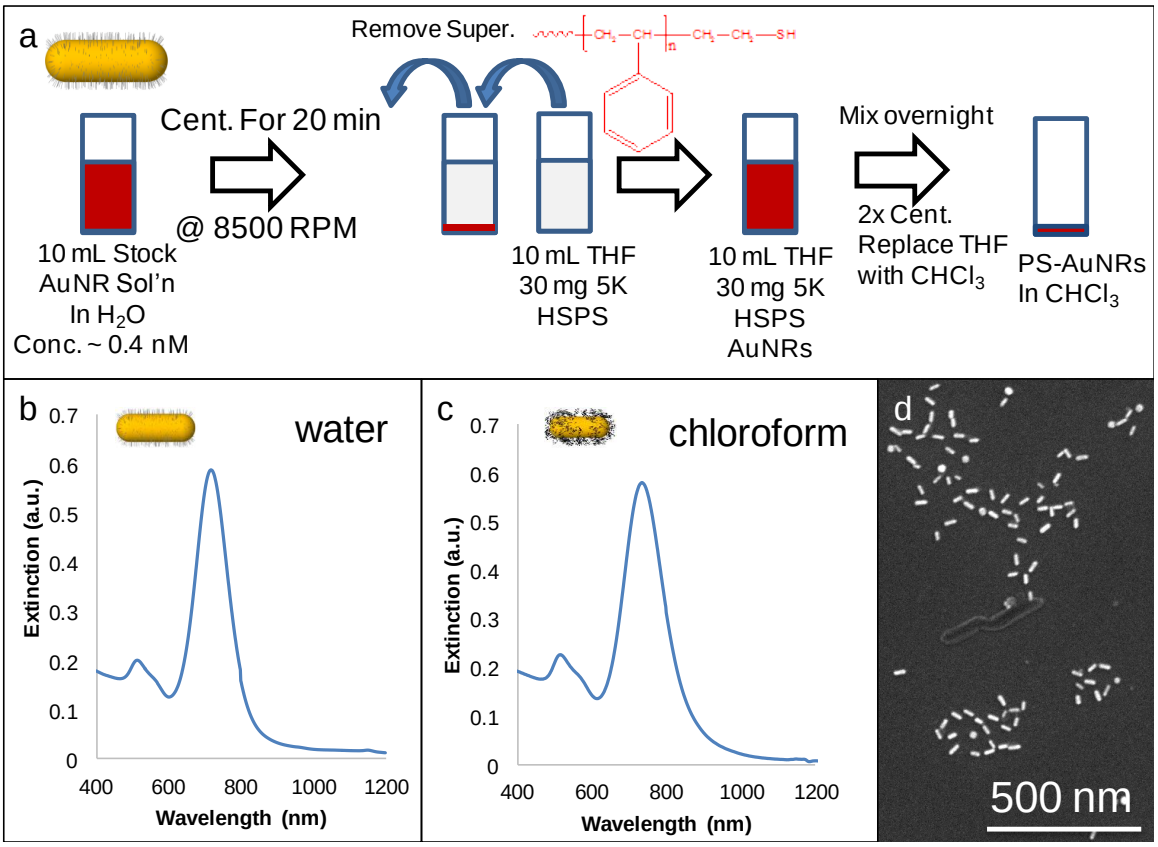

Figure 8.1 (a) Schematic detailing the functionalization of AuNRs with polystyrene brushes. (b-c) Extinction spectra of (b) AuNRs in water and (b) PS-AuNRs in chloroform. (d) SEM image of PS-AuNRs.

8.5 Control of liquid crystal surface anchoring

Square arrays of cylindrical epoxy micropillars (diameter = 10 μm, pitch = 20 μm) with various aspect ratios (=height/diameter 0.9, 1.3, and 1.6) were prepared by replica molding followed by surface functionalization to introduce different surface anchoring properties (**Figure 8.2a**). Homeotropic or planar anchoring was imposed on the surfaces of the pillars as well as the glass cover slip. PS-AuNRs dispersed in smectic-A LC, 4′-n-octyl-4-cyano-biphenyl (8CB), were sandwiched between the pillars and a glass cover slip to form a LC cell. The structure and phase transition temperatures of 8CB are shown in **Figure 8.2b**. The

cell was heated above the clearing temperature to the isotropic phase and subsequently cooled to the nematic phase.

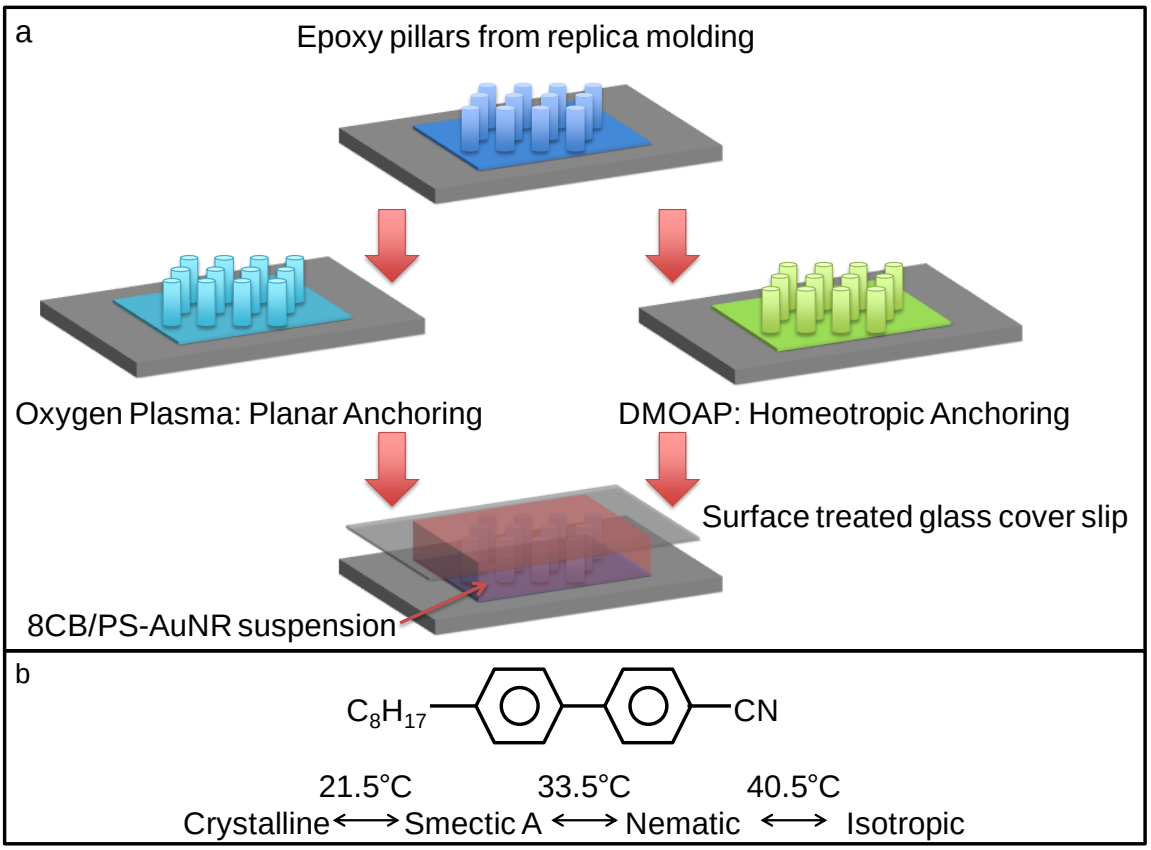

Figure 8.2 Schematic of the substrate functionalization.

When the homeotropic boundary conditions were imposed on the pillars and cover slip, distortions to the director field appeared in the form of bright lines encircling the micropillars when observed under crossed polarizers (**Figure 8.3**). Outside these bright lines, the entire region was dark even under sample rotation, due to complete homeotropic anchoring on all surfaces.

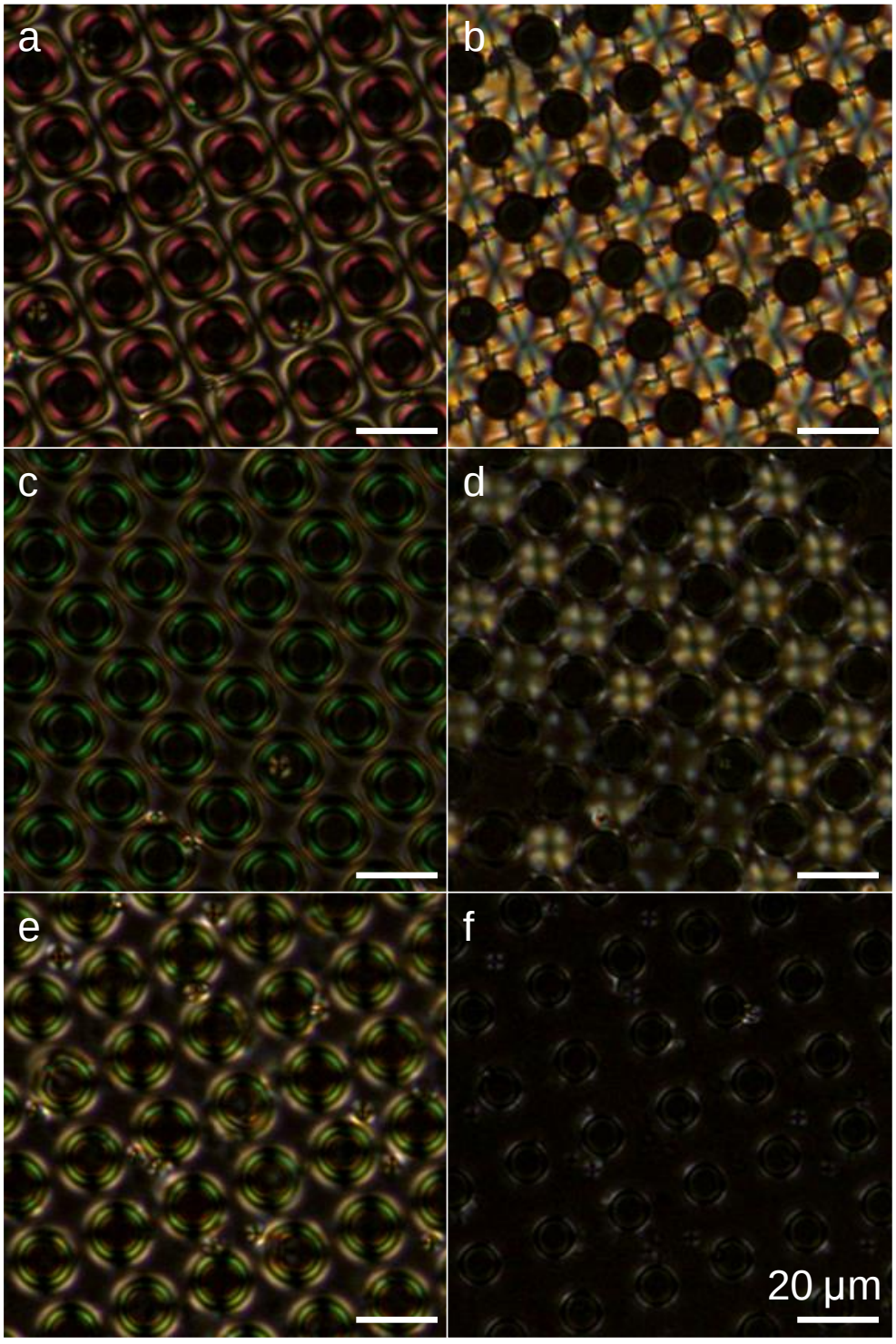

Figure 8.3 Polarized optical microscopy images of PS-AuNRs in 8CB with homeotropic anchoring epoxy pillar arrays and cover slips. Pillar dimensions are diameter = 10 µm,

spacing = 10 μm, and AR = 0.9 (a-b), 1.3 (c-d), and 1.6 (e-f). The temperature is 35°C (nematic, a, c, e) and 30°C (smectic, b, d, f). Scale bars: 20 μm.

There should be three possible LC director field configurations within the pillar arrays with homeotropic anchoring, including uniform escaping of the director field and bulk disclination lines with either +1/2 or -1/2 winding geometry (**Figure 8.4**). The director fields exhibit axial symmetry along the vertical axis and can be discussed in terms of each radial slice of the nematic LCs. The director fields correspond to the local minima of the Landau-de Gennes free energy of a nematic LC surrounding a cylindrical micropillar sandwiched between two planar substrates, all with homeotropic anchoring, as previously reported.(Cavallaro, Gharbi et al. 2013) At the top and bottom corners of the micropillar, the LC can have positive or negative winding via splay or bend elastic deformations, respectively. If there is opposite winding at the corners, then there exists uniform escaping of the director field. Bulk disclination lines with +1/2 or -1/2 winding numbers result from positive or negative winding at both corners, respectively.

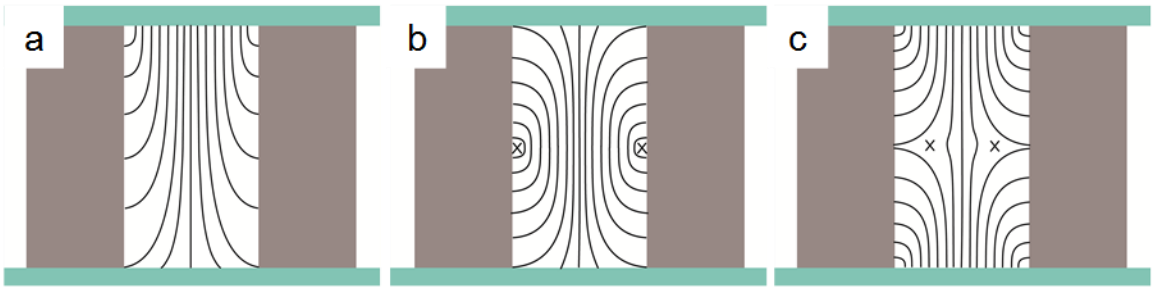

Figure 8.4 Schematic of the director field lines of 8CB in the nematic phase between two pillars. (a) Uniform escaping of the director field and (b) bulk disclination lines with +1/2 and (c) -1/2 winding number. X indicates the defect location.

Image analysis was used to further investigate the circle dimensions for homeotropically-anchoring micropillars. The radius of the rings depended on the temperature and the aspect ratio of the pillars (**Figure 8.5**). For pillars with AR = 0.9 (**Figure 8.5a**), the average ring radius in the nematic range 33-38°C was 8.8 ± 0.2 μm and the maximum ring radius was 9.1 μm. There was no clear dependence of the ring radius on the temperature. For pillars with AR = 1.3 (**Figure 8.5b**), the average ring radius in the nematic range 33-38°C was 8.3 ± 0.8 μm. The ring increased in size as the sample is cooled with the maximum ring radius 9.4 μm at 33°C. For pillars with AR = 1.6 (**Figure 8.5c**), the average ring radius in the nematic range 33-38°C was 7.7 ± 0.2 μm. The ring increased in size as the sample is cooled with the maximum ring radius 8.1 μm at 33°C. The changes in ring dimensions are summarized in **Figure 8.6**.

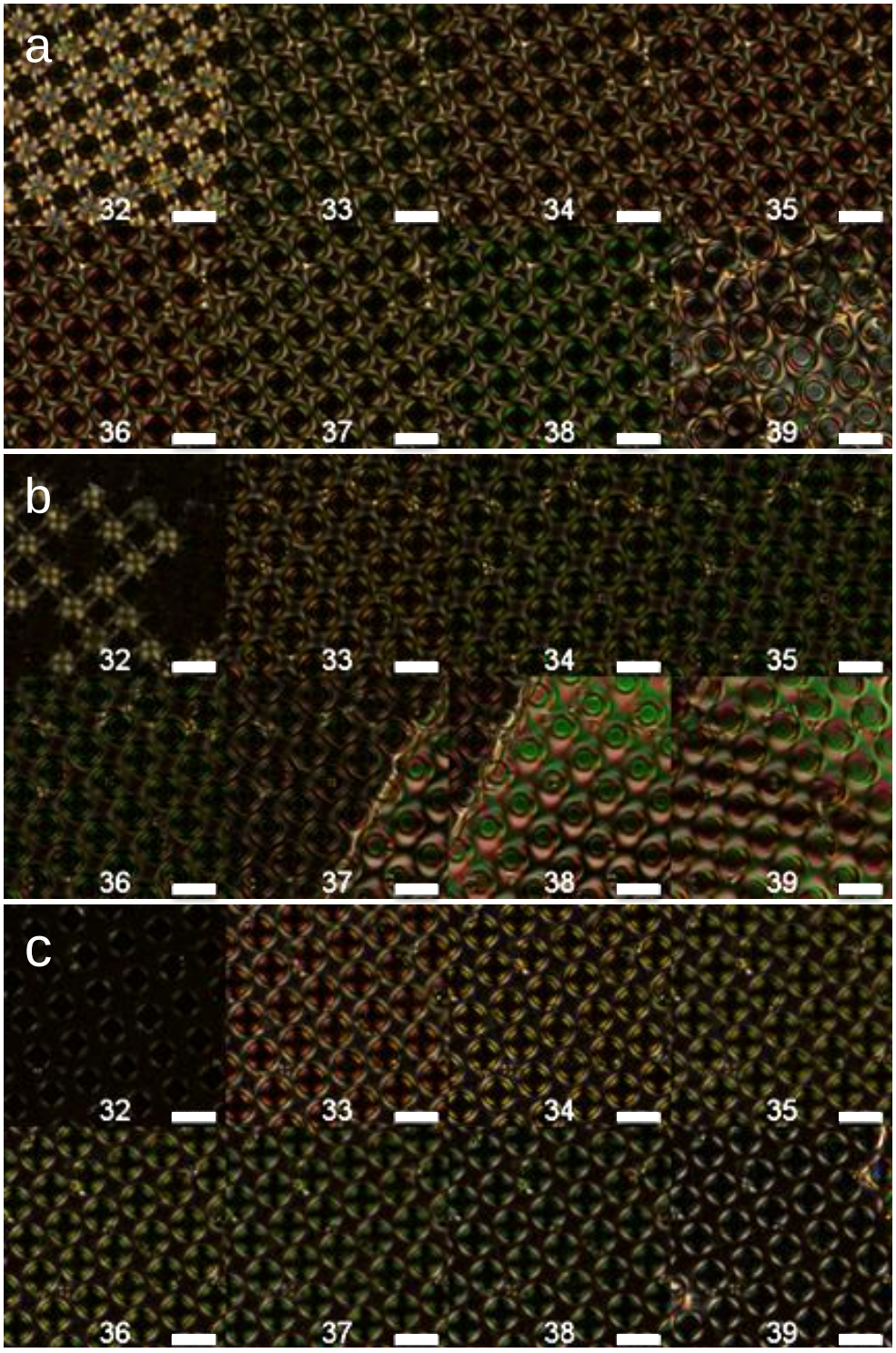

Figure 8.5 Polarized optical microscopy images of PS-AuNRs in 8CB with homeotropic anchoring epoxy pillar arrays and cover slips. Pillar dimensions are diameter = 10 μm,

spacing = 10 μm, and AR = 0.9 (a), 1.3 (b), and 1.6 (c). The temperature (°C) is indicated in the bottom center of each image. Scale bars: 20 μm.

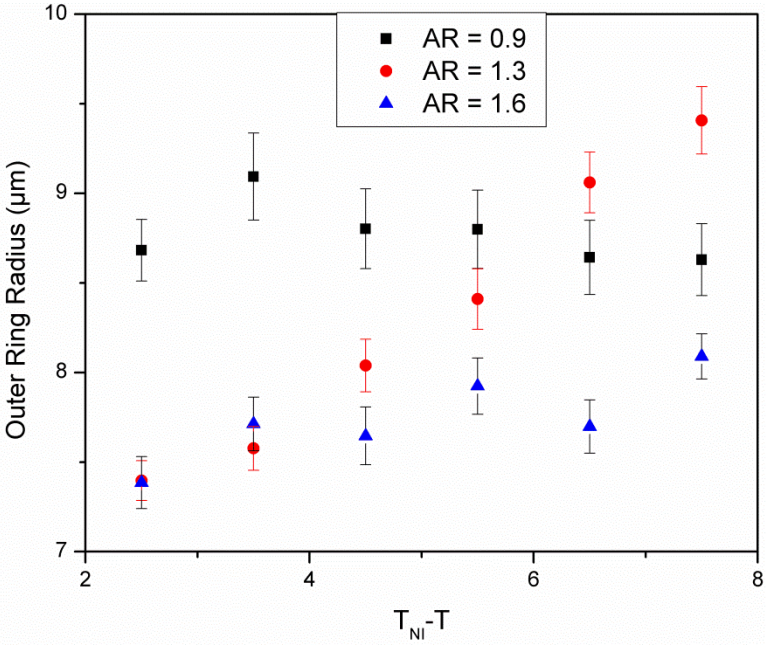

Figure 8.6 Radius of the outer defect as a function of the temperature below the nematic-to-isotropic transition temperature.

As the sample was further cooled, 8CB transitioned into the smectic phase at ~32°C. Homeotropic anchoring can induce three possible LC structures in the smectic phase due to geometric frustration between uniform layer spacing, mean curvature, and Gaussian curvature imposed by the boundary conditions. For AR = 0.9, the structure of 8CB around a single micropillar appeared as a bright square octasect by intersecting dark lines under POM (**Figure 8.3b and Figure 8.5a/32°C**). In 3D space, this should correspond to intersecting concentric cylindrical smectic layers wrapped around a lattice of intersecting line defects (**Figure 8.7a**), a smectic blue phase previously calculated by DiDonna *et al.*[DiDonna and Kamien 2003] The 2D projection of the proposed structure overlaid with the POM

image (**Figure 8.7b**) shows good agreement. For AR = 1.3, 8CB appeared dark between nearest neighbor micropillars with Maltese cross patterns between next-nearest neighboring pillars under POM (**Figure 8.3d and Figure 8.5b/32°C**). The dark regions represent smectic layers with homeotropic alignment of the LCs, with both the layer normal and local director parallel to the surface normal of the substrate. Thus, the edges of the dark regions have planar anchoring perpendicular to the surface normal. The hybrid anchoring with planar at the sides and homeotropic at the top and bottom boundaries led to the formation of focal conic domains (FCDs), where the smectic layers are wrapped around two disclination lines formed by a circle and a straight line through the circle center (**Figure 8.7c**).(Honglawan, Beller et al. 2013) The boundaries of the FCDs are overlaid with the POM image (**Figure 8.7d**) for clarity. Finally, for AR = 1.6, 8CB appeared dark throughout the sample with slight brightness around the edge of the micropillars under POM (**Figure 8.3f and Figure 8.5c/32°C**). In 3D, this should correspond to parallel smectic layers confined by homeotropic anchoring at all interfaces with defects at the side interfaces (**Figure 8.7e**). These defects may be high density dislocations created at the pillar edge due to meniscus formation during the nematic-to-smectic phase transition.(Picano, Hołyst et al. 2000) Here, the micropillars and the top and bottom surfaces form the boundaries with homeotropic anchoring (**Figure 8.7f**). The expressed configuration in the smectic phase clearly depended on the aspect ratio of the pillars and also indicates the director field configuration in the nematic phase. As the aspect ratio increases, less bending of the smectic layers was observed, resulting in uniform homeotropic anchoring. The intersecting concentric cylindrical smectic layers, FCDs, and parallel smectic layers corresponded to bulk disclination lines with +1/2 winding geometry, uniform escaping of the director field and

bulk disclination lines with -1/2 winding geometry in the nematic phase, respectively. We note that the exhibited textures could also depend on the cooling rate, which is not considered here.

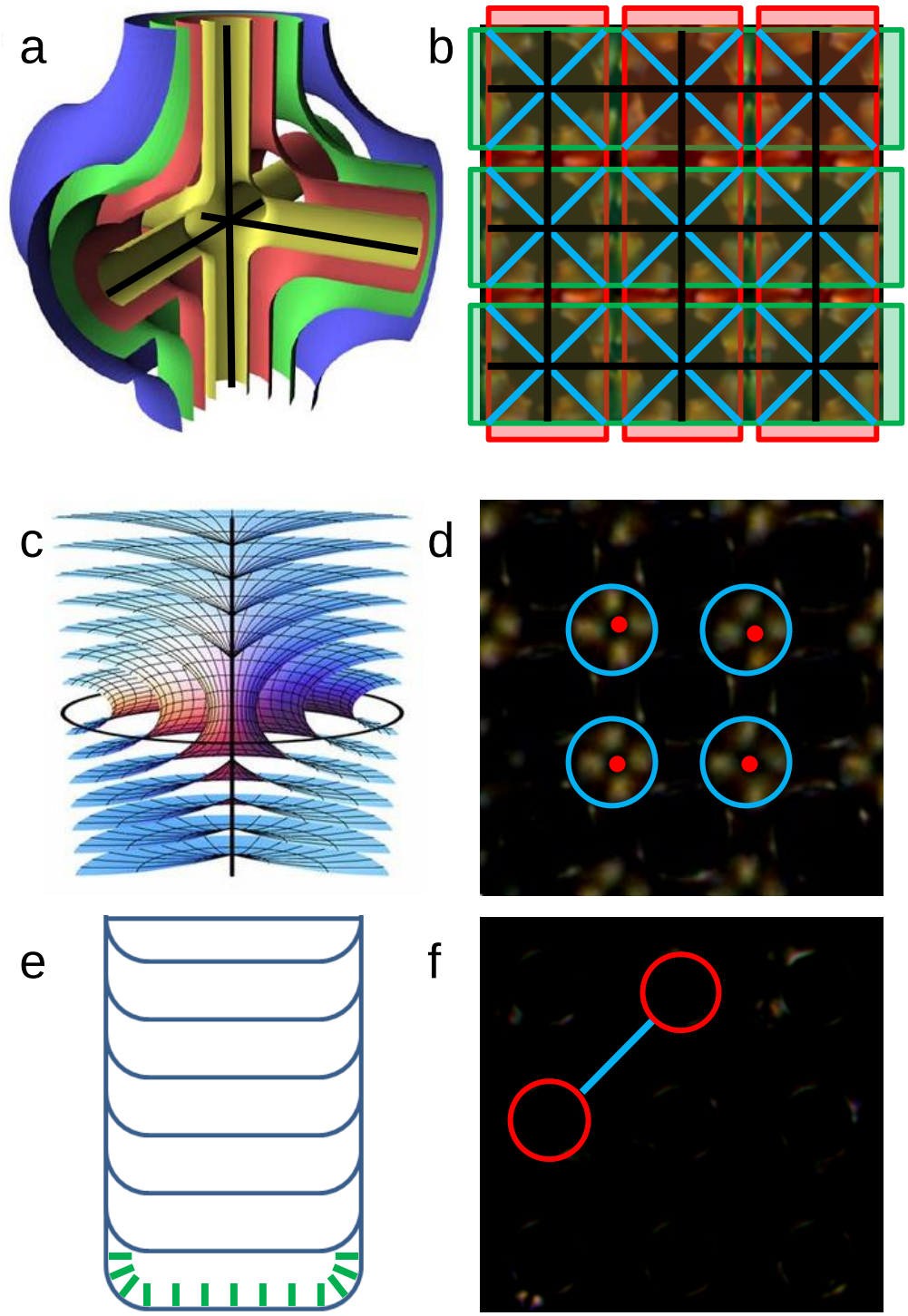

Figure 8.7 Schematic of the proposed minimum energy surfaces of 8CB in the smectic phase between micropillars (a, c, e) overlaid with the corresponding POM images (b, d, f).

Pillar dimensions are diameter = 10 μm, spacing = 10 μm, and AR = 0.9 (a-b), 1.3 (c-d), and 1.6 (e-f). (a) Surfaces constructed by intersecting concentric cylindrical smectic layers wrapped around a lattice of intersecting line defects. Reproduced with permission from reference (DiDonna and Kamien 2003). (b) POM image overlaid with the top-down view of the intersecting cylinders and line defects. Red and green rectangles indicate cylinders. Black lines indicate the line defects. Blue lines indicate where the cylinders intersect, i.e. where the smectic layers bend. (c) An FCD formed by confining smectic layers within a cylinder of planar anchoring on the sides and homeotropic anchoring at the top and bottom surfaces. Copyrighted image from reference (Honglawan, Beller et al. 2013). (d) POM image overlaid with the top-down view of the confining cylinders (blue circles). Red dots indicate the disclination lines perpendicular to the viewing plane. (e) Parallel smectic layers confined by homeotropic anchoring at all interfaces with bending of the layers at the side interfaces. (f) POM image overlaid with red circles indicating the micropillars and a blue line indicating the cross-sectional view of the smectic layers shown in (e).

For comparison, LC cells with planar anchoring were also fabricated. The defects of the planar cells were highly disordered in both the nematic and smectic phases (**Figure 8.8**).

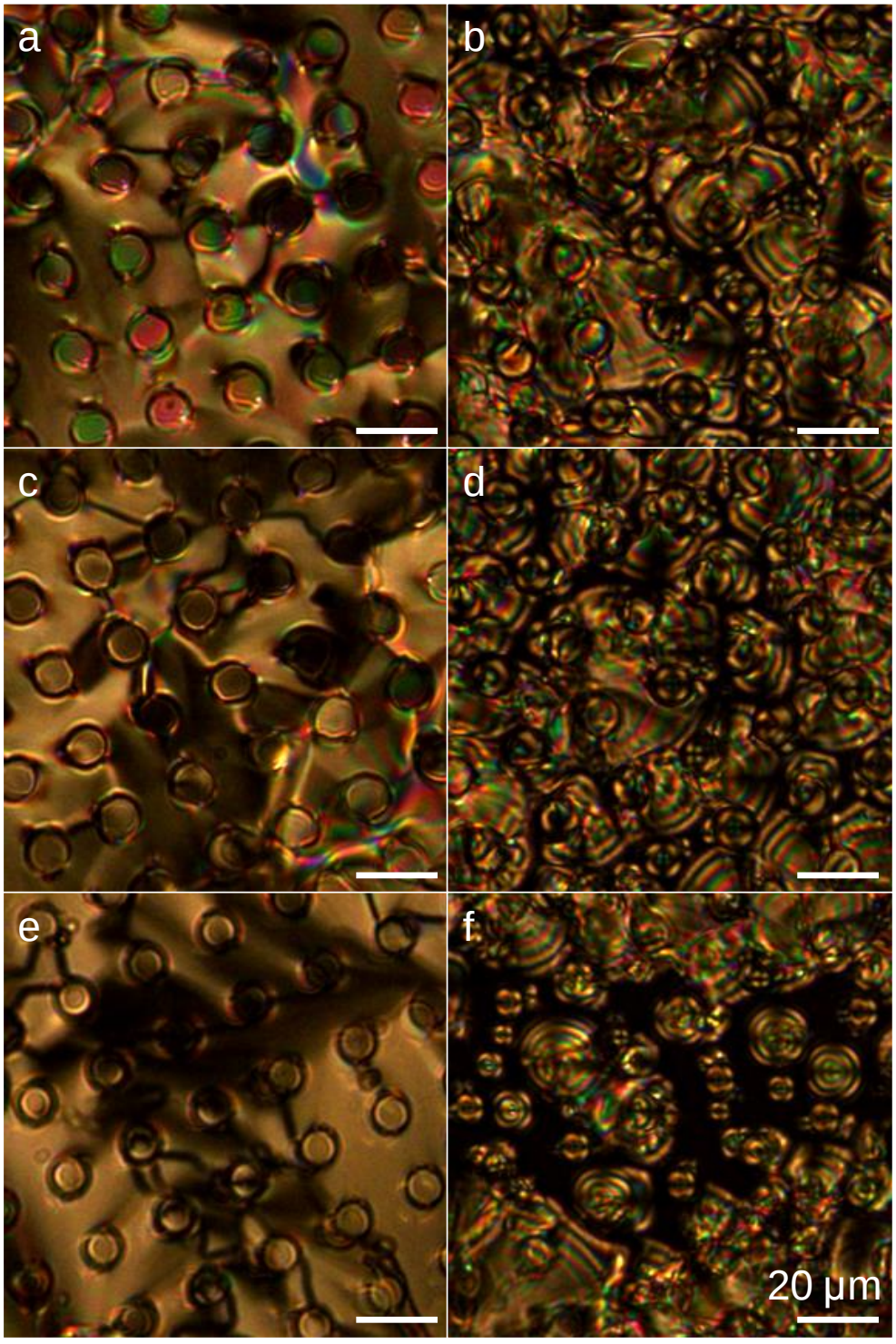

Figure 8.8 Polarized optical microscopy images of PS-AuNRs in 8CB over planar anchoring epoxy pillar arrays. Pillar dimensions are diameter = 10 µm, spacing = 10 µm,

and AR= 0.9 (a-b), 1.3 (c-d), and 1.6 (e-f). The temperature is 35°C (nematic, a, c, e) and 30°C (smectic, b, d, f). Scale bars: 20 μm.

8.6 Optical response

The transmission of PS-AuNRs in 8CB between micropillars with AR = 1.3 with homeotropic anchoring was measured as the sample was cooled from the isotropic phase. The spectra were normalized and subtracted from 1 to calculate extinction and offset for visualization (**Figure 8.9a**). At 40°C, 8CB was in the isotropic phase and an absorbance peak attributed to the PS-AuNRs could be observed at about 636 nm. At 38°C, 8CB has transitioned into the nematic phase and the peak red shifted to about 683 nm. At 36°C, two peaks could be observed at about 414 nm and 712 nm, corresponding to the transverse LSPR (TLSPR) and longitudinal LSPR (LLSPR), respectively. As the sample was further cooled through the nematic phase to 33°C, the TLSPR red shifted to 453 nm and the LLSPR red shifted to 729 nm. As the sample transitions to the smectic phase at 32°C, the plasmon peaks further red shifted to 483 nm and 789 nm, but minimal shift was observed as the sample was cooled through the smectic phase to room temperature. The total peak shifts for the TLSPR and LLSPR were 101 and 153 nm, respectively. This shift was one order of magnitude higher than that of systems previously reported based on the refractive index change of LC over metal nanoparticle arrays deposited on a surface.(Dickson, Wurtz et al. 2008, De Sio, Cunningham et al. 2012, De Sio, Klein et al. 2013) The plasmonic peak shift observed came from the dynamic interaction of the PS-AuNRs and the highly ordered LC defect ring structures. The change in the peak could be correlated to the defect ring radius (**Figure 8.9b**). As the sample was cooled, the ring radius increased, resulting in the

enlargement of the LC director field and a red shift of the plasmon peak. The peak shift was reversed upon heating the sample.

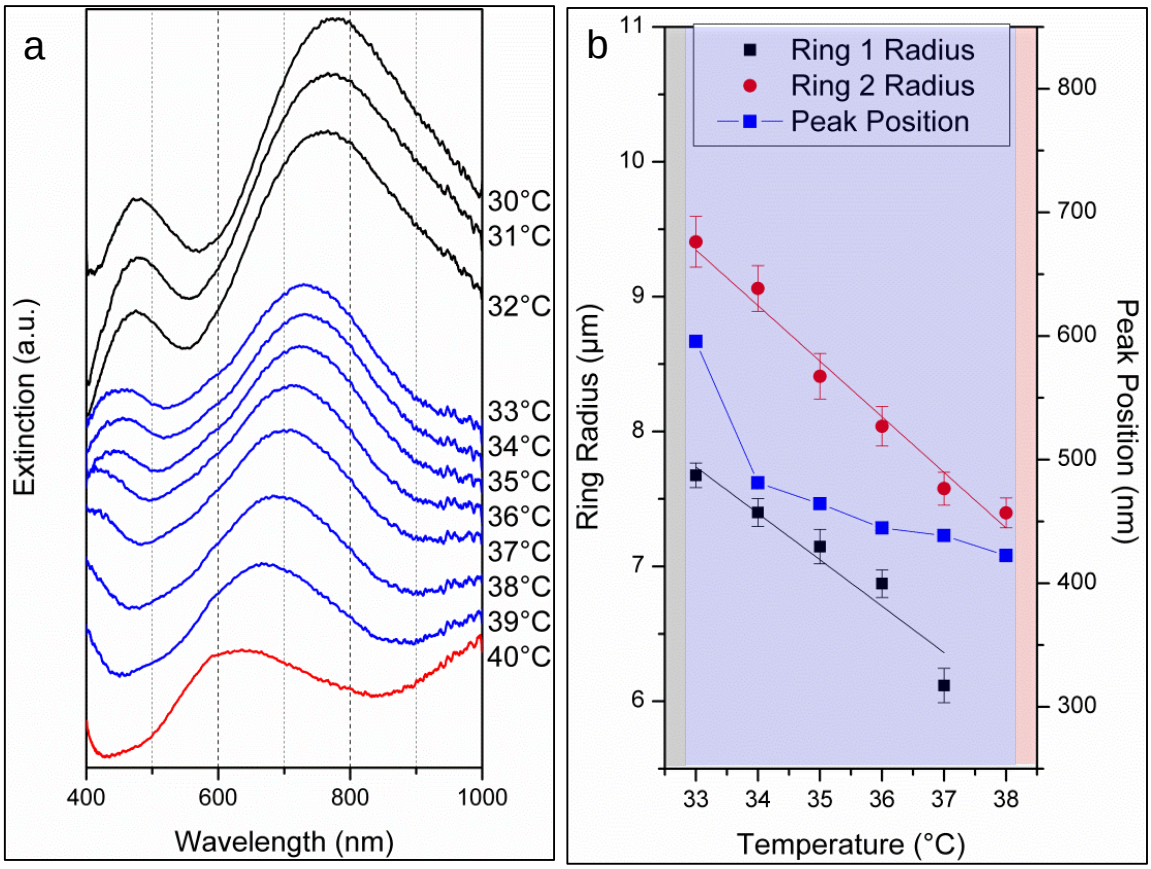

Figure 8.9 (a) Extinction spectra of PS-AuNRs in 8CB over homeotropic epoxy pillars. The extinction is offset for clarity. Red, blue, and black colors indicate isotropic, nematic, and smectic phase, respectively. (b) The defect radius of the LC and transverse localized surface plasmonic resonance wavelength of the PS-AuNRs over epoxy pillars as a function of temperature.

For comparison, the transmission of the PS-AuNRs in 8CB in a planar LC cell was measured at various temperatures (**Figure 8.10a**). At 40°C, 8CB was in the isotropic phase and slight extinction peaks were observed at ~516 and 887 nm, which might be attributed

to the TLSPR and LLSPR of the PS-AuNRs, respectively. As the cell was cooled to the nematic phase, the same peaks are observed. Due to the disordered defect structure of the planar cell, the peaks were insignificant. PS-AuNRs were randomly dispersed within the LC structure. In addition, they may have aggregated during the isotropic-nematic phase transition due to capillarity. In the smectic phase, peaks with slightly higher intensity could be observed at the same positions. This may be due to the higher order of the smectic phase. No plasmon peaks shifts were observed for PS-AuNRs dispersed between planar anchoring micropillars upon cooling, in sharp contrast to the large shifts observed for the homeotropic anchoring micropillars (**Figure 8.10b**). Therefore, it was imperative to control the anchoring conditions of the micropillar arrays to direct the assembly and optical response of PS-AuNRs in the LC defect structures.

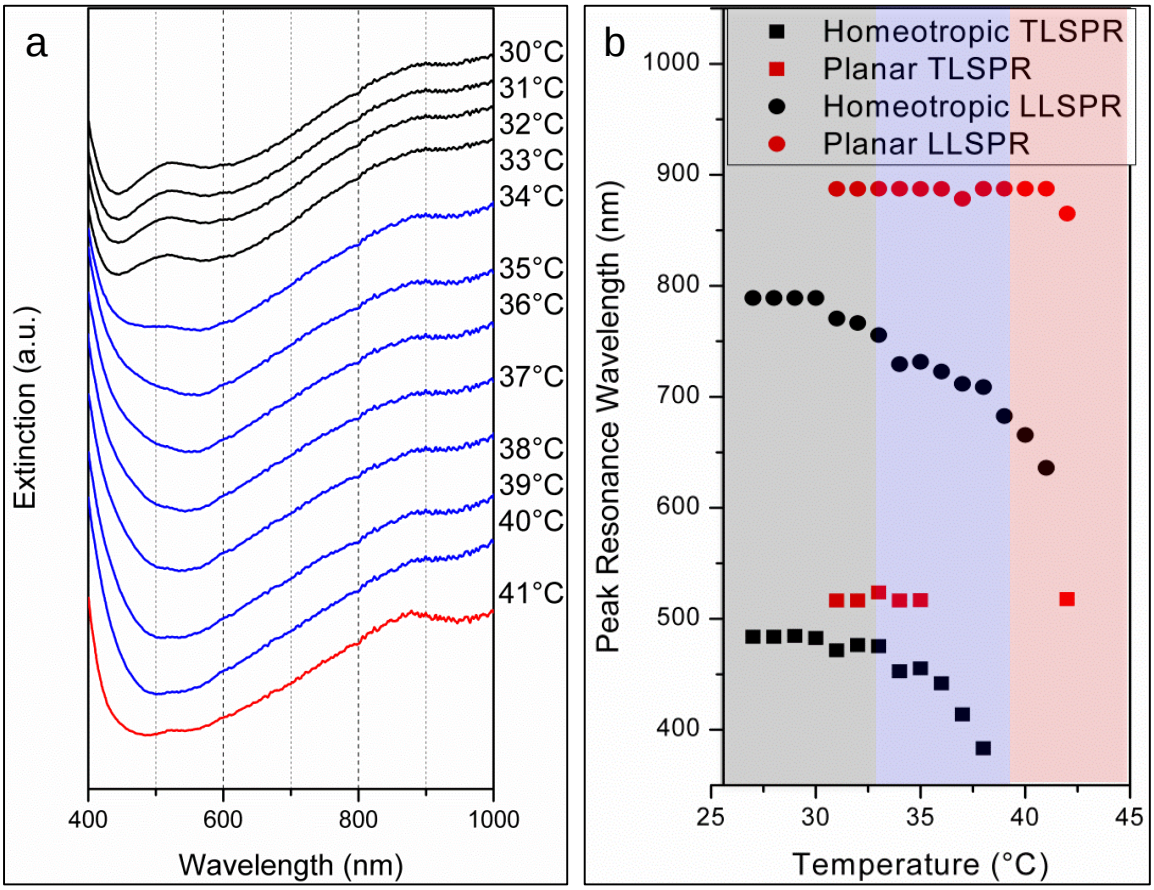

Figure 8.10 (a) Extinction spectra of PS-AuNRs in 8CB over planar epoxy pillars. The extinction is offset for clarity. Red, blue, and black colors indicate isotropic, nematic, and smectic phase, respectively. (b) The transverse and longitudinal localized surface plasmonic resonance peak position as a function of temperature for both homeotropic and planar cells.

To further demonstrate the importance of the micropillar array in assembling the AuNRs, a LC cell consisting of two flat glass slides treated with homeotropic anchoring on top and bottom was fabricated. As seen in **Figure 8.11**, no plasmon peaks were observed. In POM images, aggregation of the rods was observed when cooling the sample from the isotropic

phase to the nematic phase transition, which could be attributed to capillarity (**Figure 8.11b-e**).

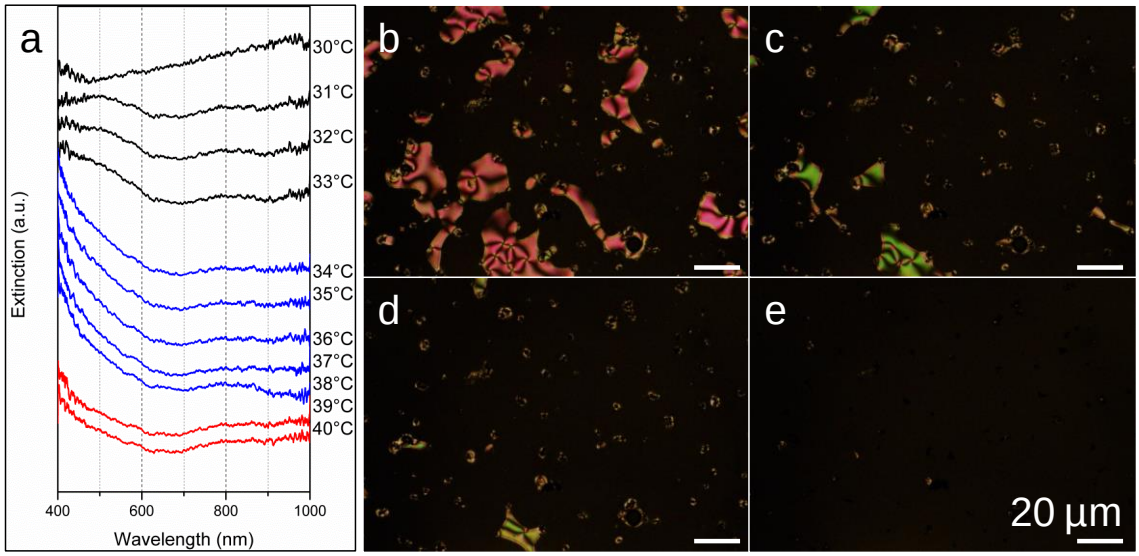

Figure 8.11 (a) Extinction spectra of PS-AuNRs in 8CB sandwiched between two glass slides with homeotropic anchoring. The extinction is offset for clarity. Red, blue, and black colors indicate isotropic, nematic, and smectic phase, respectively. (b-e) POM images of PS-AuNRs in 8CB in a homeotropic flat cell; the sample is transitioning from the nematic to the smectic phase from b to e.

As mentioned earlier, the appearance of 8CB semectic phases was highly dependent on the aspect ratio of micropillar arrays. Therefore, we expected the optical properties of AuNRs dispersed in 8CB over micropillar arrays would be dependent on AR too. As seen in Figure 5.12, for micropillars with AR = 0.9, two peaks were observed: the LLSPR shifting from 431 nm to 593 nm and the TLSPR shifting from 464 nm to outside the detector range into the UV region when cooled from 40°C to 28°C (**Figure 8.12a**). The total peak shift for the observed LLSPR was 165 nm. No peak shifts were observed for

micropillars with AR = 1.6 (**Figure 8.12b**). We correlated the peak shift to the observed ring defect size. As seen in **Table 8.1**, pillars with AR= 0.9 and 1.3 both had larger ring radii on the order of the pillar spacing. However, for AR=1.6, the ring radius was smaller and so the defect rings were not compressed against each other, therefore, there was no measureable peak shift. In addition, for AR=0.9, the change in ring radius as the temperature is swept was much smaller than that of AR=1.3. However, it shows a comparable resonance peak shift; this may indicate that the ring size change does not matter as much as the largest ring size, which allowed for the PS-AuNRs to become more disperse (**Figure 8.12c**). Our hypothesis is that the small ring size compresses the AuNRs, resulting in a blue shift in the extinction spectra (compared with dispersed PS-AuNRs (c.f. **Figure 8.1c**) due to plasmon resonance coupling, while increasing the ring size causes the PS-AuNRs to be more dispersed, which results in a red shift.

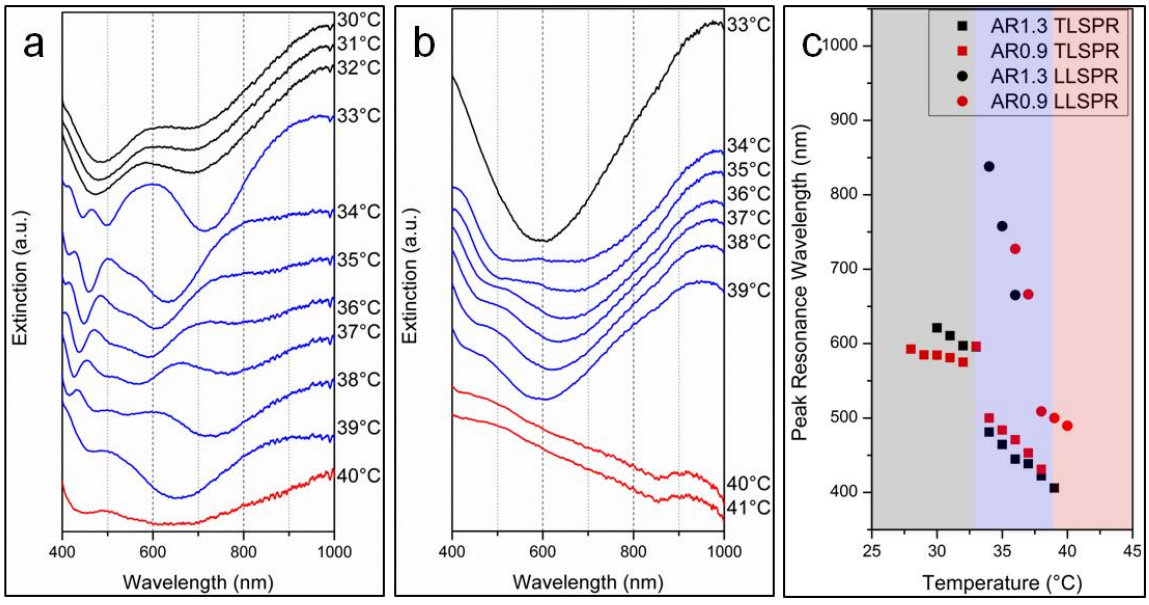

Figure 8.12 Extinction spectrum of PS-AuNRs in 8CB over homeotropic epoxy pillars, with diameter = 10 μm, spacing = 10 μm and AR = 0.9 (a) and 1.6 (b). Red, blue, and black

colors indicate isotropic, nematic, and smectic phase, respectively. (c) The transverse and longitudinal localized surface plasmonic resonance peak position as a function of temperature for epoxy pillars with AR= 1.3 and AR = 0.9.

Table 8.1 Comparison of the defect ring sizes and the plasmon peak shift of PS-AuNRs in 8CB over homeotropic pillar arrays of different aspect ratios.

Pillar Aspect Ratio	0.9	1.3	1.6
Outermost Ring Radius Max (μm)	9.1	9.4	8.1
Outermost Ring Radius Min (μm)	8.6	7.4	6.9
Change in Ring Radius (μm)	0.5	2.0	1.2
Peak Shift (nm)	165.3	173.2	N/A

Besides the aspect ratio effect, we wondered whether the anisotropy of LCs (e.g. polarization sensitivity) plays a role or not. Since AR = 1.3 gave the largest peak shift, we investigated the polarization dependence of the transmission of PS-AuNRs in 8CB within pillars with AR = 1.3 and homeotropic anchoring was measured (**Figure 8.13**). The polarization angle was fixed and the transmission spectrum was measured every 1°C as the sample was cooled from 40°C to 31°C. The polarizer was then rotated by 30° and the measurements were then repeated. As seen in **Figure 8.13**, no polarization dependence was observed, possibly because the micropillars have circular cross-sectional shapes.

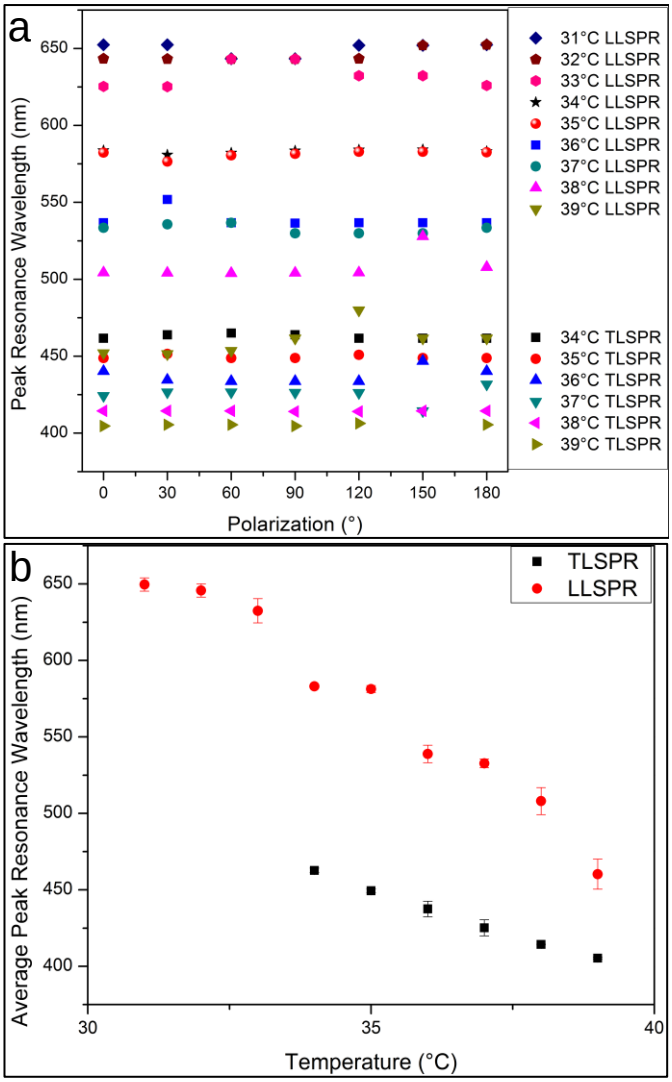

Figure 8.13 (a) The peak resonance wavelength as a function of polarization angle at various temperatures. (b) The average peak resonance wavelength as a function of temperature. Error bars indicate standard deviation of the wavelength across polarization angles.

8.7 Conclusions

PS-AuNRs were trapped into LC defects of 8CB on surface-treated epoxy pillar arrays. Comparison of different surface treatments showed that homeotropic anchoring induces a

plasmon peak shift as the sample was cooled and the LC transitioned from the isotropic to the nematic to the smectic phase sequentially due to the formation of well-ordered defects surrounding the pillars. Meanwhile, planar anchoring induced random defect structures, resulting in indistinguishable plasmon peaks with no peak shift as the sample is cooled. Comparison of pillars with different aspect ratios showed that samples with AR = 1.3 exhibited a higher peak shift than samples with AR = 0.9, while no peaks were observed for those with AR = 1.6; this was found correlated to the defect ring structure in the nematic phase. Polarization-resolved optical measurements show that the plasmonic peak resonance wavelength was not affected by the angle of light polarization due to the circular symmetry of the micropillar arrays. Dispersing PS-AuNRs in LCs in a flat homeotropic cell induced rod aggregation and a suppression of the plasmon resonance response. The ensemble assembly and actuation of PS-AuNRs demonstrated is achieved through several factors, including 1) the surface functionalization of AuNRs with PS brushes allowing for dispersion in 8CB without aggregation, 2) the control over the surface topography at a microscale, 3) the manipulation of the LC surface anchoring through surface functionalization to form well-ordered defect structures, and 4) the reversible compression of the LC director field tuned by temperature. Precise control over the surface properties of all the components in the system leads to reversible coupling of the PS-AuNRs and large plasmon peak shifts. This effect can be applied for enhanced and selective sensing applications.

Chapter 9 Summary and Future Work

9.1 Raman

Gold nanorod assembly, especially in polymer matrices, could be utilized to create a tunable platform for surface enhanced Raman spectroscopy (SERS). Other groups have demonstrated the utility of gold nanorod assembly in SERS schemes in solution and in the solid state.(Nikoobakht and El-Sayed 2003, Lee, Andrade et al. 2011) While tunability has been demonstrated in solution, there have been no studies, to my knowledge, on an easily tunable solid state SERS device. In chapter 2, I showed that we could assemble gold nanorods in solution and transfer that assembly into a polymer matrices while retaining optical properties. Here, the gold nanorods are assembled end-to-end, which creates electric field hot spots in the gaps between the nanorods, and therefore enhances the Raman signal. The analyte of interest could then be placed on top of the film, investigated by SERS, and then washed off. Tunability of this system is important. The enhancement of the Raman signal is strongest when the incident light is resonant with the surface plasmon resonance frequency. Therefore, tuning the assembly optical properties allows us to further enhance the Raman signal by matching it to the laser wavelength. The chain length as well as the polydispersity in the nanorod chain length, therefore, becomes vitally important.

9.2 DNA

Utilizing DNA in nanorod assembly schemes is a promising future direction. The specificity of base pair binding allows for specific and predictable linkages to occur. In chapter 3, I demonstrated the binding of two samples of gold nanorods each containing complimentary DNA strands. Assembly could only occur with both present and could be controllably assembled by tuning the ratio. This idea could easily be extended to two

disparate material types; instead of assembling two gold nanorods, one could assemble, say, gold nanorods and CdSe nanorods. Here the conducting gold nanorods amplify the light absorption for CdSe. The practical advantageis that the chemistry would not really need to change as thiol bonds readily with CdSe. Furthermore, another member of our group demonstrated end to end assembly of CdSe nanorods, so they can probably be anisotropically modified.

DNA gold nanorods could be an effective biosensor. DNA can be synthesized with "lesions" at particular nucleobase sites.(Cadet, Bourdat et al. 2000, Cadet, Douki et al. 2003, Gines, Saint-Pierre et al. 2014) These lesions are subtle changes in the DNA chemistry that are susceptible to attack from enzymes. Gold nanorods could be assembled with the DNA.Then, when in the presence of a particular enzyme, the DNA would be excised, the nanorods would decouple and a significant change in optical properties would occur.

Employing DNA origami to assemble gold nanorods is another interesting direction. The optical properties of gold nanorods are highly dependent on their relative orientation and separation distance. DNA origami would allow us to assemble gold nanorods into precise 3D architectures. We could envision knowing the optical properties we want for a particular application, determining the appropriate structure via FDTD simulations, and then actually building it using DNA origami.

9.3 Peptide

Like DNA, peptides can be used to precisely assemble gold nanorods. In chapter 4, I showed that we could utilize a *de novo* designed peptide to reversibly assemble gold annorods. Assembly was carried out by controlling the concentration of Zn^{2+} ions in

solution and could be reversed by adding a chelater. In the future, the optical properties of peptide / nanorod assemblies could be further tuned by changing the length of the peptide itself. However, I think there are more interesting avenues to explore.

De novo peptide design is a powerful tool. The peptide can be designed such that specific molecules or additives trigger assembly. We can think of designing a peptide that binds Zn-porphyrin. Placed between two nanorods we achieve a donor / acceptor heterojunction. In this way, we could add electrical properties as a tunable parameter. Conklin *et al.(Conklin, Nanayakkara et al. 2012)* showed that gold nanoparticles bridged by porphyrin molecules had unique electrical properties dependent upon temperature and number of porphyrin molecules bridging the nanoparticles. This could easily be extended to gold nanorods grafted with a peptide that undergoes a coil to helix transition triggered by Zn-porphyrin molecules. The Saven group has already demonstrated the design of such a peptide(Fry, Lehmann et al. 2010), so coupling with nanorods would be an easy next step.

9.4 Mesoscopic Rods

More work needs to be done to understand the dispersion of mesoscopic rods in polymer matrices. In chapter 6, I saw that the mesoscopic rods would disperse if their brush was large, but would aggregate if the brush was small, with no consideration for matrix type or matrix M_n. I calculated the free energy on the rods taking into account Van der Waal's forces and entropic forces due to grafted polymer chains. The calculations are rudimentary, but captured the trends in the experiments nicely. I think more robust calculations using SCFT would go a long way to elucidate the aggregation / dispersion mechanism. SCFT calculations would be especially useful to determine a regime where the mesoscopic rods with the largest brush would aggregate. Moving forward, investigating different sizes of

nanorods would be important. What are the cross over dimensions for the nanords where above they disperse / aggregate based on Van der Waal's but below they aggregate based on brush regime (*e.g.* dry or wet)? Understanding the underlying physics of dispersion at different nanorod size regimes is imperative for creating useful polymer nanocomposites in the future.

9.5 Mixed Brush Gold Nanorods

Grafting chemically disparate brushes to nanorods opens up a much wider parameter space with which to tune dispersion. Recent studies have shown that grafted bi-dispersed brushes, those with two different brush molecular weights, ease the traditional $\alpha < 3$ requirements for dispersion of spheres. The work presented in chapter 7 shows that chemically disparate brushes further loosen this requirement with $\alpha > 30$ leading to excellent dispersion of the gold nanorods. The factors that influence the dispersion for the disparate brush case are still wholly unexplored. From experiments, we know that the long brush seems to determine how the nanorods disperse in a particular matrix. For instance, for a long PS brush, the nanorods will disperse in PS, while for a long PMMA brush they will disperse in PMMA. What is the limit for this case? Can we achieve dispersion at alphas >100 or 1000? Will longer brushes help or hinder this?

I think an interesting study would look at the effect of long and short brush M_n in more detail. In chapter 7, we saw that even at slightly larger brush sizes of the larger brush we see significantly enhanced dispersion, but we did not investigate the length of the long brush in great detail. In the proposed study, first short PMMA (*e.g.* 5 kg/mol) would be grafted to the gold nanorod. Next, PS would be controllably polymerized from the surface via surface initiated-ATRP at various M_n. The advantage of this is that the grafting density

for both components, PS and PMMA, should be approximately constant for all values of PS. While at Kyoto University, I was able to polymerize PS from the surface of the gold nanorods without reshaping them. We could use this technique to grow the long brush to arbitrary M_n to test the limit. At high enough M_n, perhaps the nanorods will behave like they are grafted only with PS as the effect of the short brush becomes less influential.

Grafted brushes with positive χ were studied, but we have not fully investigated brushes with negative χ. Preliminary studies of gold nanorods grafted with PEO/PMMA brushes showed promising dispersion in both PMMA and PS matrices. This is interesting because both PEO and PMMA dislike PS. Perhaps we can design the brush such that the matrix does not matter and good dispersion could be achieved across all matrices. This would be a considerable boon for many applications that require good dispersion as processing could be made trivial.

Anisotropic functionalization of chemically mixed brushes could add a new dimension to tuning the assembly of the nanorods. For instance, the nanorods could be grafted with PEO on the sides and PS on the ends. This would allow them to assemble end-to-end in PEO matrices, and side-by-side in PS matrices. Furthermore, polymerization of the brushes from the surface will allow us to further tune the separation distances to dial in properties. Preliminary experiments testing this idea were performed in Japan at Kyoto University under the guidance of Prof. Ohno. Here, we modified a polymerization scheme to successfully polymerize PS at low temperatures ($T < 50$ °C), which keeps the nanorods from reshaping. A similar approach can be used for PMMA with the Ohno group having

great success synthesizing high molecular weight PMMA brushes via surface initiated ATRP.

9.6 Nanorods and Liquid Crystals

Nanorods can be combined with liquid crystals to create a platform with dynamic optical properties. The optical properties of thin films containing gold nanorods are locked in upon casting. While these are robust and not subject to easy degradation, they cannot be further tuned without reforming the PNC film. In chapter 8, we have shown that gold nanorods can be assembled in the defects formed when liquid crystals are oriented in a particular way in the presence of micropillars. The defects change with temperature, which further controls the assembly of the gold nanorods. We have demonstrated changes of 100s of nm in the LSPR band of such assemblies as the liquid crystal is swept through various phases. While further studies are needed to understand the mechanism, the assembly process is promising. Grafting the liquid crystal used in the matrix to the nanorod surface would probably cure some of the aggregation issues we encountered. Investigating the effect of nanorod length on the assemblies would also be interesting, because at higher length we could achieve a larger range of absorbance. Finally, investigating the assembly of nanorods in a liquid crystal polymer is also of interest. This work has been begun in conjunction with the Osuji (Yale) and Kasi (UConn) groups.

9.7 Nanoparticle Type

The effect of nanoparticle shape on dispersion in polymer matrices needs to be investigated. The dispersion of spheres(Chen and Green 2010, Kim and Green 2010, Sunday, Ilavsky et al. 2012) and rods(Hore and Composto 2010, Hore and Composto 2012, Hore, Frischknecht et al. 2012, Frischknecht, Hore et al. 2013) in polymer matrices have

been well studied. For these geometries, we have some understanding of the physics that governs dispersion. However, there are a whole host of other particle types (*e.g.* stars, bipyramids, plates, *etc.*) that have not received much scientific investigation. My main regret of my PhD is not utilizing my contacts in Prof. Murray's group effectively enough. In their group, they produce a wide array of particle shapes and these could be easily modified with polymers and placed in polymer matrices. Studies could follow the same procedure as Hore and Composto, but with different shapes. Experimental studies could be coupled with SCFT calculations to predict / understand the experimental results.

Different nanoparticle shapes offer wildly different optical properties (in the case of gold) and as such could allow for more diverse polymer nanocomposite properties. Bipyramids have been shown(Liu, Guyot-Sionnest et al. 2007) to enhance field at their tips even more than gold nanorods and, as such, are attractive for SERS schemes. Beyond this, I think being able to controllably assemble nanoparticles of different shapes into precise architectures would open up a huge parameter space for tuning the properties of solutions and polymer nanocomposites. This could be coupled with FDTD calculations which would allow us to predict properties prior to creating a specific assembly. Although, advancement in anisotropic surface modification techniques would need to take place before such diverse architectures could be realized.

Nanoparticle material is an interesting parameter to tune. With the advent and advancement of nanoparticle syntheses, we now have access to nanoparticles of a wide variety of shapes, sizes, and materials. Utilizing different materials allows us to access completely different property sets. Nanoparticles have been made with magnetic, semiconducting, optical, and thermoelectric properties, among others. Controllably

combining the various nanoparticles in a rational way will allow for the creation of bottom-up assembled nanodevices with unique properties. The first step in the realization of such devices is to understand how to assemble two nanoparticles of disparate material and how to achieve useful properties from such assemblies.

9.8 Final Comments

Throughout this dissertation, I have discussed how altering the surface chemistry of nanoparticles can allow us to achieve unique and tunable properties. The extant library of ligands we can utilize to change nanoparticle surface chemistry is vast and diverse, each with their own particular pros and cons. Understanding how to manipulate and combine these ligands to achieve the nanostructures we want is of paramount importance to advancing nanoscience. I have utilized and combined polymers, DNA, peptides, cysteine, alkanedithiols, and organic semiconductors with gold nanorods. I hope I have, with the work presented here, taken nanoscience a small step forward.

BIBLIOGRAPHY

Abadeer, N. S., et al. (2014). "Distance and Plasmon Wavelength Dependent Fluorescence of Molecules Bound to Silica-Coated Gold Nanorods." ACS Nano **8**(8): 8392-8406.

Akcora, P., et al. (2009). "Anisotropic self-assembly of spherical polymer-grafted nanoparticles." Nat Mater **8**(4): 354-359.

Alivisatos, A. P., et al. (1996). "Organization of 'nanocrystal molecules' using DNA." Nature **382**(6592): 609-611.

Allcock, H. R. and F. W. Lampe (1981). Contemporary polymer chemistry, Prentice-Hall.

Arbeloa, F. L., et al. (1989). "Fluorescence Self-Quenching of the Molecular Form of Rhodamine B in Aqueous and Ethanolic Solution." Journal of Luminescence(44).

Aschi, M., et al. (2008). "Physicochemical Properties of Fluorescent Probes: Experimental and Computational Determination of the Overlapping pKa Values of Carboxyfluorescein." J Org Chem **73**(9): 3411-3417.

Bakueva, L., et al. (2003). "Size-tunable infrared (1000–1600 nm) electroluminescence from PbS quantum-dot nanocrystals in a semiconducting polymer." Applied Physics Letters **82**(17): 2895-2897.

Balazs, A. C., et al. (2006). "Nanoparticle Polymer Composites: Where Two Small Worlds Meet." Science **314**(5802): 1107-1110.

Bonizzoni, M., et al. (2012). "PAMAM dendrimer-induced aggregation of 5(6)-carboxyfluorescein." J Org Chem **77**(3): 1258-1266.

Brian, K. C., et al. (2005). "Polarization effects in the linear and nonlinear optical responses of gold nanoparticle arrays." Journal of Optics A: Pure and Applied Optics **7**(2): S110.

Burke, J. (2012). Surfaces and Interfaces I: Chemical and Physical Characteristics, Springer US.

Cadet, J., et al. (2000). "Oxidative base damage to DNA: specificity of base excision repair enzymes." Mutation Research/Reviews in Mutation Research **462**(2–3): 121-128.

Cadet, J., et al. (2003). "Oxidative damage to DNA: formation, measurement and biochemical features." Mutation Research/Fundamental and Molecular Mechanisms of Mutagenesis **531**(1–2): 5-23.

Caswell, K. K., et al. (2003). "Preferential End-to-End Assembly of Gold Nanorods by Biotin−Streptavidin Connectors." Journal of the American Chemical Society **125**(46): 13914-13915.

Cavallaro, M., et al. (2013). "Exploiting imperfections in the bulk to direct assembly of surface colloids." Proceedings Of The National Academy Of Sciences Of The United States Of America **110**(47): 18804-18808.

Chalmers, J. M. and P. R. Griffiths (2002). Handbook of Vibrational Spectroscopy, Wiley.

Chanda, D., et al. (2011). "Large-area flexible 3D optical negative index metamaterial formed by nanotransfer printing." Nat Nano **6**(7): 402-407.

Chang, J.-Y., et al. (2005). "Oriented assembly of Au nanorods using biorecognition system." Chem Commun (Camb)(8): 1092-1094.

Chao, H., et al. (2014). "The distribution of homogeneously grafted nanoparticles in polymer thin films and blends." Soft Matter **10**(40): 8083-8094.

Chen, H., et al. (2008). "Shape- and Size-Dependent Refractive Index Sensitivity of Gold Nanoparticles." Langmuir **24**(10): 5233-5237.

Chen, X. C. and P. F. Green (2010). "Control of Morphology and Its Effects on the Optical Properties of Polymer Nanocomposites." Langmuir **26**(5): 3659-3665.

Conklin, D., et al. (2012). "Electronic Transport in Porphyrin Supermolecule-Gold Nanoparticle Assemblies." Nano Letters **12**(5): 2414-2419.

Corbierre, M. K., et al. (2005). "Gold Nanoparticle/Polymer Nanocomposites: Dispersion of Nanoparticles as a Function of Capping Agent Molecular Weight and Grafting Density." Langmuir **21**(13): 6063-6072.

De Sio, L., et al. (2012). "Double active control of the plasmonic resonance of a gold nanoparticle array." Nanoscale **4**(24): 7619-7623.

De Sio, L., et al. (2013). "All-optical control of localized plasmonic resonance realized by photoalignment of liquid crystals." Journal of Materials Chemistry C **1**(45): 7483-7487.

Dickson, W., et al. (2008). "Electronically Controlled Surface Plasmon Dispersion and Optical Transmission through Metallic Hole Arrays Using Liquid Crystal." Nano Letters **8**(1): 281-286.

DiDonna, B. A. and R. D. Kamien (2003). "Smectic blue phases: Layered systems with high intrinsic curvature." Physical Review E **68**(4): 041703.

Ding, B., et al. (2010). "Gold Nanoparticle Self-Similar Chain Structure Organized by DNA Origami." Journal of the American Chemical Society **132**(10): 3248-3249.

Draine, B. T. and P. J. Flatau (1994). "Discrete-Dipole Approximation For Scattering Calculations." Journal of the Optical Society of America A **11**(4): 1491-1499.

Draine, B. T. and P. J. Flatau (2010). "User Guide to the Discrete Dipole Approximation Code DDSCAT 7.1." arXiv.org e-prin archive **http://arXiv.org/abs/1002.1505v1**.

Du, F., et al. (2004). "Nanotube Networks in Polymer Nanocomposites: Rheology and Electrical Conductivity." Macromolecules **37**(24): 9048-9055.

Duan, G., et al. (2008). "Preparation and Characterization of Mesoporous Zirconia Made by Using a Poly (methyl methacrylate) Template." Nanoscale Research Letters **3**(3): 118-122.

Dujardin, E., et al. (2001). "DNA-driven self-assembly of gold nanorods." Chem Commun (Camb)(14): 1264-1265.

Esumi, K., et al. (1995). "Preparation of Rodlike Gold Particles by UV Irradiation Using Cationic Micelles as a Template." Langmuir **11**(9): 3285-3287.

Faraday, M. (1857). "The Bakerian Lecture: Experimental Relations of Gold (and Other Metals) to Light." Philosophical Transactions of the Royal Society of London **147**: 145-181.

Faure, B., et al. (2011). "Hamaker Constants of Iron Oxide Nanoparticles." Langmuir **27**(14): 8659-8664.

Ferrier, R. C., Jr., et al. (2014). "Gold nanorod linking to control plasmonic properties in solution and polymer nanocomposites." Langmuir **30**(7): 1906-1914.

Ferrier, R. C., et al. (2014). "Gold Nanorod Linking to Control Plasmonic Properties in Solution and Polymer Nanocomposites." Langmuir **30**(7): 1906-1914.

Fornes, T. D., et al. (2001). "Nylon 6 nanocomposites: the effect of matrix molecular weight." Polymer **42**(25): 09929-09940.

Freestone, I., et al. (2007). "The Lycurgus Cup — A Roman nanotechnology." Gold Bulletin **40**(4): 270-277.

Frischknecht, A. L., et al. (2013). "Dispersion of Polymer-Grafted Nanorods in Homopolymer Films: Theory and Experiment." Macromolecules **46**(7): 2856-2869.

Fry, H. C., et al. (2010). "Computational Design and Elaboration of a de Novo Heterotetrameric α-Helical Protein That Selectively Binds an Emissive Abiological (Porphinato)zinc Chromophore." Journal of the American Chemical Society **132**(11): 3997-4005.

Funston, A. M., et al. (2009). "Plasmon Coupling of Gold Nanorods at Short Distances and in Different Geometries." Nano Letters **9**(4): 1651-1658.

Gabudean, A. M., et al. (2012). "Gold Nanorods Performing as Dual-Modal Nanoprobes via Metal-Enhanced Fluorescence (MEF) and Surface-Enhanced Raman Scattering (SERS)." The Journal of Physical Chemistry C **116**(22): 12240-12249.

Gam, S., et al. (2011). "A jamming morphology map of polymer blend nanocomposite films." Soft Matter **7**(16): 7262-7268.

Gao, B., et al. (2012). "Self-orienting nanocubes for the assembly of plasmonic nanojunctions." Nat Nano **7**(7): 433-437.

Gao, J., et al. (2003). "Dependence of the Gold Nanorod Aspect Ratio on the Nature of the Directing Surfactant in Aqueous Solution." Langmuir **19**(21): 9065-9070.

Giannelis, E. P. (1996). "Polymer Layered Silicate Nanocomposites." Advanced Materials **8**(1): 29-35.

Gines, G., et al. (2014). "On-bead fluorescent DNA nanoprobes to analyze base excision repair activities." Analytica Chimica Acta **812**(0): 168-175.

Gole, A., et al. (2004). "Immobilization of Gold Nanorods onto Acid-Terminated Self-Assembled Monolayers via Electrostatic Interactions." Langmuir **20**(17): 7117-7122.

Gormley, A. J., et al. (2014). "Polymerization Amplified Detection for Nanoparticle-Based Biosensing." Nano Letters **14**(11): 6368-6373.

Green, P. F. (2011). "The structure of chain end-grafted nanoparticle/homopolymer nanocomposites." Soft Matter **7**(18): 7914-7926.

Gu, H., et al. (2010). "A proximity-based programmable DNA nanoscale assembly line." Nature **465**(7295): 202-205.

Guha, P., et al. (2004). "Direct synthesis of single crystalline In2O3 nanopyramids and nanocolumns and their photoluminescence properties." Applied Physics Letters **85**(17): 3851-3853.

Hale, J. (2006). "Boeing 787 From the Ground Up." Aero **04**(24): 7.

Hao, Q., et al. (2011). "Frequency-addressed tunable transmission in optically thin metallic nanohole arrays with dual-frequency liquid crystals." Journal of applied physics **109**(8): 084340.

Herring, N. P., et al. (2011). "Formation Mechanisms of Gold–Zinc Oxide Hexagonal Nanopyramids by Heterogeneous Nucleation using Microwave Synthesis." Langmuir **27**(24): 15146-15154.

Hickey, R. J., et al. (2014). "Size-Controlled Self-Assembly of Superparamagnetic Polymersomes." ACS Nano **8**(1): 495-502.

Hong, X., et al. (2004). "Fabrication of Magnetic Luminescent Nanocomposites by a Layer-by-Layer Self-assembly Approach." Chemistry of Materials **16**(21): 4022-4027.

Honglawan, A., et al. (2013). "Topographically induced hierarchical assembly and geometrical transformation of focal conic domain arrays in smectic liquid crystals." Proceedings of the National Academy of Sciences **110**(1): 34-39.

Höök, F., et al. (2001). "Variations in Coupled Water, Viscoelastic Properties, and Film Thickness of a Mefp-1 Protein Film during Adsorption and Cross-Linking: A Quartz Crystal Microbalance with Dissipation Monitoring, Ellipsometry, and Surface Plasmon Resonance Study." Analytical Chemistry **73**(24): 5796-5804.

Hore, M. J. A. and R. J. Composto (2010). "Nanorod Self-Assembly for Tuning Optical Absorption." ACS Nano **4**(11): 6941-6949.

Hore, M. J. A. and R. J. Composto (2012). "Using Miscible Polymer Blends To Control Depletion–Attraction Forces between Au Nanorods in Nanocomposite Films." Macromolecules **45**(15): 6078-6086.

Hore, M. J. A., et al. (2013). "Direct Measurements of Polymer Brush Conformation Using Small-Angle Neutron Scattering (SANS) from Highly Grafted Iron Oxide Nanoparticles in Homopolymer Melts." Macromolecules **46**(23): 9341-9348.

Hore, M. J. A., et al. (2012). "Nanorod Assemblies in Polymer Films and Their Dispersion-Dependent Optical Properties." ACS Macro Letters **1**(1): 115-121.

Hsiao, V. K., et al. (2008). "Light-driven plasmonic switches based on Au nanodisk arrays and photoresponsive liquid crystals." Advanced Materials **20**(18): 3528-3532.

Hu, J., et al. (2012). "Efficient Synthesis of Single Gold Nanoparticle Hybrid Amphiphilic Triblock Copolymers and Their Controlled Self-Assembly." Journal of the American Chemical Society **134**(18): 7624-7627.

Huang, H.-C., et al. (2008). "Optically Responsive Gold Nanorod−Polypeptide Assemblies." Langmuir **24**(24): 14139-14144.

Huang, X., et al. (2006). "Cancer Cell Imaging and Photothermal Therapy in the Near-Infrared Region by Using Gold Nanorods." Journal of the American Chemical Society **128**(6): 2115-2120.

Huang, Y., et al. (2015). "Synthesis of Iron Oxide Rods Coated with Polymer Brushes and Control of Their Assembly in Thin Films." Langmuir **31**(3): 1172-1179.

Hung, A. M., et al. (2010). "Large-area spatially ordered arrays of gold nanoparticles directed by lithographically confined DNA origami." Nat Nano **5**(2): 121-126.

Imsick, B. G., et al. (2013). "Surface-Immobilized Monolayers of Conjugated Oligomers as a Platform for Fluorescent Sensors Design: The Effect of Exciton Delocalization on Chemosensing Performance." Advanced Materials **25**(1): 120-124.

Israelachvili, J. N. (1985). Intermolecular and Surface Forces: With Applications to Colloidal and Biological Systems, Academic Press.

Jain, P. K., et al. (2006). "Plasmon Coupling in Nanorod Assemblies: Optical Absorption, Discrete Dipole Approximation Simulation, and Exciton-Coupling Model." The Journal of Physical Chemistry B **110**(37): 18243-18253.

Jain, T., et al. (2012). "End-to-end assembly of gold nanorods via oligopeptide linking and surfactant control." Journal of Colloid and Interface Science **376**(1): 83-90.

Jana, N. R., et al. (2001). "Wet Chemical Synthesis of High Aspect Ratio Cylindrical Gold Nanorods." The Journal of Physical Chemistry B **105**(19): 4065-4067.

Jhon, Y. K., et al. (2006). "Salt-Induced Depression of Lower Critical Solution Temperature in a Surface-Grafted Neutral Thermoresponsive Polymer." Macromolecular Rapid Communications **27**(9): 697-701.

Johan, M. R., et al. (2011). "Effects of Al2O3 nanofiller and EC plasticizer on the ionic conductivity enhancement of solid PEO–LiCF3SO3 solid polymer electrolyte." Solid State Ionics **196**(1): 41-47.

Junxi, Z., et al. (2012). "Surface plasmon polaritons: physics and applications." Journal of Physics D: Applied Physics **45**(11): 113001.

Kang, Y., et al. (2005). "Plasmonic Nanoparticle Chains via a Morphological, Sphere-to-String Transition." Journal of the American Chemical Society **127**(40): 13800-13801.

Karker, N., et al. (2014). "Thermal Energy Harvesting Plasmonic Based Chemical Sensors." ACS Nano **8**(10): 10953-10962.

Khatua, S., et al. (2014). "Resonant Plasmonic Enhancement of Single-Molecule Fluorescence by Individual Gold Nanorods." ACS Nano **8**(5): 4440-4449.

Kim, J. and P. F. Green (2010). "Phase Behavior of Thin Film Brush-Coated Nanoparticles/Homopolymer Mixtures." Macromolecules **43**(3): 1524-1529.

Kim, S., et al. (2015). "Nanoscale Phase Behavior of Mixed Polymer Ligands on a Gold Nanoparticle Surface." ACS Macro Letters **4**(4): 417-421.

Koski, J., et al. (2015). "Predicting the structure and interfacial activity of diblock brush, mixed brush, and Janus-grafted nanoparticles." Chem Commun (Camb) **51**(25): 5440-5443.

Krantz, B. A. and T. R. Sosnick (2001). "Engineered metal binding sites map the heterogeneous folding landscape of a coiled coil." Nature Structural Biology **8**(12): 1042-1047.

Krishnamoorti, R. and E. P. Giannelis (1997). "Rheology of End-Tethered Polymer Layered Silicate Nanocomposites." Macromolecules **30**(14): 4097-4102.

Kumar, J., et al. (2013). "Surface plasmon coupling in end-to-end linked gold nanorod dimers and trimers." Physical Chemistry Chemical Physics **15**(12): 4258-4264.

Kumar, S. K., et al. (2013). "Nanocomposites with Polymer Grafted Nanoparticles." Macromolecules **46**(9): 3199-3214.

Lakowicz, J. R. (2007). Principles of Fluorescence Spectroscopy, Springer.

Lee, A., et al. (2011). "Probing Dynamic Generation of Hot-Spots in Self-Assembled Chains of Gold Nanorods by Surface-Enhanced Raman Scattering." Journal of the American Chemical Society **133**(19): 7563-7570.

Lee, H.-S. and L. S. Penn (2008). "In Situ Study of Polymer Brushes as Selective Barriers to Diffusion." Macromolecules **41**(21): 8124-8129.

Lee, J. H., et al. (2009). "High efficiency polymer solar cells with wet deposited plasmonic gold nanodots." Organic Electronics **10**(3): 416-420.

Leung, T. Y. B., et al. (2000). "1,6-Hexanedithiol Monolayers on Au(111): A Multitechnique Structural Study." Langmuir **16**(2): 549-561.

Li, X., et al. (2009). "Fluorescence quenching of quantum dots by gold nanorods and its application to DNA detection." Applied Physics Letters **94**(6): 063111.

Li, Y., et al. (2013). "Bimodal Surface Ligand Engineering: The Key to Tunable Nanocomposites." Langmuir **29**(4): 1211-1220.

Link, S., et al. (1999). "Simulation of the Optical Absorption Spectra of Gold Nanorods as a Function of Their Aspect Ratio and the Effect of the Medium Dielectric Constant." The Journal of Physical Chemistry B **103**(16): 3073-3077.

Liu, B. and H. C. Zeng (2003). "Hydrothermal Synthesis of ZnO Nanorods in the Diameter Regime of 50 nm." Journal of the American Chemical Society **125**(15): 4430-4431.

Liu, K., et al. (2013). "In Situ Plasmonic Counter for Polymerization of Chains of Gold Nanorods in Solution." ACS Nano **7**(7): 5901-5910.

Liu, K., et al. (2010). "Step-Growth Polymerization of Inorganic Nanoparticles." Science **329**(5988): 197-200.

Liu, K., et al. (2012). "Salt-mediated kinetics of the self-assembly of gold nanorods end-tethered with polymer ligands." Nanoscale **4**(20): 6574-6580.

Liu, M., et al. (2007). "Optical properties of rodlike and bipyramidal gold nanoparticles from three-dimensional computations." Physical Review B **76**(23): 235428.

Liu, M., et al. (2014). "Recent advance in research on halloysite nanotubes-polymer nanocomposite." Progress in Polymer Science **39**(8): 1498-1525.

Liu, Q., et al. (2014). "Shape-dependent dispersion and alignment of nonaggregating plasmonic gold nanoparticles in lyotropic and thermotropic liquid crystals." Physical Review E **89**(5): 052505.

Liu, Q., et al. (2014). "Electrically and Optically Tunable Plasmonic Guest–Host Liquid Crystals with Long-Range Ordered Nanoparticles." Nano Letters **14**(7): 4071-4077.

Liu, Y., et al. (2009). "Tuning optical properties of gold nanorods in polymer films through thermal reshaping." Journal of Materials Chemistry **19**(18): 2704-2709.

Lopez-Leon, T., et al. (2011). "Nematic-Smectic Transition in Spherical Shells." Physical Review Letters **106**(24): 247802.

López Arbeloa, I. and P. Ruiz Ojeda (1982). "Dimeric states of rhodamine B." Chemical Physics Letters **87**(6): 556-560.

Ma, L., et al. (2014). "Functionalized graphene/thermoplastic polyester elastomer nanocomposites by reactive extrusion-based masterbatch: preparation and properties reinforcement." Polymers for Advanced Technologies **25**(6): 605-612.

Ma, X., et al. (2012). "Controllable self-assembling of gold nanorods via on and off supramolecular noncovalent interactions." Langmuir **28**(47): 16263-16267.

Ma, Y., et al. (2006). "Enhanced Sensitivity for Biosensors: Multiple Functions of DNA-Wrapped Single-Walled Carbon Nanotubes in Self-Doped Polyaniline Nanocomposites." The Journal of Physical Chemistry B **110**(33): 16359-16365.

Martin, T. B., et al. (2013). "Polydispersity for Tuning the Potential of Mean Force between Polymer Grafted Nanoparticles in a Polymer Matrix." Physical Review Letters **110**(1): 018301.

Martin, T. B., et al. (2013). "Effect of blockiness in grafted monomer sequences on assembly of copolymer grafted nanoparticles: a Monte Carlo simulation study." Soft Matter **9**(1): 155-169.

Mbhele, Z. H., et al. (2003). "Fabrication and Characterization of Silver−Polyvinyl Alcohol Nanocomposites." Chemistry of Materials **15**(26): 5019-5024.

McFarland, A. D., et al. (2004). "Color My Nanoworld." Journal of Chemical Education **81**(4): 544A.

MerleinJorg, et al. (2008). "Nanomechanical control of an optical antenna." Nat Photon **2**(4): 230-233.

Mie, G. (1908). "Beiträge zur Optik trüber Medien, speziell kolloidaler Metallösungen." Annalen der Physik **330**(3): 377-445.

Miguez, H., et al. (2002). "Mechanical stability enhancement by pore size and connectivity control in colloidal crystals by layer-by-layer growth of oxide." Chemical Communications(22): 2736-2737.

Milner, S. T. (1988). "Compressing Polymer "Brushes": a Quantitative Comparison of Theory and Experiment." EPL (Europhysics Letters) **7**(8): 695.

MILNER, S. T. (1991). "Polymer Brushes." Science **251**(4996): 905-914.

Milner, S. T., et al. (1988). "Theory of the grafted polymer brush." Macromolecules **21**(8): 2610-2619.

Mirkin, C. A., et al. (1996). "A DNA-based method for rationally assembling nanoparticles into macroscopic materials." Nature **382**(6592): 607-609.

Mitchell, C. A., et al. (2002). "Dispersion of Functionalized Carbon Nanotubes in Polystyrene." Macromolecules **35**(23): 8825-8830.

Nair, N., et al. (2011). "Effect of bidispersity in grafted chain length on grafted chain conformations and potential of mean force between polymer grafted nanoparticles in a homopolymer matrix." The Journal of Chemical Physics **134**(19): 194906.

Nguyen, T. D. and S. C. Glotzer (2010). "Reconfigurable Assemblies of Shape-Changing Nanorods." ACS Nano **4**(5): 2585-2594.

Ni, W., et al. (2010). "Evidence for Hydrogen-Bonding-Directed Assembly of Gold Nanorods in Aqueous Solution." The Journal of Physical Chemistry Letters **1**(8): 1181-1185.

Nie, et al. (2008). "“Supramolecular” Assembly of Gold Nanorods End-Terminated with Polymer “Pom-Poms”: Effect of Pom-Pom Structure on the Association Modes." Journal of the American Chemical Society **130**(11): 3683-3689.

Nie, Z., et al. (2007). "Self-assembly of metal-polymer analogues of amphiphilic triblock copolymers." Nat Mater **6**(8): 609-614.

Nie, Z., et al. (2007). "Self-assembly of metal-polymer analogues of amphiphilic triblock copolymers." Nature Materials **6**(8): 609-614.

Nikoobakht, B. and M. A. El-Sayed (2003). "Preparation and Growth Mechanism of Gold Nanorods (NRs) Using Seed-Mediated Growth Method." Chemistry of Materials **15**(10): 1957-1962.

Nikoobakht, B. and M. A. El-Sayed (2003). "Surface-Enhanced Raman Scattering Studies on Aggregated Gold Nanorods†." The Journal of Physical Chemistry A **107**(18): 3372-3378.

Nikoobakht, B., et al. (2002). "Surface-enhanced Raman scattering of molecules adsorbed on gold nanorods: off-surface plasmon resonance condition." Chemical Physics Letters **366**(1–2): 17-23.

Odian, G. (2004). Principles of Polymerization, Wiley.

Oh, H. and P. F. Green (2009). "Polymer chain dynamics and glass transition in athermal polymer/nanoparticle mixtures." Nat Mater **8**(2): 139-143.

Ozaki, M. and E. Matijević (1985). "Preparation and magnetic properties of monodispersed spindle-type γ-Fe2O3 particles." Journal of Colloid and Interface Science **107**(1): 199-203.

Pandian Senthil, K., et al. (2008). "High-yield synthesis and optical response of gold nanostars." Nanotechnology **19**(1): 015606.

Park, C., et al. (2002). "Dispersion of single wall carbon nanotubes by in situ polymerization under sonication." Chemical Physics Letters **364**(3–4): 303-308.

Park, K., et al. (2013). "Growth Mechanism of Gold Nanorods." Chemistry of Materials **25**(4): 555-563.

Peng, Q., et al. (2002). "Selective Synthesis and Characterization of CdSe Nanorods and Fractal Nanocrystals." Inorganic Chemistry **41**(20): 5249-5254.

Petit, C., et al. (1990). "Synthesis of cadmium sulfide in situ in reverse micelles. 2. Influence of the interface on the growth of the particles." The Journal of Physical Chemistry **94**(4): 1598-1603.

Picano, F., et al. (2000). "Coupling between meniscus and smectic-A films: Circular and catenoid profiles, induced stress, and dislocation dynamics." Physical Review E **62**(3): 3747.

Pramod, P. and K. G. Thomas (2008). "Plasmon Coupling in Dimers of Au Nanorods." Advanced Materials **20**(22): 4300-4305.

Qian, X., et al. (2009). "Stimuli-Responsive SERS Nanoparticles: Conformational Control of Plasmonic Coupling and Surface Raman Enhancement." Journal of the American Chemical Society **131**(22): 7540-7541.

Robertson, T., et al. (2013). "Fluorescein Derivatives in Intravital Fluorescence Imaging." Cells **2**(3): 591-606.

Rothemund, P. W. K. (2006). "Folding DNA to create nanoscale shapes and patterns." Nature **440**(7082): 297-302.

Rubinstein, M. and R. H. Colby (2003). Polymer Physics, OUP Oxford.

Rungta, A., et al. (2012). "Grafting Bimodal Polymer Brushes on Nanoparticles Using Controlled Radical Polymerization." Macromolecules **45**(23): 9303-9311.

Sau, T. K. and C. J. Murphy (2004). "Seeded High Yield Synthesis of Short Au Nanorods in Aqueous Solution." Langmuir **20**(15): 6414-6420.

Sauerbrey, G. (1959). "Verwendung von Schwingquarzen zur Wägung dünner Schichten und zur Mikrowägung." Zeitschrift für Physik **155**(2): 206-222.

Schreiber, A., et al. (2015). "Molecular protein adaptor with genetically encoded interaction sites guiding the hierarchical assembly of plasmonically active nanoparticle architectures." Nat Commun **6**: 6705.

Seeman, N. C. (1982). "Nucleic acid junctions and lattices." Journal of Theoretical Biology **99**(2): 237-247.

Senyuk, B., et al. (2012). "Shape-Dependent Oriented Trapping and Scaffolding of Plasmonic Nanoparticles by Topological Defects for Self-Assembly of Colloidal Dimers in Liquid Crystals." Nano Letters **12**(2): 955-963.

Sethi, M., et al. (2009). "Linear Assembly of Au Nanorods Using Biomimetic Ligands." Langmuir **25**(3): 1572-1581.

Shao, L., et al. (2010). "Angle- and Energy-Resolved Plasmon Coupling in Gold Nanorod Dimers." ACS Nano **4**(6): 3053-3062.

Sharma, J., et al. (2009). "Control of Self-Assembly of DNA Tubules Through Integration of Gold Nanoparticles." Science **323**(5910): 112-116.

Sharma, V., et al. (2009). "Colloidal dispersion of gold nanorods: Historical background, optical properties, seed-mediated synthesis, shape separation and self-assembly." Materials Science and Engineering: R: Reports **65**(1–3): 1-38.

Shibu Joseph, S. T., et al. (2006). "Gold Nanorods to Nanochains: Mechanistic Investigations on Their Longitudinal Assembly Using α,ω-Alkanedithiols and Interplasmon Coupling." The Journal of Physical Chemistry B **110**(1): 150-157.

Shull, K. R. (1994). "Wetting autophobicity of polymer melts." Faraday Discussions **98**(0): 203-217.

Sides, S. W., et al. (2006). "Hybrid Particle-Field Simulations of Polymer Nanocomposites." Physical Review Letters **96**(25): 250601.

Skrabalak, S. E., et al. (2007). "Facile synthesis of Ag nanocubes and Au nanocages." Nat. Protocols **2**(9): 2182-2190.

Slaughter, L. S., et al. (2010). "Effects of Symmetry Breaking and Conductive Contact on the Plasmon Coupling in Gold Nanorod Dimers." ACS Nano **4**(8): 4657-4666.

Sreeprasad, T. S. and T. Pradeep (2011). "Reversible Assembly and Disassembly of Gold Nanorods Induced by EDTA and Its Application in SERS Tuning." Langmuir **27**(7): 3381-3390.

Srivastava, S., et al. (2012). "Tethered Nanoparticle–Polymer Composites: Phase Stability and Curvature." Langmuir **28**(15): 6276-6281.

Srivastava, S., et al. (2012). "Tethered Nanoparticle Polymer Composites–Phase Stability and Curvature." Langmuir **28**(15): 6276.

Stöber, W., et al. (1968). "Controlled growth of monodisperse silica spheres in the micron size range." Journal of Colloid and Interface Science **26**(1): 62-69.

Strong, L. and G. M. Whitesides (1988). "Structures of self-assembled monolayer films of organosulfur compounds adsorbed on gold single crystals: electron diffraction studies." Langmuir **4**(3): 546-558.

Sudeep, P. K., et al. (2005). "Selective Detection of Cysteine and Glutathione Using Gold Nanorods." Journal of the American Chemical Society **127**(18): 6516-6517.

Sun, Y. and Y. Xia (2002). "Large-Scale Synthesis of Uniform Silver Nanowires Through a Soft, Self-Seeding, Polyol Process." Advanced Materials **14**(11): 833-837.

Sun, Z., et al. (2008). "pH-Controlled Reversible Assembly and Disassembly of Gold Nanorods." Small **4**(9): 1287-1292.

Sunday, D., et al. (2012). "A Phase Diagram for Polymer-Grafted Nanoparticles in Homopolymer Matrices." Macromolecules **45**(9): 4007-4011.

Tan, S. M. and M. R. Johan (2011). "Effects of MnO2 nano-particles on the conductivity of PMMA-PEO-LiClO4-EC polymer electrolytes." Ionics **17**(6): 485-490.

Thomas, K. G., et al. (2004). "Uniaxial Plasmon Coupling through Longitudinal Self-Assembly of Gold Nanorods." The Journal of Physical Chemistry B **108**(35): 13066-13068.

Tuan, H.-Y., et al. (2005). "Germanium Nanowire Synthesis: An Example of Solid-Phase Seeded Growth with Nickel Nanocrystals." Chemistry of Materials **17**(23): 5705-5711.

Umadevi, S., et al. (2013). "Large Area Self-Assembly of Nematic Liquid-Crystal-Functionalized Gold Nanorods." Advanced Functional Materials **23**(11): 1393-1403.

Ungureanu, C., et al. (2009). "Discrete dipole approximation simulations of gold nanorod optical properties: Choice of input parameters and comparison with experiment." Journal of Applied Physics **105**(10): 102032.

Vial, S., et al. (2013). "Linear Mesostructures in DNA–Nanorod Self-Assembly." ACS Nano **7**(6): 5437-5445.

Vogt, B. D., et al. (2004). "Effect of Film Thickness on the Validity of the Sauerbrey Equation for Hydrated Polyelectrolyte Films." The Journal of Physical Chemistry B **108**(34): 12685-12690.

Wang, M., et al. (2014). "Recognition of Cu2+ and Hg2+ in physiological conditions by a new rhodamine based dual channel fluorescent probe." Sensors and Actuators B: Chemical **192**(0): 512-521.

Wang, Y., et al. (2010). "Solvent-Mediated End-to-End Assembly of Gold Nanorods." The Journal of Physical Chemistry Letters **1**(18): 2692-2698.

Watson, J. H. L., et al. (1962). "THE INTERNAL STRUCTURE OF COLLOIDAL CRYSTALS OF β-FeOOH AND REMARKS ON THEIR ASSEMBLIES IN SCHILLER LAYERS." The Journal of Physical Chemistry **66**(10): 1757-1763.

Weaver, J. H. and P. Fachinformationszentrum Energie, Mathematik Optical Properties of Metals: Noble metals, Aluminum, Scandium, Yttrium, the Lanthanides and the Actinides (0.1 ≲ h[Greek letter nu] ≲ 500 eV), Fachinformationszentrum Energie, Physik, Mathematik.

White, S. I., et al. (2010). "Electrical Percolation Behavior in Silver Nanowire–Polystyrene Composites: Simulation and Experiment." Advanced Functional Materials **20**(16): 2709-2716.

White, S. I., et al. (2011). "Resistive Switching in Bulk Silver Nanowire–Polystyrene Composites." Advanced Functional Materials **21**(2): 233-240.

Wurth, C., et al. (2013). "Relative and absolute determination of fluorescence quantum yields of transparent samples." Nat Protoc **8**(8): 1535-1550.

Xu, C., et al. (2009). "Simultaneous Block Copolymer and Magnetic Nanoparticle Assembly in Nanocomposite Films." Macromolecules **42**(4): 1219-1228.

Xu, X., et al. (2013). "A plasmonically enhanced polymer solar cell with gold–silica core–shell nanorods." Organic Electronics **14**(9): 2360-2368.

Yang, Y., et al. (2015). "High-performance multiple-donor bulk heterojunction solar cells." Nat Photon **9**(3): 190-198.

Yasun, E., et al. (2013). Cancer cell sensing and therapy using affinity tag-conjugated gold nanorods.

Ye, X., et al. (2012). "Improved Size-Tunable Synthesis of Monodisperse Gold Nanorods through the Use of Aromatic Additives." ACS Nano **6**(3): 2804-2817.

Young, K. L., et al. (2014). "Using DNA to Design Plasmonic Metamaterials with Tunable Optical Properties." Advanced Materials **26**(4): 653-659.

Yu, et al. (1997). "Gold Nanorods: Electrochemical Synthesis and Optical Properties." The Journal of Physical Chemistry B **101**(34): 6661-6664.

Yu, K.-K., et al. (2014). "Rhodamine based pH-sensitive "intelligent" polymers as lysosome targeting probes and their imaging applications in vivo." Polymer Chemistry **5**(19): 5804-5812.

Zhang, H. and D. Wang (2008). "Controlling the Growth of Charged-Nanoparticle Chains through Interparticle Electrostatic Repulsion." Angewandte Chemie **120**(21): 4048-4051.

Zhang, J., et al. (2000). "Two-Dimensional Cysteine and Cystine Cluster Networks on Au(111) Disclosed by Voltammetry and in Situ Scanning Tunneling Microscopy." Langmuir **16**(18): 7229-7237.

Zhang, Q., et al. (2011). "A Systematic Study of the Synthesis of Silver Nanoplates: Is Citrate a "Magic" Reagent?" Journal of the American Chemical Society **133**(46): 18931-18939.

Zhang, X., et al. (2008). "Band-Selective Optical Polarizer Based on Gold-Nanowire Plasmonic Diffraction Gratings." Nano Letters **8**(9): 2653-2658.

Zhang, X., et al. (2012). "Wavelength, Concentration, and Distance Dependence of Nonradiative Energy Transfer to a Plane of Gold Nanoparticles." ACS Nano **6**(10): 9283-9290.

Zhao, D., et al. (2013). "Reversible gold nanorod assembly triggered by pH-responsive DNA nanomachine." Applied Physics Letters **102**(12): 123101.

Zhou, J., et al. (2014). "Interfacial Assembly of Mussel-Inspired Au@Ag@ Polydopamine Core–Shell Nanoparticles for Recyclable Nanocatalysts." Advanced Materials **26**(5): 701-705.

Zijlstra, P., et al. (2012). "Optical detection of single non-absorbing molecules using the surface plasmon resonance of a gold nanorod." Nat Nano **7**(6): 379-382.

Zocher, H. and W. Heller (1929). "Schillerschichten als Reaktionsprodukte der langsamen Eisenchlorid-Hydrolyse." Zeitschrift für anorganische und allgemeine Chemie **186**(1): 75-96.